



## Crystallization Phenomena and Local Structure in Oligomer Thin Films and Polymer Fibers

Huss-Hansen, Mathias Kasper

*Publication date:*  
2021

*Document Version*  
Publisher's PDF, also known as Version of record

[Link back to DTU Orbit](#)

*Citation (APA):*  
Huss-Hansen, M. K. (2021). *Crystallization Phenomena and Local Structure in Oligomer Thin Films and Polymer Fibers*. Technical University of Denmark.

---

### General rights

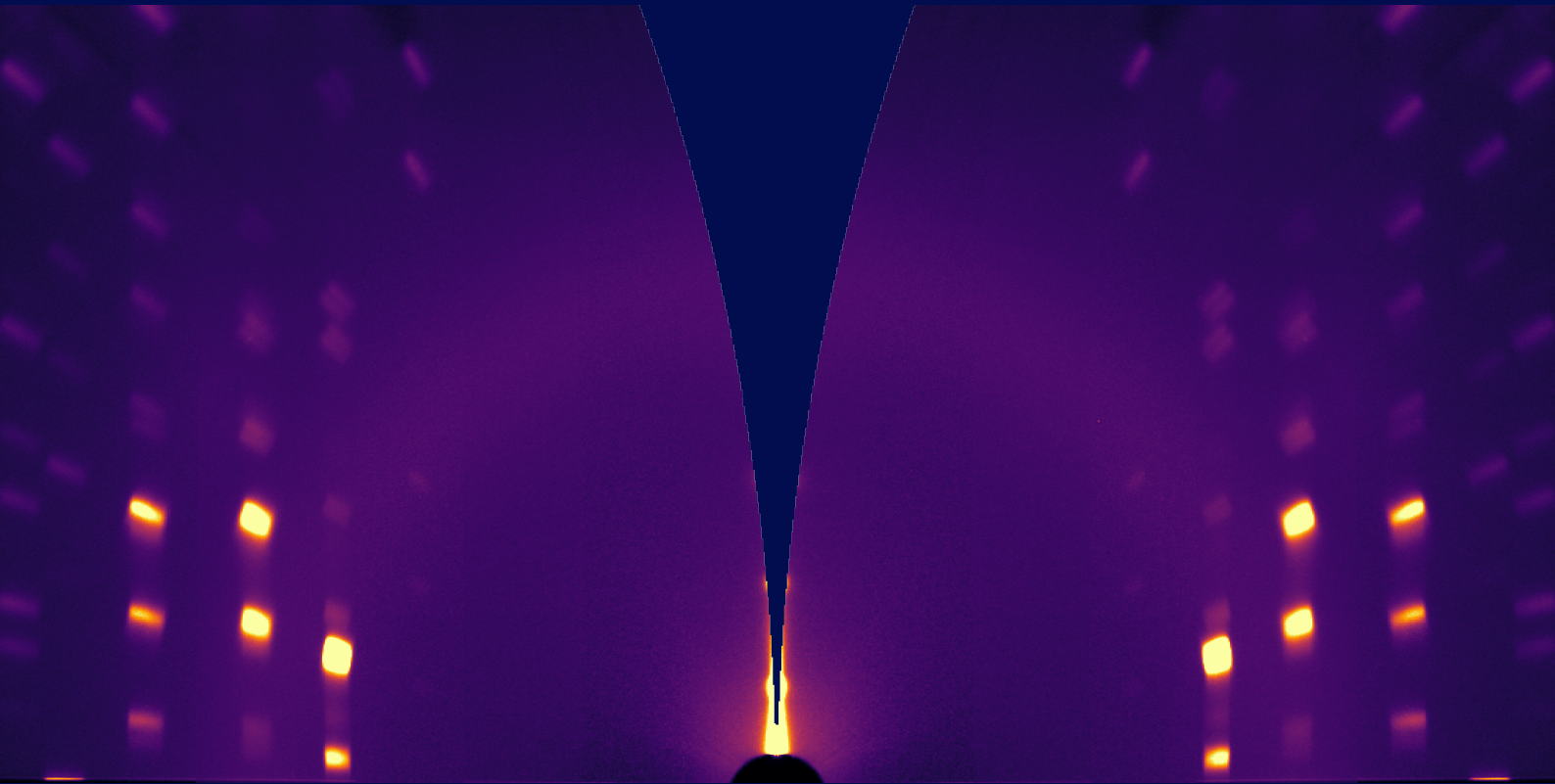
Copyright and moral rights for the publications made accessible in the public portal are retained by the authors and/or other copyright owners and it is a condition of accessing publications that users recognise and abide by the legal requirements associated with these rights.

- Users may download and print one copy of any publication from the public portal for the purpose of private study or research.
- You may not further distribute the material or use it for any profit-making activity or commercial gain
- You may freely distribute the URL identifying the publication in the public portal

If you believe that this document breaches copyright please contact us providing details, and we will remove access to the work immediately and investigate your claim.

# Crystallization Phenomena and Local Structure in Oligomer Thin Films and Polymer Fibers

Mathias K. Huss-Hansen  
PhD Thesis





## **Crystallization Phenomena and Local Structure in Oligomer Thin Films and Polymer Fibers**

PhD Thesis  
February 2021

By  
Mathias K. Huss-Hansen

Principal supervisor: Matti Knaapila (DTU Physics)

Co-supervisor: Luigi Balzano (Royal DSM)

Copyright: Reproduction of this publication in whole or in part must include the customary bibliographic citation, including author attribution, report title, etc.

Cover photo: GIWAXS pattern of 5 nm NaT<sub>2</sub> film. By Mathias K. Huss-Hansen.

Published by: DTU, Department of Physics, Fysikvej, Building 311, 2800 Kgs. Lyngby Denmark  
[www.fysik.dtu.dk](http://www.fysik.dtu.dk)



# Acknowledgments

---

This thesis represents the culmination of my PhD project, and for better or for worse, a large part of the last three years of my life. None of this would have been possible without all the support and guidance I have received throughout and I would like to take this opportunity to thank the people involved.

The work was carried out the section for Neutron and X-rays for Materials Physics (NEXMAP) at the Department of Physics of the Technical University of Denmark. Funding for this project was in part provided by Royal DSM, The Netherlands. I would also like to acknowledge the Danish Agency for Science, Technology, and Innovation for funding the instrument center DanScatt, and the Otto Mønsted Foundation and the European Cooperation in Science and Technology (COST) for financial support.

Above all, I am indebted to my supervisor Matti Knaapila for the opportunity to carry out this project and explore my interests in material science. I have enjoyed the freedom to pick and choose what I found most interesting under his supervision, and he has been excellent in guiding the research. I wish you all the best in future and hope that our paths may cross again someday.

I would like to extend the same gratitude to my co-supervisor Luigi Balzano. I am thankful for his support and guidance in carrying out the part of my research on polymers, and for all of the interesting discussions and stories. Even though the originally envisioned project never got off the ground, I am happy with what we ended up accomplishing in its place.

I would also like to thank Jakob Kjelstrup-Hansen, who has been like a third supervisor to me. I am grateful for our discussions and for all the experimental assistance he has provided. I wish you the best of luck with being a father.

A huge thanks goes to all of the beamline scientists in Hamburg, Lund, Grenoble, and Trieste, for all the help in setting up and running experiments. I will always look back on my beamline experiences with great fondness, and the work they do to make the everyday operation appear seamless is nothing less than incredible. I would especially like to thank Anton Davydok of HZG for his enormous help in setting up the fiber diffraction experiments at P03.

I am grateful for the time I got to spend with Peter Siffalovic and his group in Bratislava.

Through our collaboration I got to meet some incredible people, including Nada Mrkyvkova and Jakub Hagara, who supported me in acquiring, analyzing and interpreting data. I am humbled by their willingness to always put aside their own work to help. I would also like to thank Martin Hodas and the rest of the Frank Schreiber group for the opportunity to join their beamtime and for their invaluable assistance in carrying out experiments.

A huge thanks goes to Michael Winokur of the University of Wisconsin for great discussion and company. I hope you enjoyed your time in Denmark, and if I ever find myself in or near Madison, Wisconsin, I will make sure to get in touch.

I would also like to thank all my colleagues at DTU Physics for good company and for all the inspiring talks I have had the privilege to listen to throughout the years. A special thanks goes to Søren Nimb for his help in designing and printing our custom sample holder.

Throughout these last three years I have thoroughly enjoyed the company of friends and family, who have helped in making this adventure a memorable one. There are far too many to list here (officemates, classmates, old friends and new), but each and every one of you are greatly appreciated. A special thanks to Andreas for all the comments on the manuscript and for great conversation; to the group of friendly faces at DSM (Marie, Emily, Alessandro, Simone, Patricia, Jesse, and Kelly), whom I have to thank for some of the best times during this project; and to Wenjie, whom I have had the pleasure to share an office with during this entire project. Most importantly, I am privileged to have the unwavering support of my parents and sister. Thank you for putting up with me for all these years.

# Abstract

---

This thesis explores the structure formation of two different soft material systems: naphthyl end-capped oligothiophenes in thin film configuration and ultra-high molecular weight polyethylene (UHMWPE) fibers.

The molecular packing of organic semiconductors in thin films determines their optoelectronic properties. Although the final state of these films is often well known, the fundamental dynamic processes governing the self-organization of the molecules are not yet fully understood. In the first part of the thesis, by using in situ grazing incidence X-ray scattering, we study the crystallization of naphthyl end-capped oligothiophene thin films in realtime during vacuum deposition. We find that the thin film packing deviates from the one found in single crystals, and that surface-molecule interactions play a dominant role in the formation of the first few molecular layers of the film. On silicon substrates, these early layers grow in a layer-by-layer fashion with a strained unit cell. Upon reaching a critical thickness, subsequent layers follow three-dimensional growth and the unit cell is relaxed. On strongly interacting substrates, such as graphene, we observe a change in the molecular orientation, which may be used to control and enhance the optical absorption. These results are complemented by scattering experiments with microfocused X-ray beams, which reveal lateral variations in the film's microstructure, for example in the proximity of the bottom-contact electrodes in organic field-effect transistors.

Fibers made from ultra-high molecular weight polyethylene have remarkable tensile strength and modulus, owing to their high degree of crystallinity and near perfect alignment of the polyethylene chains along the fiber direction. While these fibers are known to exhibit skin-core structures, in which the structure near the surface deviates from the structure in the core, few attempts have been made to quantify this phenomenon. In the second part of the thesis, we present a framework based on micro- and nanofocused X-ray scattering techniques supported by polarized Raman spectroscopy for mapping the spatially resolved microstructure and morphology in polymer fibers with 1  $\mu\text{m}$  resolution. We demonstrate its usefulness by showing mapping results from individual gel-spun UHMWPE fibers, whose diameter falls within limits of tens to hundreds of micrometers. All samples display clear skin-core structure, with an increased degree of orientation of the PE crystallites and increased interlamellar spacing in the skin region.

Our findings have importance in both fundamental science and engineering applications.



## Resumé

---

Denne afhandling omhandler strukturdannelsen af to forskellige bløde materialer: naphthyl endeafluttede oligothiophener i tyndfilm og ultrastærke polyethylenfibre.

Pakningen af molekylerne i organiske tyndfilmshalvledere er afgørende for deres optoelektroniske egenskaber. Selvom sluttetilstanden af disse tyndfilm ofte er kendt, så mangler der stadig en større forståelse for de grundlæggende dynamiske processer, der styrer selvorganiseringen af molekylerne. I den første del af afhandlingen undersøger vi, ved brug af in situ røntgenspredning under græsningsincidens, tyndfilmsdannelsen af naphthyl endeafluttede oligothiophener i realtid under vakuumdeponering. Vi viser hvordan pakningen af molekylerne i tyndfilm afviger fra pakningen i enkeltkrystaller, og hvordan vekselvirkningen mellem molekylerne og underlagsoverfalden er afgørende for dannelsen af de første molekulære lag. På silicium underlag dannes de første molekulære lag et lag ad gangen med en anstrengt enhedscelle. Efter at filmen har nået en kritisk tykkelse, skifter lagdannelsen til tredimensionel lagdannelse med en mere afslappet enhedscelle. På stærkt vekselvirkende underlag, såsom grafen, observerer vi en ændring i molekylernes orientering, hvilket kan bruges til at forbedre den optiske absorption i tyndfilmene. Disse resultater er suppleret med røntgenspredningseksperimenter med en mikrofokuseret stråle, der viser at mikrostrukturen varierer på tværs af tyndfilmene, for eksempel i nærheden af elektroderne i organiske felteffekttransistorer.

Den høje trækstyrke af fibre fremstillet af polyethylen med ultrahøj molekylvægt skyldes, at de udstrakte polymerkæder danner højkrystallinske strukturer med nær perfekt orientering af kæderne langs fiberaksen. Tidligere studier har vist at fibre indeholder skind-kerne strukturer, hvor materialestrukturen i den yderste del af fiberen afviger fra strukturen i kernen. På trods af at dette er et velkendt fænomen, eksisterer der meget få studier, hvor skind-kerne strukturen er forsøgt kvantificeret. I den anden del af afhandling foreslår vi en metoderamme, baseret på røntgenspredningstekniker med en smalt fokuseret stråle og polariseret Raman spektroskopi, til at kortlægge mikrostrukturen og morfologien i polymerfibre med en rummelig opløsning på én mikrometer. Vi demonstrerer metoderammens brugbarhed ved at vise resultater fra gel-spundne polyethylenfibre, der har diametre på få hundrede mikrometer. De undersøgte fibre viser alle klare skind-kerne strukturer, med en forøget krystalorientering og større interlamellære afstande i skind regionen.

Vores resultater er vigtige både for grundforskning og for tekniske anvendelsesmuligheder.



# List of Publications

---

## Paper I

Structural basis for a naphthyl end-capped oligothiophene with embedded metallic nanoparticles for organic field-effect transistors

Mathias K. Huss-Hansen, Marie Hansteen, Jes Linnet, Anders Runge Walther, Jakob Kjelstrup-Hansen, and Matti Knaapila.

*Appl. Phys. Lett.* **113**, 251903 (2018)

## Paper II

Surface-Controlled Crystal Alignment of Naphthyl End-Capped Oligothiophene on Graphene: Thin-Film Growth Studied by in situ X-ray Diffraction

Mathias K. Huss-Hansen, Martin Hodas, Nada Mrkyvkova, Jakub Hagara, Bjarke Bror Egede Jensen, Andreas Osadnik, Arne Lützen, Eva Majková, Peter Siffalovic, Frank Schreiber, Luciana Tavares, Jakob Kjelstrup-Hansen, and Matti Knaapila.

*Langmuir* **36**, 1898-1906 (2020)

## Paper III

Early-stage growth observations of orientation-controlled vacuum-deposited naphthyl end-capped oligothiophenes

Mathias K. Huss-Hansen, Martin Hodas, Nada Mrkyvkova, Jakub Hagara, Peter Nadazdy, Michaela Sojkova, Simon O. Høegh, Alina Vlad, Pallavi Pandit, Eva Majkova, Peter Siffalovic, Frank Schreiber, Jakob Kjelstrup-Hansen, and Matti Knaapila.

*Submitted to Phys. Rev. Mater. in revised form, January 2021*

## Paper IV

Structural effect of electrode proximity in vacuum deposited organic semiconductors studied by microfocused X-ray scattering

Mathias K. Huss-Hansen, Jakob Kjelstrup-Hansen, and Matti Knaapila.

*Submitted to Adv. Eng. Mater., January 2021*

## Paper V

Local Structure Mapping of Gel-Spun Ultrahigh-Molecular-Weight Polyethylene Fibers

Mathias K. Huss-Hansen, Erik G. Hedlund, Anton Davydok, Marie Hansteen, Jildert Overdijk, Gert de Cremer, Maarten Roeffaers, Matti Knaapila, and Luigi Balzano.

*(To be submitted to Macromolecules)*



# Contents

---

<b>Acknowledgments</b>	<b>iii</b>
<b>Abstract</b>	<b>v</b>
<b>Resumé</b>	<b>vii</b>
<b>List of Publications</b>	<b>ix</b>
<b>Introduction</b>	<b>xiii</b>
<b>Part I Background</b>	<b>1</b>
<b>1 X-rays and their Interaction with Matter</b>	<b>3</b>
1.1 X-ray scattering . . . . .	3
1.2 Synchrotron radiation . . . . .	7
1.3 X-ray focusing . . . . .	8
<b>2 Small-Molecule Semiconductor Thin Films</b>	<b>11</b>
2.1 Organic semiconductors . . . . .	11
2.2 Structure and packing . . . . .	16
2.3 Charge transport . . . . .	18
2.4 Thin film preparation . . . . .	21
2.5 Thin film growth . . . . .	22
2.6 Surface templating . . . . .	25
<b>3 Methods for Characterizing Thin Films</b>	<b>27</b>
3.1 Grazing incidence wide-angle X-ray scattering . . . . .	27
3.2 Grazing incidence small-angle X-ray scattering . . . . .	36
3.3 Atomic force microscopy . . . . .	38
3.4 UV-Vis absorption spectroscopy . . . . .	38
<b>4 Ultra-High Molecular Weight Polyethylene Fibers</b>	<b>41</b>

4.1	General properties . . . . .	41
4.2	Gel-spinning . . . . .	44
4.3	Structure and morphology . . . . .	48
<b>5</b>	<b>Methods for Characterizing Polymer Fibers</b>	<b>55</b>
5.1	Wide-angle X-ray scattering . . . . .	55
5.2	Small-angle X-ray scattering computed tomography . . . . .	62
	<b>Summary and Conclusions</b>	<b>69</b>
	<b>Bibliography</b>	<b>73</b>
	<b>Part II Results and Publications</b>	<b>89</b>
	<b>Paper I</b>	<b>91</b>
	<b>Paper II</b>	<b>97</b>
	<b>Paper III</b>	<b>115</b>
	<b>Paper IV</b>	<b>151</b>
	<b>Paper V</b>	<b>163</b>

# Introduction

---

The macroscopic properties of any material is ultimately defined by the materials internal structure on the microscopic level. Different materials posses different properties, and one of the first steps in improving material performance is to understand the fundamental structure-property relationships in play. The properties of interest vary based on the material application. For example, some applications require materials with a certain response to an externally applied force, while other applications require materials with the ability to absorb light or conduct current. A fundamental understanding of material structure is thus paramount in the design and development of new engineering materials of all kinds.

Soft organic materials are particular interesting, since their solid-state structure is often distinctly complex. Organic molecules are largely made up of carbon atoms that are covalently bonded to each other and other elements, such as hydrogen. Unlike inorganic solids (e.g. metals), which are almost always crystalline in their solid-state, organic materials can be either amorphous or crystalline (or both, i.e. semicrystalline), and their solid-state structure depends largely on the preceding processing. Moreover, due to the anisotropic nature of most organic molecules, their material properties are likewise often anisotropic on a macroscopic scale.

In this thesis, we study the fundamental structure of two markedly different organic materials. The majority of the thesis concerns the microstructure and crystallization processes of organic semiconductor thin-films based on naphthyl end-capped oligothiophenes. These materials belong to the family of molecular organic semiconductors, and are characterized by being rigid rod-like molecules with a high degree of structural anisotropy, and consequently, anisotropic material properties. The single-crystal bulk structures of these materials are already well known, and in this work, we extend our knowledge by studying their microstructure and morphology in the device relevant thin-film configuration. Of particular interest is the first few molecular layers of the thin-film structure, as the structure of these layers is governed by substrate-molecule interactions and play a crucial role for the optoelectronic properties of the final films [1].

The rest of the thesis concerns the local structure of a specific class of high-strength synthetic polymer fibers based on ultra-high molecular weight polyethylene (UHMWPE). Fibers made from UHMWPE have remarkable mechanical properties, including high ten-

sile strength and modulus at low weight, originating from near perfect alignment of the molecular chains along the fiber direction. The structural development and structure-property relationships of these fibers have been studied extensively since the discovery of their unique gel spinning process in the late 1970s. Despite this, a number of challenges still impose themselves, including the need for a quantitative understanding of the local variations in structure inside the fiber. While it is known that UHMWPE fibers exhibit some degree of structural inhomogeneity along their radial axis [2, 3], the topic is far less explored and only few comprehensive studies exist. To this end, we present a framework for studying the local microstructure and morphology in synthetic polymer fibers with high spatial resolution ( $\sim 1 \mu\text{m}$ ) and apply it to the case of gel spun UHMWPE fibers.

The structural studies of both of these materials presented in this thesis rely heavily on the use of X-ray scattering. The small wavelengths of X-rays enable direct probing of structures on the molecular length scale, making them ideal for structural studies of solid-state matter. Since the discovery of X-rays in the late 19th century by Wilhelm Röntgen, and the subsequent discoveries by Max von Laue and William and Lawrence Bragg on X-ray diffraction, X-ray techniques have served as the principal methods for determining the structural arrangement of atoms and molecules in crystals. Today, X-ray scattering and diffraction are used to determine everything from the inner structure of protein complexes to chemical reactions on a femtosecond timescale. Much of this work is facilitated by the increased availability of synchrotron radiation sources, where a high photon flux can be combined with high beam collimation and tunable X-ray energies.

Due to the diverse material nature of this work, the scope of this thesis goes beyond any single scientific field. Rather, it is interdisciplinary work that combines aspects from several fields, including material science, condensed matter physics, surface science, and polymer physics. We approach the fundamental questions of material structure from an applied engineering perspective, as the materials chosen for the most part are relevant for engineering applications.

For this same reason, it is counterproductive to boil the aim of this thesis down to a single question or hypothesis. Instead, the scientific challenges and questions are presented and put into broader context along the way. However, on an overall level, the results presented in this thesis contribute the fundamental understanding of the material structure in the two classes of materials, and to the understanding of the underlying physics governing their structure formation.

This thesis consists of two parts: (I) a scientific background of the two classes of the materials studied and (II) our results presented in the form of five self-contained publications. The first part is made up of Chapters 1-5. Chapter 1 describes the basics of X-ray scattering, Chapters 2-3 introduces the materials and experimental techniques relevant for the thin-film studies, and Chapter 4-5 explores the material and methodological background of the fiber studies. At the end of part I, the main results and conclusions of the five papers are presented together with an outlook for future research. The second part of the thesis is made up of Papers I-V. In Papers I-IV, our results on thin-films are presented, while Paper V presents our results on UHMWPE fibers.

# **Part I**

## **Background**



## CHAPTER 1

# X-rays and their Interaction with Matter

---

This chapter introduces the basic properties of X-rays and their interaction with matter. The specific scattering experiments used in this work and their instrumental setups are presented later in Chapters 3 and 5.

## 1.1 X-ray scattering

X-rays are useful tools for studying the complex structure of organic materials, since their wavelength is on the same order of magnitude as the relevant structural features. In the classical description, X-rays are electromagnetic waves with wavelengths in the region of angstrom ( $10^{-10}$  m). It is common to distinguish between hard X-rays (with wavelengths of  $\sim 0.1$  Å to 2 Å) and soft X-rays ( $\sim 2$  Å to 100 Å). A monochromatic X-ray beam can be described as a linearly polarized plane wave propagating along a direction in space. The electric field of the propagating wave can be written as  $\mathbf{E}(\mathbf{r}, t) = \hat{\mathbf{e}}E_0e^{i(\mathbf{k}\mathbf{r}-\omega t)}$ , where  $\hat{\mathbf{e}}$  is the unit vector of the electric field polarization,  $\mathbf{k}$  is the wavevector and  $\omega$  is the angular frequency. The electric field is perpendicular to the propagation direction in (transverse) electromagnetic waves, that is  $\hat{\mathbf{e}} \cdot \mathbf{k} = 0$ .

In the quantum mechanical description, the monochromatic X-ray beam is quantized into individual photons with energy  $\hbar\omega$  and momentum  $\hbar\mathbf{k}$ . When the X-ray photons interact with matter, they are either scattered or absorbed. Let us consider the simplest process of an X-ray being scattered by a single electron. The scattering can be either elastic, where the photon energy is conserved, or inelastic, where a portion of the photon energy is transferred to the electron resulting in a scattered photon with lower frequency. Since elastic scattering is the main process being exploited in structure determination, the following considerations are limited to this type. Elastic scattering can be described sufficiently by only considering the classical picture, and the following arguments and notations follow those given in Ref. [4].

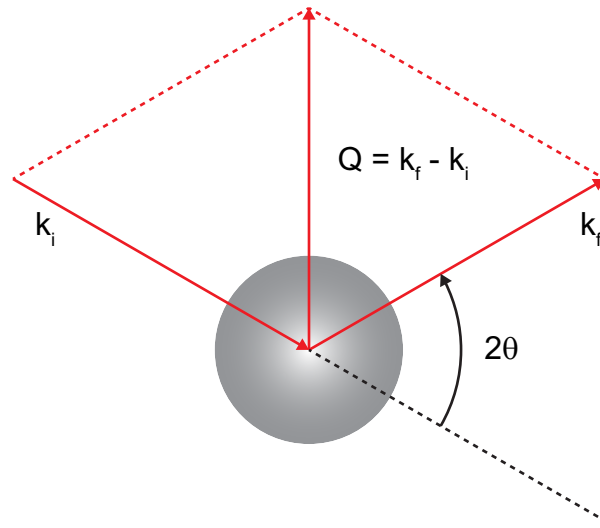


**Figure 1.1:** Scattering triangle relating the incoming and outgoing wave vectors  $\mathbf{k}_i$  and  $\mathbf{k}_f$  with the scattering vector  $\mathbf{q}$ .

### 1.1.1 Scattering vector

Elastic scattering is described by the scattering vector or momentum transfer vector  $\mathbf{q}$  as

$$\mathbf{q} = \mathbf{k}_f - \mathbf{k}_i, \quad (1.1)$$

where  $\mathbf{k}_f$  and  $\mathbf{k}_i$  are the final and initial wavevectors of the scattered photon, respectively. The scattering event is illustrated in Fig. 1.1. Since the scattering is elastic, the lengths of the two wavevectors are equal (i.e.  $|\mathbf{k}_f| = |\mathbf{k}_i|$ ), and from the scattering triangle we have

$$|\mathbf{q}| = 2|\mathbf{k}| \sin \theta = \frac{2\pi}{\lambda} \sin \theta, \quad (1.2)$$

where  $2\theta$  denotes the scattering angle and  $\lambda$  is the wavelength of the X-rays. The scattering vector  $\mathbf{q}$  is located in the conceptual three-dimensional reciprocal space, and is accordingly expressed in units of  $\text{\AA}^{-1}$ .

### 1.1.2 Scattering from one electron

The fundamental quantity determined in an X-ray scattering experiment is the differential scattering cross-section ( $\frac{d\sigma}{d\Omega}$ ), which is essentially a measure of the number of scattered photons measured by the detector per second per solid angle  $\Delta\Omega$  normalized to the flux of the incident X-ray beam. In the case of an electromagnetic plane wave, the photon flux of the incident beam is proportional to  $|\mathbf{E}_{\text{in}}|^2$ , and the number of scattered photons measured by the detector at distance  $R$  subtending the solid angle  $\Delta\Omega$  is proportional to  $|\mathbf{E}_{\text{rad}}|^2 R^2 \Delta\Omega$ . The differential scattering cross-section is then given by

$$\left(\frac{d\sigma}{d\Omega}\right) = \frac{|\mathbf{E}_{\text{rad}}|^2 R^2}{|\mathbf{E}_{\text{in}}|^2}. \quad (1.3)$$

The elastic scattering from a single electron can be thought of as a propagating spherical wave with its origin at the electron. When the electron is placed in the electric field of the incident X-ray beam, it starts to oscillate, which then creates the radiating spherical wave. The ratio of the radiated electric field to that of the incident electric field is

$$\frac{E_{\text{rad}}(R, t)}{E_{\text{in}}} = -r_0 \frac{e^{ikR}}{R} |\hat{\boldsymbol{\epsilon}}_i \cdot \hat{\boldsymbol{\epsilon}}_f|, \quad (1.4)$$

where  $r_0 = e^2/(4\pi\epsilon_0 mc^2)$  is the Thomson scattering length (or sometimes the classical radius) of the electron. From Eq. (1.3), the differential scattering cross-section of an electromagnetic wave by a free electron is then given by

$$\left(\frac{d\sigma}{d\Omega}\right) = r_0^2 |\hat{\epsilon}_i \cdot \hat{\epsilon}_f|^2 = r_0^2 p(\psi). \quad (1.5)$$

Here,  $p(\psi) = |\hat{\epsilon}_i \cdot \hat{\epsilon}_f|^2$  is defined as the polarization factor, which depends on the X-ray source.

### 1.1.3 Scattering from one atom

Now let us consider the case where the X-ray scatters from several electrons in the form of an atom. The distribution of the electrons can classically be described by a charge cloud surrounding the nucleus with number density  $\rho(\mathbf{r})$ . The radiated waves from the electrons will interact and cause constructive or destructive interference depending on their relative difference in phase. The total radiated field can thus be described as a superposition of scattering contributions from different volume elements  $d\mathbf{r}$ , with each contribution amounting to  $-r_0\rho(\mathbf{r})d\mathbf{r}$  plus a phase factor of  $e^{i\mathbf{q}\cdot\mathbf{r}}$ . By integrating over contributions from all volume elements, the total scattering length of the atom is then given by

$$F_0(\mathbf{q}) = -r_0 f^0(\mathbf{q}) = -r_0 \int \rho(\mathbf{r}) e^{i\mathbf{q}\cdot\mathbf{r}} d\mathbf{r}, \quad (1.6)$$

where  $f^0(\mathbf{q})$  is called the atomic form factor. Equation (1.6) is just the Fourier transform of the electron density distribution in the sample. In the limit  $\mathbf{q} \rightarrow 0$ , all scattering contributions from the individual volume elements are necessarily in phase so that  $f^0(\mathbf{q} = 0) = Z$ , that is the number of electrons in the atom. Similarly, as  $\mathbf{q}$  increases, the volume elements will start to scatter out-of-phase and  $f^0(\mathbf{q} \rightarrow \infty) = 0$ .

In principle, the atomic form factor is dependent on the energy of the external X-ray field as [4]

$$f(\mathbf{q}, \hbar\omega) = f^0(\mathbf{q}) + f'(\hbar\omega) + i f''(\hbar\omega), \quad (1.7)$$

where  $f'$  and  $f''$  are known as the dispersion corrections to  $f^0$ . The former is related to the binding energies of the electrons, while the latter denotes the phase lag of the electron with respect to the driving field, and is related to the absorption in the atom.

### 1.1.4 Scattering from a molecule

The scattering length of a molecule can be derived using a similar approach. If the molecule consists of  $N$  atoms, and each atom is treated as an isolated electron distribution sphere, then the total scattering length of the molecule is a simple superposition

$$F^{\text{mol}}(\mathbf{q}) = -r_0 \sum_j^N f_j(\mathbf{q}) e^{i\mathbf{q}\cdot\mathbf{r}_j}, \quad (1.8)$$

where  $f_j(\mathbf{q})$  is the atomic form factor of the  $j$ 'th atom in the molecule.

### 1.1.5 Scattering from a crystal

Finally, let us consider the case where the scattering molecules are arranged in a periodic way on a lattice (i.e. a crystal). For a crystal lattice with a set of lattice planes set a

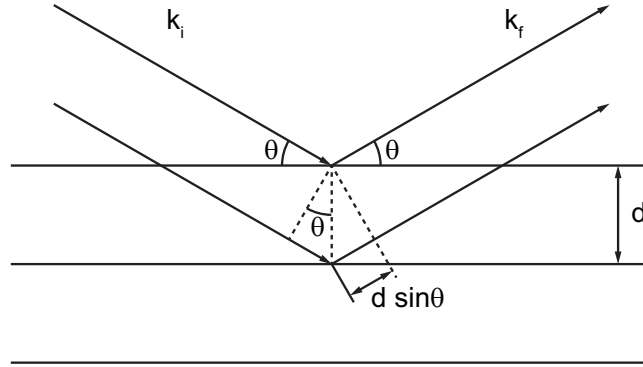


**Figure 1.2:** Derivation of Bragg's law in a crystal with a set of lattice planes set a distance  $d$  apart.

distance  $d$  apart (see Fig. 1.2), the condition for constructive interferences of the scattered waves is given by Bragg's law

$$m\lambda = 2d \sin \theta, \quad (1.9)$$

where  $m$  is an integer and  $\theta$  is the angle of the incident wave to the lattice planes. Bragg's law is convincing in that it gives the correct result, and is a consequence of the periodicity of the lattice. However, it does not take into account the compositions of atoms inside the lattice structure. In general, the scattering amplitude from a crystalline material comprised of atoms is

$$F^{\text{crystal}}(\mathbf{q}) = \sum_l^{\text{All atoms}} f_l(\mathbf{q}) e^{i\mathbf{q}\cdot\mathbf{r}_l}, \quad (1.10)$$

where  $f_l(\mathbf{q})$  is the atomic form factor from Eq. (1.6) for the  $l$ 'th atom located at  $\mathbf{r}_l$  and the factor of  $-r_0$  has been dropped. The lattice of a crystalline material can be specified by a set of lattice vectors

$$\mathbf{R}_n = n_1 \mathbf{a}_1 + n_2 \mathbf{a}_2 + n_3 \mathbf{a}_3, \quad (1.11)$$

where  $n_1, n_2, n_3$  are arbitrary integers and  $(\mathbf{a}_1, \mathbf{a}_2, \mathbf{a}_3)$  defines the basis vectors of the unit cell, which is a structural basis group of atoms that forms the crystal structure by regular repetition in space. In other words, the crystal structure can be described as a convolution of the lattice, constituting a mathematical set of repeating points in space, and the unit cell [5]. Thus, the position of any atom in the crystal structure can be written as  $\mathbf{r}_l = \mathbf{R}_n + \mathbf{r}_j$ , where  $\mathbf{R}_n$  is the lattice vector and  $\mathbf{r}_j$  is the position of the atom within the unit cell. The expression for scattering amplitude in Eq. (1.10) can thus be decomposed as

$$F^{\text{crystal}}(\mathbf{q}) = \sum_n e^{i\mathbf{q}\cdot\mathbf{R}_n} \sum_j f_j(\mathbf{q}) e^{i\mathbf{q}\cdot\mathbf{r}_j}. \quad (1.12)$$

Here, the first term sums over the lattice while the second term is a sum over the atoms inside the unit cell, also known as the structure factor. The decomposition corresponds to taking the Fourier transform of the crystal structure, which must be the product of the Fourier transforms of the lattice and the unit cell basis, since the crystal structure is a convolution of the two.

The sum of the phases in the lattice term of Eq. (1.12) is on the order of unity, except when all the phases are a multiple of  $2\pi$ , that is

$$\mathbf{q} \cdot \mathbf{R}_n = 2\pi \times (\text{integer}). \quad (1.13)$$

In wavevector space, we define a lattice spanned by the basis  $(\mathbf{a}_1^*, \mathbf{a}_2^*, \mathbf{a}_3^*)$ , which fulfills  $\mathbf{a}_i \cdot \mathbf{a}_j^* = 2\pi\delta_{ij}$ . Points on this reciprocal lattice are given by

$$\mathbf{G} = h\mathbf{a}_1^* + k\mathbf{a}_2^* + l\mathbf{a}_3^*, \quad (1.14)$$

where  $h, k, l$  are arbitrary integers. A vector of this form is called a reciprocal lattice vector, and it satisfies the condition of Eq. (1.13) since

$$\mathbf{G} \cdot \mathbf{R}_n = 2\pi(hn_1 + kn_2 + ln_3) = 2\pi \times (\text{integer}), \quad (1.15)$$

because the term in the parenthesis is an integer, being the sum of products of integers. The so-called Laue condition for observed diffraction is thus fulfilled when the scattering vector coincides with the reciprocal lattice vector, that is  $\mathbf{q} = \mathbf{G}$ . It can be shown that the Laue condition is equivalent to the diffraction condition given by Bragg's law (Eq. (1.9)) [4].

## 1.2 Synchrotron radiation

Many of the X-ray scattering experiments presented in this thesis are only possible with the use of synchrotron radiation available at large scale facilities. Synchrotron radiation is a generic term used to describe radiation originating from charged particles traveling at relativistic speeds that are subject to an applied transverse magnetic field, which forces them to move radially [4]. At synchrotron facilities, bunches of electrons are accelerated to relativistic speeds in evacuated storage-rings, reaching kinetic energies in the GeV range. The electrons are steered by large bending magnets mounted along the peripheries of the rings. The radial acceleration of the electrons in turn emits photons tangentially to the plane of the electron beam. Radiation from a bending magnet covers a wide spectrum of wavelengths and the brilliance is inherently limited as a consequence. The brilliance is a figure-of-merit describing several aspects of the X-ray beam and is defined as

$$\text{Brilliance} = \frac{\text{Photons/second}}{(\text{mrad})^2(\text{mm}^2 \text{ source area})(0.1\% \text{ BW})}, \quad (1.16)$$

where the photon flux is normalized to the beam divergence in mrad, the area of the source in  $\text{mm}^2$ , and 0.1% of the relative energy bandwidth (BW).

Newer synchrotron facilities make use of insertion devices, such as undulators, situated in straight sections of the storage ring in addition to bending magnets. In undulators, the electrons are subjected to an alternating applied magnetic field, forcing them to move along an oscillating path. This generates a much more brilliant and coherent beam, where the wavelength of the X-rays can be tuned by changing the gap between the alternating magnets.

Synchrotron facilities are equipped with several beamlines, each with their own unique optic- and experimental end-station setups. This means that each individual beamline is specifically designed for certain types of experiments. The experimental work in Papers I-V was performed at several different synchrotron beamlines, including the Micro- and Nanofocus X-ray Scattering beamline (P03) at the PETRA III Synchrotron (Hamburg, Germany) [6, 7], and the MaxIV NanoMax beamline (Lund, Sweden) [8]. Unique to both of these two beamlines is the ability to narrowly focus the beam in the sample plane, allowing for detailed measurements with high spatial resolution. The focusing of X-ray beams is briefly discussed below.

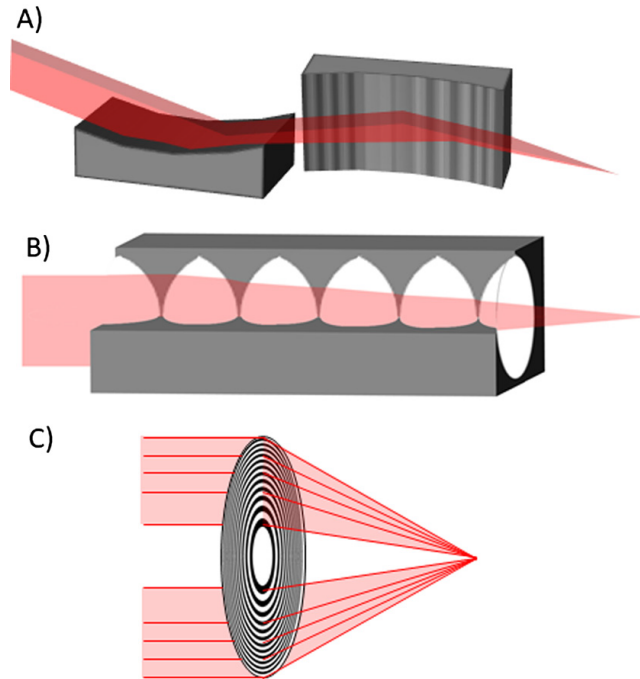


**Figure 1.3:** Focusing optics for X-ray beams. a) Kirkpatrick–Baez (KB) mirror system, b) compound refractive lenses (CRLs), and c) Fresnel zone-plates (FZP). Reprinted from Ref. [9] under the Creative Commons License.

### 1.3 X-ray focusing

The experiments carried out in Papers I, IV and V all rely on narrowly focused X-ray beams in order to enable mapping of the microstructure in our samples with high spatial resolution. This requires the use of specific beamlines equipped with advanced focusing optic systems. In the following, a brief overview will be given of the focusing optics of the two micro- and nanofocus beamlines employed.

The Micro- and Nanofocus X-ray Scattering beamline (P03) of PETRA III [6, 7] is supplied with photons from an undulator source located in the PETRA III storage ring. The undulator source is a critical prerequisite for achieving a microfocused beam with high flux and low divergence. After passing through a silicon (111) monochromator, where the beam is monochromatized by Bragg reflections in a set of near perfect Si crystals, higher harmonics are suppressed by a coated planar double mirror. Two sets of compound refractive lenses (CRLs) are used for collimation and initial focusing of the beam, with each set of CRLs containing multiple lenses that can be moved in and out of the X-ray beam independently, allowing for optimization of the beam size and divergence. CRLs consists of tens or hundreds of individual concave lenses arranged in series along the optical axis [10], see Fig. 1.3b. In its most simple form, the lenses are made by boring a series of holes in a low-Z material, such as aluminum. The X-rays are refracted at the aluminum-vacuum interface with focal length  $F = \frac{R}{2\delta}$ , where R is the radius of curvature and  $\delta$  is the real component of the refractive index, which is small ( $\delta \sim 10^{-5} - 10^{-7}$ ) for X-rays in matter. By using a large number ( $N$ ) of lenses in series, the focusing distance becomes  $N$  times shorter compared to using a single lens. Focusing along two dimensions can even be achieved by arranging an array of holes in crossed geometry [10].

After prefocusing by the CRLs, the beam is focused to its final spot size by superpolished,

nanofocusing Kirkpatrick-Baez (KB) mirrors [7, 11]. KB mirrors are elliptical and rely on grazing incidence reflection of the X-ray beam off the curved surface. Two mirrors are aligned perpendicular to each other in series (Fig. 1.3a), resulting in a beam that is focused in both dimensions. The KB mirror system at P03 can achieve a spot size of  $1.4 \mu\text{m} \times 1.4 \mu\text{m}$  while maintaining a total photon flux of  $3 \times 10^{10} \text{ s}^{-1}$ .

The NanoMAX beamline of Max IV [8] also uses an undulator source to supply the photons. Two mirrors are used for the initial focusing of the beam, with the first mirror focusing the beam in the vertical direction by sagittal focusing, and the second mirror focusing the beam in the horizontal direction by meridional focusing. The beam is then monochromatized by a double Si(111) crystal monochromator, employed in a horizontal diffraction geometry for improved beam stability. Afterwards, the beam encounters a secondary source aperture with two pairs of slits, which acts as a flexible source for the subsequent nanofocusing optics. In its current form, the final focusing optics at NanoMAX uses KB mirrors to achieve a spot size of 100 to 1000 nm. A secondary experimental station is currently in development that relies on Fresnel zone plates (FZPs) to achieve an even smaller beam diameter of 10 nm. FZPs (Fig. 1.3c) are chromatic diffractive lenses and rely on diffraction rather than reflection. The detailed working principles of FZPs are described in detail in Ref. [12].



## CHAPTER 2

# Small-Molecule Semiconductor Thin Films

---

This chapter provides the introduction and material background for Papers I-IV.

## 2.1 Organic semiconductors

Organic semiconductors (OSCs) are carbon-based optoelectronic materials with electrical conductivities between that of insulators  $\sigma < 10^{-8}$  (s/cm) and that of metals  $\sigma > 10^3$  (s/cm). Unlike conventional semiconductors, organic molecules are predominantly bonded by soft van der Waals forces, that gives rise to unique solid-state properties [13–16]. The softness provided by the weaker van der Waals bonds can lead to rich mechanical properties that are not unlike those of some plastics, including a high degree of flexibility of the films [17–19]. At the same time, many OSCs facilitate low cost, large area deposition onto a large variety of substrates at ambient or near ambient conditions [20–22]. They can be chemically tailored for specific applications, including facile tuning of the optical and electronic properties.

The promises of OSCs has lead to a large growth of the field in recent years. In general, the field can be simplified into the following subfields: the design and synthesis of new OSC molecules, the design and fabrication of new organic electronic devices, and fundamental studies of the structure-property relationships in OSCs, including the crystallization of the solid-state structure during deposition. The content of Papers I-IV relates mostly to the latter topic. OSCs have also established themselves as commercialized technologies across a vast range of applications, with the most notable ones being organic light-emitting diode (OLED) display technology, which became a US\$25 billion industry in 2018 [23], and organic photovoltaics (OPVs), which has emerged as a promising alternative to conventional Si-based solar cells. Other applications of OSCs, owing to their unique ability to combine mixed electronic and ionic conduction, include organic electrochemical transistors (OECTs) [24], suitable for biological interfacing, and chemical and biological sensors [25]. Of course, one would be amiss not to mention the organic field-effect transistor (OFET), which constitutes the foundation for many of the established and emerging OSC

technologies. While the charge transport properties of OSCs have improved dramatically since the infant stages of OFETs in the 1980s, they have yet to reach levels close to that of conventional crystalline silicon. A main performance metric for OFETs is the charge carrier mobility  $\mu$  ( $\text{cm}^{-1} \text{V}^{-1} \text{s}^{-1}$ ). The best performing OSCs reliably reach mobility values of  $\mu > 1 - 10 \text{ cm}^{-1} \text{V}^{-1} \text{s}^{-1}$  [23], which is still a ways off the typical mobility values for crystalline Si (on the order of  $1000 \text{ cm}^{-1} \text{V}^{-1} \text{s}^{-1}$  for electrons and  $100 \text{ cm}^{-1} \text{V}^{-1} \text{s}^{-1}$  for holes).

Organic semiconductors are typically employed in the form of thin films (on the order of a few nm to hundreds of micron), and their active electronic and optical properties originate from the  $\pi$ -conjugated bonding structure, where the electrons are delocalized over larger areas (detailed discussing below). For this reason, the majority of OSCs are composed of a core of aromatic unit that are linked together (see Fig 2.1). The aromatic units allows for  $\pi$ -bonding along the length of the molecule, and charge transport between neighboring molecules generally occurs via a thermally activated hopping mechanism (Section 2.3). In general, OSCs can be divided into two groups: conjugated polymers and small molecules. Polymers are larger molecules with several repeating units and inherent conformational flexibility, and as a consequence, their thin-film structure is typically less crystalline (or even amorphous) with a high degree of disorder. On the other hand, small molecules are typically rigid and rod-like, and their crystalline structure in films is often well ordered. In Papers I-IV, the focus lies on the structural properties of small organic compounds and the following discussion is therefore limited to this class of materials.

### 2.1.1 Selected small molecules

Figure 2.1 lists some of the commonly studied small-molecule organic semiconductors together with the naphthyl end-capped oligothiophenes employed in Papers I-IV. The selected molecules are not meant to be an exhaustive list of all relevant compounds; such a list would be well beyond the scope of this introductory chapter. Rather, it is a selection representing some of the most typical cases, many of which are referenced in Papers I-IV. A more exhaustive list of good performing small molecules can be found in Ref. [13].

One of the most studied rod-like OSCs is pentacene, which is composed of five benzene rings arranged in a linear structure. It belongs to the family of fused ring acenes. Pentacene is used extensively as a model system for understanding the fundamental growth of OSC films [26–28], and is known to grow via different surface induced polymorphs depending on the growth conditions and underlying substrate [29]. Studies of the submonolayer and monolayer regime has revealed a particular molecular arrangement, with the pentacene molecules standing completely upright (i.e. no tilt) on the substrate surface [30]. The thin-film phase (which is different from the submonolayer phase discussed above) and the bulk phases of pentacene all have the same molecular arrangement, with the molecules packed in a herringbone structure. In addition, pentacene films exhibit relatively high field effect mobilities ( $\mu > 1 \text{ cm}^{-1} \text{V}^{-1} \text{s}^{-1}$ ) in ambient conditions [31]. Anthony et al. first synthesized a solution-processable variant of pentacene [32], namely 6,13-bis(triisopropylsilylethynyl)pentacene (TIPS-pentacene), where the TIPS group is substituted onto the central 6- and 13-position of the pentacene core. TIPS-Pentacene exhibits high mobilities exceeding  $1 \text{ cm}^{-1} \text{V}^{-1} \text{s}^{-1}$  [33], originating from the slipped  $\pi$ - $\pi$  stacking, in which the stacking direction lies in the plane parallel to the substrate plane [34].

Historically, rubrene is one of the most studied OSC molecules besides pentacene due to its high carrier mobility. Different polymorphs of rubrene are found in the literature

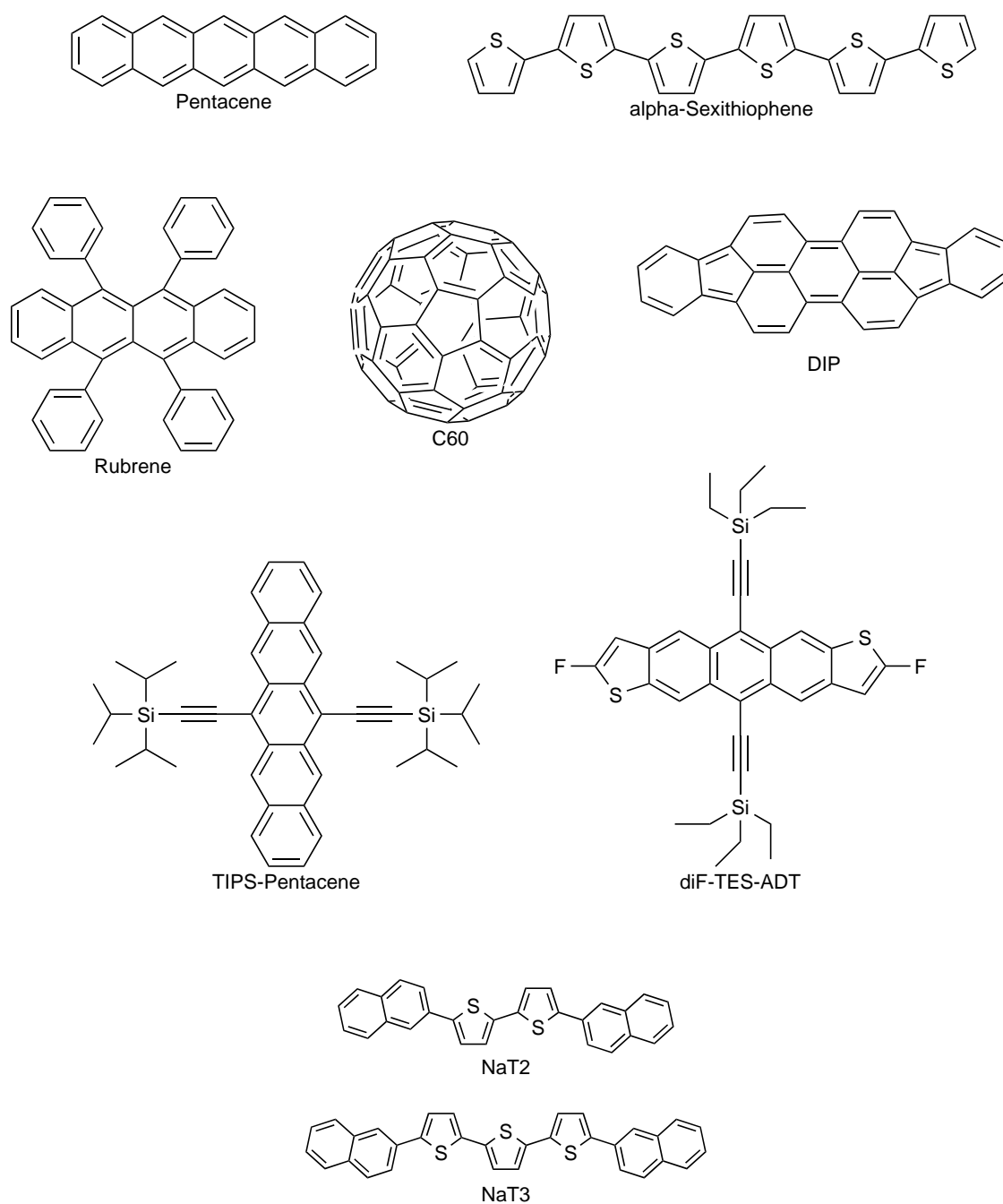


**Figure 2.1:** Selection of small molecule organic semiconductors discussed in this introduction. Chemical structure from top right: Pentacene,  $\alpha$ -sexithiophene ( $\alpha$ -6T), rubrene, C60, diindenoperylene (DIP), triisopropyl (TIPS) pentacene, 2,8-difluoro-5,11-bis(triethylsilylethynyl)anthradithiophene (diF-TES-ADT), 5,5'-bis(naphth-2-yl)-2,2'-bithiophene (NaT2), and 5,5''-bis(naphth-2-yl)-2,2':5',2''-terthiophene (NaT3).

[29], with the orthorhombic phase with space group  $Cmca$  exhibiting the highest carrier mobilities of up to  $40 \text{ cm}^{-1} \text{ V}^{-1} \text{ s}^{-1}$  [35].

Fullerene C60 constitutes a special case as one of the simplest model systems available for small molecules due to its simple isotropic shape. Fullerene is most commonly used as the acceptor material in organic bulk heterojunction solar cells [36], where a  $\pi$ -conjugated polymer is used as the donor material completing the fullerene:polymer blend films. The multilayer growth of fullerene was extensively studied by Bommel et al. [37], elucidating the fundamental processes for van der Waals bonded molecules in the intermediate case between atoms and colloids.

Much like pentacene, diindenoperylene (DIP) is an often used model system for studying thin film growth [38–41]. It belongs to the family of perylene derivatives and is a prototypical example of a rigid molecule with planar conformation. DIP shows an enantiotropic polymorphic phase transformation at 403 K from a low T triclinic  $\alpha$ -phase with doubled unit cell volume to a high T monoclinic  $\beta$ -phase [42]. The transformation can be understood as a structural reorientation of the molecules and rearrangements due to strong shearing of the layers against each other. Real-time studies have shown a dynamic transition from layer-by-layer growth to rapid roughening after  $\sim 10 \text{ ML}$  [40], with the thin-film induced phase being identical to the high T  $\beta$ -phase [29].

Other prototypical conjugated materials are based on thiophenes. The most simple variants hereof are the unsubstituted oligothiophenes, including the oligomers with four to eight thiophene rings. Figure 2.1 shows one such unsubstituted oligothiophene with six thiophene rings in the form of  $\alpha$ -sexithiophene ( $\alpha$ -6T).  $\alpha$ -6T is a prototypical compound used in growth studies [43, 44], and in OPVs [45, 46] due to its combination of high carrier mobilities and favorable optical gap. Much like pentacene,  $\alpha$ -6T forms several different polymorphs in films. Common features for these polymorphs are herringbone packing motifs and planar conformations. By functionalizing either the  $\alpha$ - or  $\beta$ -positions of the thiophene rings, the solubility or solid-state ordering can be increased dramatically [47]. Halik et al. evaluated a series of alkyl-substituted oligothiophenes [48], and found that the length of the alkyl chains had a significant influence on the carrier mobility in top contact devices, with improved field-effect-mobility values over their non-substituted counterparts. In another study, Merlo et al. [49] showed that hybrid acene-thiophene (i.e. oligothiophenes with acene end-group substitutions) formed highly crystalline films with a high degree of thermal stability and overall better stability in ambient conditions compared to pentacene, while still retaining a relatively high carrier mobility. More recently, acceptor–donor–acceptor type oligothiophenes have attracted some interest for use as donor materials in small molecule organic solar cells [50, 51]. The molecules employed in Papers I–IV all belong to the family of substituted oligothiophenes and are discussed below.

For completeness, 2,8-difluoro-5,11-bis(triethylsilylethynyl)anthradithiophene (diF-TES-ADT), which is the fluorinated derivative of TES-ADT, is shown as well in Fig. 2.1. This molecule is discussed in Paper IV, and represents a solution-processable molecule widely discussed in the literature [29]. The synthesis of diF-TES-ADT was first reported by Anthony et al. in Ref. [52]. Their high performance ( $\mu \simeq 6 \text{ cm}^{-1} \text{ V}^{-1} \text{ s}^{-1}$ ) is attributed to the brick-wall packing motif, which allows for a large orbital overlap between four nearest neighbor molecules.

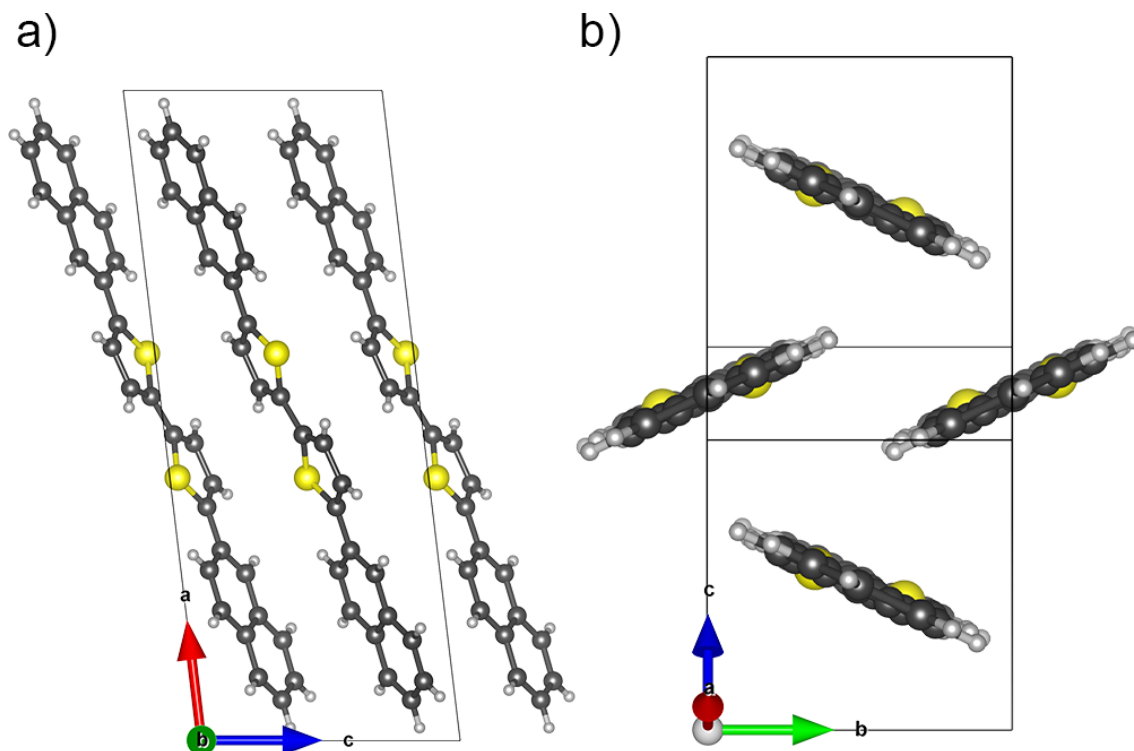


**Figure 2.2:** Single crystal packing of NaT2 after Ref. [53]. a) View along the b-axis and b) view along the molecular backbone showing the herringbone motif.

### 2.1.2 Naphthyl end-capped oligothiophenes

Papers I-IV all concern the structure and self-organization of naphthyl end-capped oligothiophenes, namely 5,5'-bis(naphth-2-yl)-2,2'-bithiophene (NaT2) and 5,5''-bis(naphth-2-yl)-2,2':5',2''-terthiophene (NaT3, see Fig. 2.1). Both molecules belong to the family of substituted oligothiophenes, where the bithiophene (NaT2) and terthiophene (NaT3) core units are terminated by naphthyl end groups. They were first synthesized by Tian et al. in 2007 by means of Suzuki or Stille cross-couplings [53]. From a structural point of view, the NaT $n$  molecules (where  $n$  represents the number of thiophene rings) represent two cases of stiff, rod-like small molecules. Their bulk single-crystal structures were reported in Ref. [53], with NaT2 having a monoclinic unit cell with  $P2_1/c$  symmetry and parameters  $a = 20.552 \text{ \AA}$ ,  $b = 5.964 \text{ \AA}$ ,  $c = 8.120 \text{ \AA}$  and  $\beta = 96.845^\circ$  (see Fig. 2.2). Here, the authors use the (non-conventional) notation of  $a$  as the molecular long-axis. For this reason, we employ the same notation throughout Papers I-IV. Each unit cell contains two molecules, that locally pack into a repeating herringbone motif. On the other hand, the NaT3 single-crystal packing is more complex, with the molecules adopting an unusual three-layer repeat, in which the molecules in the middle layer adopt a slightly more coplanar conformation and a slightly different tilt angle. Due to the unusual packing, the monoclinic unit cell of NaT3 ( $a = 73.996 \text{ \AA}$ ,  $b = 5.917 \text{ \AA}$ ,  $c = 8.866 \text{ \AA}$  and  $\beta = 92.564^\circ$ ) contains a total of 6 molecules, that likewise pack into a herringbone motif. We have previously determined the thin-film packing of NaT2 to be similar to the bulk single-crystal packing [54]. The thin-film packing of NaT3 is reported for the first time in Paper I.

Furthermore, the NaT $n$  molecules represent interesting cases for fundamental studies of structure and self-organization in small molecule OSC films. Importantly, they both tend to form highly crystalline films, enabling X-ray diffraction studies of very thin layers

with thicknesses comparable to the length of the molecules. Moreover, they represent two symmetrically different yet chemically similar cases. The NaT2 molecule exhibits inversion symmetry with respect to its geometric center, while NaT3 has mirror symmetry about a plane bisecting the central thiophene ring. These symmetry considerations are further discussed in Paper III.

We have also carried out molecular dynamic simulations of the NaT $n$  films in parallel with the experimental work presented in Papers I-IV. Our findings, which are presented in Ref. [55], point towards an appreciable amount of disorder in both systems, with a large number of flipped molecules (i.e. flipped 180° about its long axis) incorporated into the thin-film structure.

From an application point of view, the NaT $n$  molecules have promising potentials in low-voltage organic phototransistors [56, 57], and they display a high structural stability in atmospheric conditions under load [54]. In addition, they can self-assemble into one-dimensional so-called nanofibers on muscovite mica surfaces in vacuum [58].

## 2.2 Structure and packing

The structure and molecular arrangement of OSC thin films are highly complex entities, that involve structural phenomena on length scales from nanoscale to device scale (see Fig. 2.3). It is important to understand the film's structure on all the length scales in order to fully describe the structure-property relationships. In this section, we will briefly discuss some of the structural phenomena at play in small molecule OSC films. It is by no means exhaustive and for further information, the reader is directed to the excellent body of literature on the subject, including Refs. [16, 59, 60].

On the molecular level, OSCs are based on the delocalization of electrons in the  $\pi$  bond via conjugation. In  $\pi$ -conjugated materials, the molecular backbone consists primarily of carbon and hydrogen atoms. Carbon atoms are composed of an atomic nuclei and six electrons, which are distributed into the  $1s^2 2s^2 2p^2$  orbital structure in the ground state. In  $\pi$ -conjugated materials, one electron from the  $2s$  orbitals and two electrons from the  $2p$  orbitals are hybridized into three identical  $sp^2$  orbitals, all of which are arranged in the same plane forming  $\sigma$  bonds with neighboring carbon atoms. This leaves one electron forming a  $p_z$  orbital perpendicular to the plane of the  $\sigma$  bonds, which is then available for  $\pi$ -bonding. By conjugation of neighboring  $\pi$  bonds, the electrons become delocalized over a larger area, facilitating the carrier transport in the OSC. For example, benzene, which is an aromatic ring composed of six carbon atoms, is held together by  $\sigma$  bonds in the plane, leaving six electrons in the delocalized  $\pi$  state. The majority of OSCs are composed of aromatic rings linked together, providing delocalization of the  $\pi$  electrons over the entire backbone of the molecule. The delocalization or conjugation length of the  $\pi$  orbitals is a common parameter used to control the bandgap in OSCs [59], as well as the energy levels of the highest occupied molecular orbital (HOMO) and lowest unoccupied molecular orbital (LUMO), which determines properties such as absorption onset and charge carrier injection [61].

Neighboring molecules are then held together predominantly by van der Waals forces, and it is their solid-state packing (i.e. their crystal structure) that dictates the local optoelectronic properties of the OSC film [23, 62]. Depending on the packing motif, the overlap of adjacent orbitals in neighboring molecules can vary significantly (see Fig. 2.5), influencing carrier transport (discussed in Section 2.3) and optical absorption, among others. The molecular arrangement of OSCs is sensitive not only to the chemical nature

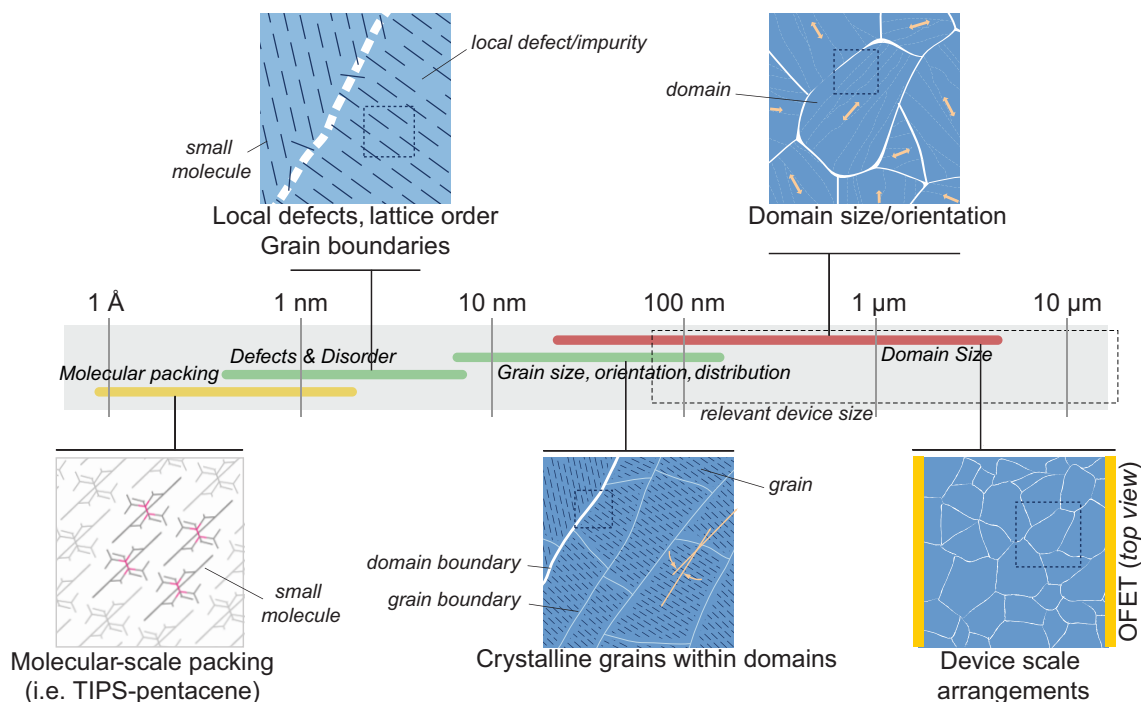


**Figure 2.3:** Size scales and relevant morphological features in single-component small-molecule semiconductor films. Within each schematic, the square denotes the enlarged region preceding it. Adapted with permission from Ref. [59]. Copyright 2012 American Chemical Society.

of the materials, including size, aspect-ratio (anisotropy), and side-chains or end-groups [34, 63], but also to the dynamic processes involved in film growth (see Section 2.5). The (ideal) crystal structure of OSCs is described by the crystalline unit cell and the molecule arrangement inside this unit cell, with characteristic feature sizes on the angstrom to nanometer scale (see Fig. 2.3). However, the crystalline structure of OSC films is never perfect, and crystalline defects exist on many different length scales. These defects inevitably affect the optoelectronic properties of the materials, for example by acting as charge traps or scattering centers that limits the charge carrier mobility [64]. Defects on the nanometer length scale include local one-dimensional defects, such as dislocations of the same types as found in inorganic crystals (edge, screw etc.) [65], and impurities from chemically different or degraded molecules incorporated into the lattice structure. Other types of local defects include two-dimensional stacking faults.

In OSC thin films (or, more precisely, in any crystalline material), the accumulation of defects and distortions to the crystalline lattice over longer length scales lead to cumulative disorder. Cumulative disorder, also termed paracrystalline disorder, therefore describes the long-range statistical variations in the lattice parameters (compared with the ideal lattice), and gives rise to characteristic broadening of the diffraction peaks in X-ray diffraction [66]. Cumulative disorder should be distinguished from noncumulative disorder, which includes lattice fluctuations due to thermal motion.

On intermediate length scales, the structure of OSC films is characterized by features ascribed to the crystallites (i.e. the small individual crystals forming the macroscopic film) such as size, interfacial boundaries, and orientation and texture. In any polycrystalline film, grain-boundaries will inevitably exist between adjacent crystalline grains due to the crystallographic mismatch between them. In OSC films, one often distinguishes between

low-angle grain boundaries and high-angle grain boundaries, relating to the misorientation angle between the neighboring crystallites [64, 67]. Low-angle grain-boundaries separate adjacent crystallites that are only slightly misoriented, and they are typically not observed by direct imaging methods such as scanning probe techniques [64]. On the other hand, high-angle grain boundaries are characterized by a high degree of misorientation between adjacent crystallites. Neighboring crystalline structures separated by high-angle grain-boundaries are sometimes referred to as domains (see Fig. 2.3). In the literature, the umbrella term of grains is often used to describe the two cases interchangeably without distinction. However, this distinction is rather important since the two types of grain-boundaries affect charge transport differently, the details of which are discussed in Ref. [67]. The apparent domains visible in thin films on the microscale (see Fig. 2.3) are sometimes misidentified as single grains, when they in reality are composed of many smaller crystalline grains (or simply crystallites) separated by low-angle grain-boundaries. It should be mentioned that grain-boundaries in OSCs are fundamentally different from grain-boundaries in inorganic crystals, since no covalent bonds are broken or strained at the boundary in OSCs. This is because the OSC crystallites have more degrees of freedom to relax and reorganize due to their soft, van-der-Waals-bonded nature. Grain-boundaries can exist along any direction, but in polycrystalline thin films with in-plane texture (i.e. the crystallites have common out-of-plane orientation, but are randomly oriented in the plane), the misorientation angles between neighboring crystallites are typically greatest in the plane. However, as we shall see in Paper IV, the crystallites also exhibit a varying degree of misorientation along the out-of-plane direction. The orientation of the crystallites (and the molecules making up the crystallites) is also of importance, and depending on the application, certain molecular orientations are preferable. For example, the photoabsorption can be maximized by aligning the molecular backbone, and thus the dominant transition dipole, in the plane of the substrate, while optimal charge transport in OFETs usually requires the  $\pi$  orbitals to be in the plane parallel to the dielectric layer, that is, in a configuration with the molecules are standing near upright on the substrate.

Finally, on device relevant length-scales, it is the connectivity and size of the domains that ultimately determines the material performance. In OFETs, the charge transport is generally thought to be faster within the domains than across the domain-boundaries [67, 68], and possibilities for controlling the grain (domain) size has been studied extensively. For example, the grain sizes can be controlled by surface-treatments [69], or by incorporation small amounts of nucleation seed material in the film [70]. Moreover, the crystalline structure and morphology can vary locally on the device scale due to variations in the local surface environment, for example near the contact electrodes in bottom-contact OFETs (see rightmost image in Fig. 2.3). Paper IV explores these electrode proximity effect on the film's microstructure in detail.

## 2.3 Charge transport

The charge transport in organic semiconductors is a complex subject and it has been debated for many years. The following discussion is by no means exhaustive and serves to present the reader with an overview of some of the mechanisms involved. For a more complete picture, the reader is referred to one of the many excellent review articles on the topic [13, 23, 71, 72, & references therein].

In general, the transport mechanisms in solids are different depending on the chemical and structural nature of the materials. and yield vastly different mobilities as a consequence. In conventional inorganic semiconductors (such as Si), the charge carriers are so-called Bloch

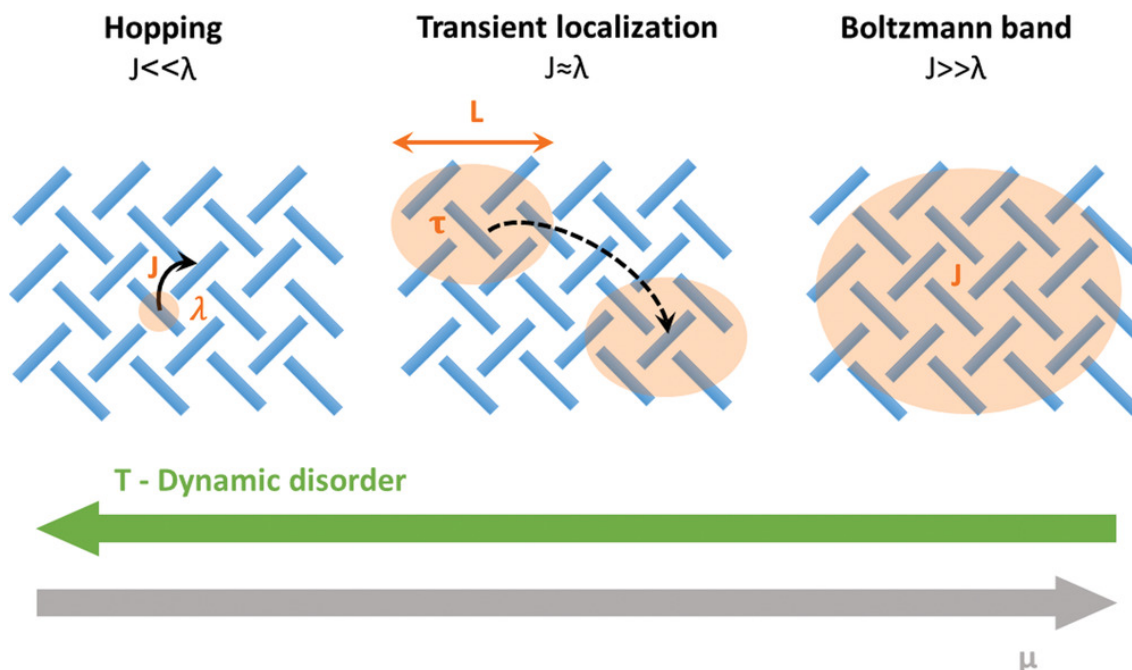


**Figure 2.4:** Schematic illustration of the models describing charge transport in organic and inorganic semiconductors. The shaded orange area represents the charge delocalization. Reprinted from [13] under the Creative Commons License.

electrons with their wavefunctions delocalized and extended over the crystalline lattice. The propagating Bloch electrons may be scattered by lattice vibrations or defects in an otherwise perfect lattice. If the mean free path of the carriers, that is, the path between collisions, is much larger than the lattice spacing, this semiclassical band picture holds. However, this is generally not the case for OSCs, where the weak van der Waals bonding results in strong electron-phonon coupling [13]. The dynamic disorder, combined with the relatively high degree of static disorder compared with inorganic crystals, means that the mean free path of the electrons in OSCs typically are on the order of the lattice itself [13]. In organic solids with low mobilities, the charge transport can instead be described by the hopping model [13, 23]. In this model, the charge carriers are localized to individual molecules and the transport takes place through a series of hopping events, with charges jumping between adjacent interacting molecules. If the residence time of the carrier charge at the molecule is sufficiently long, the molecule (and the surrounding molecules) has time to undergo a relaxation process, creating an energy barrier for the carrier to overcome in the hopping process.

For high performing OSCs in the intermediate regime, the charge carrier transport can be described by a third model called the transient localization model [73]. In this regime, the measured charge carrier mobilities are faster than what is expected from the hopping model, but the carrier mean free path is still not sufficiently large for the transport to be described by the Boltzmann band model. In the transient localization model, the larger thermal vibrations of the molecules are thought to cause a quantum localization of the wavefunctions on timescales shorter than oscillation period of the molecules. This physical mechanism is denoted as transient localization, and strongly suppresses the charge diffusivity, limiting the carriers ability to fully delocalize. Another way to consider the carrier transport in the transient localization regime is as follows [13]: on timescales short than the molecular vibrations, the charge carriers are localized by the dynamic disorder of the

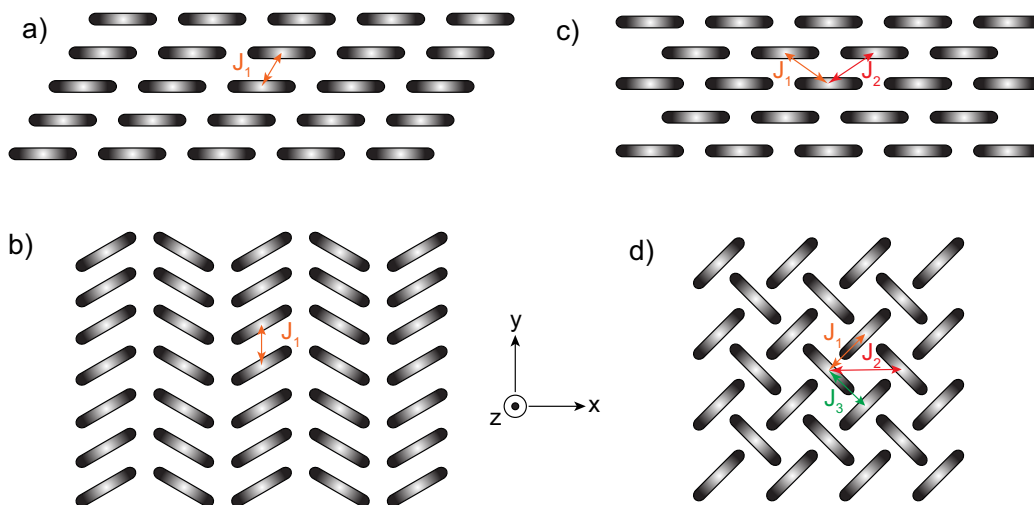


**Figure 2.5:** Schematic illustration of the most common packing motifs of organic semiconductors. a) Slipped-stack and b) slipped  $\pi$ -stack arrangements with one major transfer integral ( $J_i$ ). c) Brick-wall arrangement with two major transfer integrals. d) Herringbone arrangement with three major transfer integrals, allowing more isotropic transport in the  $x$ - $y$  plane.

molecules, while on timescale longer than the molecular vibrations, they undergo diffusive motion, explaining the observations of certain band-like qualities such as decreasing mobilities with increasing temperatures [23].

The three regimes can also be described in terms of the reorganization energy of the molecules  $\lambda$  and the wavefunction overlap of neighboring molecular orbitals  $J$ . The situations are sketched on Fig. 2.4. The hopping model applies in the weak coupling regime ( $J \ll \lambda$ ), where the wavefunction is localized to a single molecule. In the strong coupling regime ( $J \gg \lambda$ ), the Boltzmann band model applies and the wavefunctions are fully delocalized and extended over large areas. The intermediate regime, where the wavefunction overlap  $J$  and the molecular reorganization energy  $\lambda$  are similar, the charge transport can be described by the transient localization model. For the sake of completeness, it is worth mentioning the approximate mobility values for the different regimes. Fratini et al. [23] provide the lower limit for charge transport via the Boltzmann band model as  $\mu \gtrsim 50 \text{ cm}^{-1} \text{ V}^{-1} \text{ s}^{-1}$ , and the breakdown of the transient localization regime at  $\mu \lesssim 0.5 \text{ cm}^{-1} \text{ V}^{-1} \text{ s}^{-1}$ , below which charge transport takes place via hopping. In the same reference, the authors also give calculated  $J$  values for a number of high mobility OSCs.

Due to the highly anisotropic nature of most OSC molecules, the charge transport is likewise highly anisotropic, with carrier mobilities being significantly higher in specific directions (in some cases, the difference is several orders of magnitude). Figure 2.5 summarizes the four most common packing motifs observed in OSCs. The pathways for charge transport are determined by the overlap of the molecular orbitals, also denoted as the charge transfer integrals  $J$ . In slipped-stack and slipped  $\pi$ -stack arrangements (Figs. 2.5a and b), the transfer integral is strong in only one direction, resulting in unidirectional charge transport properties. The brick-wall packing (Fig. 2.5c) gives access to a second major charge transfer integral, while the common herringbone packing has three large transfer

integrals (Fig. 2.5d), resulting in the most isotropic charge transport in the plane (specifically the  $x$ - $y$  plane in Fig. 2.5). The charge carrier mobilities are typically found to be highest in OSCs with herringbone configurations [23], likely due to the isotropic nature of the charge transfer integrals. It has also been shown that high-angle grain-boundaries are less detrimental in herringbone-packed materials compared to slip-stacked materials [67], which makes intuitively sense in light of the isotropic charge transfer integrals, and due to the fact that a high-angle grain-boundary in herringbone-packed materials does not necessarily equate to a high degree of misorientation between the molecules because of the two-molecule basis. As previously mentioned, pentacene (along with most small molecules OSCs) films pack according to the herringbone motif, while TIPS-pentacene is an example of molecules packed in the brick-wall motif [34].

The anisotropic nature of OSCs suggests that the charge transport properties can be manipulated by controlling the solid-state packing in films, in addition to lowering the amount of (static) disorder.

## 2.4 Thin film preparation

Organic semiconductor thin films are grown by various processes depending on the chemical nature of the material and the desired properties of the film. In general, smaller molecules such as rod-like oligomers are grown by deposition in vacuum from vapor, while larger molecules such as  $\pi$ -conjugated polymers or functionalized oligomers are deposited from solution [15, 47, 74, 75]. Solution processing involves dissolving the organic semiconductor in an organic solvent and subsequently coating the substrate by either drop-casting, spin-coating, dip-coating or printing [18, 76, 77]. The molecules then form crystalline (or semicrystalline) films upon solvent evaporation and supersaturation of the solution. The films studied in this work are exclusively prepared by evaporation from vacuum, and the following discussion will therefore be limited to these types of films.

### 2.4.1 Vacuum deposition

The most common deposition technique for small molecule organic semiconductors is deposition in vacuum from vapor (sometimes known as physical vapor deposition (PVD), vacuum sublimation or deposition, or organic molecular beam deposition). Vacuum deposition involves heating of the molecules until they vaporize and then subsequently condensing them into a film on a desired substrate. The molecules are vaporized either from liquid form or directly from solid powder form (sublimation). They then travel some distance in vacuum until impinging upon the substrate surface. The rate (or flux) at which the molecules arrive at the substrate is controlled by the heating temperature of the material, and is typically measured in terms of film thickness per unit time. The vacuum chamber is equipped with a series of pumps that maintain the pressure (typically on the order of  $\sim 10^{-8} - 10^{-9}$  mbar), a crucible where the material is heated, a shutter to control the deposition, a temperature-controlled substrate stage, and a quartz crystal microbalance used to measure the deposited thickness. Custom made chambers, such as the one described in Section 3.1.4, can include additional features to facilitate realtime in situ X-ray scattering measurements during growth.

In reality, the pressure in any vacuum chamber is never zero, and residual molecules can in theory interact with the growing film. Kinetic theory of gases gives the rate of ambient impinging molecules as [78]

$$F_{\text{amb}} = \frac{p}{\sqrt{2\pi BTm}}, \quad (2.1)$$

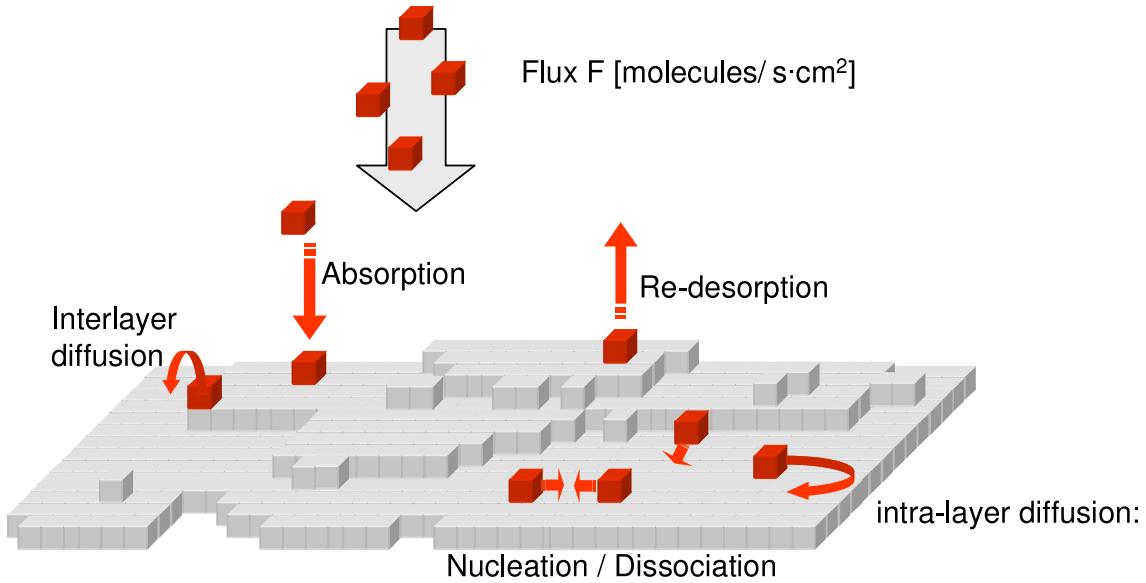


**Figure 2.6:** Molecular representation of thin film growth including relevant processing parameters during vacuum deposition. © IOP Publishing. Reproduced with permission from Ref. [39]. All rights reserved.

where  $p$  is the partial pressure of a gas with molecular mass  $m$  and temperature  $k_B T$ . If we consider a monolayer composed of  $10^{15}$  molecules per square centimeter, then the time in seconds for one monolayer of ambient molecules to absorb is [15]

$$t \sim 10^{-6} p^{-1} s^{-1}, \quad (2.2)$$

where  $p$  is measured in millibars and  $s$  is the sticking coefficient. This translates to a minimum formation time of 1 monolayer of approximately 1 s at  $10^{-6}$  mbar [15], and illustrates the need for high vacuum during the thin film deposition.

## 2.5 Thin film growth

### 2.5.1 General considerations

The microstructure of organic semiconductor thin films depends on the fundamental growth processes and may vary significantly from that of the bulk material. Of particular importance are the early stages of the growth, since these first few layers are important from optical and, if the device electrodes are located in the plane, charge-transport point of view. Therefore, in order to fully understand the structure-property relationship in organic semiconductors, it is important to understand these early stage growth processes and how they can be manipulated in order to control the microstructure in the final-state films. The following section is not an exhaustive review of thin film growth; rather it serves to introduce some of the concepts discussed in Papers II and III. For a full treatment of the underlying physics, the reader is referred to Refs. [79–83].

In general, the growth process of organic thin films can be considered using different approaches, including static equilibrium considerations or analysis of correlation lengths and surface roughness [39]. However, it is important to emphasize that the thin-film growth in organic molecules is a non-equilibrium phenomenon by nature, and thus it cannot be fully described by pure equilibrium considerations [39, 84]. The dynamic processes involved in

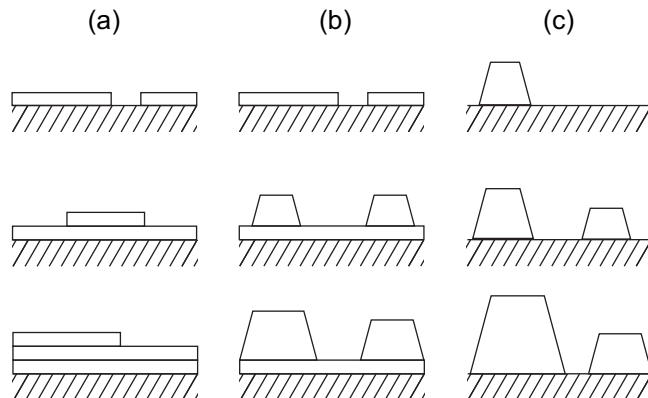


**Figure 2.7:** Schematic illustration of the three growth modes describing the out-of-plane evolution of the thin film. (a) Layer-by-layer (Frank-van-der-Merwe) growth, (b) layer-plus-island (Stranski-Krastanov) growth, and (c) island (Volmer-Weber) growth.

film growth by vacuum deposition are sketched in Fig. 2.6 and include: flux of molecules towards the surface, the absorption and desorption of molecules at the surface, diffusion processes on the surface in one layer (intra-layer diffusion) or between layers (interlayer), and the crystallite nucleation. All of these processes are determined by parameters that are either given by the deposition conditions, or parameters intrinsic to the material itself. Many of the deposition parameters can be controlled, including the evaporation temperature, which determines the flux (and initial kinetic energy) of the molecules arriving at the surface, and the substrate temperature, which determines the kinetic energy of the molecules during the diffusion processes. Intrinsic material properties include surface energy of the substrate, the respective energetic barriers involved in the diffusion processes, and the nucleation barrier. The dynamic processes involved in the growth of organic semiconductors often lead to non-equilibrium structures, that can be observed by either in situ measurements during the growth process [40, 85], or by significant post-growth structural reorganization (e.g. dewetting) [41, 86, 87]. Theoretical frameworks exist that relate the growth mechanism to a set of scaling exponents, which describe the film roughness in terms of thickness and lateral length scale [39, 84]. The three scaling components are the typical surface slope  $a$ , the correlation length  $\xi$ , beyond which the height of two points of the film becomes uncorrelated, and the standard deviation of the film height  $\sigma$ . These parameters scale with film thickness as  $a \sim T^\lambda$ ,  $\xi \sim T^{1/z}$  and  $\sigma \sim T^\beta$ . Here,  $\lambda$  is the steepening exponent,  $z$  is the dynamic exponent and  $\beta$  is the growth exponent (or roughening parameter).

### 2.5.2 Equilibrium considerations

While the growth of organic molecules is an inherently complex non-equilibrium phenomenon, a qualitative understanding of the growth modes typically observed for organic semiconductors can be obtained from consideration of the surface energies involved. There are three well-known and distinct growth modes that describe the out-of-plane evolution of the thin film. These are shown in Fig. 2.7 and will now be discussed in turn.

#### Frank-van der Merwe growth

In Frank-van der Merwe or layer-by-layer growth (Fig. 2.7a), the one molecule tall layers are formed one by one as planar sheets. The nucleation of each layers is two dimensional, and the nucleation of the second layer will only begin once the first monolayer is fully

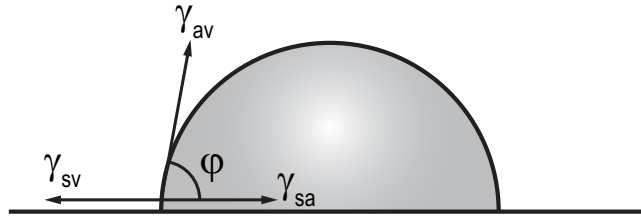


**Figure 2.8:** Schematic illustration of the surface free energies between the surface, adsorbate, and vapor, and the related contact angle  $\varphi$ .

completed (i.e. the material completely wets the substrate).

### Volmer-Weber growth

In Volmer-Weber or island growth (Fig. 2.7c), the growth is three dimensional from the onset and occurs mainly the vertical direction. The molecules nucleate in clusters on the surface and proceed to grow into island-like structures. This type of growth typically results in low surface coverage during early stages of growth, and increased roughness of the final film. The three-dimensional growth may also give rise to an increase in the number of grain boundaries [75, 88, 89].

### Stranski-Krastanov growth

An intermediate case between layer-by-layer growth and island growth is Stranski-Krastanov or layer-plus-island growth (Fig. 2.7b). The growth initially proceeds in layer-by-layer manner until it changes to island growth at a critical film thickness. This type of growth is the most common for organic semiconductors [39, 43, 90], and occurs because of changes to the energetic landscape during the growth process in combination with kinetic effects. For example, strong molecule-substrate interactions that lead to layer growth are shielded by the initial (wetting) layer, after which island growth occurs [91, 92]. Another example is the emergence of an energetic barrier limiting interlayer diffusion [90].

It is common practice to invoke equilibrium surface free energies to explain the occurrence of the different growth modes discussed above [78, 93–95]. The equilibrium growth is described by the balance of surface free energies between the surface, adsorbate, and vapor (see Fig. 2.8), all of which are related to the change in the Gibbs free energy required to create the surface or interface. For typical thin-film deposition of organic semiconductors, the vapor density is low and approximately corresponds to vacuum. The angle between the adsorbate (approximated by a liquid droplet of material) and the surface is denoted as the contact angle (or wetting angle), and it is related to the surface energies by

$$\cos \varphi = \frac{\gamma_{sv} - \gamma_{sa}}{\gamma_{av}}. \quad (2.3)$$

In cases where the surface-adsorbate and vapor-adsorbate surface energies are greater than the surface-vapor surface energy,  $\gamma_{sa} + \gamma_{av} > \gamma_{sv}$ , the contact angle will be finite (i.e.  $\varphi > 0$ ), and the interface and surface areas of the adsorbate will be minimized, leading to island growth.

If instead, the energies are balanced,  $\gamma_{sa} + \gamma_{av} \geq \gamma_{sv}$ , the contact angle is zero and the film growth proceeds in layer-by-layer fashion. This corresponds to the situation where the adsorbate completely wets the surface.

Finally, the Stranski-Krastanov growth occurs when the wetting angle  $\varphi$  changes with increasing film thickness. After initially being zero,  $\varphi$  becomes finite after the deposition of a critical number of monolayers, and the growth mode transitions from layer-by-layer to island growth.

### 2.5.3 Considerations specific to small organic molecules

The general considerations above apply to films of both organic and inorganic materials. However, there are several issues specific to OSCs which further complicate matters, and lead to distinctively different growth behaviors. These issues are described in detail in Refs. [39, 84] and are briefly outlined here.

- The most fundamental difference is that the OSC molecules are anisotropic objects in all but the most simple cases. This means that, in addition to the translational degrees of freedom, the OSC molecules also exhibit several internal degrees of freedom related to orientation and conformation. The orientational freedom of the molecule can give rise to additional sources of disorder [40, 96], or manifest itself as a significant contribution to the nucleation barrier [97, 98]. Even in cases where the transition during growth is not considered, the final structure is often distinguished by whether the molecules are predominantly standing-up or lying-down on the surface [99, 100].
- The intermolecular and molecule-substrate interaction potentials are often dominated by weak van der Waals forces. It should be noted that, while the van der Waals forces are considered weak by comparison, the total binding energies obtained by integrating over all atoms in the molecule are still substantial. The result is typically a softer material, that can potentially accommodate more strain. The build-up of strain in the film can lead to a change in growth mode at a critical film thickness, which is then typically lower for organic thin films. This has for example been observed as a change in the Ehrlich-Schwoebel step-edge barrier (describing the energy barrier for interlayer transport across a molecular step-edge) with increasing film thickness [90, 101, 102].
- The unit cell size is typically much greater compared with inorganic materials simply due to the size of the molecules. This is relevant in cases of epitaxial growth on inorganic substrates, where the larger unit cell of the OSC molecule can lead to more translational domains (and ultimately, more disorder). The effective corrugation of the substrate is also felt by the molecules to a lesser extent, since lateral variations in the interaction potential are distributed over the large unit cell.

## 2.6 Surface templating

Modifying the substrate surface is a common way to control the structure of the overlying OSC film, particularly for films deposited from vacuum [103–106]. In Papers II and III, the orientation of molecules during growth is controlled by employing various (two-dimensional) templating substrates. In general, the orientation of OSC molecules in thin films is governed by the interplay of intermolecular interactions and substrate-molecule interactions. It therefore follows, that if the interaction strength between molecules and substrate change, the orientation of the OSC molecules may change accordingly. On weakly interacting substrates, such as oxides, rod-like aromatic molecules tend to adopt a standing orientation with their molecular backbone aligned approximately parallel with the surface normal. On the other hand, strongly interacting templating layers can induce

substrate-molecule interactions comparable to the molecule-molecule interactions, resulting in a lying-down configuration of the molecules [107]. For example, two-dimensional materials such as graphene can act as templating layers for  $\pi$ -conjugated molecules, whereupon the molecules adopt the lying-down configuration through predominantly  $\pi$ - $\pi$  interactions. This type of growth characteristic was reported for pentacene on monolayer graphene by Lee et al. [108], and similar results have been reported for para-hexaphenyl [109] and other small molecules [107, 110, 111]. The molecular epitaxial growth of crystalline overlayers onto two-dimensional materials is described in detail in Ref. [112].

## CHAPTER 3

## Methods for Characterizing Thin Films

---

This chapter discusses some of the experimental techniques used to study the structure of OSC thin films in Papers I-IV.

### 3.1 Grazing incidence wide-angle X-ray scattering

In order to probe the structure of organic thin films, the experimental geometry must be chosen with care. Since the thin films are almost always deposited onto a supporting substrate with a thickness many times that of the actual film, conventional transmission geometry is not very useful, as most of the scattering signal would stem from the substrate itself. Instead, X-ray diffraction techniques where the incident X-ray beam enters the sample at very small angles are used. The simplest variant is grazing incidence X-ray scattering (GIXS) or diffraction (GIXRD/GIXD) [59, 113]. Depending on the structural feature size of interest, the detector can be positioned to probe either large or small scattering angles. In the case of grazing incidence wide-angle X-ray scattering (GIWAXS), the feature sizes probed at typical X-ray energies (on the order of 10 keV) correspond to the size of the crystalline lattice.

The experimental configuration of GIWAXS is schematically shown in Fig. 3.1. In this configuration, the incidence angle  $\alpha_i$  of the primary X-ray beam relative to the sample surface, is chosen to be close to the critical angle of total external reflection. The critical angles of OSC thin films are typically lower than those of the employed substrates, which means that by choosing a grazing angle that is slightly higher than the critical angle of the film, but slightly below the critical angle of the substrate, only the bulk structure of the film is probed during the measurement. In the material studies presented in Paper I-IV, the typically employed incidence angle is  $\sim 0.17^\circ$ , which falls between the critical angle of the film ( $\alpha_c^{\text{NaT2}} = 0.14$ ) and the substrate ( $\alpha_c^{\text{SiO2}} = 0.19$ ). Both values are calculated for an X-ray energy of 10 keV. The grazing angle can also be chosen to be below the critical angle of the film, in which case only the microstructure near the film surface is probed, or it can be varied during the experiment to obtain depth-resolved structural profiles. Due to

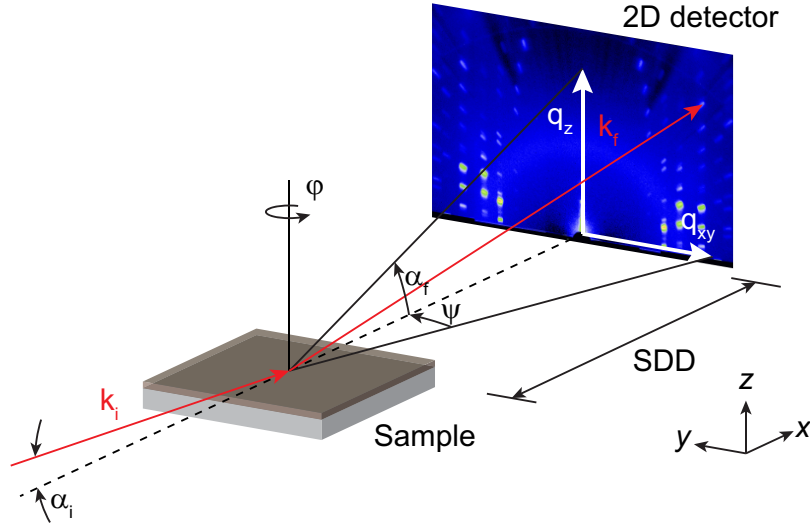


**Figure 3.1:** Grazing incidence wide-angle X-ray scattering geometry on thin films. The primary beam  $k_i$  enters the sample a shallow angle  $\alpha_i$  and scatters at an angle.  $\psi$  denotes the in-plane scattering angle of the scatter beam  $k_f$ , while  $\alpha_f$  denotes the out-of-plane scattering angle. A 2D detector, placed at a given sample-to-detector distance (SDD) downstream from the sample, records the entire scattering image.  $\phi$  denotes the rotation of the sample about the surface normal.

the very shallow angle, the travel path  $l$  of the X-ray inside a film of thickness  $t$  is on the order of  $l = t / \sin \alpha$ , resulting in a large effective beam footprint, and a correspondingly large area of the film being probed. This means that even very thin films (on the order of nanometers) can be successfully probed in GIWAXS [114, 115].

The scattering signal from a GIWAXS measurement can be measured by use of either point or area detectors. With point detectors, the incidence angles  $\alpha_i$  is kept constant while the detector is moved to collect scattering signals at different scattering angles. Point detectors allow for accurate high-resolution data, but it comes at the cost of very slow acquisition times. Instead, most modern GIWAXS experiments rely on two-dimensional (2D) area detectors (see Fig. 3.1), where the scattering pattern over a wide range of angles is collected in a single measurement. This enables GIWAXS experiments with much shorter acquisition times, which in turn allows for in situ and time-resolved experiments [77, 116]. In modern 2D detectors, the trade-off in angular resolution is minimal [117, 118]. The angular resolution is determined by factors such as pixel size, beam size and sample-to-detector distance [119]. The area detector is shielded with a beamstop in order to protect it against the high intensity of the transmitted primary beam. The region of the detector surrounding the beamstop is often dominated by diffuse scattering for typical thin-film samples due to lack of structural order on larger length scales (i.e. scattering from grains with ill-defined sizes). In particular, the specular rod of diffuse scattering along the  $q_z$  axis can be attributed to roughness of the surface. In Paper III, we use this diffuse scattering along the specular rod to infer information about the thin film growth, since the surface roughness oscillates with island coalescence. However, a full treatment of the diffuse scattering requires the use of GISAXS (see Section 3.2). If the experiment is not carried out in vacuum, diffuse scattering from the primary beam in air will also contribute to increased scattering intensity around the beamstop.

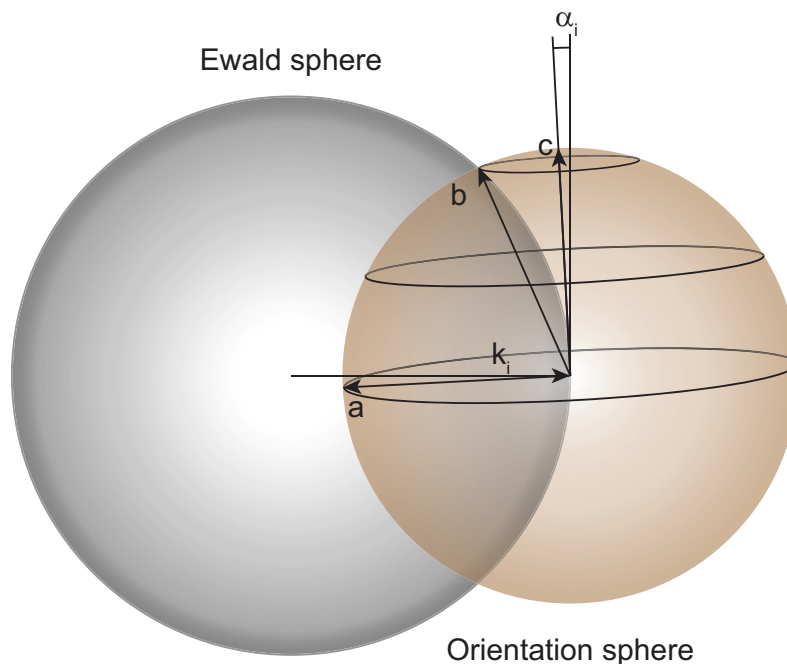


**Figure 3.2:** Intersection of the Ewald sphere with the crystallite orientation sphere, indicating the allowed diffraction events in grazing incidence geometry. Crystallites with near in-plane orientation (vector  $a$ ) can intersect the Ewald sphere, while crystallites with out-of-plane orientation (vector  $c$ ) do not result in any observable scattering. Vector  $b$  denotes the case where scattering vectors that are not vertical will result in observable scattering along the vertical  $q_z$  line on the detector.

### 3.1.1 Texture and detector distortion

In the GIWAXS geometry, the sample rotation  $\phi$  (see Fig. 3.1) is fixed during the measurement, meaning that the 2D area detector only records a slice of the reciprocal space. In most cases, this is not a problem, since OSC thin films typically possess an isotropic distribution of the crystallites in the substrate plane. This isotropic in-plane distribution gives rise to the scattering rings in reciprocal space [120], which are always intersected by the detector plane (or strictly speaking, the Ewald sphere) independent of the rotation angle. In other words, the in-plane orientation of the crystallites is random, meaning that at any given  $\phi$ , an equal number of crystallites are in Bragg condition and give rise to reflections in the scattering pattern. Films with isotropic in-plane crystalline structure are referred to as having thin-film texture or fiber-texture. If the sample is not fiber-textured, information on the in-plane orientation of the molecules is obtained by performing  $\phi$ -scans, where the sample is rotated about the substrate normal [67]. In cases where the in-plane molecular orientation is controlled, for example by mechanical rubbing [100] or by epitaxial growth on highly ordered substrates [121], the samples will not exhibit fiber-texture.

Moreover, the fixed incidence angle GIWAXS means that the true specular ( $q_{xy} = 0$ ) is probed only for  $\alpha_f = \alpha_i$ . This is caused by the curvature of the Ewald sphere, which is schematically illustrated in Fig. 3.2. The Ewald sphere is a geometric representation of the scattering equation with radius  $k_i$  and origin at the sample, and any point on the

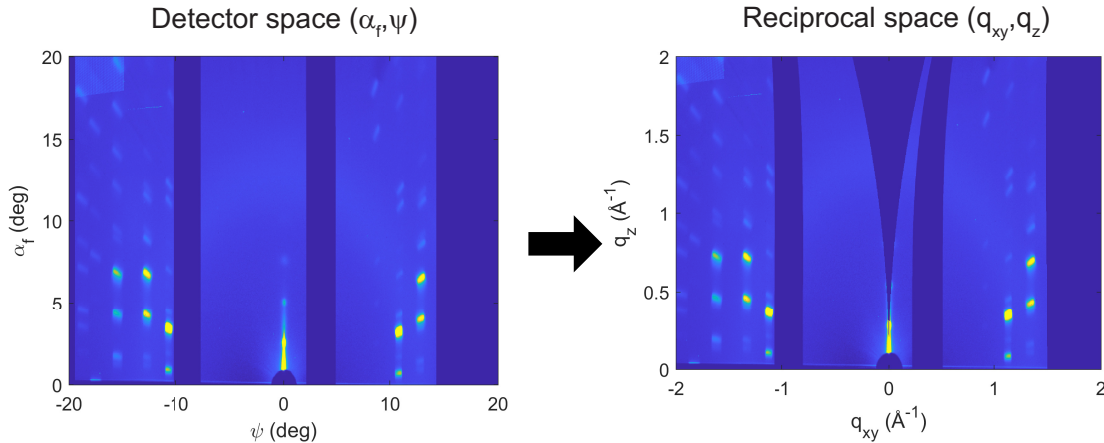


**Figure 3.3:** Example of image transformation from detector space to reciprocal space.

surface of the Ewald sphere satisfies the diffraction condition given in Chapter 1. Now let us imagine a sphere representing the orientation of thin film crystallites in reciprocal space. The sphere has radius  $\mathbf{q}_B$ , corresponding to the scattering vector of interest, and is located with its center on the surface of the Ewald sphere at the head of the incoming  $k_i$  vector. The intersection of the two spheres thus corresponds to all observable diffraction in the grazing incidence geometry. From Fig. 3.2 we see that crystallites with scattering vectors  $\mathbf{q}_B$  pointing in the in-plane direction will intersect the Ewald sphere (vector  $a$ ), while those crystallites with  $\mathbf{q}_B$  pointing out-of-plane will not intersect the Ewald sphere (vector  $c$ ), unless in the special case of  $\alpha_f = \alpha_i$  (corresponding to a situation where  $c$  in Fig. 3.2 exactly terminates at the Ewald sphere). In practice, this means that linecuts along the  $q_z$  direction in 2D GIWAXS images does not provide true specular information, but rather information from planes that are misoriented from the substrate normal (vector  $b$  in Fig. 3.2), with greater distortions at higher scattering angles. The 2D detector patterns can be transformed into reciprocal space maps by applying the appropriate distortion correction (see Fig. 3.3), that is, by correctly projecting the three-dimensional curvature of the Ewald sphere onto the 2D detector image [120]. Unfortunately, this step is often ignored in the literature.

### 3.1.2 Determining the Crystalline Unit Cell

Once the diffraction data has been correctly converted to reciprocal space, information on the crystalline unit cell of the thin film can be obtained. The unit cell information is contained in the positions of the Bragg peaks, and the analysis is analogous to the lattice refinement in X-ray crystallography of single crystals [123]. However, for most thin films, only a limited number of diffractions peaks are available compared with diffraction from single crystals, where the refinement of the unit cell is based on thousands of observed peaks [53]. This means that the unit cell refinement in many cases relies on prior knowledge of the sample, such as expected packing direction and distances, or data from single-crystal refinements. In some systems, the thin film processing might even favor the crystallization of different polymorphs [30], in which case the structure from single-crystal refinement will not give information on the thin film structure. Moreover, for many OSCs, it is difficult (or even impossible) to grow single crystals that are sufficiently large for single crystal refinement [59].

Diffraction from crystalline thin films occur at specific  $\mathbf{q}$  vectors, where neighboring crystalline planes give rise to constructive interference of the scattered waves. Bragg's law

(Eq. (1.9)) then relates the magnitude of the reciprocal lattice vector to the interplanar lattice spacings. In the reciprocal space, the crystallographic planes are described by their Miller indices  $h$ ,  $k$  and  $l$ , which denote a family of planes orthogonal to the reciprocal space vector

$$\mathbf{q}_{hkl} = (h\mathbf{a}^* + k\mathbf{b}^* + l\mathbf{c}^*). \quad (3.1)$$

Here, the common notation  $\mathbf{a}_1 = \mathbf{a}$ ,  $\mathbf{a}_2 = \mathbf{b}$  and  $\mathbf{a}_3 = \mathbf{c}$  is used. The reciprocal space lattice  $(\mathbf{a}^*, \mathbf{b}^*, \mathbf{c}^*)$  is then related to the real-space lattice  $(\mathbf{a}, \mathbf{b}, \mathbf{c})$  by

$$\begin{aligned} \mathbf{a}^* &= 2\pi \frac{\mathbf{b} \times \mathbf{c}}{\mathbf{a} \cdot (\mathbf{b} \times \mathbf{c})}, \\ \mathbf{b}^* &= 2\pi \frac{\mathbf{c} \times \mathbf{a}}{\mathbf{a} \cdot (\mathbf{b} \times \mathbf{c})}, \\ \mathbf{c}^* &= 2\pi \frac{\mathbf{a} \times \mathbf{b}}{\mathbf{a} \cdot (\mathbf{b} \times \mathbf{c})}. \end{aligned} \quad (3.2)$$

If the orientation of the crystalline lattice with respect to the substrate surface is known, then the unit cell refinement reduces to a problem of 6 unknowns:  $a, b, c, \alpha, \beta, \gamma$ , that is, the magnitudes of the real-space lattice vectors and the angles between them. The direct lattice parameters and the reciprocal lattice parameters  $a^*, b^*, c^*, \alpha^*, \beta^*, \gamma^*$  are related through Eq. 3.2. A complete list of all the relationships is given in Table 1 of Ref. [124].

In the following, let us consider the case where the (001) lattice plane of the thin film is parallel to the substrate surface. This corresponds to one of the most common cases in small molecule thin films, where the molecules adopt a standing configuration with the molecular long-axis oriented near out-of-plane [30, 34, 49, 54, 125]. In this case, following the notations of Merlo et al. [49], the in-plane and out-of-plane components of the scattering vector can be separated. The in-plane component of the scattering vector  $\mathbf{q}$  can be written as

$$q_{xy}^2 = q_x^2 + q_y^2 = h^2(a_{\parallel}^*)^2 + k^2(b_{\parallel}^*)^2 - 2hk \cos \gamma_{\parallel}^*, \quad (3.3)$$

where  $a_{\parallel}^*$  and  $b_{\parallel}^*$  are the magnitudes of the in-plane components of the reciprocal lattice vectors, and  $\gamma_{\parallel}^*$  is the in-plane angle between  $\mathbf{a}^*$  and  $\mathbf{b}^*$ .

In a similar manner, the out-of-plane component of the scattering vector  $\mathbf{q}$  can be written as

$$q_z = ha_{\perp}^* + kb_{\perp}^* + lc^*, \quad (3.4)$$

where  $a_{\perp}^*$  and  $b_{\perp}^*$  are the magnitudes of the out-of-plane components of the reciprocal lattice vectors.

In order to solve Eqs. (3.3) and (3.4), the integers  $h$ ,  $k$  and  $l$  need to be varied and  $q_{xy}$  and  $q_z$  values from at least three independent Bragg peaks are required. Once the parallel and perpendicular components of  $\mathbf{a}^*$  and  $\mathbf{b}^*$  are obtained, the three reciprocal lattice angles can be calculated using the following equations:

$$\begin{aligned} \alpha^* &= \frac{\pi}{2} - \tan^{-1} \left( \frac{b_{\perp}^*}{b_{\parallel}^*} \right) \\ \beta^* &= \frac{\pi}{2} - \tan^{-1} \left( \frac{a_{\perp}^*}{a_{\parallel}^*} \right) \\ \gamma^* &= \cos^{-1} \left( \frac{a_{\perp}^* b_{\perp}^* + a_{\parallel}^* b_{\parallel}^* \cos \gamma_{\parallel}^*}{\sqrt{(a_{\parallel}^{*2} + a_{\perp}^{*2})(b_{\parallel}^{*2} + b_{\perp}^{*2})}} \right). \end{aligned} \quad (3.5)$$

The magnitudes of the reciprocal scattering vectors  $\mathbf{a}^*$  and  $\mathbf{b}^*$  are calculated in a straightforward manner as

$$\begin{aligned} a^* &= \sqrt{a_{\parallel}^{*2} + a_{\perp}^{*2}}, \\ b^* &= \sqrt{b_{\parallel}^{*2} + b_{\perp}^{*2}} \end{aligned} \quad (3.6)$$

Finally, the real-space lattice is calculated by using the relationships given through Eq. (3.2).

In practice, Eq. (3.3) is solved using educated guesses for  $(hk)$  and the three unknown in-plane components of the reciprocal lattice parameters. Once a set of self-consistent  $(hk)$  values is determined for all Bragg peaks, the three unknown lattice parameter components are found by least squares minimization of  $q_{xy}$  for all Bragg peaks. Subsequently, Eq. (3.4) is solved using the same self-consistent set of  $(hk)$  values together with educated guesses of the three unknown out-of-plane components of the reciprocal lattice parameters and  $l$ . This is once again done by least squares minimization of  $q_z$  for all Bragg peaks.

The situation is more complicated if the lattice orientation is not known a priori. In this case, an additional three parameters must be determined, corresponding to the lattice rotation. A full mathematical expression for this problem was eloquently derived by Simbrunner et al. [124, 126].

From Ref. [124], in the case of the (001) lattice plane being parallel to the substrate surface, the reciprocal space vector can be represented by the matrix equation

$$\mathbf{q} = \begin{pmatrix} q_x \\ q_y \\ q_z \end{pmatrix} = \begin{pmatrix} a^* \sin \beta^* \sin \gamma & 0 & 0 \\ -a^* \sin \beta^* \cos \gamma & b^* \sin \alpha^* & 0 \\ a^* \cos \beta^* & b^* \cos \alpha^* & c^* \end{pmatrix} \begin{pmatrix} h \\ k \\ l \end{pmatrix} = \mathbf{A}_{001}^* \begin{pmatrix} h \\ k \\ l \end{pmatrix}. \quad (3.7)$$

If the contact plane, that is, the plane parallel to the substrate surface, is different from the (001) plane, the reciprocal lattice vectors become

$$\mathbf{q} = \mathbf{R} \mathbf{A}_{001}^* \begin{pmatrix} h \\ k \\ l \end{pmatrix}, \quad (3.8)$$

where  $\mathbf{R}$  describes the rotation around the zone vector  $\mathbf{n}$ , which is orthogonal to the (001) plane normal and the new contact plane normal. If the lattice parameters are known a priori, the problem reduces to simply finding the rotation matrix  $\mathbf{R}$  that gives rise to the rotated reflections [54, 108].

While the unit cell describes the smallest repeating unit of the crystalline structure, it does not explicitly describe the exact packing and orientation of the film molecules. One approach to determine the molecular arrangement inside the unit cell is to make an educated guess on the number of molecules based on the unit cell size. The "exact" spatial arrangement can then be calculated using energy-minimization methods such as density functional theory (DFT) calculations [55, 127]. However, there are inherent limitations in the DFT treatment of dispersion forces, and while the approach can yield good approximations, total accuracy cannot be expected for most OSC systems because of the importance of van der Waals interactions.

A more detailed approach involves extracting information from the peak intensities in the scattering pattern [34, 59]. In the GIWAXS geometry, the area detector captures the full

spatial extent of the diffraction peak, and the integrated peak intensity is given by [34]

$$I(hkl) = I_0 \frac{e^4}{m_e^2 c^4} N K \|F_{hkl}\|^2, \quad (3.9)$$

where  $I_0$  is the incident beam intensity and  $N$  is the number of unit cells in Bragg condition. The structure factor  $\|F_{hkl}\|^2$  is defined in Chapter 1. The  $K$  term encompasses several correction terms, including Lorentz and polarization corrections, and the Debye-Waller factor, which accounts for dynamic disorder of the molecules. The number of measurable peaks in GIWAXS is typically much less than what is needed to refine the positions of the individual atoms [34], and assumptions must therefore be made. By assuming the molecules to be rigid, the number of independent variables is drastically reduced to just six per molecule in the unit cell, corresponding to the three translational and three rotational variables. The molecular arrangement can then be determined by minimizing the theoretical intensities versus the experimental data. The work presented in Papers I-IV involves only limited calculations of the molecular arrangements, and the reader is referred to our work in Ref. [55] for a detailed study on the molecular arrangement of naphthyl end-capped oligothiophenes in films.

### 3.1.3 Determining crystallite size

As briefly discussed in Section 2.2, the crystallite size (sometimes grain size) is an important feature for effective charge transport in OSCs. Information on the size of the crystallites is contained within the width of the diffraction peaks, and the simplest way to extract the crystallite size is by application of the Scherrer formula. The Scherrer formula relates the full-width at half-maximum (FWHM) of a diffraction spot ( $hkl$ ) to the correlation length of the lattice (i.e. the distance over which the lattice repetitions are well correlated) as

$$D_{hkl} = \frac{2\pi K}{\Delta q_{hkl}}, \quad (3.10)$$

where the Scherrer constant  $K$  is a shape factor (typical values range from 0.8 to 1 in the literature) and  $\Delta q_{hkl}$  is the FWHM of the diffraction peak in units of  $q$ . Very sharp diffraction peaks indicate large coherence lengths, while broad peaks indicate small coherence lengths. This inverse relationship originates from the inverse nature of the reciprocal space. In the literature, the correlation length obtained from the Scherrer equation is often called the grain size or crystallite size, and is meant to refer to the average distance between neighboring regions in the crystal lattice that are similarly ordered. However, the coherence length  $D_{hkl}$  of the crystallites is not only a factor of the finite crystal size, but also depends on other factors such as non-uniform distortion of the lattice, long range disorder, and thermal fluctuations. Thus, strictly speaking, only in cases where there are no other contributions to peak broadening (which is never the case for real materials), or when all other contributions are accounted for, does the Scherrer equation provide the actual size of the finite crystallites. In OSCs, where the crystallinity is never absolute, the coherence length obtained from the width of a diffraction peak provides only a minimum value for the crystallite size, since all other contributions lead to an increase in the FWHM. It should be noted that the crystallite size or grain size obtained by X-ray diffraction is often different from morphological domain size observed by imaging or probe microscopes.

In practice, the experimentally observed peak broadening is also affected by instrumental broadening as

$$\Delta q_{\text{exp}} = \sqrt{\Delta q_{hkl} + \Delta q_{\text{res}}}. \quad (3.11)$$

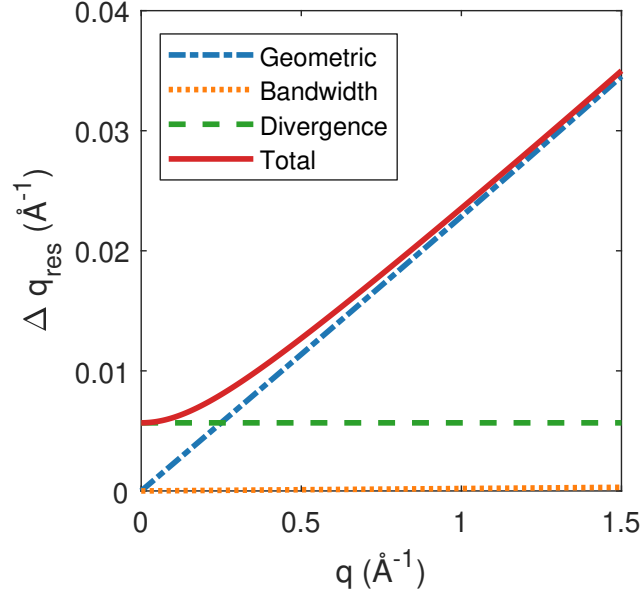


**Figure 3.4:** Resolution limits for typical GIWAXS setup. The experimental parameters are given in the text.

The diffraction peak broadening due to the instrumental setup in GIWAXS has been described in detail by Smilgies [119]. In the following, a brief overview is given including an example of the instrumental broadening at one of the beamlines used in Papers I-IV. The principal contributions to the instrumental broadening are the divergence of the X-ray beam, the beam-energy bandwidth and the finite footprint of the beam on the sample.

The beam divergence contribution can be divided into a horizontal component  $\sigma'_H$  and a vertical component  $\sigma'_V$ , assuming an elliptical beam profile. For a given azimuthal angle  $\chi$ , the radial beam divergence is

$$\sigma'_R(\chi) = \frac{1}{\left([\cos^2 \chi / \sigma'_H{}^2] + [\sin^2 \chi / \sigma'_V{}^2]\right)^{1/2}}. \quad (3.12)$$

Assuming that the whole incident radiation cone is reflected, the divergence of scattered beam is equal to the beam divergence  $B_{\text{div}} = \sigma'_R$ .

The broadening due to the energy bandwidth of the incident X-rays is given by

$$B_{\text{BW}} = 2\eta \tan(2\theta/2), \quad (3.13)$$

where  $2\theta$  is the scattering angle and  $\eta$  is the energy Bandwidth of the X-rays.

Finally, the broadening due to finite footprint of the beam on the sample is given by

$$B_{\text{geo}} = \frac{w \tan 2\theta}{SDD}. \quad (3.14)$$

Because of the shallow angle in grazing incidence geometry, the longitudinal beam footprint typically spans the entire width of the sample. Thus, the peak width broadening in Eq. (3.14) is effectively due to the width of the sample.

The total instrumental broadening is then given by

$$B_{\text{res}} = \sqrt{B_{\text{div}}(\chi)^2 + B_{\text{BW}}(\eta, 2\theta)^2 + B_{\text{geo}}(w, 2\theta)^2}, \quad (3.15)$$

or in units of the scattering vector  $q$

$$\Delta q_{\text{res}} = \frac{4\pi}{\lambda} \cos\left(\frac{2\theta}{2}\right) \frac{B_{\text{res}}}{2}. \quad (3.16)$$

Figure 3.4 shows the typical instrumental resolution for GIWAXS at the P03 Micro- and Nanofocus X-ray Scattering (MiNaXS) beamline of PETRA III, DESY [6]. For this particular setup, the horizontal and vertical beam divergence are estimated from the size of the primary beam at the sample and at the detector to  $\sigma'_H = 0.8$  mrad and  $\sigma'_V = 0.6$  mrad, respectively. The energy bandwidth of the Si(111) equipped monochromator is  $\eta = \Delta E/E \simeq 10^{-4}$  [6], and the calculations assume a sample width of 5 mm. It can be seen that the peak width resolution is strongly limited by the geometric smearing at higher scattering angles, while the beam divergence is the limiting factor at small angles. Due to the very low energy bandwidth of modern synchrotron monochromators, the attributed peak broadening is negligible.

In principle, it is possible to decouple the effect of finite crystal size from that of cumulative disorder on the diffraction peak broadening, and various techniques have been applied with success to systems of OSCs. Cumulative disorder describes the long range distortions the ideal crystalline lattice that stem from accumulation of distortions and defects [66, 128]. In a diffraction pattern, cumulative disorder will manifest itself as a distinct increase in peak broadening at higher orders of diffraction in the same set of crystal planes, for example (100), (200), (300) and so forth [67]. Since the broadening of a diffraction peaks due to finite crystallite size is independent of the diffraction order, this progressive broadening effect can be used to effectively decouple the finite crystallite size and lattice disorder contributions. By plotting the peak width as a function of diffraction order, one can extract the finite size of the crystallites from the zero intercept, and the magnitude of lattice disorder from the slope. This simple method, referred to as Williamson-Hall analysis [129], is useful for highly ordered and strongly diffracting systems, where at least three orders of diffraction are present in the scattering pattern. Hence, its applicability is limited in systems with high cumulative disorder or low crystallinity, such as most polymers [130–132]. Nevertheless, the William-Hall analysis method has successfully been applied to both polymers, such as PBTTC [133, 134], and small molecules [135].

Another more involved approach is based on the Fourier-transform of individual diffraction peaks. In this technique, first introduced by Warren and Averbach [136, 137], the entire peak shape is utilized, and finite size and cumulative disorder contributions are decoupled due to their specific functional dependences on diffraction order and Fourier frequency [66, 138]. The Warren-Averbach method can be applied to system with as little as 2 diffraction orders, but requires high-resolution and low noise data, and the multi-step analysis is not straight-forward.

### 3.1.4 In situ GIWAXS

The thin film formation during vacuum deposition (see Section 2.4.1) can be studied in realtime by employing a portable ultra-high vacuum (UHV) chamber installed at a synchrotron beamline [39, 40, 116, 139], or with a high flux laboratory X-ray source, as demonstrated in Paper II. An illustration of the portable UHV chamber used in Papers II and III is sketched in Fig. 3.5. The main chamber of the device is encompassed by a cylindrical beryllium construction that acts as a transparent window for the incoming and outgoing X-rays. The chamber is mounted on a goniometer stage (or equivalent) whereby the sample substrate can be precisely inclined with respect to the incidence beam at grazing angle  $\alpha_i$  and the 2D GIWAXS pattern can be recorded. During deposition, the

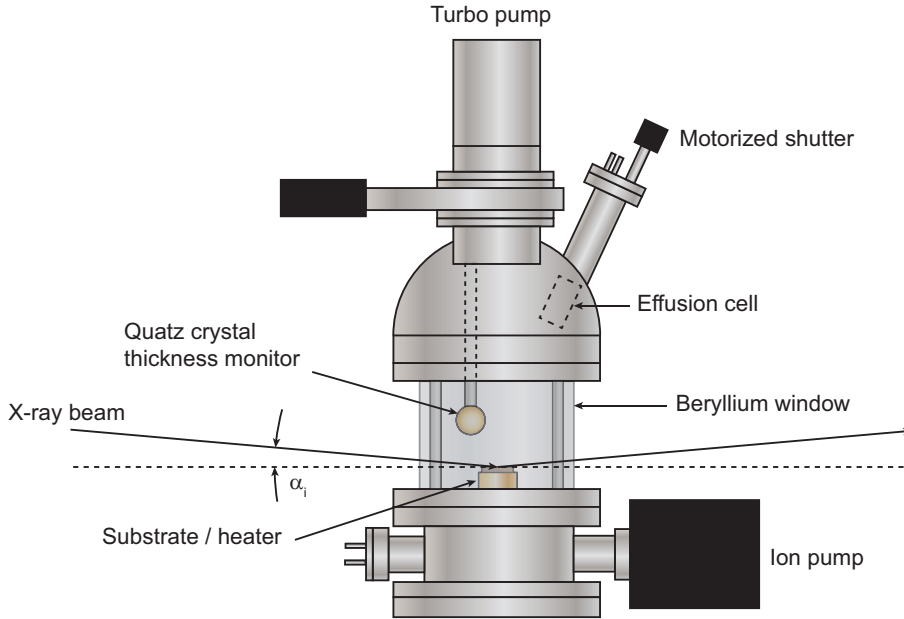


**Figure 3.5:** Schematic illustration of a portable UVH chamber for realtime in situ measurements of thin film growth used in Papers II and III. The cylindrical beryllium construction allows acts as a transparent window for the X-rays, allowing for the incoming primary beam and the scattered signal to pass through. The chamber can be installed directly into the synchrotron beamline.

vacuum inside the chamber is maintained via a series of membrane-, turbomolecular-, and ion pumps, yielding a typical base pressure of  $\sim 10^{-8}$  mbar. The chamber is equipped with a Knudsen effusion cell containing the OSC material, and upon heating of the cell, a steady flow of evaporated molecules will be generated. The molecules are adsorbed upon reaching the substrate surface, initiating the thin film growth. A motorized shutter controls the deposition, and the molecular flux is controlled by adjusting the evaporation temperature. The growth rate (on the order of  $\sim 0.03$  Å/s in this work) is monitored by a calibrated quartz crystal microbalance positioned inside the chamber. The sample stage is equipped with a substrate heater in order to control the growth temperature.

The resulting four-dimensional dataset contains information on the realtime evolution of the crystalline structure. Realtime in situ growth observations are therefore indispensable for capturing important dynamic processes and transient structure, that otherwise would be missed by post-growth measurements alone [40, 140, 141].

### 3.2 Grazing incidence small-angle X-ray scattering

Grazing incidence small-angle X-ray scattering (GISAXS) is, as the name implies, analogous to GIWAXS but with a focus on smaller scattering angles (typically  $2\theta < 5^\circ$ ). Like GIWAXS, GISAXS is a surface sensitive technique used to measure correlations in electron density in thin films. The setup geometry in GISAXS is identical to GIWAXS, with the exception of a longer sample-to-detector distance (see Fig. 3.6), which allows for measuring of very small scattering angles with sufficiently high angular resolution. Therefore, GISAXS probes larger size correlations corresponding to the nanostructure (typically 1-100 nm) of the films. It is often used in conjunction with GIWAXS in order to cover the entire length scale from lattice to nanostructure, for example in realtime studies of

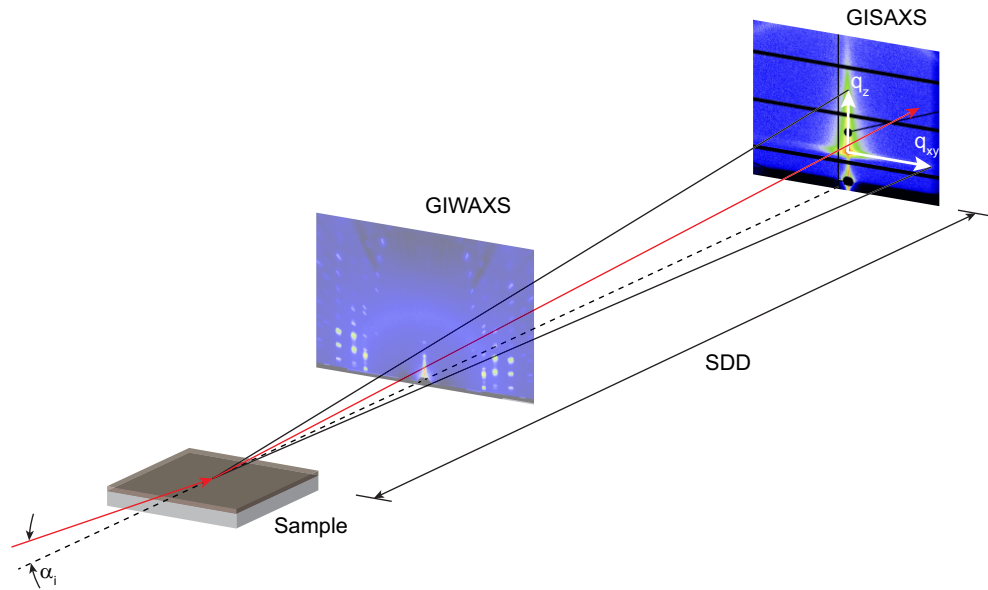


**Figure 3.6:** Grazing incidence small-angle X-ray scattering (GISAXS) geometry on thin films with comparison to GIWAXS. The sample-to-detector distances are not drawn to scale, and are typically tens of cm for GIWAXS and 2-5 m for GISAXS.

nucleation and growth of small molecules, where the formation and coalescence of islands can be probed [37, 43, 116]. It is also a useful technique for studying blend films, where long range phase separation is important [77, 142].

Due to the very small scattering angles, the distortion of the scattering pattern due to the curvature of the Ewald sphere is not very prominent. For small scattering angles, the  $x$  component of the scattering vector  $\mathbf{q}$  is very small and the approximation  $q_{xy} \simeq q_y$  holds. In practice, this means that the transformation from detector space to  $q$ -space can be done in a straight-forward manner.

The resolution analysis shown in Fig. 3.4 is also applicable in GISAXS, and it illustrates the importance of having a low beam divergence for GISAXS experiments. Moreover, due to the long sample-to-detector distance, a flight tube is typically employed along the path between the sample and the detector to minimize air scattering and thus intensity loss of the scattered signal. In addition the primary beamstop also found in GIWAXS, GISAXS makes use of a second beamstop to block the strongly reflected specular beam at  $\alpha_f = \alpha_i$ . This secondary beamstop is not necessary in GIWAXS, since the angle of the specular beam is relatively small and can be blocked by the same beamstop as the primary beam.

The analysis of GISAXS scattering data is not straight-forward because of the dynamic effects which occur at small angles close to the critical angles of the involved materials [143]. To account for these effects, the scattering is typically analysed in the so-called Distorted Wave Born Approximation (DWBA), in which the Born approximation (where the total field inside the material is simply assumed equal to the incident field) is extended to account for perturbations by higher order multiple scattering effects [144, 145]. The effects of these perturbations are seen most strongly at scattering angles matching the critical angle of the film, where the scattering is greatly enhanced - this is known as the Yoneda peak [146].

### 3.3 Atomic force microscopy

Atomic force microscopy is a scanning probe technique used to probe the local structural features of surfaces in the the nanometer to micrometer regime [147, 148]. AFM is commonly employed to study the surface morphology and structure in OSC thin films due to its widespread availability and ease of use [53, 86, 102, 149, 150]. The technique works by scanning a sharp tip positioned at the free end of a cantilever across the sample surface, whereby the sample topography can be evaluated at high precision and resolution. The interactions between the tip and the surface are governed by interatomic attractive and repulsive forces, that are of extremely short range nature.

The AFM can be operated either in contact mode, where the sample-tip interactions cause a static deflection of the cantilever, or in oscillatory modes, where the cantilever oscillates at or close to its resonant frequency, and changes in the dynamic parameters of the oscillation gives information about the sample. Due to the soft nature of OSC films, the contact mode, in which the tip stays in constant contact with the sample, is seldom used. Instead, most studies of organic materials use an oscillatory mode called tapping [151]. In tapping mode, the tip oscillates with a constant frequency equal to the resonant frequency of the cantilever. A focused laser beam is aimed at and reflected by the top of the cantilever, and the deflection pattern of the reflected beam is recored by a photodiode, generating an electronic AC signal. Upon the tips encounter with the surface, the signal from the reflected beam changes, revealing information about the vertical height of the sample surface. Thus, by continuously adjusting the distance between the tip and the sample based on feedback from the return signal, the amplitude of the oscillation is kept constant as the tip follows the surface's topographic features. The resolution of tapping mode AFM is primarily governed by the shape of the tip, but also by tip-sample interactions [147].

While AFM is useful for investigating morphological features in thin films, the information is inherently limited by the fact that AFM only probes the film surface, and changes in the longitudinal structure (i.e. along the surface normal) are not observed. Moreover, the obtained information is also highly localized, and care must be taken to ensure that the imaged area is indeed representative of the entire sample. It is sometimes possible to retrieve material information from the phase-shift between the drive signal and the return signal, the details of which can be found elsewhere [147].

### 3.4 UV-Vis absorption spectroscopy

UV-Vis absorption spectroscopy measures the absorption of light in a material in the ultra-violet and visible spectrum. The technique can be used to determine the absorption bands of the material, and provide information on the vibrational modes of the molecules through electron-phonon interactions. It works by measuring the amount of light transmitted through a sample at a specific wavelength and calculating back the amount of light absorbed by the material. The absorption spectrum is typically measured in terms of absorbance [152], which is defined as

$$A(\lambda) = \log_{10} \frac{I_0(\lambda)}{I(\lambda)}, \quad (3.17)$$

where  $I_0$  and  $I$  are the intensity of the light before and after hitting the sample, respectively, and  $\lambda$  is the wavelength of the light. According to Beer-Lambert's law, the

transmitted intensity decreases exponentially with the sample thickness  $l$  as

$$I = I_0 10^{-\alpha l}, \quad (3.18)$$

where  $\alpha$  is the absorption coefficient and is related to the absorbance as  $A = \alpha l$ . Since the absorbance depends on the film thickness, the absorption spectrum must be normalized to the thickness in order to facilitate a quantitative comparison between multiple samples. In practice, the absorption spectrum is measured by depositing the film onto a transparent substrate (e.g. glass) and measuring the entire sample along the substrate normal. Hence, the absorption spectrum of the bare substrate is to be measured separately and subtracted from the film spectrum.

In  $\pi$ -conjugated OSCs, the orbitals of the carbon atoms are hybridized into highly anisotropic  $\sigma$  and  $\pi$  orbitals, located in-plane with and perpendicular to the molecular backbone, respectively [153]. The overlap of the  $\sigma$  orbitals of adjacent carbon atoms is large, and the strong  $\sigma$  bonds are therefore not excited by photons in the UV-Vis range. On the other hand, the relatively weak  $\pi$  bonds have energy gaps that correspond to the energy of a photon in the UV-Vis range. Typically, the lowest electronic transition, that is, between the highest occupied molecular orbital (HOMO) and the lowest unoccupied molecular orbital (LUMO), is a transition between  $\pi$  states with alternating sign. This transition is named the  $\pi$ - $\pi^*$  transition, and is typically the dominating feature in the absorption spectrum of  $\pi$ -conjugated OSCs. Due to the highly anisotropic band structure, information about the average molecular orientation can be extracted from the absorption spectrum by polarizing the light.

It should be noted that the absorption spectrum is also affected by the molecular ordering. The molecules in a well-ordered film will adopt a more planar conformation, increasing the delocalization length of the  $\pi$  electrons, which reduces the resonance energy [153]. The absorption spectrum of a well-ordered film is therefore typically red-shifted with respect to a disordered film of the same material. UV-Vis absorption spectroscopy (polarized and non-polarized) is commonly used as a complementary technique to characterize OSC thin-films [100].



## CHAPTER 4

# Ultra-High Molecular Weight Polyethylene Fibers

---

Man-made polymeric fibers have attracted much attention by scientist and engineers with the desire to create materials with ultimate properties. One such fiber with very high modulus and tensile strength is made from ultra-high molecular weight polyethylene (UHMWPE). In this chapter, the basic properties of UHMWPE fibers are outlined, providing a material background for the study presented in Paper V. These strong fibers became commercially available with the invention of the gel-spinning process, where the polymer is first dissolved in solvent, then spun, and finally drawn at elevated temperatures. The gel-spinning process is discussed in detail in this chapter, including the roles of the high-molecular weight on tensile strength and the dissolution in solvent on drawability. Finally, the structural characteristics following from the gel-spinning process are presented, including a discussion on important transient structures and their kinetic pathway, and structural inhomogeneities along the fiber diameter.

## 4.1 General properties

### 4.1.1 Chemical nature

Polymeric fibers with the highest modulus and tensile strength are made of polyethylene (PE), one of the simplest and most widely used polymers. PE chains are composed of methylene groups  $(-\text{CH}_2-)_n$  connected through C-C bonds in series, and are polymerized from ethylene gas. At room temperature, PE exists in a semi-crystalline state with regions of crystalline PE and regions of amorphous PE. In its most common crystalline phase [154], PE crystallites take the form of an orthorhombic lattice (see Fig. 4.1), where the molecular chains are oriented along the  $c$ -axis. The detailed structure of UHMWPE fibers is discussed in Section 4.3. Chemically, the polymer chains used for high-strength fibers are no different from other types of PE. However, the molecular weight (i.e. the length of the chain) is much higher, typically  $\overline{M}_w > 10^6$  g/mol.

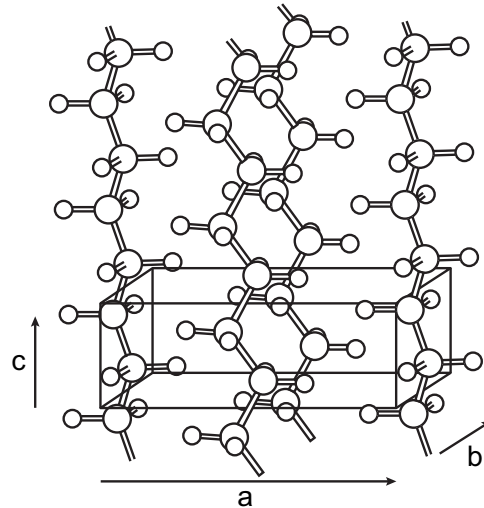


**Figure 4.1:** Orthorhombic unit cell of PE crystallites.

In contrast to other high strength polymeric fibers, the high strength and modulus of UHMWPE fibers are not inherent to the structure of the chain molecules. While for examples aramids tend to form straight rodlike molecules, that only needs to be oriented in order to achieve high tensile properties [155], UHMWPE chains are flexible by nature, and needs to be forced into an extended conformation in addition to being oriented. The process of physically extending the molecular chains is not straightforward, and it was not until the invention of gel-spinning that high modulus and high strength fibers made from UHMWPE were made possible.

#### 4.1.2 Mechanical properties

The primary properties of UHMWPE fibers are their high tensile strength and high modulus. Table 4.1 lists the tensile strength and Young's modulus for UHMWPE fibers, along with other polymeric fibers and steel. The high strength and modulus in UHMWPE fibers is a consequence of the high degree of alignment of the polymer chains, utilizing the strength of the covalent C-C bonds in the backbone of the molecules. The best commercially available UHMWPE fibers have tensile strengths and moduli of around 4 and 160 GPa, respectively. In the literature, the highest ultimate properties (tensile strength of 6 GPa and modulus of 220 GPa) were reported for UHMWPE drawn from single crystal mats [156, and references therein]. Several theoretical studies on the ultimate tensile strength and modulus of UHMWPE fibers exists [157–160], predicting values ranging from 18–30 GPa for tensile strength and 280–355 GPa for the modulus (Table 4.1). The calculations of the highest theoretical strength is based on the breaking of the molecular C-C bonds located along the backbone of a polymer with perfectly aligned, infinitely long chains. The true picture is of course much more nuanced, and a full discussion on the discrepancy between theoretical and experimental values is beyond the scope of this work. The reader is instead referred some of the previous work on the subject [161–164, and references therein]. However, the significant gap between the experimental values and maximum theoretical values ( $4\text{--}5\times$  for the ultimate tensile strength, less for the modulus) indicates that there are still improvement to be made.

Another important quality of UHMWPE fibers is their high strength to weight ratio. The density of PE is lower compared to other fiber materials (cf. Table 4.1), and the

**Table 4.1:** Mechanical properties of UHMWPE and other fibers. All values are reproduced from Ref. [165] unless otherwise stated.

	Tensile strength (GPa)	Modulus (GPa)	Density (g/cm <sup>3</sup> )	Melting temperature (°C)
UHMWPE				
- commercial [166]	4.1	159	0.97	150
- experimental [156, and refs. therein]	6.0	220	0.97	150
- theoretical [157–160]	18-30	280-355	0.97	150
Aramid commercial	3.0	112	1.44	560
PBO commercial	5.8	270	1.56	650
Polyarylate commercial	3.2	75	1.41	540
Steels [156, and refs. therein]	~ 1	~ 210	~ 8	~ 1500

high strength to weight ratio is attractive for weight-sensitive applications such as personal ballistic protection. The mechanical properties in UHMWPE are naturally highly anisotropic due to the high degree of alignment of the polymer chains in the fiber direction. The tensile strength and modulus values in the transverse direction of the fiber are correspondingly much lower [167]. UHMWPE fibers also have a relatively low compressive yield strength of about 2-3% of their tensile strength [167].

### 4.1.3 Applications

In this section, a brief overview of some of the applications of UHMWPE fibers is given. Since 1990, UHMWPE fibers have been commercially produced by Royal DSM in the Netherlands under the brand name Dyneema, and by Honeywell Specialty Materials in the USA (with brand name Spectra) and Toyobo Co. in Japan (under the current brand name Izanas).

#### Ropes

A big market for UHMWPE fibers is in the form of heavy-duty ropes, made by braiding multiple yarns of fibers together. Ropes made from UHMWPE fibers have similar tensile strength and elongation at break compared to steel wires, but at only a fraction of the weight. This is useful in applications where weight is of critical importance, for example as mooring and tugging ropes, where traditional steel wires have become too heavy. The low density of PE means that the UHMWPE ropes float on water, greatly enhancing their applicability in maritime environments. For example, during the installation of offshore constructions, such as windmills or oil platforms, the ability of the ropes to float on water greatly reduces the risk of rope loss during the installation process. Moreover, ropes made from UHMWPE are not affected by seawater, do not rot, and have high UV resistive properties. The low weight of UHMWPE ropes is also advantageous in lifting applications, for example in the form of crane ropes or hoisting slings, where the rope's own weight inherently limits the lifting capabilities. Even in rope applications where steel wires are otherwise applicable, lighter polymer ropes are easier to replace than heavy steel wires. Smaller ropes are also used for running rigging on yachts or as nets in commercial-scale fishing.

## Textiles

UHMWPE fibers can be woven into fabrics to provide additional strength, durability and abrasion resistance. For example, UHMWPE fibers can be woven into sports clothing, such as cycling shorts, to provide increased protection without sacrificing comfort. They are also used in dedicated protective clothing like safety gloves, where high cut and stab resistance is critical.

## Ballistic protection

High strength fibers made from UHMWPE are used in ballistic applications mainly in the form of composites. In ballistic applications, the primary properties of interest are light weight and the ability to absorb high amounts of energy. The energy absorption is determined by the specific strength (strength divided by density), elongation, and sonic velocity (determined by the specific modulus) [167]. Therefore, the high specific strength and specific modulus values of UHMWPE make them ideal candidates for this kind of application. Typical UHMWPE ballistic composites are made from unidirectional layers of fibers in a thermoplastic matrix. The layers are stacked with alternating fiber directions, with each layer rotated by 90 degrees compared with surrounding layers [168]. For flexible ballistic applications, two layers of alternating fibers are enclosed on both sides by a thin polymer film. In cases where flexibility is not a concern, several alternating layers are pressed at higher temperatures into the desired shape. In principle, fibers woven into textile fabrics can be used as well, but they generally show lower ballistic performance compared with UHMWPE composites. This is most likely due to the low coefficient of friction of the fibers, which allows the fibers to move in relation to each other upon projectile impact, lowering the effective amount of energy absorbed.

## Medical

UHMWPE is a much utilized biomaterial within the medical community. A high biocompatibility and biostability, in combination with the aforementioned high strength and low weight, makes UHMWPE fibers one of the most frequently used materials for bearing surfaces in orthopedic implants [167].

## 4.2 Gel-spinning

In order to realize fibers with high mechanical properties, the polymer chains need to be extended and oriented in parallel along the fiber axis. Typically, fibers made from flexible polymer chains can be extended and oriented by drawing the material from melt, that is where the polymer is in a liquid state and the chains are able to move independently. This can for example be done by melt-spinning, where the polymer melt is extruded through the holes of spinneret. However, the high molecular weight of UHMWPE gives rise to an extremely high viscosity, making it almost impossible to spin UHMWPE fibers from melt. Furthermore, the high density of polymer chain entanglements in UHMWPE melts severely limits the drawability of the fibers. The invention of the gel-spinning process in 1979 by DSM presented a solution to both of these problems. Firstly, by dissolving UHMWPE in solution, the viscosity is lowered to a point where extrusion through a spinneret becomes possible. Secondly, the entanglement density is drastically lowered in the spun filaments, allowing for the fibers to be drawn to a extremely high draw ratios (DRs). The resulting fibers exhibit high tensile strength and modulus through a combination of high levels of crystallinity and molecular orientation.

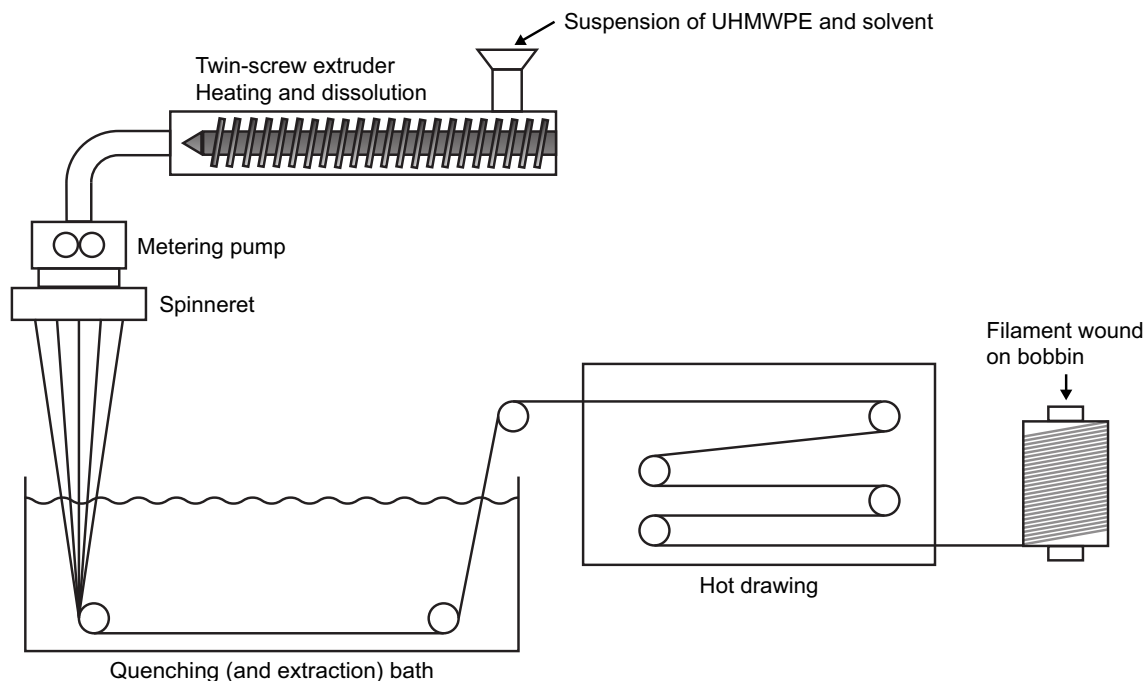


**Figure 4.2:** Schematic illustration of the gel-spinning process of UHMWPE fibers.

#### 4.2.1 Gel-spinning process

The gel-spinning process was first demonstrated in a series of papers by Smith and Lemstra [169–172]. Figure 4.2 shows a schematic illustration of the process. In brief, the main steps are as follows: A suspension of polymer and solvent, for example decalin or paraffin, is fed into a twin-screw type of mixer (extruder). The polymer suspension is subsequently heated above the melting point of the polymer, dissolving the polymer in the solvent. The solution is then continuously extruded through a spinneret at the end of the extruder. A spinneret is essentially a device consisting of a flat plate with a pattern of conical holes, forming capillaries through which the polymer solution flows. The flow of the polymer solution through the capillaries forces the molecules into a more extended form, and is the first step in achieving high chain extension and orientation. Upon exiting the spinneret, the polymer solution is quenched in a bath after passing through a small air-gap. The quenching bath facilitates crystallization of the polymer chains, fixing the less entangled state of the polymer in solution. From this point on, the fiber is referred to as gel-like, with the important distinction that the polymer chains are not chemically bonded to each other (rather, it is a 'physical' network formed by the entanglements). In some setups the liquid quenching bath is replaced by quenching in a controlled atmosphere, where the solution is cooled instead (sometimes referred to as dry-spinning).

The next step is removing the solvent from the polymer gel, and this is either accomplished by extraction in the quenching bath, or by evaporation in a controlled atmosphere (drying of the polymer gel). Following the removal of the solvent from the polymer gel, the individual fiber filaments are drawn by means of hot drawing. The drawing process induces further reorientation of the polymer chains, resulting in the final state of the fiber with the desired high degree of chain orientation and extension. Further discussion on the drawing step is presented in the next section.

There are several parameters of the spinning process that needs optimization in order to produce fibers with optimal qualities. These include solvent type and concentration,

molecular weight of the polymer, spinneret geometry, extrusion speed and quenching temperature, to name a few.

### 4.2.2 Drawing process

Proceeding the spinning process outlined in the previous section, the fibers are subjected to a drawing stage, where the high orientation and chain extension of the final fibers are achieved. As mentioned, spinning the fiber from solution is a key step for achieving high drawability, because the low entanglements density of the polymer in solution is fixed in the system upon crystallization. The drawing of the fibers are performed by wounding the fiber filaments over a series of rollers at an elevated temperature, roughly in between the dissolution temperature of the gel and the melting temperature of the pure polymer [170]. The difference in wounding speed between two rollers determine the drawing force applied to the fiber, and ultimately, the final DR. The DR is defined as

$$\lambda = \frac{L}{L_0}, \quad (4.1)$$

where  $L$  is the final length of the fiber after drawing and  $L_0$  is the initial length of the fiber. For example, a fiber being wound across an initial roller with speed  $v_1 = u$  and a second roller with speed  $v_2 = 10u$  will have a DR of  $\lambda = 10$ . Depending on the processing conditions, it is possible to achieve DRs of over 100 in UHMWPE [173].

### 4.2.3 The role of molecular weight

A high molecular weight is essential for achieving high tensile strength in polyethylene fibers [174], and UHMWPE with an average weights above  $1 \times 10^6$  g/mol is used in commercial fibers. In a simple picture, the molecular chains inside the fibers are bound to each other through van der Waals forces, which are several times weaker than the covalent bonds found between the carbon molecules in the polymer chains. Therefore, it follows that polymers with a high degree of polymerization, that is polymers with long chains, are more likely to have a large overlap between adjacent chains, and thus stronger inter-chain bonds due to the additive nature of the van der Waals forces.

The relationship between (weight-averaged) molecular weight ( $\overline{M}_w$ ) and tensile strength was studied by Smith et al. [175]. They concluded that the tensile strength scaled with  $\overline{M}_w$  as  $\sigma = \overline{M}_w^{0.4}$  in the range of  $5 \times 10^3$  g/mol to  $4 \times 10^6$  g/mol. The molecular weight dependence of the maximum tensile strength in PE fibers was also described using theoretical modeling in the work of Termonia and Smith [176]. Their results suggested no presence of a simple power law dependence outside the experiential range employed by Smith et al. [175], and that failure predominantly involves chain slippage at low  $\overline{M}_w$  and bond fracture at high  $\overline{M}_w$ .

On the other hand, the molecular weight of the feed polymer also negatively influences the ultimate drawability of the fiber. Bastiaansen [177] showed that the maximal attainable DR in melt-crystallized polyethylene scales with weight-averaged molecular weight as  $\lambda_{max} = \overline{M}_w^{-0.5}$ . In solution-cast PE, the maximum attainable DR scales with the Bueche parameter ( $c\overline{M}_w$ ) instead as

$$\lambda_{max} = (c\overline{M}_w)^{-0.5}. \quad (4.2)$$

This is in contrast to expectations based on the maximum DR of a single polymer chain, which is expected to have a maximum extension that scales with molecular weight roughly as

$$\lambda_{max} = (\overline{M}_w)^{0.5}. \quad (4.3)$$

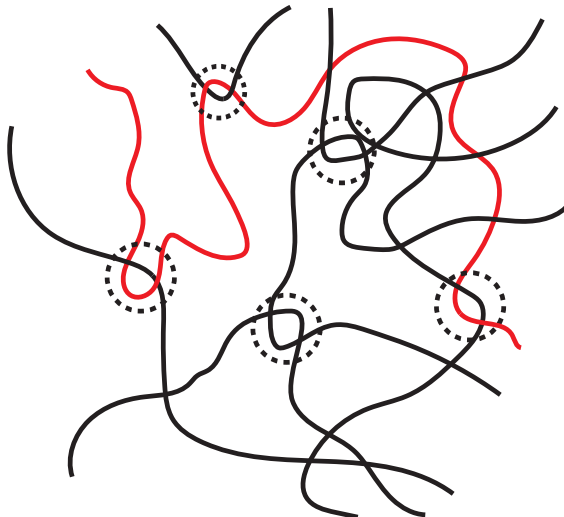


**Figure 4.3:** Illustration of topological entanglements in polymers.

The above relationship is derived from the ratio between the length of a fully extended chain and the radius of gyration of an ideal chain [178].

In addition to having a high average molecular weight, the polydispersity of the polymer is also important for achieving high fiber strength. Ideally the polydispersity of the polymer should be as low as possible. Shorter polymer chains are less effective at transferring the load in the fiber, and represent possible points of failure, while longer chains may hinder drawing based on the above discussion.

#### 4.2.4 The role of polymer concentration and entanglements

In the previous section, it was established that the maximum attainable drawability of a PE fibers is limited by the molecular weight. The reasoning for this can be found in the concept of entanglements. In a simple picture, entanglements can be understood as topological restrictions of the polymer chain motion by adjacent polymer chains, since the one-dimensional chains cannot pass through each other (illustrated in Fig. 4.3). Entanglements effects in polymers have been extensively studied by de Gennes [179], and later by Doi and Edwards [180]. In the tube model by Edwards, the polymer chain is divided into strands between adjacent entanglements, and the motion of individual strands are assumed to be driven by the thermal motion. The thermal motion of the strands in the transverse direction can be described by a quadratic potential. The strand is unlikely to move to a transverse position with an energy more than  $kT$  above the minimum of this potential. This means that the strands are confined inside a tube-like region with diameter  $a$ , which can be interpreted as the end-to-end distance of the entanglement strand

$$a \approx bN_e^{1/2}. \quad (4.4)$$

Here,  $b$  is the Kuhn length and  $N_e$  is the number of monomers comprising the entanglement strand. The number of entanglements  $Z = N/N_e$  is a function of the polymer's molecular weight. This can intuitively be understood by considering that longer chains are more likely to entangle than shorter chains. The molecular weight between entanglements is defined as  $M_e = N_e M_0$ , where  $M_0$  is the molar mass of the polymer.

In UHMWPE, the entanglement density in melt is thought to be a limiting factor of drawability in melt-spun fibers [181]. The argument is based on entanglements in polymer

melts, where the entangled chains form a transient network, with the entanglements acting as non localized junction points for the applied stress. This hinders large deformation, and instead, the fibers fracture during drawing. By dissolving the polymer in solution, the molecular weight between entanglements changes and becomes inversely proportional to the volume fraction  $\phi$  of the polymer as [182]

$$(M_e)_{sol} = M_e/\phi, \quad (4.5)$$

when the polymer concentration exceeds the value of random overlap between polymer coils. Hence, the number of entanglements is also inversely proportional to the volume fraction.

Upon crystallization from solution, Smith et al. [182] argues that the favorable entanglement density of the polymer in solution is maintained, that is, the intermolecular topology is essentially unchanged when removing the solvent from the polymeric gel (corresponding to the quenching step in Fig. 4.2). Therefore, it must follow that the maximum attainable DR is dependent on the initial concentration of the polymer in solution. Indeed, the authors use theory for rubber elasticity to argue that the maximum DR must be a function of the number of chain segments  $N_c$  between crosslinks as

$$\lambda_{max} = (N_c)^{1/2}. \quad (4.6)$$

Assuming that most of the entanglements trapped in the polymer upon crystallization from solution acts as crosslinks ( $N_c \approx N_e$ ), combining Eqs. (4.6) and (4.5) yields

$$\lambda_{max} = (N_e/\phi)^{1/2}. \quad (4.7)$$

The above relationship is derived on the assumption that the entanglements are trapped upon crystallization from solution, and other effects, such as chain slippage and the influence of crystallites, are not taken into account. In the paper, Smith et al. argues that these effects are small on the time scale of their experiments, and their results demonstrate excellent agreement with the scaling proposed by Eq. (4.7).

However, if the polymer concentration falls below the critical concentration  $c^*$  for coil-overlap, the drawability is also impacted negatively due to poor interconnectivity of the polymer chains. Therefore, the polymer concentration must be chosen to balance low entanglement density with sufficient coil-overlap. From an economic point of view, the polymer concentration must also be sufficiently high to ensure optimal productivity. Because of the extremely high molecular weight of UHMWPE, the coil-overlap concentration is very low. For example, a 10 wt% UHMWPE-decalin solution containing UHMWPE with weight-average molecular weight of  $2 \times 10^6$  and a polydispersity index ( $M_w/M_n$ ) of 12 has a concentration of  $c/c^* \sim 22$  [3].

### 4.3 Structure and morphology

The structure of the gel-spun UHMWPE fibers undergoes extensive changes throughout the spinning and drawing processes. This structural evolution has been studied extensively, and is summarized in this section. The less entangled state of the polymer in solution is crucial for the development of highly oriented extended chains in the final fiber. However, the simple picture of chain extension induced by flow of the polymer is nowhere near the full story, and as we shall see, the structural evolution involves important transient structures and multiple chain rearranging phenomena. Particularly interesting is the role of the so-called shish-kebab superstructure, which is thought to originate from the extensional

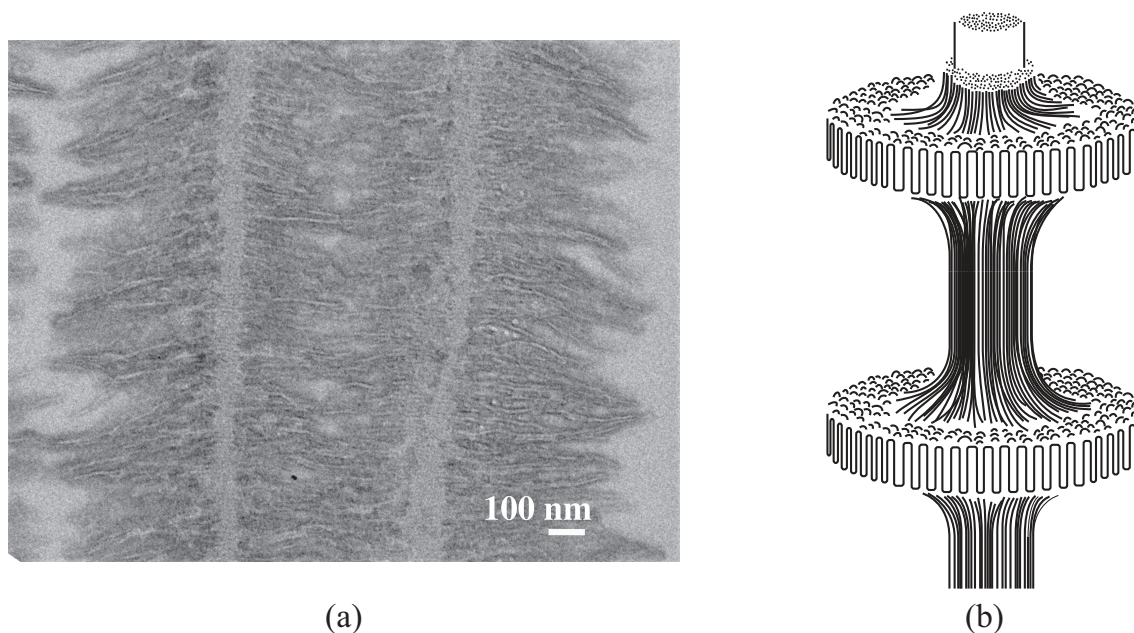


**Figure 4.4:** (a) TEM image of a shish-kebab superstructure found in a gel-spun UHMWPE fiber. (b) Schematic illustration of the shish-kebab superstructure. The structure is composed of chain-folded lamellae connected by a core of extended chain crystals. Figure (a) is reprinted with permission from [183]. Copyright 2011 American Chemical Society.

flow of the molecules during the spinning process. In the subsequent drawing process, the shish-kebab superstructures are transformed and the morphology of highly oriented extended chains is achieved.

### 4.3.1 Structural evolution during the spinning process

#### Polymer in solution

In the initial solution, the polymer chains can be described as coils with a degree of overlap between neighboring chains, assuming that the polymer concentration is above the critical concentration  $c^*$  [178]. On large length scales, the polymer is expected to exhibit some amount of concentration fluctuations due to the thermodynamics of the system. Indeed, evidence of such density fluctuations have been show for UHMWPE in solutions with polymer concentrations above  $c^*$  [183]. Upon extrusion through the spinneret hole, the polymer solution is subjected to a shear flow, leading to a enhancement of these concentration fluctuations [184, 185]. In the literature, the shear flow and subsequent enhancement of concentration fluctuations, ultimately resulting in phase separation, has been proposed as the main driving force for the formation of the important shish-kebab superstructure.

#### Shish-kebab superstructure

After crystallization of the polymer from solution, but before extraction of the solvent, the morphology of the as-spun fiber is that of polymer-rich domains interspersed with solvent rich domains. The polymer rich domains are composed predominantly of crystalline shish-kebab superstructures [2, 3, 183, 186], which are shown in Fig. 4.4. From the figure, it is apparent that the shish-kebab superstructure consists of two characteristic parts: a core

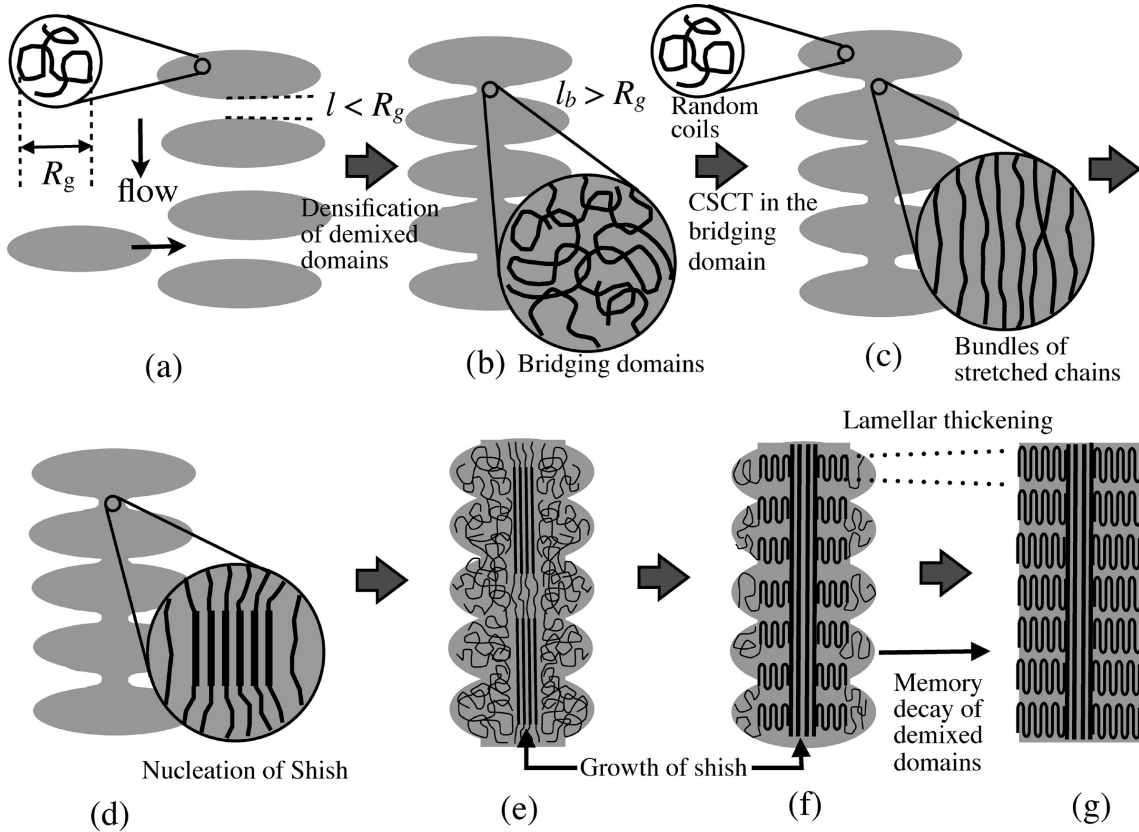


**Figure 4.5:** Illustration sketching the kinetic pathway from demixed domains in flow to shish-kebab superstructure: (a) Oblong demixed domains in flow are aligned in strings parallel with the flow direction. Bridging domains of polymer chains are formed between neighboring domains (b), which are subsequently formed into bundles of stretched chains (c), and nucleated into shish (d). The nucleated shish grows into the interior of the domains (e), forming the backbone of the shish-kebab superstructure (f). Simultaneously, coils in the demixed domains crystallize onto the surface of the shish (f), and finally, long-range rearrangements of the polymer chains within the as-grown shish-kebab causes memory decay of the demixed domains, forming the final ordered shish-kebab superstructure (g). Reprinted with permission from [183]. Copyright 2011 American Chemical Society.

of extended chain crystals, called the shish, along which several spherical chain-folded crystals (the kebabs) are located. The extended chains of the shishes are highly oriented, forming densely packed fibrillar crystals. The kebabs, on the other hand, are formed by polymer chains folded into large 3-dimensional lamellae regions, extending perpendicular to the shish core. The dimensions of the shish-kebab vary with processing parameters, but typically for as-spun (not drawn) UHMWPE fibers, the shish diameter is on the order of tens of nm, while the kebabs are much larger, with diameters on the order of  $\mu\text{m}$  [3]. The shish-kebab structure were first observed in stirred dilute solutions of UHMWPE in the 1960s [187], and has been observed in other polymeric systems crystallized during flow [188, 189]. While the exact origin of the shish kebab structure is still under debate [189–193], a scenario based on observations of gel-spun UHMWPE fibers is presented in the next section.

## Development of shish-kebab structure

A scenario for the formation of shish-kebab superstructures in UHMWPE during gel-spinning has been proposed by Murase et al. [183]. Here, the authors were able to isolate individual UHMWPE filaments from different stages of the gel-spinning process, and provide eloquent real-space images of the corresponding fiber morphology using transmission electron microscopy (TEM). The different stages of the shish-kebab formation is illustrated in Fig. 4.5. Initially, the concentration fluctuations found in the polymer solution are enhanced by the flow of the solution through the spinneret. This is manifested as plane-wave type fluctuations with wave vectors parallel to the flow direction. As the amplitude of the plane-wave fluctuations increases, the increased hydrodynamic interactions between solvent and polymer destabilize the waves and break them into demixed domains with oblong shape (see Fig. 4.5a). The demixed domains orient themselves in strings parallel with the flow due to hydrodynamic interactions, with the long axis of the oblong domain aligned perpendicular to the flow. The concentration fluctuations in the demixed domains give rise to regions with higher and lower entanglement densities. In the shear flow, the stresses on the entanglement rich regions are higher than on the regions with less entanglements. If the shear stress is above the critical relaxation rate of the polymer, the entanglements are not able to disentangle in time, and the excess stress is relieved by squeezing solvent out of the entanglement-rich domains.

In the next stage, domains of bridging chains are formed in the regions of two impinging domains (Fig. 4.5b). The authors speculate that an enhancement of the local strain rate causes the bridging domains to form bundles of stretched chains (Fig. 4.5c) and subsequent nucleation of shish (Fig. 4.5d). These shish then grow into the interior of the demixed domains, forming the crystalline backbone of the shish-kebab superstructure (Fig. 4.5e). This is followed by epitaxial overgrowth of the coils in the demixed domains onto the surface of the shish, resulting in the crystallization of the kebab (Fig. 4.5f). Finally, long range rearrangements of the chain molecules are observed, which causes memory loss of the demixed domains, and as a result, a more ordered shish-kebab superstructure is formed.

The outlined scenario provides one possible kinetic pathway of the molecules from a system of entangled coils in solution, to the semi-crystalline shish-kebab superstructure found in gel-spun UHMWPE fibers. This kinetic pathway is naturally affected by the processing parameters in the gel-spinning process, and there is strong evidence that involved timescales varies locally within the fibers themselves. This results in a spatially inhomogeneous structure, which will be discussed in Section 4.3.3.

### 4.3.2 Structural evolution during drawing process

Following the transformation from entangled coils to the semicrystalline shish-kebab structure during gel-spinning, the final rearrangement and extension of the molecular chains happens during the drawing stage. The structural evolution of the UHMWPE fibers was studied in detail by Ohta et al. [3]. In the study, UHMWPE fibers spun from solution were drawn in multiple steps to achieve DRs ranging from 1 to 10. The morphology of the drawn fibers were studied by TEM, and a simple model for the breaking force was proposed. The undrawn fibers were shown to consist of the same shish-kebab morphology as discussed in the previous section. Moreover, the results showed that the shish-kebab morphology remained the principal morphology even after drawing. Even at the highest draw ratio (DR = 9), the morphology of the fiber was consistent with that a shish-kebab superstructure with very small kebabs. These findings implies that the fibrillar morphology of extended chains originates directly from the shish-kebab morphology. The situation



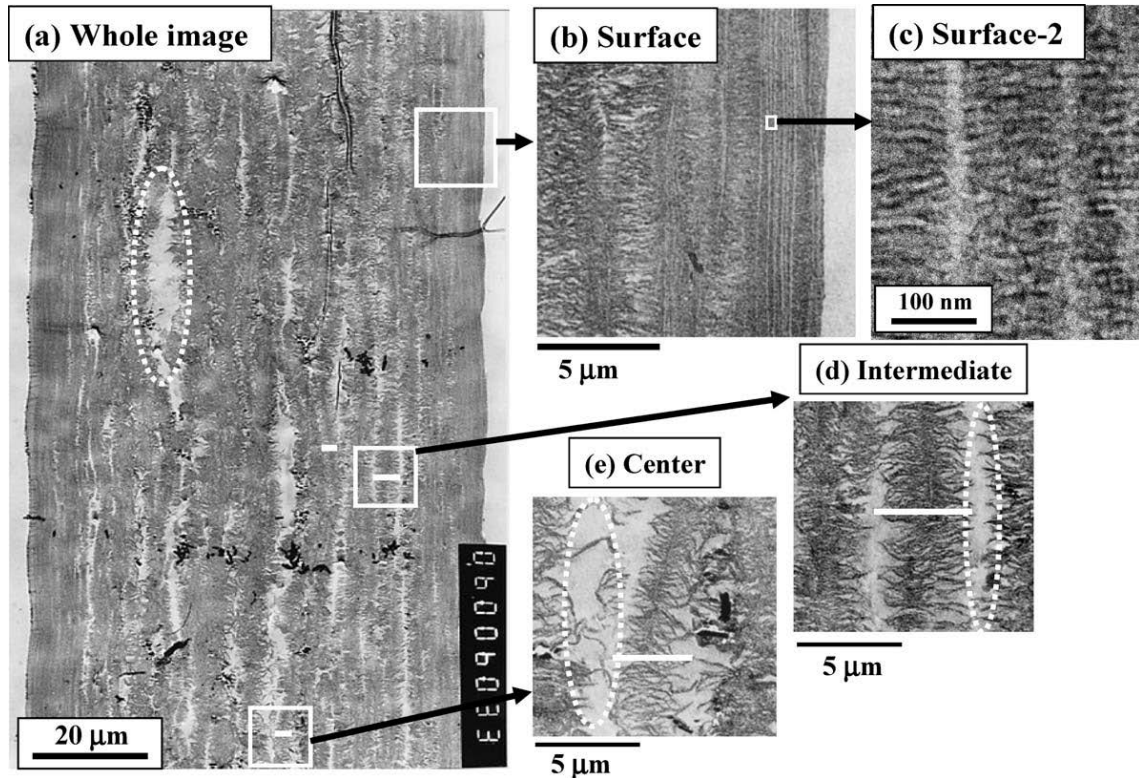


**Figure 4.7:** TEM images of a gel-spun UHMWPE fiber showing the whole cross section of the fiber (a) and higher magnification images focused on the surface (b,c), intermediate (d) and core regions (e), encompassed by white squares in parts (a,b). Reproduced with permission from Ref. [3]. Copyright 2010, John Wiley & Sons, Inc.

### 4.3.3 Structural inhomogeneities in gel-spun fibers

In the previously outlined scenario for the formation of shish-kebabs in UHMWPE fibers during gel-spinning by Murase et al. [183], the authors noticed that the fiber's structure varied along the lateral dimension of the fiber. Essentially, the timescale of the kinetic pathway outlined in Fig. 4.5 is faster closer to the surface of the fiber. This is thought to be primarily an effect of the temperature gradient across the fiber radius, since the cooling rate is necessarily higher at the surface compared with the core region. The authors propose, that the increased cooling at the fiber surface results in higher stress and higher work done by the flow near the surface, accelerating the kinetic pathway. This effect is seen in Fig. 4.7 by the lateral variations of the fiber structure. The shown fiber is extracted from the gel-spinning process before drawing [3]. For this particular study, the fibers were cooled by nitrogen gas at room temperature in place of the liquid quenching bath (cf. Fig. 4.2) after leaving the spinneret (i.e. they are dry-spun). It is evident that the morphology near the surface of the fiber differs from the morphology near the fiber core, with the surface region consisting of closely packed shish-kebabs with intercalated kebabs, and the core region consisting thicker shish-kebabs with interspersed solvent-rich regions. It has also been proposed that the temperature gradient across the fiber radius can induce a polymer concentration gradient, giving rise to inhomogeneities in crystallinity and molecular orientation [2].



## CHAPTER 5

## Methods for Characterizing Polymer Fibers

---

The following chapter serves to outline the experimental techniques and analysis methods employed to characterize the local structure of UHMWPE fibers in Paper V.

### 5.1 Wide-angle X-ray scattering

One of the most commonly used techniques to obtain information on the crystalline structure in polymers is wide-angle X-ray scattering (WAXS). As the name implies, WAXS utilizes a close sample-to-detector distance in order to capture scattering information at wide  $2\theta$  angles, and in accordance with Bragg's law (Eq. (1.9)), resolve feature sizes on the order of the crystalline lattice. From a single WAXS image of a polymer sample, one can obtain information on the crystallographic unit cell, different crystalline phases, the degree of crystallinity, crystallite size (or coherence length), the orientation distribution of the crystallites, and so forth. Moreover, WAXS is a highly versatile technique that can be performed using a laboratory or synchrotron source. Several companies offer simple all-in-one solutions, allowing the end user to perform X-ray scattering experiments in a plug-and-play manner, while advanced high brilliance synchrotron sources allow for complex studies of for example crystallization or deformation in real-time or detailed structural analysis with high spatial resolution. WAXS can be performed on a wide range of samples, including isotropic samples (powders, isotropic bulk, polymer in solution) and anisotropic samples with preferred orientation (e.g. fibers). As will be explained below, detailed information on the crystallite orientation distribution can be readily obtained from a single WAXS image in the special case of polymer samples with inherent cylindrical rotational symmetry, otherwise known as "fiber symmetry". In the literature, measurements of this kind have historically been referred to as fiber diffraction [197].

#### 5.1.1 Basic concepts and experimental configuration

As outlined in Chapter 1, a fraction of the incident X-ray plane waves propagating through the polymer is diffracted by periodic changes in the electron density. In WAXS, this

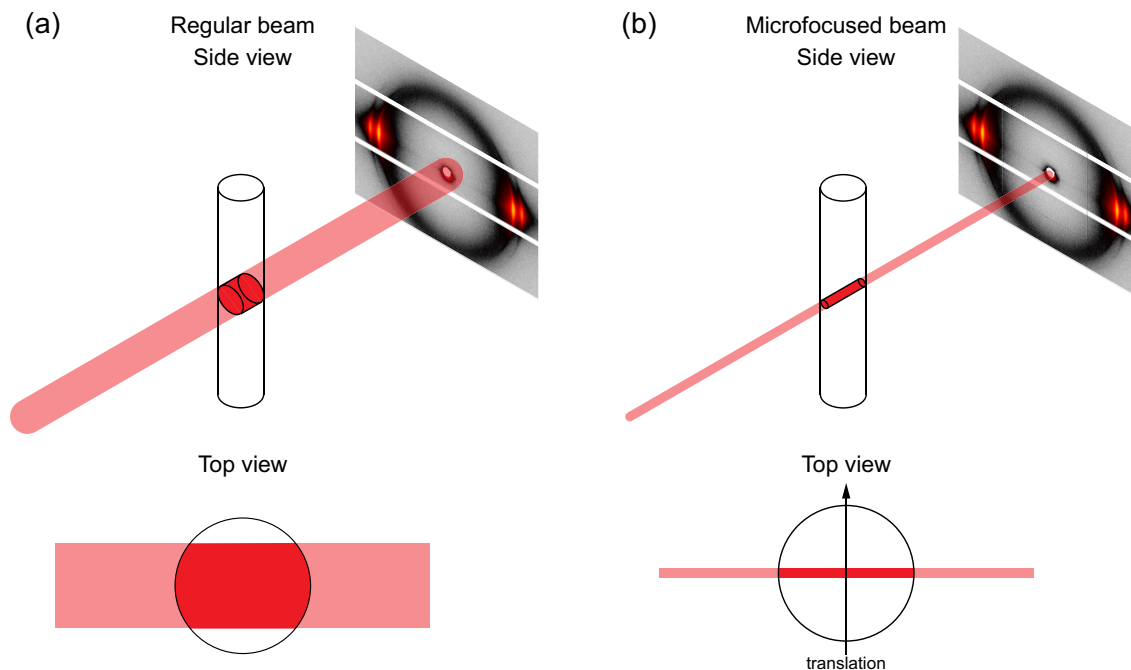


**Figure 5.1:** Illustration of the experimental geometry employed in WAXS with the average scattering volume highlighted. (a) A regular sized beam probes a large part of the fiber in one measurement. (b) A microfocused beam probes a smaller sample volume, and scattering images are obtained from multiple positions along the transverse fiber direction by scanning the sample with the beam.

periodicity stems from the adjacent crystalline planes. The typical transmission WAXS geometry is sketched in Fig. 5.1. In this configuration, the point focused X-ray beam impinges the fiber sample perpendicular to fiber axis. Beyond the fiber sample, a 2D area detector records the entire scattered signal in one frame. Just as in the case of GIWAXS (Section 3.1), the 2D area detector captures a snapshot of the scattered X-rays, and the angular resolution of the scattering signal depends on the beam size, the sample-to-detector distance, and the pixel size. In a typical WAXS experiment, the X-ray beam size is on the order of hundreds of micrometers, meaning that a large sample volume is illuminated at one time (Fig. 5.1a). This is highly advantageous if the sample is spatially homogeneous, since a larger number of crystallites are probed simultaneously and the intensity loss from beam focusing is minimized.

Conversely, in samples where the microstructure is not homogeneous on the length scale of the beam size, the microstructure determined from the volume-averaged scattering is exactly that, that is an average of the microstructure in the probed volume. Loss of information is therefore expected. Recent advances in synchrotron focusing optics (see Section 1.3) have made high-brilliance micro- and nanofocused beams possible, greatly enhancing the spatial resolution available in X-ray scattering experiments. Therefore, by scanning the micro- or nanofocused X-ray beam across the transverse direction of the fiber (Fig. 5.1b), we can obtain profiles of the microstructure as a function of the beam position. However, simply scanning the beam across the fiber will not provide information on the true radially profiled microstructure inside the sample, since the scattering patterns are still volume-averaged along the longitudinal direction of the beam. We will discuss this issue, and how to circumvent it, in Section 5.1.4.

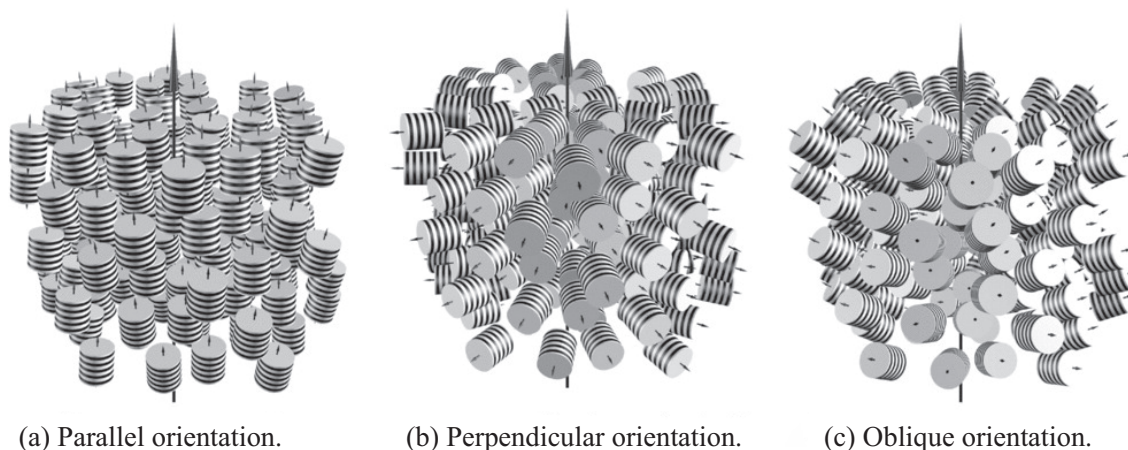


**Figure 5.2:** Illustration of various systems with fiber symmetry. The individual structural units (cylinders of alternating stacks) are cylindrically symmetric with respect to their own symmetry axis (small arrows), while the orientation distribution of the structural units is centered about the primary fiber axis (large vertical arrow). Reproduced with permission from [198]. Copyright 2010 Taylor & Francis.

### 5.1.2 Fiber symmetry

Fiber symmetry is defined as uniaxial or cylindrical symmetry [199]. As the naming implies, fiber symmetry is often observed in actual fibers (synthetic or natural), but it is not limited to only these cases. In fact, many different systems exhibit fiber symmetry, for example organic thin-films with random in-plane symmetry (Section 3.1.1). General for systems with fiber symmetry is that the scattering pattern remains unchanged when the sample is rotated about the fiber axis. Figure 5.2 shows schematics of various systems with fiber symmetry. In the figure, the structural units (depicted as cylinders of alternating stacks) are distributed in 3D space. If the orientation distribution of the structural units is centered about the fiber axis (large vertical arrow in Fig. 5.2), the system is fiber symmetric.

Moreover, if the individual structural units themselves exhibit cylindrical symmetry about their own symmetry axis (depicted as small arrows for each cylinder in Figure 5.2), the system is said to exhibit "simple fiber symmetry". This condition is fulfilled in systems where the scattering structures themselves naturally exhibit cylindrical symmetry (an example hereof is the cylindrically symmetric shish-kebab superstructures discussed in Section 4.3.1), or because of an actual rotational average, that is the scattering of the average representative scattering structure is symmetrical [198]. The latter is often the case in WAXS, where the individual crystallites themselves are not cylindrically symmetric, but are randomly oriented in the plane perpendicular to the fiber axis, and thus the recorded scattering pattern is a rotational average. The ideas and relationships presented in the following section is limited to the case of simple fiber symmetry.

### 5.1.3 Determination of crystalline orientation

The orientation of crystallites inside a polymer sample is often of interest. The high-strength of fibers made from UHMWPE is a direct consequence of the polymer chain orientation, and thus being able to quantify the degree of orientation is important. The strongest density fluctuations in the uniaxially oriented polymer molecules are due to the lateral packing of the extended structural units. In this case, the strongest scattering

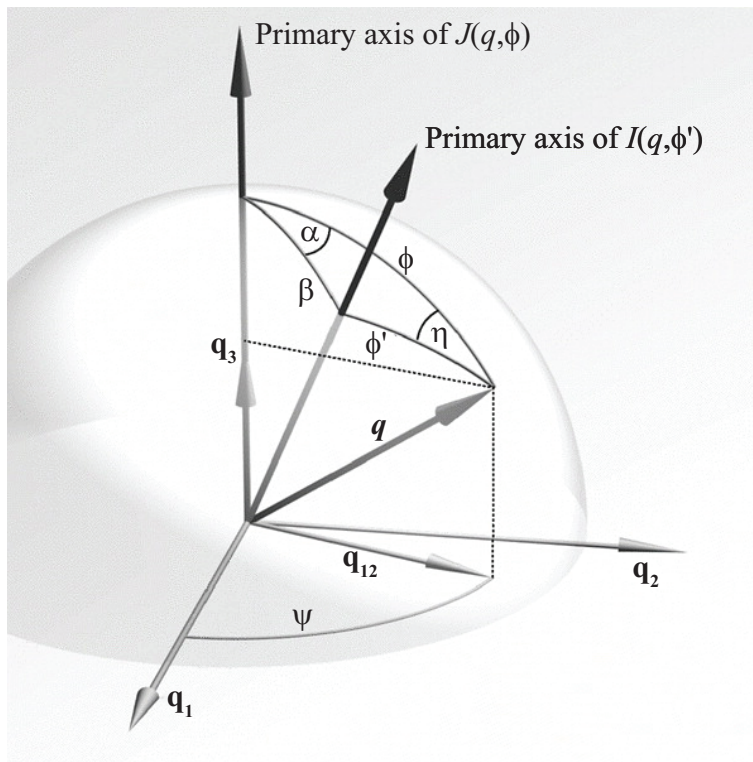


**Figure 5.3:** Spherical-trigonometric relationship between the scattering vector  $\mathbf{q}$ , the main fiber axis, and the primary axis of the individual structural unit. Adapted with permission from [198]. Copyright 2010 Taylor & Francis.

signal is usually located along the equatorial of the scattering pattern (assuming the vertical arrangement of the fiber seen in Fig. 5.1). For PE, the strongest scattering peak originates from the (110)-plane of the orthorhombic unit cell (see Fig. 4.1), whose normal is indeed perpendicular to the fiber axis. Thus, in order to determine the orientation around the fiber axis, a relationship between the equatorial scattering arc of the (110)-planes and the true orientation distribution needs to be established.

The following argument is based on the arguments and notations of Burger et al. [198], but similar arguments are presented in the work of Lovell and Mitchel [200] and later in Ref. [201].

If the structural units in Fig. 5.2 form an orientation angle  $\beta$  with respect to the fiber axis, the resulting orientation distribution of the structural units can be described as a function of the angle  $g(\beta)$ , also known as the orientation distribution function (ODF). As a consequence of the simple fiber symmetry in the system, the ODF is exclusively a function of  $\beta$  and the orientation in the system is fully described by  $g(\beta)$ . Since  $g(\beta)$  is a probability distribution, we normalize it choosing the following normalization

$$\int_0^{\pi/2} g(\beta) \sin \beta \, d\beta = 1. \quad (5.1)$$

Now let us denote the intensity distribution of the individual structural units as  $I(q, \phi')$ , and the intensity distribution of the entire ensemble of structural units as  $J(q, \phi)$ . The polar angles  $\phi$  and  $\phi'$  denote the angle between the scattering vector and the main fiber axis, and the angle between the scattering vector and the primary axis of the structural unit, respectively. They are illustrated in Fig. 5.3. For constant  $q$ , we introduce the

shorthand notation  $J(\phi)$  and  $I(\phi')$ . In order to calculate the intensity distribution  $J(\phi)$ , we need to average over the entire ensemble of  $I(\phi')$ , weighted by the ODF.

$$J(\phi) = \frac{1}{4\pi} \int_{\alpha=0}^{2\pi} \int_{\beta=0}^{\pi} I(\phi') g(\beta) \sin \beta \, d\beta \, d\alpha. \quad (5.2)$$

From the trigonometric relationship in Fig. 5.3, we obtain

$$\begin{aligned} \cos \phi' &= \cos \phi \cos \beta + \sin \phi \sin \beta \cos \alpha, \\ \cos \beta &= \cos \phi \cos \phi' + \sin \phi \sin \phi' \cos \eta. \end{aligned} \quad (5.3)$$

By changing the variables of the integration from  $(\alpha, \beta)$  to  $(\phi', \eta)$  we obtain the Jacobian [202, 203]

$$\sin \beta \, d\beta \, d\alpha = \sin \phi' \, d\phi' \, d\eta \quad (5.4)$$

and Eq. (5.2) becomes

$$\begin{aligned} J(\phi) &= \frac{1}{4\pi} \int_{\eta=0}^{2\pi} \int_{\phi'=0}^{\pi} I(\phi') g(\beta) \sin \phi' \, d\phi' \, d\eta \\ &= \frac{1}{2} \int_{\phi'=0}^{\pi} \left[ \frac{1}{2\pi} \int_{\eta=0}^{2\pi} I(\phi') g(\beta) \, d\eta \right] \sin \phi' \, d\phi' \\ &= \int_0^{\pi/2} I(\phi') F(\phi, \phi') \sin \phi' \, d\phi', \end{aligned} \quad (5.5)$$

where the integration kernel  $F$  is defined as

$$F(\phi, \phi') = \frac{1}{\pi} \int_0^{\pi} g(\beta) \, d\eta. \quad (5.6)$$

The kernel  $F$  can intuitively be understood as the function that transforms a narrow peak (approximated by a  $\delta$ -function) of  $I(\phi')$  at a given angle  $\phi_0$  into the peak profile of  $J(\phi)$

$$I(\phi') = \frac{\delta(\phi' - \phi_0)}{\sin \phi_0} \implies J(\phi) = F(\phi, \phi_0). \quad (5.7)$$

Now let us introduce the expansion of  $g$  into a series of Legendre polynomials  $P_n^m$  [203, 204]. Due to symmetry constraints, only the terms with  $m = 0$  and even  $n$  survives. Thus

$$g(\beta) = \sum_{n=0}^{\infty} a_n P_{2n}(\cos \beta), \quad (5.8)$$

where the coefficient  $a_n$  is given by

$$a_n = (1 + 4n) \int_0^{\pi/2} g(\beta) P_{2n}(\cos \beta) \sin \beta \, d\beta. \quad (5.9)$$

The kernel can now be written as [203, 204]

$$F(\phi, \phi') = \sum_{n=0}^{\infty} a_n P_{2n}(\cos \phi) P_{2n}(\cos \phi'). \quad (5.10)$$

From Eqs. 5.2 and (5.9), we see that the Legendre polynomials are eigenfunctions to Eq. 5.5

$$\int_0^{\pi/2} P_{2n}(\cos \phi') F(\phi, \phi') \sin \phi' \, d\phi' = \frac{a_n}{1 + 4n} P_{2n}(\cos \phi). \quad (5.11)$$

The normalization of  $g$  requires  $a_0 = 1$ , and therefore the first expansion coefficient of interest is  $a_1$ . This coefficient is related to the so-called Herman's orientation parameter  $\overline{P}_2$  as

$$\overline{P}_2 = \int_0^{\pi/2} \frac{3 \cos^2 \beta - 1}{2} g(\beta) \sin \beta d\beta = \frac{a_1}{5}. \quad (5.12)$$

The Herman's orientation parameter is in many cases sufficient when it comes to describing the orientation in fibers [162, 205, 206]. It takes on values between -0.5 and 1, where -0.5 represents the case of perfect perpendicular orientation to the fiber axis, 0 represents the isotropic case and 1 represents the case of perfect parallel orientation to the fiber axis. Higher order coefficient are sometimes used to obtain a more complete description of the ODF, and they are especially useful in systems with a very high degree of orientation ( $\overline{P}_2 \sim 1$ ) [201, 207]. Setting  $\phi' = \pi/2$  in Eq. 5.10 we get

$$F(\phi, \pi/2) = \sum_{n=0}^{\infty} \frac{(-1)^n (2n)!}{4^n n! n!} a_n P_{2n}(\cos \phi), \quad (5.13)$$

which then leads us to the important relationship

$$\overline{P}_{2, \pi/2} = -\frac{\overline{P}_{2,0}}{2}. \quad (5.14)$$

Thus, the Herman's orientation parameter of the ODF can be extracted from the radial broadening of an equatorial pea by multiplying by -2, if the approximation of simple fiber symmetry holds.

Furthermore, provided that the scattering peaks are narrow along the equatorial (i.e. the crystallites are sufficiently large and the system has sufficient long range order), the intensity distribution  $J(q, \phi')$  can be factorized into

$$J(q, \phi) \propto H(q)F(\phi, \phi'). \quad (5.15)$$

In this case, we can determine the Herman's orientation parameter of the ODF from the radial arc of the scattered intensity. This is done by numerical integration and normalization [199]

$$\overline{P}_2 = \frac{\int_0^{\pi/2} J(q_0, \varphi) \frac{1}{2} (3 \cos^2 \varphi - 1) \sin \varphi d\varphi}{\int_0^{\pi/2} J(q_0, \varphi) \sin \varphi d\varphi}. \quad (5.16)$$

Equations (5.14) and (5.16) are used to determine the orientation of the PE crystallites in Paper V.

#### 5.1.4 On the issue of smearing

Spatially resolved X-ray scattering experiments of fibers, where the fiber specimen is scanned by a microfocused X-ray beam along the direction perpendicular to the fiber axis, are inherently affected by the issue of smearing. The scattering images collected by these types of scans are not giving information on the true radially profiled microstructure. Rather, they represent a projection of the volume-averaged microstructure inside the fiber along the path of the X-ray beam. This situation is illustrated in Fig. 5.4.

If the X-ray beam is scanned along the y-dimension, the measured intensity can be thought of as a projection of the irradiated volume onto the y-axis given by

$$I_{proj}(\mathbf{q}, y) = \int_{-\infty}^{\infty} I(\mathbf{q}, \sqrt{x^2 + y^2}) dx, \quad (5.17)$$

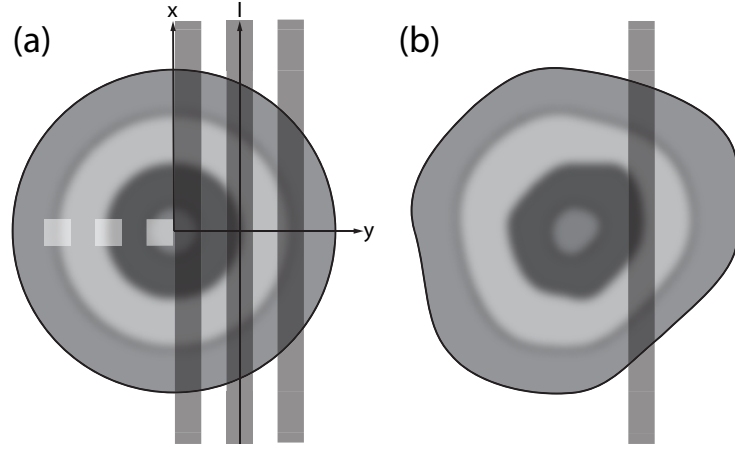


**Figure 5.4:** Illustration of the X-ray beam's path through the fiber in the standard geometry. The X-ray beam (dark lines) probes the entire longitudinal volume of the fiber during each measurement, and the resulting scattering is thus a projection onto the  $y$ -axis ( $x$  is the integration variable). If the fiber is cylindrically symmetric (a), then true radial profiles of the internal structure (white squares) can be obtained using the inverse Abel transformation. If the fiber is not cylindrically symmetric (b), the Abel transformation is no longer valid.

where  $I_{proj}$  denotes the projected (measured) scattering intensity and  $I$  denotes the true scattering intensity from a small voxel (on the order of the beam size) around the the position  $(x, y)$ . If the sample under consideration is fully cylindrically symmetric (see Fig. 5.4a), and if the local structure everywhere inside the irradiated volume exhibits simple fiber symmetry (i.e. local fiber symmetry), then the local scattering information can be recovered using the inverse Abel transform [208, 209]. If Eq. (5.17) is rewritten as a function of the radius  $r = \sqrt{x^2 + y^2}$

$$I_{proj}(\mathbf{q}, y) = 2 \int_y^\infty \frac{I(\mathbf{q}, r) r dr}{\sqrt{r^2 - y^2}}, \quad (5.18)$$

then the inverse Abel transform is defined as

$$I(\mathbf{q}, y) = -\frac{1}{\pi} \int_y^\infty \frac{dI_{proj}(\mathbf{q}, r)}{dr} \frac{dr}{\sqrt{r^2 - y^2}}. \quad (5.19)$$

In principle, the Abel transform is a form of onion peeling [210], where the individual contributions to the projected scattering images are slowly peeled off starting from the outer shell. In practice, the solution to Eq. (5.19) is often found using computational algorithms such as the two-point or three-point Abel inversions [211], or by expanding the projection in a basis set of Gaussian functions (BASEX algorithm) [212]. The deconvolution or desmearing of the scattering information is sometimes referred to as one-dimensional tomography [208, 211, 213]. However, these techniques are no longer applicable when the fiber sample is not cylindrically symmetric (see Fig. 5.4b), or when the local fiber symmetry is violated. Stribeck and co-workers eloquently describe the reconstruction artifacts resulting from measurements of samples without local fiber symmetry in Ref. [210]. In Paper V, we attempted to desmear the WAXS data using both two-point Able inversion and the BASEX algorithm, without success. This is not surprising considering the lack of cylindrical symmetry of the fiber cross-section.

Other solutions to the smearing problem have been proposed in the literature. Roth et al. [214] simulated the smeared intensity profiles of single fibers of poly(*p*-phenylene terephthalamide) (PPTA) using a three-layer model and a Monte Carlo approach. Davies et al. [215] circumvented the problem of smearing altogether by employing a different scattering geometry, where fiber sections of 15  $\mu\text{m}$  length were prepared and irradiated by an X-ray beam pointed parallel to the fiber axis. However, the information in the scattering patterns from these so-called on-axis experiments is limited by the conditions of diffractions in samples with fiber symmetry [216], and the technique requires sophisticated and destructive preparation of the fibers.

## 5.2 Small-angle X-ray scattering computed tomography

### 5.2.1 Small-angle X-ray scattering

In small-angle X-ray scattering (SAXS) measurements, the nanoscale structure of the sample is investigated by measuring the scattering signal at small angles. The geometry of a SAXS experiment is similar to WAXS but with a much larger sample-to-detector distance (cf. Fig. 5.1). It is long range fluctuations in the electron density that give rise to the scattering signal in SAXS. In two-phase systems with nanoscale structural ordering, the difference in electron density between the two phases gives rise to scattering patterns with peaks at  $q$ -values corresponding to the periodic distance between identical domains. For example, in semicrystalline polymers the crystalline lamellae are contained in an amorphous matrix, and the structural differences give rise to variation in the electron density between the two phases. Another example is thermoplastic elastomers, where hard domains are contained in a soft matrix. Bulk polymer system rarely give rise to more than two orders of reflections due to the absence of long range order, and in many cases, only one broad first order peak is observed. This single peak is associated with the so-called long period of the structure, that is the average period between identical domains. In semicrystalline polymers, the long period equates to the average distance between neighboring crystalline lamellae.

For isotropic systems, the dimensionality of the scattering patterns is often reduced by azimuthal integration [199]. In the case of anisotropic systems, that is systems with some degree of preferred orientation, it is common to extract and analyze intensity profiles along certain directions. For semicrystalline polymer systems, additional information can then be obtained either by means of direct evaluation of the intensity profiles using autocorrelation function analysis [199, 217, 218], or by fitting the data with an appropriate model. For examples of models describing stacks of crystalline lamellae, see the works of Blundell [219] or Ruland and Smarsly [220]. In some cases, the entire two-dimensional scattering pattern can be analyzed, for example by means of multidimensional chord distribution functions [221].

### 5.2.2 Tomography basics

SAXS measurements collected by a microfocused X-ray beam is subject to the same smearing outlined for WAXS in Section 5.1.4. One way of desmearing the scattering images and obtain fully localized information is to combine the SAXS with computed tomography (CT) [12, 222]. By recording scattering patterns at many different angles of sample rotation about its own axis, it is possible to reconstruct the local scattering cross-section everywhere inside the sample, if the criteria of rotational invariance is fulfilled (see Section 5.2.5). There are several advantages of using SAXS-CT to reconstruct the local scattering

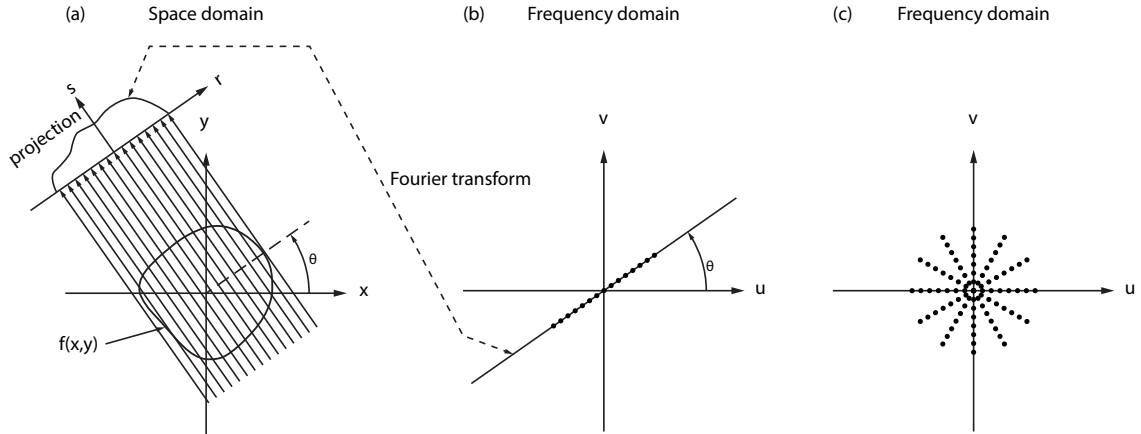


**Figure 5.5:** (a) The Fourier Slice theorem, which relates the one-dimensional Fourier transform of a projected object in the space domain to a radial slice of the two-dimensional Fourier transform of the object in the frequency domain. (b) The two-dimensional Fourier transform in the frequency domain is filled by collecting projections of the object at a large number of angles. The dots represent the discrete points in the Fourier transform. Drawn based on [223].

signal: The sample does not need to exhibit cylindrical symmetry, which a requirement for the 1-dimensional tomographic reconstruction outlined in Section 5.1.4; The technique does not require complicated or destructive preparation of the sample; The only additional experimental requirement compared with translation mapping is the ability to rotate the sample about its own axis.

Key to the concept of tomographic imaging is the Fourier Slice Theorem. The theorem relates the projected data to the two-dimensional Fourier transform of the object's cross-section. In the following, a brief introduction to the Fourier Slice Theorem is given. The arguments and notations follows those of Kak and Slaney [223].

Let us consider an object in real space with object function  $f$  describing its shape (see Fig. 5.5a). The two-dimensional Fourier transform of the object function is defined as

$$F(u, v) = \int_{-\infty}^{\infty} \int_{-\infty}^{\infty} f(x, y) \exp(-j2\pi(ux + vy)) dx dy, \quad (5.20)$$

where  $(u, v)$  is the coordinates in frequency space and  $(x, y)$  is the coordinates in real space. The object function can be projected onto the  $r$ -axis (see Fig. 5.5a) by combining a set of line integrals taken along parallel lines in the  $s$ -direction. We denote this projection, taken at an angle  $\theta$ , as  $P_{\theta}(r)$  and its Fourier transform as

$$S_{\theta}(w) = \int_{-\infty}^{\infty} P_{\theta}(r) \exp(-j2\pi wr) dr. \quad (5.21)$$

$P_{\theta}(r)$  is known as the Radon transform of the object function  $f(x, y)$ . In the simplest case of  $\theta = 0$ , Eq. (5.20) simplifies to

$$F(u, 0) = \int_{-\infty}^{\infty} \left[ \int_{-\infty}^{\infty} f(x, y) dy \right] \exp(-j2\pi(ux)) dx. \quad (5.22)$$

The term in brackets is the projection of the object function onto the  $x$ -axis, and thus we obtain the simplest form of the Fourier Slice theorem

$$F(u, 0) = \int_{-\infty}^{\infty} P_{\theta=0}(x) \exp(-j2\pi(ux)) dx = S_{\theta=0}(u). \quad (5.23)$$

If the coordinate system of the projection  $(r, s)$  is rotated at an arbitrary angle  $\theta$ , the resulting Fourier transform of the projection is simply the two-dimensional Fourier transform of the object along a line rotated by  $\theta$ . This situation is illustrated in Fig. 5.5b. The Fourier Slice Theorem then states that: "the Fourier transform of a parallel projection of an image  $f(x, y)$  taken at angle  $\theta$  gives a slice of the two-dimensional transform,  $F(u, v)$ , subtending an angle  $\theta$  with the  $u$ -axis" [223]. By recording projections at many different  $\theta$  angles, one can therefore reconstruct the entire two-dimensional Fourier transform of the object (in frequency space). In principle, this then allows us to reconstruct the object function (in real space) by mean of inverse Fourier transformation.

However, in practice, only a finite number of projections can be recored and therefore only a finite number of points in frequency are known. These lie along radial lines, as illustrated in Fig. 5.5c. At the same time, the inverse Fourier transformation is often computed by numerical measures. This typically involves dividing the frequency domains into a grid and extrapolating the missing values from the radial points. Figure 5.5c implies that the error due to extrapolation becomes greater, the further away from the center one gets, since the point density is lower. One way of solving this problem is by using different reconstruction techniques. The most commonly employed reconstruction technique is know as filtered back projection (FBP).

In FBP, the algorithm takes the projection data and applies a weight in the frequency domain (high frequencies are weighted higher to ensure even contribution). This is then followed by a back-projection step, where each of the weighted projections are transformed back into real-space by a 1-dimensional inverse Fourier transformation and smeared across the image space (real space). The final reconstructed image is then obtained by summing all the back-projected images. However, the work presented in Paper V does not rely on FBP. Rather, we employ the simultaneous algebraic reconstruction technique outlined in Section 5.2.6.

### 5.2.3 Experiment

The experimental setup of SAXS-CT is sketch in Fig. 5.6. The geometry is very similar to that of transmissions WAXS, expect the sample-to-detector distance is much greater in order to resolve smaller scattering angles. The laboratory coordinate system is given by  $(x_{\text{lab}}, y_{\text{lab}}, z_{\text{lab}})$ , with  $x_{\text{lab}}$  located along the path of the primary X-ray beam,  $z_{\text{lab}}$  pointing up, and  $y_{\text{lab}}$  completing the right-handed coordinate system. The sample coordinate system is defined by its axes  $(x, y, z)$ , with the vertical axis  $z$  aligned parallel to the vertical axis of the laboratory coordinate system. The angle  $\theta$  denotes the rotation of  $(x, y, z)$  with respect to  $(x_{\text{lab}}, y_{\text{lab}}, z_{\text{lab}})$  around  $z$ . During the experiment, scattering patterns are collected by scanning the sample through the X-ray beam along  $y_{\text{lab}}$ . The beam size ultimately determines the step size during the scan, and a more narrowly focused beam (in the  $y_{\text{lab}}$ -direction) therefore allows for smaller steps during scanning. This ultimately determines the voxel size of the reconstruction. After scanning across the entire fiber in the transverse direction it is rotated by an increment  $\Delta\theta$ , and the steps are repeated until the samples has undergone one half rotation of  $180^\circ$ .

In principle, the number of translational steps should be chosen in accordance with the Nyquist-Shannon sampling theorem [223], which states that the signal must be sampled

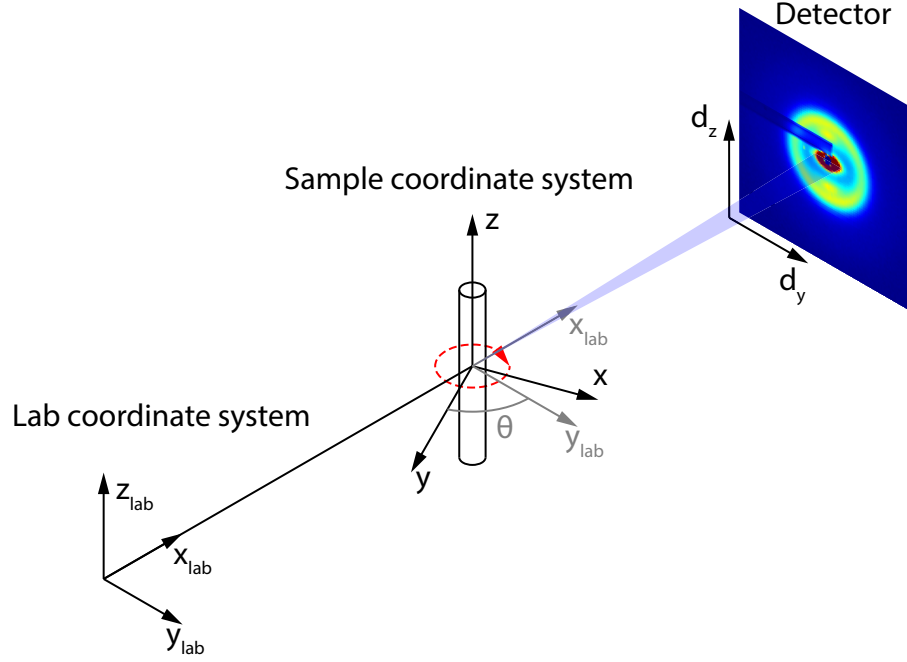


**Figure 5.6:** Experimental geometry of SAXS-CT experiments with corresponding coordinate systems of the laboratory and sample frame of reference, respectively. A single projection at rotation angle  $\theta$  is measured by scanning the sample through the beam along  $\mathbf{r}$ .

with a frequency at least twice that of the highest frequency in the sample. For our setup, this means that the translational step size should be at least half the lateral size of the X-ray beam (which limits the resolution of the experiment). Then, in order to maintain the spatial resolution given by the translational step size, the number of rotational steps (i.e. projections) should be chosen to be  $N_{proj} = \pi/2 \times$  the number of translational steps. However, for very small beam sizes, this typically means that an unreasonable number of projections must be measured. In practice, the number of acquired projections are often much lower [224–226], and then counterbalanced by employing reconstruction algorithms well suited for undersampled data. This greatly speeds up the acquisition process, as the number of acquisitions scales with the number of translational steps  $N$  as  $N^2$ .

#### 5.2.4 Tomographic problem

The goal of SAXS-CT is to obtain the local scattering cross-section from every voxel inside the sample. Schroer et al. [12] gives the SAXS pattern within the first Born approximation (i.e. multiple scattering event are not taken into account) as

$$I_{\mathbf{q}}(y_{lab}, \theta) = I_0 \int f(\theta, x_{lab}, y_{lab}) p_{\mathbf{q}, \theta}(x, y) g(\theta, x_{lab}, y_{lab}) dx_{lab}, \quad (5.24)$$

where  $I_{\mathbf{q}}(y_{lab}, \theta)$  is the full SAXS pattern as a function of  $\mathbf{q} = (q_y, q_z)$  measured at point  $(y_{lab}, \theta)$ ,  $f(\theta, x_{lab}, y_{lab}) = \exp\{-\int_{-\infty}^{x_{lab}} \mu[x(x_{lab}', y_{lab}), y(x_{lab}', y_{lab})] dx_{lab}'\}$  is the attenuation of the incident X-ray beam in the sample with attenuation coefficient  $\mu$ ,  $g(\theta, x_{lab}, y_{lab}) = \exp\{-\int_{x_{lab}}^{\infty} \mu[x(x_{lab}', y_{lab}), y(x_{lab}', y_{lab})] dx_{lab}'\}$  is attenuation of the forward scattered beam, and  $p_{\mathbf{q}, \theta}(x, y)$  is the SAXS cross-section at sample position  $(x, y)$ . Here it is assumed that the incident beam and the forward scattered beam lie on the same path. This approximation is usually valid in small-angle scattering, where the scattering angles typically are so

small, that the divergence of the scattered beam is negligible [222]. By combining  $f$  and  $g$  they can be pulled out of the integral in Eq. (5.24) as

$$\frac{I_{\mathbf{q}}(y_{\text{lab}}, \theta)}{I_1} = \int p_{\mathbf{q}, \theta}[x(x_{\text{lab}}, y_{\text{lab}}), y(x_{\text{lab}}, y_{\text{lab}})] dx_{\text{lab}}, \quad (5.25)$$

where  $\frac{I_{\mathbf{q}}(y_{\text{lab}}, \theta)}{I_1}$  is the transmission corrected intensity of the sample. Equation 5.25 is the SAXS equivalent of the projection function  $P_{\theta}(r)$  introduced in Section 5.2.2).

### 5.2.5 Rotational invariance

The concept of rotational invariance in SAXS-CT is introduced in the work of Feldkamp [227], and the arguments here follows those presented therein. The reconstruction of the scattering cross-section given by Eq. (5.25) is in general an ill-posed problem. The left-hand side of the equation is a function of 4 variables ( $\mathbf{q} = [q_y, q_z], y_{\text{lab}}, \theta$ ), while the right-hand side is a function of 5 variables ( $\mathbf{q} = [q_r, q_{\theta}, q_z], y_{\text{lab}}, x_{\text{lab}}$ ). Thus, to solve the reconstruction problem of Eq. (5.25), the number of variable on the right hand side must be reduced, either by limiting the problem to a sub-set of the original problem, or by invoking additional information about the sample.

In general, Eq. (5.25) can only solved for cases where the local scattering cross-section  $p_{\mathbf{q}, \theta}(x, y)$  is independent of the sample rotation  $\theta$ . If this is the case, the scattering vector becomes a function of  $q_r$  and  $q_z$  only, and the radial component  $q_r$  becomes equal to the horizontal component  $q_y$ . Equation (5.25) is now reduced to a function of 4 variables on both sides, and the local scattering cross-section can be reconstructed. The local scattering cross-section is said to be locally rationally invariant in this case. Another way to understand the requirement of rotational invariance is to consider the small part of the sample located at position  $(x_0, y_0)$  with local scattering cross-section  $p_{\mathbf{q}, \theta}(x_0, y_0)$ . If we were to measure this part alone (i.e. by removing it physically from the rest of the sample), the scattering pattern would have to remain unchanged under illumination from all angles.

The trivial case is given for scattering along the vertical axis, that is, when the horizontal component of the scattering vector is zero ( $q_y = 0$ ). For this case, the scattering is limited to a single point in reciprocal space, and is therefore independent of the rotation  $\theta$  (i.e.  $\mathbf{q} = (0, q_z) = (0, 0, q_z)$ ), and Eq. (5.25) reduces to a function of three variables on both sides.

A special case of rotational invariance is found in samples with additional local symmetry about the rotational axis, such as local fiber symmetry. In local fiber symmetry, the scattering pattern is per definition unchanged under rotation about the fiber axis.

In practice, the scattering is measured by a 2D detector, where every single pixel represents a fixed point in  $q$ -space. Let us for for each pixel assign a value  $w_{\mathbf{q}}$  to the sum of all intensities measured at this pixel during a single line scan as

$$w_{\mathbf{q}}(d_y, d_z) = \sum_{y_{\text{lab}}=0}^N I_{\mathbf{q}}(d_y, d_z, y_{\text{lab}}). \quad (5.26)$$

In order to reconstruct the full scattering pattern, this value must necessarily be constant under rotation for each pixel - that is, the features of the corresponding sinogram can move horizontally but are not lost (the sinogram is said to be well behaved). Thus, a pixel-wise

rotational invariance check can be performed on a sample by calculating the ratio of the standard deviation to the mean of  $w_{\mathbf{q}}$  over all rotations

$$\frac{\sigma(w_{\mathbf{q}}[d_y, d_z])}{w_{\mathbf{q}}(d_y, d_z)}. \quad (5.27)$$

It is important to note that rotational invariance is independent of the macroscopic symmetry of the sample, since the only requirement is local rotational invariance on the length scale of the individual reconstructed segments. In practice, this typically means that the local structure should be approximately homogeneous on the length scale of the beam size.

### 5.2.6 Reconstruction

The reconstruction of the SAXS pattern in Paper V was carried out using a simultaneous algebraic reconstruction technique (SART) with total variation regularization (TV) on a per pixel basis. The SART-TV reconstruction technique was chosen for its performance in cases with strong undersampling of the data [225, 228]. A detailed description of the SART-TV algorithm, and its implementation in the employed Matlab toolbox TIGRE, can be found in the work of Biguri [229]. A condensed description follows below following the notation of Biguri.

As the name implies, the SART-TV algorithm is an iterative algebraic reconstruction algorithm, that solves the problem by iteratively comparing the reconstructed image with the measured data. The reconstruction problem outlined in Section 5.2.2 can alternatively be described by the linearized model

$$Ax = b + \varepsilon, \quad (5.28)$$

where  $x$  is a vector representing the image (object function) in terms of voxels,  $b$  is a vector representing the projection data, and  $A$  is a matrix describing the intersection of X-rays and voxels in the image. Inevitable erroneous contributions to the image arising from errors in measurement data or errors in the linearized model are contained in the  $\varepsilon$  term. The exact solution for  $x$  cannot be found since the system is underdetermined [229], and the problem instead turns into a minimization problem as

$$\hat{x} = \operatorname{argmin}_x \|Ax - b\|^2 + G(x), \quad (5.29)$$

where  $G(x)$  describes an optional regularization function. In the SART-TV algorithm,  $G$  corresponds to the total variation norm  $\|x\|_{TV}$  as

$$\hat{x} = \operatorname{argmin}_x \|Ax - b\|^2 + \lambda \|x\|_{TV}. \quad (5.30)$$

If we consider the optimal condition of the minimization as

$$\frac{\partial}{\partial x_\alpha} \|Ax - b\|^2 + \lambda \frac{\partial}{\partial x_\alpha} \|x\|_{TV} = 0, \quad (5.31)$$

then Eq. (5.30) can be split into two equations as

$$\lambda \frac{\partial}{\partial x_\alpha} \|x\|_{TV} = \mu(x - g), \quad (5.32)$$

$$\frac{\partial}{\partial x_\alpha} \|Ax - b\|^2 = -\mu(x - g), \quad (5.33)$$

where we have introduced the intermediate image  $g$  and the constant  $\mu > 0$ .

Conceptually, the SART-TV algorithm can now be described as an iterative three step process. In the first step, Eq. (5.33) is solved for  $g$  using a SART algorithm. The SART algorithm [230] works by creating a projection of the current image (forward projection), comparing said projection with all the experimental X-ray projection data simultaneously, and then systematically updating the image based on the difference (back projection). This is repeated multiple times per iteration.

The second step then tries to find the image  $x$  with the minimum total variation subject to having minimal deviation from the image  $g$  determined in step 1. In CT imaging, the total variation norm describes the sum of the total change occurring in the image, and regularization with the TV norm yields images that are piecewise smooth [229]. The strength of the regularization can be controlled by the parameter  $\mu$ , with higher values restricting the image close the value of  $g$ .

Finally, the algorithm enforces positivity of the result by elevating any negative values to 0. The entire iterative process is repeated until the reconstructed image satisfies the convergence criteria, or the maximum number of iterations is reached.

In practice, the reconstruction is done on a per pixel level (with each pixel representing a constant value in q-space). The individual reconstructions are then stitched together in the end to form a complete scattering pattern. The details of this process is outlined in the supplementary information of Paper V.

## Summary and Conclusions

---

In this thesis, we study the crystallization and (local) structure of two anisotropic soft organic systems. In particular, we present results from two thiophene-based organic semiconductors in thin-film configuration and high-strength polyethylene fibers fabricated by gel-spinning. The results are presented in the back half of the thesis in the form of five self-contained papers. Several conclusions can be drawn based on our results and they are presented below.

### Conclusions on organic semiconductor thin films

For **NaT2**, the packing structure was investigated in thin films grown on monolayer graphene. The molecules are found to adopt a face-on configuration, with their molecular long-axis aligned parallel with the substrate plane. This configuration differs from their more common edge-on configuration, where the molecules are standing near upright on the substrate. Consequently, the monoclinic unit cell is oriented in one of two ways, with the *a*-axis titled approximately  $20^\circ$  from the substrate plane in both cases, and the *b*-axis lying either parallel to the substrate plane, or titled approximately  $22^\circ$  away from the substrate plane. The face-on configuration of the molecules results in a 2.5 times increase in the photoabsorption at the absorption maximum, which is located at approximately 350 nm. Moreover, the film morphology is found to differ depending on the whether or not the graphene surfaces contains polymer residue. On graphene surfaces with no polymer residue, the NaT2 molecules grow as faceted crystalline grains with limited interconnectivity. On the other hand, on graphene surfaces with polymer residue, the molecules grow either as fiber-like grains (with face-on oriented molecules) or as terraced islands (with edge-on oriented molecules). Areas of the distinct morphologies are found to coexist in the film.

On device-relevant silicon dioxide substrates, NaT2 is found to follow Stranski-Krastanov type growth. In this growth mode, two-dimensional layer-by-layer growth is followed by three-dimensional island growth after reaching a threshold thickness. For the specific condition employed in our work, the threshold thickness is found to be at least two molecular layers. The NaT2 unit cell undergoes collective in-plane changes ( $\sim 0.5\%$ ) within the first 3 molecular layers, indicating surface-induced strain. The strain is fully relieved after the

formation of the first 3 molecular layers, approximately corresponding to the transition from layer-by-layer to island growth. The in-plane changes to the unit cell is accompanied by a compression of the out-of-plane  $a$ -axis, which asymptotically approaches the bulk value.

**NaT3** is found to crystallize in a monoclinic thin-film phase on silicon dioxide with unit cell parameters  $a = 25.7 \text{ \AA}$ ,  $b = 5.87 \text{ \AA}$ ,  $c = 8.03 \text{ \AA}$ , and  $\beta = 98.9^\circ$ . The proposed unit cell with 2 molecules differs significantly from the one reported for single crystals with six molecules. GIWAXS patterns indicate a crystalline lattice with significantly more disorder compared to NaT2, especially in the out-of-plane direction.

The growth of NaT3 on silicon dioxide substrates is likewise found to proceed via the Stranski-Krastanov growth mode. The transition from layer-by-layer growth to island growth happens at a film thickness of approximately 3 molecular layers. During the early-stages of growth, the unit cell of NaT3 undergoes significant changes in both the in-plane and out-of-plane dimensions ( $> 5\%$ ). Unlike the NaT2 film, the surface-induced strain is not fully relieved even after formation of 6 molecular layers.

Furthermore, the thin-film structure and growth of NaT3 deposited on few-layer MoS<sub>2</sub> was studied. On  $\parallel$ -MoS<sub>2</sub>, where the MoS<sub>2</sub> layers are aligned parallel to the substrate plane, the NaT3 molecules adopt a face-on configuration with (102)-texture, and a film of interconnected fiber-like grains is formed via Volmer-Weber type growth. On the other hand, on  $\perp$ -MoS<sub>2</sub>, where the MoS<sub>2</sub> layers are aligned perpendicular to the substrate plane, the molecules adopt edge-on orientation and form tall isolates pillars via Volmer-Weber type growth.

The thin-film microstructure of NaT3 is found to change in the proximity of bottom contact gold electrodes in OFET devices. This is manifested by an increase in the out-of-plane misorientation ( $\sim 15\%$  increase in the angular FWHM) of the crystallites, and a decrease in the in-plane crystallite size. Williamson-Hall analysis shows an increase in the out-of-plane disorder of the film in areas on top of the electrodes. On the other hand, silver nanoparticles with a diameter of 30 nm are not found to affect the microstructure of the NaT3 film when incorporated into the OFET device structure.

Based on our results, we can draw some general conclusions for naphthyl end-capped oligothiophenes.

Their molecular orientation in the thin-film configuration can be controlled by employing templating substrates, which can be rationalized by considering the molecule-substrate interactions. On strongly interacting substrates, naphthyl end-capped oligothiophenes tend to adopt a face-on configuration of the molecules, owing to the  $\pi$ -conjugated nature of the molecules. On weaker interacting substrates, such as oxides, naphthyl end-capped oligothiophenes tend to adopt edge-on configuration. In this scenario, the intermolecular interactions are dominating. Moreover, small local perturbations to the surface landscape can lead to significant changes in the film morphology, as seen in the case of NaT2 grown on monolayer graphene with small amounts of polymer residue.

On silicon dioxide, the growth of both NaT2 and NaT3 proceeds according to Stranski-Krastanov type growth. The surface-induced strain is increased for the longer NaT3 molecules, and this may be a source of the increased film disorder observed for NaT3 compared to NaT2.

## Conclusions on UHMWPE fibers

Gel-spun fibers made from UHMWPE are known to exhibit structural inhomogeneities in the radial direction of the fiber. In order to quantify these local inhomogeneities, we develop a methodological framework based on adaptations of previous X-ray and polarized Raman spectroscopy techniques. By combining nanofocused WAXS, microfocused SAXS-CT and polarized Raman spectroscopy, structural inhomogeneities can be discerned on multiple length scales in UHMWPE fibers. This framework is immediately put to work to study the skin-core structure of four individual UHMWPE filaments spun from spinnerets with varied processing conditions.

The local orientation of PE crystallites can be described in terms of the  $\langle P_2 \rangle$  orientation parameter, which is calculated in a straightforward manner from the WAXS data owing to the simple fiber symmetry of the samples. The  $\langle P_2 \rangle$  profiles obtained from WAXS shows skin-core structure in all of the studied filaments, with an increase in the crystallite orientation in the skin region. The absolute values differ depending on the processing conditions.

Laboratory polarized Raman spectroscopy can be used to discern skin-core structure in the filaments with highest overall degree of orientation of the molecular bonds in the crystalline phase. While WAXS provides the orientation of the crystalline lattice, Raman spectroscopy probes the orientation on an even smaller length scale, that is, on the scale of the molecular bonds. Our results show that first indications of skin-core features in UHMWPE fibers can be readily obtained from polarized Raman spectroscopy.

By reconstruction of the local SAXS patterns using microfocused SAXS-CT, detailed information on the real-space morphology becomes available with a  $\sim 1 \mu\text{m}$  spatial resolution SAXS-CT is used to investigate the morphology of two out of the four filaments, with both samples showing clear skin-core structure. The skin-core structure manifests itself by an increased lamellar long-period and  $q_z$  scattering intensity in the skin region. The thickness of the skin layer can be directly estimated from the real-space maps of the morphological features, providing a direct quantitative measure of the skin thickness in UHMWPE fibers for the first time.

From a material processing point of view, our results points towards the following trends: The degree of orientation of the PE crystallites, expressed in terms of the  $\langle P_2 \rangle$  orientation parameter, is found to increase with drawn down ratio (keeping the quench temperature constant), and decrease with an increase in quench temperature (keeping the draw down ratio constant). These findings can be rationalized in terms of the underlying physics involved in the processing.

## Outlook

It is abundantly clear that the structures and structure-property relationships in the two types of organic molecules studied in this thesis are exceedingly complex by nature. The results presented herein are by no means exhaustive, and should only be considered as a small contribution to the vast amount of existing literature. Only by the combined efforts from scientist and researchers across the world can a "complete" picture be obtained. With this in mind, a few considerations for future studies are presented below.

Regarding naphthyl end-capped oligothiophenes, it is still unclear what leads to the increased disorder observed in NaT3 thin-films on silicon dioxide compared to NaT2. Our

results point towards an increased substrate-induced strain in films of NaT3, possibly brought about by the differences in molecule length. However, another possible source for the increased disorder is the difference in symmetry between NaT2 and NaT3. This was only briefly discussed in Paper III, but has been studied in more detail in Ref. [55]. The findings in Ref. [55] suggest that the NaT3 thin-film structure incorporates a larger number of flipped molecules compared with the NaT2 film structure. In this context, a flipped molecule means that one of the molecules in the unit cell is flipped  $180^\circ$  about its long axis. It would be particularly interesting to perform similar structure and growth studies of longer naphthyl end-capped oligothiophenes, such as NaT4 with four thiophene rings in the core [53]. NaT4 has similar symmetry to NaT2, but with increased molecule length. Structural comparisons between the NaT4 films and NaT2/3 might then offer valuable insight into the origin of the increased disorder. Interestingly, NaT4 has been reported to exhibit mobilities that are approximately a factor of 10 higher than NaT2/3 [53], suggesting a less disordered film structure. Alternatively, a better understanding of the growth could be achieved by molecular dynamics or Monte Carlo simulations. However, this requires the establishment of a complex model that takes all of the considerations specific to small organic molecules (see Section 2.5.3), including accurate description of the molecular anisotropy. Consequently, parameters that are normally scalars for model of atomistic growth, would need to be variables of the molecular orientation [231].

For OSC thin-films in general, the microstructure will inevitably vary based on the local surface landscape. This means that detailed studies on the structure-property relationship in OSCs thin-films cannot rely solely on single measurements of whole devices. Instead, lateral variations in microstructure, for example in the proximity of contact electrodes, should be considered. While this thesis is focused on a specific family of small organic molecules, the concepts and findings presented in Paper IV are directly applicable to other, more complex systems, such as polymers, blend-films, and organic-inorganic hybrid materials.

Regarding the methodological framework presented in Paper V, several improvements can be made. First of all, the tomographic reconstruction principles used to reconstruct the local SAXS patterns can be generalized and used for WAXS data as well, provided that the WAXS patterns exhibit rotational invariance. This will generally be the case for fiber-symmetric scattering patterns. Moreover, radiation damage of the samples is a strong concern during the SAXS tomography experiment due to the prolonged exposure. Improvements to the experimental protocol, such as cryo-cooling the sample or placing it in vacuum, could potentially reduce the amount of radiation damage and allow for the reconstruction of single slices.

From a material perspective, it would be particularly interesting to extend the local structure mapping of UHMWPE fibers to samples taken from different parts of the spinning line. Of particular interest are highly drawn samples from later stages of the drawing process, where the morphology consists primarily of PE chains with near full extension. Information on the local structure of such highly drawn samples could provide valuable insight into the evolution of the observed skin-core structure, and potentially reveal structural features that limits the mechanical performance of the fiber. In turn, this could help guide the design of improved and better performing fibers.

## Bibliography

---

- [1] F. Dinelli, M. Murgia, P. Levy, M. Cavallini, F. Biscarini, and D. M. de Leeuw, Spatially correlated charge transport in organic thin film transistors, *Phys. Rev. Lett.* **92**, 116802 (2004).
- [2] Y. Ohta, H. Murase, and T. Hashimoto, Effects of spinning conditions on the mechanical properties of ultrahigh-molecular-weight polyethylene fibers, *J. Polym. Sci., Part B: Polym. Phys.* **43**, 2639–2652 (2005).
- [3] Y. Ohta, H. Murase, and T. Hashimoto, Structural development of ultra-high strength polyethylene fibers: transformation from kebabs to shishs through hot-drawing process of gel-spun fibers, *J. Polym. Sci., Part B: Polym. Phys.* **48**, 1861–1872 (2010).
- [4] J. Als-Nielsen and D. McMorrow, *Elements of Modern X-ray Physics* (John Wiley & Sons, 2011).
- [5] C. Kittel, *Introduction to Solid State Physics*, 8th ed. (John Wiley & Sons).
- [6] A. Buffet, A. Rothkirch, R. Döhrmann, V. Körstgens, M. M. A. Kashem, J. Perlich, G. Herzog, M. Schwartzkopf, R. Gehrke, P. Müller-Buschbaum, and S. V. Roth, P03, the microfocus and nanofocus X-ray scattering (MiNaXS) beamline of the PETRA III storage ring: the microfocus endstation, *Journal of Synchrotron Radiation* **19**, 647–653 (2012).
- [7] C. Krywka, J. Keckes, S. Storm, A. Buffet, S. V. Roth, R. Döhrmann, and M. Müller, Nanodiffraction at MINAXS (p03) beamline of PETRA III, *J. Phys. Conf. Ser.* **425**, 072021 (2013).
- [8] U. Johansson, U. Vogt, and A. Mikkelsen, NanoMAX: a hard X-ray nanoprobe beamline at MAX IV, in *X-ray nanoimaging: instruments and methods*, edited by B. Lai (2013).
- [9] M. Cotte, A. Genty-Vincent, K. Janssens, and J. Susini, Applications of synchrotron X-ray nano-probes in the field of cultural heritage, *C. R. Phys.* **19**, 575–588 (2018).
- [10] A. Snigirev, V. Kohn, I. Snigireva, and B. Lengeler, A compound refractive lens for focusing high-energy X-rays, *Nature* **384**, 49–51 (1996).

- [11] H. Yumoto, H. Mimura, S. Matsuyama, H. Hara, K. Yamamura, Y. Sano, K. Ueno, K. Endo, Y. Mori, M. Yabashi, Y. Nishino, K. Tamasaku, T. Ishikawa, and K. Yamauchi, Fabrication of elliptically figured mirror for focusing hard x rays to size less than 50nm, *Rev. Sci. Instrum.* **76**, 063708 (2005).
- [12] C. G. Schroer, Focusing hard X-rays to nanometer dimensions using fresnel zone plates, *Phys. Rev. B* **74**, 033405 (2006).
- [13] G. Schweicher, G. Garbay, R. Jouclas, F. Vibert, F. Devaux, and Y. H. Geerts, Molecular semiconductors for logic operations: dead-end or bright future?, *Adv. Mater.* **32**, 1905909 (2020).
- [14] H. Sirringhaus, 25th anniversary article: organic field-effect transistors: the path beyond amorphous silicon, *Adv. Mater.* **26**, 1319–1335 (2014).
- [15] Z. Bao and J. Lockling, eds., *Organic Field Effect Transistors* (CRC Press Taylor and Francis Group, 2007).
- [16] H. Klauk, *Organic electronics. more materials and applications* (Wiley-VCH, Weinheim, 2012).
- [17] A. Briseno, R. Tseng, M.-M. Ling, E. Falcao, Y. Yang, F. Wudl, and Z. Bao, High-performance organic single-crystal transistors on flexible substrates, *Adv. Mater.* **18**, 2320–2324 (2006).
- [18] Y. Wang, L. Sun, C. Wang, F. Yang, X. Ren, X. Zhang, H. Dong, and W. Hu, Organic crystalline materials in flexible electronics, *Chem. Soc. Rev.* **48**, 1492–1530 (2019).
- [19] S. E. Root, S. Savagatrup, A. D. Printz, D. Rodriguez, and D. J. Lipomi, Mechanical properties of organic semiconductors for stretchable, highly flexible, and mechanically robust electronics, *Chem. Rev.* **117**, 6467–6499 (2017).
- [20] F. C. Krebs, N. Espinosa, M. Hösel, R. R. Søndergaard, and M. Jørgensen, 25th anniversary article: rise to power - OPV-based solar parks, *Adv. Mater.* **26**, 29–39 (2013).
- [21] L. Shaw and Z. Bao, The large-area, solution-based deposition of single-crystal organic semiconductors, *Isr. J. Chem.* **54**, 496–512 (2014).
- [22] M. Eritt, C. May, K. Leo, M. Toerker, and C. Radehaus, OLED manufacturing for large area lighting applications, *Thin Solid Films* **518**, 3042–3045 (2010).
- [23] S. Fratini, M. Nikolka, A. Salleo, G. Schweicher, and H. Sirringhaus, Charge transport in high-mobility conjugated polymers and molecular semiconductors, *Nat. Mater.* **19**, 491–502 (2020).
- [24] J. Rivnay, S. Inal, A. Salleo, R. M. Owens, M. Berggren, and G. G. Malliaras, Organic electrochemical transistors, *Nat. Rev. Mater.* **3**, 17086 (2018).
- [25] H. Li, W. Shi, J. Song, H.-J. Jang, J. Dailey, J. Yu, and H. E. Katz, Chemical and biomolecule sensing with organic field-effect transistors, *Chemical Reviews* **119**, 3–35 (2018).
- [26] F.-J. M. zu Heringdorf, M. C. Reuter, and R. M. Tromp, Growth dynamics of pentacene thin films, *Nature* **412**, 517–520 (2001).

- [27] A. C. Mayer, R. Ruiz, R. L. Headrick, A. Kazimirov, and G. G. Malliaras, Early stages of pentacene film growth on silicon oxide, *Org. Electron.* **5**, 257–263 (2004).
- [28] S. Kowarik, A. Gerlach, W. Leitenberger, J. Hu, G. Witte, C. Wöll, U. Pietsch, and F. Schreiber, Energy-dispersive X-ray reflectivity and GID for real-time growth studies of pentacene thin films, *Thin Solid Films* **515**, 5606–5610 (2007).
- [29] A. O. F. Jones, B. Chattopadhyay, Y. H. Geerts, and R. Resel, Substrate-induced and thin-film phases: polymorphism of organic materials on surfaces, *Adv. Funct. Mater.* **26**, 2233–2255 (2016).
- [30] S. E. Fritz, S. M. Martin, C. D. Frisbie, M. D. Ward, and M. F. Toney, Structural characterization of a pentacene monolayer on an amorphous SiO<sub>2</sub> substrate with grazing incidence X-ray diffraction, *J. Am. Chem. Soc.* **126**, 4084–4085 (2004).
- [31] M. Kitamura and Y. Arakawa, Pentacene-based organic field-effect transistors, *J. Phys.: Condens. Matter* **20**, 184011 (2008).
- [32] J. E. Anthony, J. S. Brooks, D. L. Eaton, and S. R. Parkin, Functionalized pentacene: improved electronic properties from control of solid-state order, *J. Am. Chem. Soc.* **123**, 9482–9483 (2001).
- [33] S. K. Park, T. N. Jackson, J. E. Anthony, and D. A. Mourey, High mobility solution processed 6,13-bis(triisopropyl-silylethynyl) pentacene organic thin film transistors, *Appl. Phys. Lett.* **91**, 063514 (2007).
- [34] S. C. B. Mannsfeld, M. L. Tang, and Z. Bao, Thin film structure of triisopropylsilylethynyl-functionalized pentacene and tetraceno[2,3-b]thiophene from grazing incidence X-ray diffraction, *Adv. Mater.* **23**, 127–131 (2010).
- [35] E. Menard, V. Podzorov, S.-H. Hur, A. Gaur, M. E. Gershenson, and J. A. Rogers, High-performance n- and p-type single-crystal organic transistors with free-space gate dielectrics, *Adv. Mater.* **16**, 2097–2101 (2004).
- [36] M. Campoy-Quiles, T. Ferenczi, T. Agostinelli, P. G. Etchegoin, Y. Kim, T. D. Anthopoulos, P. N. Stavrinou, D. D. C. Bradley, and J. Nelson, Morphology evolution via self-organization and lateral and vertical diffusion in polymer:fullerene solar cell blends, *Nat. Mater.* **7**, 158–164 (2008).
- [37] S. Bommel, N. Kleppmann, C. Weber, H. Spranger, P. Schäfer, J. Novak, S. Roth, F. Schreiber, S. Klapp, and S. Kowarik, Unravelling the multilayer growth of the fullerene C<sub>60</sub> in real time, *Nat. Commun.* **5**, 5388 (2014).
- [38] A. C. Dürr, F. Schreiber, K. A. Ritley, V. Kruppa, J. Krug, H. Dosch, and B. Struth, Rapid roughening in thin film growth of an organic semiconductor (diindenoperylene), *Phys. Rev. Lett.* **90**, 016104 (2003).
- [39] S. Kowarik, A. Gerlach, A. Hinderhofer, S. Milita, F. Borgatti, F. Zontone, T. Suzuki, F. Biscarini, and F. Schreiber, Structure, morphology, and growth dynamics of perfluoro-pentacene thin films, *Phys. Status Solidi RRL* **2**, 120–122 (2008).
- [40] S. Kowarik, A. Gerlach, S. Sellner, F. Schreiber, L. Cavalcanti, and O. Konovalov, Real-time observation of structural and orientational transitions during growth of organic thin films, *Phys. Rev. Lett.* **96**, 125504 (2006).

- [41] S. Kowarik, A. Gerlach, S. Sellner, L. Cavalcanti, and F. Schreiber, Dewetting of an organic semiconductor thin film observed in real-time, *Adv. Eng. Mater.* **11**, 291–294 (2009).
- [42] M. A. Heinrich, J. Pflaum, A. K. Tripathi, W. Frey, M. L. Steigerwald, and T. Siegrist, Enantiotropic polymorphism in di-indenoperylene, *J. Phys. Chem. C* **111**, 18878–18881 (2007).
- [43] T. L. Derrien, A. E. Lauritzen, P. Kaienburg, J. F. M. Hardigree, C. Nicklin, and M. Riede, In situ observations of the growth mode of vacuum-deposited  $\alpha$ -sexithiophene, *J. Phys. Chem. C* **124**, 11863–11869 (2020).
- [44] C. Lorch, R. Banerjee, C. Frank, J. Dieterle, A. Hinderhofer, A. Gerlach, and F. Schreiber, Growth of competing crystal phases of  $\alpha$ -sexithiophene studied by real-time in situ X-ray scattering, *J. Phys. Chem.* **119**, 819–825 (2014).
- [45] J. Sakai, T. Taima, T. Yamanari, and K. Saito, Annealing effect in the sexithiophene:C70 small molecule bulk heterojunction organic photovoltaic cells, *Sol. Energy Mater. Sol. Cells* **93**, 1149–1153 (2009).
- [46] T. Taima, M. Shahiduzzaman, T. Ishizeki, K. Yamamoto, M. Karakawa, T. Kuwabara, and K. Takahashi, Sexithiophene-based photovoltaic cells with high light absorption coefficient via crystalline polymorph control, *J. Phys. Chem. C* **121**, 19699–19704 (2017).
- [47] A. R. Murphy and J. M. J. Fréchet, Organic semiconducting oligomers for use in thin film transistors, *Chem. Rev.* **107**, 1066–1096 (2007).
- [48] M. Halik, H. Klauk, U. Zschieschang, G. Schmid, S. Ponomarenko, S. Kirchmeyer, and W. Weber, Relationship between molecular structure and electrical performance of oligothiophene organic thin film transistors, *Adv. Mater.* **15**, 917–922 (2003).
- [49] J. A. Merlo, C. R. Newman, C. P. Gerlach, T. W. Kelley, D. V. Muyres, S. E. Fritz, M. F. Toney, and C. D. Frisbie, P-channel organic semiconductors based on hybrid acene-thiophene molecules for thin-film transistor applications, *J. Am. Chem. Soc.* **127**, 3997–4009 (2005).
- [50] Y. Chen, X. Wan, and G. Long, High performance photovoltaic applications using solution-processed small molecules, *Acc. Chem. Res.* **46**, 2645–2655 (2013).
- [51] R. Fitzner, E. Mena-Osteritz, K. Walzer, M. Pfeiffer, and P. Bäuerle, A-D-A-Type oligothiophenes for small molecule organic solar cells: extending the  $\pi$ -system by introduction of ring-locked double bonds, *Adv. Funct. Mater.* **25**, 1845–1856 (2015).
- [52] S. Subramanian, S. K. Park, S. R. Parkin, V. Podzorov, T. N. Jackson, and J. E. Anthony, Chromophore fluorination enhances crystallization and stability of soluble anthradithiophene semiconductors, *J. Am. Chem. Soc.* **130**, 2706–2707 (2008).
- [53] H. Tian, J. Shi, B. He, N. Hu, S. Dong, D. Yan, J. Zhang, Y. Geng, and F. Wang, Naphthyl and thionaphthyl end-capped oligothiophenes as organic semiconductors: effect of chain length and end-capping groups, *Adv. Funct. Mater.* **17**, 1940–1951 (2007).
- [54] M. K. Huss-Hansen, A. E. Lauritzen, O. Bikondoa, M. Torkkeli, L. Tavares, M. Knaapila, and J. Kjelstrup-Hansen, Structural stability of naphthyl end-capped

- oligothiophenes in organic field-effect transistors measured by grazing-incidence X-ray diffraction in operando, *Org. Electron.* **49**, 375–381 (2017).
- [55] M. J. Winokur, M. K. Huss-Hansen, A. E. Lauritzen, M. Torkkeli, J. Kjelstrup-Hansen, and M. Knaapila, Modeling of grazing-incidence X-ray diffraction from naphthyl end-capped oligothiophenes in organic field-effect transistors, *Cryst. Growth Des.* **20**, 3968–3978 (2020).
- [56] X. Liu, L. Tavares, A. Osadnik, J. L. Lausen, J. Kongsted, A. Lützen, H.-G. Rubahn, and J. Kjelstrup-Hansen, Low-voltage organic phototransistors based on naphthyl end-capped oligothiophene nanofibers, *Org. Electron.* **15**, 1273–1281 (2014).
- [57] J. Linnet, A. R. Walther, O. Albrechtsen, L. Tavares, R. L. Eriksen, P. B. W. Jensen, A. Osadnik, S. Hassing, A. Lützen, and J. Kjelstrup-Hansen, Enhanced photoresponsivity in organic field effect transistors by silver nanoparticles, *Org. Electron.* **46**, 270–275 (2017).
- [58] F. Balzer, M. Schiek, A. Osadnik, I. Wallmann, J. Parisi, H.-G. Rubahn, and A. Lützen, Substrate steered crystallization of naphthyl end-capped oligothiophenes into nanofibers: the influence of methoxy-functionalization, *Phys. Chem. Chem. Phys.* **16**, 5747 (2014).
- [59] J. Rivnay, S. C. B. Mannsfeld, C. E. Miller, A. Salleo, and M. F. Toney, Quantitative determination of organic semiconductor microstructure from the molecular to device scale, *Chem. Rev.* **112**, 5488–5519 (2012).
- [60] J.-L. Bredas and S. R. Marder, eds., *The WSPC Reference on Organic Electronics: Organic Semiconductors* (World Scientific, 2016).
- [61] M. Waldrip, O. D. Jurchescu, D. J. Gundlach, and E. G. Bittle, Contact resistance in organic field-effect transistors: conquering the barrier, *Adv. Funct. Mater.* **30**, 1904576 (2020).
- [62] J. L. Bredas, J. P. Calbert, D. A. da Silva Filho, and J. Cornil, Organic semiconductors: a theoretical characterization of the basic parameters governing charge transport, *Proc. Natl. Acad. Sci. U.S.A.* **99**, 5804–5809 (2002).
- [63] R. J. Kline, D. M. DeLongchamp, D. A. Fischer, E. K. Lin, L. J. Richter, M. L. Chabinyc, M. F. Toney, M. Heeney, and I. McCulloch, Critical role of side-chain attachment density on the order and device performance of polythiophenes, *Macromolecules* **40**, 7960–7965 (2007).
- [64] A. Salleo, Impact of organic semiconductor microstructure on transport: basic concepts, in *The WSPC reference on organic electronics: organic semiconductors*, edited by J.-L. Bredas and S. R. Marder (WORLD SCIENTIFIC, 2016) Chap. 9, pp. 293–323.
- [65] B. Nickel, R. Barabash, R. Ruiz, N. Koch, A. Kahn, L. C. Feldman, R. F. Haglund, and G. Scoles, Dislocation arrangements in pentacene thin films, *Phys. Rev. B* **70**, 125401 (2004).
- [66] J. Rivnay, R. Noriega, R. J. Kline, A. Salleo, and M. F. Toney, Quantitative analysis of lattice disorder and crystallite size in organic semiconductor thin films, *Phys. Rev. B* **84**, 045203 (2011).
- [67] J. Rivnay, L. H. Jimison, J. E. Northrup, M. F. Toney, R. Noriega, S. Lu, T. J. Marks, A. Facchetti, and A. Salleo, Large modulation of carrier transport by grain-

- boundary molecular packing and microstructure in organic thin films, *Nat. Mater.* **8**, 952–958 (2009).
- [68] G. Horowitz and M. E. Hajlaoui, Mobility in polycrystalline oligothiophene field-effect transistors dependent on grain size, *Adv. Mater.* **12**, 1046–1050 (2000).
- [69] S. Y. Yang, K. Shin, and C. E. Park, The effect of gate-dielectric surface energy on pentacene morphology and organic field-effect transistor characteristics, *Adv. Funct. Mater.* **15**, 1806–1814 (2005).
- [70] S. S. Lee, C. S. Kim, E. D. Gomez, B. Purushothaman, M. F. Toney, C. Wang, A. Hexemer, J. E. Anthony, and Y.-L. Loo, Controlling nucleation and crystallization in solution-processed organic semiconductors for thin-film transistors, *Adv. Mater.* **21**, 3605–3609 (2009).
- [71] V. Coropceanu, J. Cornil, D. A. da Silva Filho, Y. Olivier, R. Silbey, and J.-L. Brédas, Charge transport in organic semiconductors, *Chem. Rev.* **107**, 926–952 (2007).
- [72] O. Ostroverkhova, Organic optoelectronic materials: mechanisms and applications, *Chem. Rev.* **116**, 13279–13412 (2016).
- [73] S. Fratini, D. Mayou, and S. Ciuchi, The transient localization scenario for charge transport in crystalline organic materials, *Adv. Funct. Mater.* **26**, 2292–2315 (2016).
- [74] S. R. Forrest, Ultrathin organic films grown by organic molecular beam deposition and related techniques, *Chem. Rev.* **97**, 1793–1896 (1997).
- [75] A. A. Virkar, S. Mannsfeld, Z. Bao, and N. Stingelin, Organic semiconductor growth and morphology considerations for organic thin-film transistors, *Adv. Mater.* **22**, 3857–3875 (2010).
- [76] C. Dimitrakopoulos and P. Malenfant, Organic thin film transistors for large area electronics, *Adv. Mater.* **14**, 99–117 (2002).
- [77] L. J. Richter, D. M. DeLongchamp, and A. Amassian, Morphology development in solution-processed functional organic blend films: an in situ viewpoint, *Chem. Rev.* **117**, 6332–6366 (2017).
- [78] J. A. Venables, *Introduction to Surface and Thin Film Processes* (Cambridge University Press, Cambridge, 2000).
- [79] B. Lewis and J. C. Anderson, *Nucleation and growth of thin films* (Academic Press, New York, 1978).
- [80] Barabási, *Fractal concepts in surface growth* (Press Syndicate of the University of Cambridge, New York, NY, USA, 1995).
- [81] A. Pimpinelli and J. Villain, *Physics of crystal growth* (Cambridge University Press, 1998).
- [82] I. V. Markov, *Crystal growth for beginners* (WORLD SCIENTIFIC, 2003).
- [83] A. Silinsh and V. Cápek, *Organic molecular crystals: interaction, localization and-transport phenomena* (AIP Press, New York, 1994).
- [84] F. Schreiber, Organic molecular beam deposition: growth studies beyond the first monolayer, *Phys. Status Solidi A* **201**, 1037–1054 (2004).

- [85] C. Lorch, K. Broch, V. Belova, G. Duva, A. Hinderhofer, A. Gerlach, M. Jankowski, and F. Schreiber, Growth and annealing kinetics of  $\alpha$ -sexithiophene and fullerene C60 mixed films, *J. Appl. Crystallogr.* **49**, 1266–1275 (2016).
- [86] T. Breuer, A. Karthäuser, H. Klemm, F. Genuzio, G. Peschel, A. Fuhrich, T. Schmidt, and G. Witte, Exceptional dewetting of organic semiconductor films: the case of dinaphthothienothiophene (DNTT) at dielectric interfaces, *ACS Appl. Mater. Interfaces* **9**, 8384–8392 (2017).
- [87] G. Yoshikawa, J. T. Sadowski, A. Al-Mahboob, Y. Fujikawa, T. Sakurai, Y. Tsuruma, S. Ikeda, and K. Saiki, Spontaneous aggregation of pentacene molecules and its influence on field effect mobility, *Appl. Phys. Lett.* **90**, 251906 (2007).
- [88] S. Steudel, D. Janssen, S. Verlaak, J. Genoe, and P. Heremans, Patterned growth of pentacene, *Appl. Phys. Lett.* **85**, 5550–5552 (2004).
- [89] A. Virkar, S. Mannsfeld, J. H. Oh, M. F. Toney, Y. H. Tan, G.-y. Liu, J. C. Scott, R. Miller, and Z. Bao, The role of OTS density on pentacene and C60 nucleation, thin film growth, and transistor performance, *Adv. Funct. Mater.* **19**, 1962–1970 (2009).
- [90] X. Zhang, E. Barrena, D. Goswami, D. G. de Oteyza, C. Weis, and H. Dosch, Evidence for a layer-dependent Ehrlich-Schwöbel barrier in organic thin film growth, *Phys. Rev. Lett.* **103**, 136101 (2009).
- [91] A. J. Fleming, F. P. Netzer, and M. G. Ramsey, Nucleation and 3D growth of para-sexiphenyl nanostructures from an oriented 2D liquid layer investigated by photoemission electron microscopy, *J. Phys.: Condens. Matter* **21**, 445003 (2009).
- [92] R. Zimmerleiter, M. Hohage, and L. Sun, Real-time in situ fluorescence study of  $\alpha$ -6t thin film growth on muscovite mica, *Phys. Rev. Mater.* **3**, 083402 (2019).
- [93] J. Israelachvili, *Intermolecular and Surface Forces* (London Academic, 1991).
- [94] A. Zangwill, *Physics at Surfaces* (Cambridge University Press, Cambridge, 1988).
- [95] S. A. Burke, J. M. Topple, and P. Grütter, Molecular dewetting on insulators, *J. Phys.: Condens. Matter* **21**, 423101 (2009).
- [96] J. Yang, S. Yim, and T. S. Jones, Molecular-orientation-induced rapid roughening and morphology transition in organic semiconductor thin-film growth, *Sci. Rep.* **5**, 9441 (2015).
- [97] A. Al-Mahboob, Y. Fujikawa, T. Sakurai, and J. T. Sadowski, Real-time microscopy of reorientation driven nucleation and growth in pentacene thin films on silicon dioxide, *Adv. Funct. Mater.* **23**, 2653–2660 (2013).
- [98] S. Nagai, Y. Inaba, T. Nishi, H. Kobayashi, and S. Tomiya, Collective orientation barrier in growth of organic thin films revealed by pMAIRS, *Phys. Rev. Mater.* **5**, 013801 (2021).
- [99] M. K. Huss-Hansen, M. Hodas, N. Mrkyvkova, J. Hagara, B. B. E. Jensen, A. Osadnik, A. Lützen, E. Majková, P. Siffalovic, F. Schreiber, L. Tavares, J. Kjelstrup-Hansen, and M. Knaapila, Surface-Controlled Crystal Alignment of Naphthyl End-Capped Oligothiophene on Graphene: Thin-Film Growth Studied by in Situ X-ray Diffraction, *Langmuir* **36**, 1898–1906 (2020).

- [100] J.-C. Ribierre, T. Tanaka, L. Zhao, Y. Yokota, S. Matsumoto, D. Hashizume, K. Takaishi, T. Muto, B. Heinrich, S. Méry, F. Mathevet, T. Matsushima, M. Uchiyama, C. Adachi, and T. Aoyama, Simultaneous edge-on to face-on reorientation and 1d alignment of small  $\pi$ -conjugated molecules using room-temperature mechanical rubbing, *Adv. Funct. Mater.* **28**, 1707038 (2018).
- [101] O. M. Roscioni, G. D’Avino, L. Muccioli, and C. Zannoni, Pentacene crystal growth on silica and layer-dependent step-edge barrier from atomistic simulations, *J. Phys. Chem. Lett.* **9**, 6900–6906 (2018).
- [102] A. Winkler, On the nucleation and initial film growth of rod-like organic molecules, *Surf. Sci.* **652**, 367–377 (2016).
- [103] H. Ma, H.-L. Yip, F. Huang, and A. K.-Y. Jen, Interface engineering for organic electronics, *Adv. Funct. Mater.* **20**, 1371–1388 (2010).
- [104] J. W. Ward, M. A. Loth, R. J. Kline, M. Coll, C. Ocal, J. E. Anthony, and O. D. Jurchescu, Tailored interfaces for self-patterning organic thin-film transistors, *J. Mater. Chem.* **22**, 19047 (2012).
- [105] M. Surin, P. Leclère, S. D. Feyter, M. M. S. Abdel-Mottaleb, F. C. D. Schryver, O. Henze, W. J. Feast, and R. Lazzaroni, Molecule-molecule versus molecule-substrate interactions in the assembly of oligothiophenes at surfaces, *J. Phys. Chem. B* **110**, 7898–7908 (2006).
- [106] J. Yang, D. Yan, and T. S. Jones, Molecular template growth and its applications in organic electronics and optoelectronics, *Chem. Rev.* **115**, 5570–5603 (2015).
- [107] L. Zhang, S. S. Roy, N. S. Safron, M. J. Shearer, R. M. Jacobberger, V. Saraswat, R. J. Hamers, M. S. Arnold, and T. L. Andrew, Orientation control of selected organic semiconductor crystals achieved by monolayer graphene templates, *Adv. Mater. Interfaces* **3**, 1600621 (2016).
- [108] W. H. Lee, J. Park, S. H. Sim, S. Lim, K. S. Kim, B. H. Hong, and K. Cho, Surface-directed molecular assembly of pentacene on monolayer graphene for high-performance organic transistors, *J. Am. Chem. Soc.* **133**, 4447–4454 (2011).
- [109] M. Kratzer and C. Teichert, Thin film growth of aromatic rod-like molecules on graphene, *Nanotechnology* **27**, 292001 (2016).
- [110] H. Huang, Y. Huang, S. Wang, M. Zhu, H. Xie, L. Zhang, X. Zheng, Q. Xie, D. Niu, and Y. Gao, Van der waals heterostructures between small organic molecules and layered substrates, *Crystals* **6**, 113 (2016).
- [111] N. N. Nguyen, H. C. Lee, K. Baek, M. S. Yoo, H. Lee, H. Lim, S. Choi, C.-J. Kim, S. Nam, and K. Cho, Atomically smooth graphene-based hybrid template for the epitaxial growth of organic semiconductor crystals, *Adv. Funct. Mater.*, 2008813 (2020).
- [112] T. Tian and C.-J. Shih, Molecular epitaxy on two-dimensional materials: the interplay between interactions, *Ind. Eng. Chem. Res.* **56**, 10552–10581 (2017).
- [113] P. Müller-Buschbaum, The active layer morphology of organic solar cells probed with grazing incidence scattering techniques, *Adv. Mater.* **26**, 7692–7709 (2014).

- [114] S. C. B. Mannsfeld, A. Virkar, C. Reese, M. F. Toney, and Z. Bao, Precise structure of pentacene monolayers on amorphous silicon oxide and relation to charge transport, *Adv. Mater.* **21**, 2294–2298 (2009).
- [115] E. M. Mannebach, J. W. Spalenka, P. S. Johnson, Z. Cai, F. J. Himpsel, and P. G. Evans, High hole mobility and thickness-dependent crystal structure in  $\alpha,\omega$ -dihexylsexithiophene single-monolayer field-effect transistors, *Adv. Funct. Mater.* **23**, 554–564 (2012).
- [116] S. Kowarik, Thin film growth studies using time-resolved X-ray scattering, *J. Phys.: Condens. Matter* **29**, 043003 (2016).
- [117] P. Kraft, A. Bergamaschi, C. Broennimann, R. Dinapoli, E. F. Eikenberry, B. Henrich, I. Johnson, A. Mozzanica, C. M. Schlepütz, P. R. Willmott, and B. Schmitt, Performance of single-photon-counting PILATUS detector modules, *J. Synchrotron Radiat.* **16**, 368–375 (2009).
- [118] D. Pennicard, S. Lange, S. Smoljanin, H. Hirsemann, H. Graafsma, M. Epple, M. Zuvic, M.-O. Lampert, T. Fritsch, and M. Rothermund, The LAMBDA photon-counting pixel detector, *J. Phys. Conf. Ser.* **425**, 062010 (2013).
- [119] D.-M. Smilgies, Scherrer grain-size analysis adapted to grazing-incidence scattering with area detectors, *J. Appl. Crystallogr.* **42**, 1030–1034 (2009).
- [120] D. W. Breiby, O. Bunk, J. W. Andreasen, H. T. Lemke, and M. M. Nielsen, Simulating X-ray diffraction of textured films, *J. Appl. Crystallogr.* **41**, 262–271 (2008).
- [121] M. Hodas, P. Siffalovic, P. Nadazdy, N. Mrkyvkova, M. Bodik, Y. Halahovets, G. Duva, B. Reisz, O. Konovalov, W. Ohm, M. Jergel, E. Majkova, A. Gerlach, A. Hinderhofer, and F. Schreiber, Real-time monitoring of growth and orientational alignment of pentacene on epitaxial graphene for organic electronics, *ACS Appl. Nano Mater.* **1**, 2819–2826 (2018).
- [122] J. L. Baker, L. H. Jimison, S. Mannsfeld, S. Volkman, S. Yin, V. Subramanian, A. Salleo, A. P. Alivisatos, and M. F. Toney, Quantification of thin film crystallographic orientation using X-ray diffraction with an area detector, *Langmuir* **26**, 9146–9151 (2010).
- [123] B. E. Warren, *X-ray diffraction* (Addison-Wesley, Reading, MA, 1969).
- [124] J. Simbrunner, C. Simbrunner, B. Schrode, C. Röthel, N. Bedoya-Martinez, I. Salzmann, and R. Resel, Indexing of grazing-incidence X-ray diffraction patterns: the case of fibre-textured thin films, *Acta Crystallogr. A* **74**, 373–387 (2018).
- [125] A. Pickett, M. Torkkeli, T. Mukhopadhyay, B. Puttaraju, A. Laudari, A. E. Lauritzen, O. Bikondoa, J. Kjelstrup-Hansen, M. Knaapila, S. Patil, and S. Guha, Correlating charge transport with structure in deconstructed diketopyrrolopyrrole oligomers: a case study of a monomer in field-effect transistors, *ACS Appl. Mater. Interfaces* **10**, 19844–19852 (2018).
- [126] J. Simbrunner, S. Hofer, B. Schrode, Y. Garmshausen, S. Hecht, R. Resel, and I. Salzmann, Indexing grazing-incidence X-ray diffraction patterns of thin films: lattices of higher symmetry, *J. Appl. Crystallogr.* **52**, 428–439 (2019).
- [127] N. Mrkyvkova, M. Hodas, J. Hagara, P. Nadazdy, Y. Halahovets, M. Bodik, K. Tokar, J. W. Chai, S. J. Wang, D. Z. Chi, A. Chumakov, O. Konovalov, A. Hin-

- derhofer, M. Jergel, E. Majkova, P. Siffalovic, and F. Schreiber, Diindenoperylene thin-film structure on MoS<sub>2</sub> monolayer, *Appl. Phys. Lett.* **114**, 251906 (2019).
- [128] B. Crist and J. B. Cohen, Fourier analysis of polymer X-ray diffraction patterns, *J. Polym. Sci., Polym. Phys. Ed.* **17**, 1001–1010 (1979).
- [129] G. Williamson and W. Hall, X-ray line broadening from filed aluminium and wolfram, *Acta Metall.* **1**, 22–31 (1953).
- [130] Y.-J. Kim, S. Lee, M. R. Niazi, K. Hwang, M.-C. Tang, D.-H. Lim, J.-S. Kang, D.-M. Smilgies, A. Amassian, and D.-Y. Kim, Systematic study on the morphological development of blade-coated conjugated polymer thin films via in situ measurements, *ACS Appl. Mater. Interfaces* **12**, 36417–36427 (2020).
- [131] T. Schuettfort, L. Thomsen, and C. R. McNeill, Observation of a distinct surface molecular orientation in films of a high mobility conjugated polymer, *J. Am. Chem. Soc.* **135**, 1092–1101 (2013).
- [132] H. Chen, M. Hurhangee, M. Nikolka, W. Zhang, M. Kirkus, M. Neophytou, S. J. Cryer, D. Harkin, P. Hayoz, M. Abdi-Jalebi, C. R. McNeill, H. Sirringhaus, and I. McCulloch, Dithiopheneindenofluorene (TIF) semiconducting polymers with very high mobility in field-effect transistors, *Adv. Mater.* **29**, 1702523 (2017).
- [133] X. Jiao, M. Statz, L. Lai, S. Schott, C. Jellett, I. McCulloch, H. Sirringhaus, and C. R. McNeill, Resolving different physical origins toward crystallite imperfection in semiconducting polymers: crystallite size vs paracrystallinity, *J. Phys. Chem. B* **124**, 10529–10538 (2020).
- [134] L. H. Jimison, A. Salleo, M. L. Chabinyc, D. P. Bernstein, and M. F. Toney, Correlating the microstructure of thin films of poly[5,5-bis(3-dodecyl-2-thienyl)-2,2-bithiophene] with charge transport: effect of dielectric surface energy and thermal annealing, *Phys. Rev. B* **78**, 125319 (2008).
- [135] W. L. Tan, Y.-B. Cheng, and C. R. McNeill, Direct assessment of structural order and evidence for stacking faults in layered hybrid perovskite films from X-ray scattering measurements, *J. Mater. Chem. A* **8**, 12790–12798 (2020).
- [136] B. E. Warren and B. L. Averbach, The effect of cold-work distortion on X-ray patterns, *J. Appl. Phys.* **21**, 595–599 (1950).
- [137] B. E. Warren and B. L. Averbach, The separation of cold-work distortion and particle size broadening in X-ray patterns, *J. Appl. Phys.* **23**, 497–497 (1952).
- [138] T. J. Prosa, J. Moulton, A. J. Heeger, and M. J. Winokur, Diffraction line-shape analysis of poly(3-dodecylthiophene): a study of layer disorder through the liquid crystalline polymer transition, *Macromolecules* **32**, 4000–4009 (1999).
- [139] K. A. Ritley, B. Krause, F. Schreiber, and H. Dosch, A portable ultrahigh vacuum organic molecular beam deposition system for in situ X-ray diffraction measurements, *Rev. Sci. Instrum.* **72**, 1453 (2001).
- [140] C. D. Liman, S. Choi, D. W. Breiby, J. E. Cochran, M. F. Toney, E. J. Kramer, and M. L. Chabinyc, Two-dimensional GIWAXS reveals a transient crystal phase in solution-processed thermally converted tetrabenzoporphyrin, *J. Phys. Chem. B* **117**, 14557–14567 (2013).

- [141] M. C. Weidman, D.-M. Smilgies, and W. A. Tisdale, Kinetics of the self-assembly of nanocrystal superlattices measured by real-time in situ X-ray scattering, *Nat. Mater.* **15**, 775–781 (2016).
- [142] L. J. Richter, D. M. DeLongchamp, F. A. Bokel, S. Engmann, K. W. Chou, A. Amassian, E. Schaible, and A. Hexemer, In situ morphology studies of the mechanism for solution additive effects on the formation of bulk heterojunction films, *Adv. Energy Mater.* **5**, 1400975 (2014).
- [143] A. Hexemer and P. Müller-Buschbaum, Advanced grazing-incidence techniques for modern soft-matter materials analysis, *IUCrJ* **2**, 106–125 (2015).
- [144] G. H. Vineyard, Grazing-incidence diffraction and the distorted-wave approximation for the study of surfaces, *Phys. Rev. B* **26**, 4146–4159 (1982).
- [145] S. K. Sinha, E. B. Sirota, S. Garoff, and H. B. Stanley, X-ray and neutron scattering from rough surfaces, *Phys. Rev. B* **38**, 2297–2311 (1988).
- [146] Y. Yoneda, Anomalous surface reflection of X-rays, *Phys. Rev.* **131**, 2010–2013 (1963).
- [147] H. Yang, Scanning Probe Techniques, in *Organic Field-Effect Transistors*, edited by Z. Bao and J. Locklin (CRC Press, 2007) Chap. 4.3.
- [148] G. Friedbacher, Atomic Force Microscopy, in *Surface and thin film analysis: a compendium of principles, instrumentation, and applications*, edited by G. Friedbacher and H. Bubert, 2nd ed. (Wiley-VCH Verlag GmbH & Co., 2011) Chap. 29.
- [149] H. Yang, T. J. Shin, M.-M. Ling, K. Cho, C. Y. Ryu, and Z. Bao, Conducting AFM and 2D GIXD studies on pentacene thin films, *J. Am. Chem. Soc.* **127**, 11542–11543 (2005).
- [150] N. E. Persson, P.-H. Chu, M. McBride, M. Grover, and E. Reichmanis, Nucleation, growth, and alignment of poly(3-hexylthiophene) nanofibers for high-performance OFETs, *Acc. Chem. Res.* **50**, 932–942 (2017).
- [151] Q. Zhong, D. Inniss, K. Kjoller, and V. Elings, Fractured polymer/silica fiber surface studied by tapping mode atomic force microscopy, *Surf. Sci. Lett.* **290**, L688–L692 (1993).
- [152] J. M. Hollas, *Modern Spectroscopy* (John Wiley & Sons, 2004).
- [153] T. Kobayashi and H. Naito, Optical Properties of Organic Semiconductors, in *Optical Properties of Materials and Their Applications*, edited by J. Singh, 2nd ed. (John Wiley & Sons, 2020) Chap. 11, pp. 295–321.
- [154] C. W. Bunn, The crystal structure of long-chain normal paraffin hydrocarbons. the "shape" of the CH<sub>2</sub> group, *Trans. Faraday Soc.* **35**, 482–491 (1939).
- [155] D. Tanner, J. A. Fitzgerald, and B. R. Phillips, The kevlar story—an advanced materials case study, *Angew. Chem. Int. Ed. Engl.* **28**, 649–654 (1989).
- [156] R. S. Porter, T. Kanamoto, and A. E. Zachariades, Property opportunities with polyolefins: a review. preparations and applications of high stiffness and strength by uniaxial draw, *Polymer* **35**, 4979–4984 (1994).

- [157] Y. Termonia, P. Meakin, and P. Smith, Theoretical study of the influence of strain rate and temperature on the maximum strength of perfectly ordered and oriented polyethylene, *Macromolecules* **19**, 154–159 (1986).
- [158] J. P. Penning, H. van der Werff, M. Roukema, and A. J. Pennings, On the theoretical strength of gelspun/hotdrawn ultra-high molecular weight polyethylene fibres, *Polym. Bull.* **23**, 347–352 (1990).
- [159] D. J. Lacks and G. C. Rutledge, Simulation of the temperature dependence of mechanical properties of polyethylene, *J. Phys. Chem.* **98**, 1222–1231 (1994).
- [160] J. C. L. Hageman, G. A. de Wijs, R. A. de Groot, and R. J. Meier, Bond scission in a perfect polyethylene chain and the consequences for the ultimate strength, *Macromolecules* **33**, 9098–9108 (2000).
- [161] L. Berger, H. Kausch, and C. Plummer, Structure and deformation mechanisms in UHMWPE-fibres, *Polymer* **44**, 5877–5884 (2003).
- [162] V. M. Litvinov, J. Xu, C. Melian, D. E. Demco, M. Möller, and J. Simmelink, Morphology, chain dynamics, and domain sizes in highly drawn gel-spun ultrahigh molecular weight polyethylene fibers at the final stages of drawing by SAXS, WAXS, and 1h solid-state NMR, *Macromolecules* **44**, 9254–9266 (2011).
- [163] L. Balzano, B. Coussens, T. Engels, F. Oosterlinck, M. Vlasblom, H. van der Werff, and D. Lellinger, Multiscale structure and microscopic deformation mechanisms of gel-spun ultrahigh-molecular-weight polyethylene fibers, *Macromolecules* **52**, 5207–5216 (2019).
- [164] I.-C. Yeh, L. Balzano, H. van der Werff, R. A. Mrozek, J. L. Lenhart, and J. W. Andzelm, Effects of finite lengths of chains on the structural and mechanical properties of polyethylene fibers, *Macromolecules* **53**, 18–28 (2019).
- [165] Y. Fukushima, H. Murase, and Y. Ohta, Dyneema®: super fiber produced by the gel spinning of a flexible polymer, in *High-performance and specialty fibers* (Springer Japan, 2016), p. 110.
- [166] M. Vlasblom, The manufacture, properties, and applications of high-strength, high-modulus polyethylene fibers, in *Handbook of properties of textile and technical fibres* (Elsevier, 2018), p. 706.
- [167] M. Vlasblom, The manufacture, properties, and applications of high-strength, high-modulus polyethylene fibers, in *Handbook of properties of textile and technical fibres* (Elsevier, 2018), pp. 699–755.
- [168] H. van der Werff and U. Heisserer, High-performance ballistic fibers, in *Advanced fibrous composite materials for ballistic protection* (Elsevier, 2016), pp. 71–107.
- [169] P. Smith, P. Lemstra, B. Kalb, and A. Pennings, Ultrahigh-strength polyethylene filaments by solution spinning and hot drawing, *Polym. Bull.* **1**, 733–736 (1979).
- [170] P. Smith and P. J. Lemstra, Ultra-high-strength polyethylene filaments by solution spinning/drawing, *J. Mater. Sci.* **15**, 505–514 (1980).
- [171] P. Smith and P. J. Lemstra, Ultrahigh-strength polyethylene filaments by solution spinning/drawing, 2†. influence of solvent on the drawability, *Makromol. Chem.* **180**, 2983–2986 (1979).

- [172] P. Smith and P. J. Lemstra, Ultra-high strength polyethylene filaments by solution spinning/drawing. 3. influence of drawing temperature, *Polymer* **21**, 1341–1343 (1980).
- [173] P. Smith, P. J. Lemstra, J. P. L. Pijpers, and A. M. Kiel, Ultra-drawing of high molecular weight polyethylene cast from solution, *Colloid Polym. Sci.* **259**, 1070–1080 (1981).
- [174] P. J. Flory, Tensile strength in relation to molecular weight of high polymers, *J. Am. Chem. Soc.* **67**, 2048–2050 (1945).
- [175] P. Smith, P. J. Lemstra, and J. P. L. Pijpers, Tensile strength of highly oriented polyethylene. II. effect of molecular weight distribution, *J. Polym. Sci., Polym. Phys. Ed.* **20**, 2229–2241 (1982).
- [176] Y. Termonia, P. Meakin, and P. Smith, Theoretical study of the influence of the molecular weight on the maximum tensile strength of polymer fibers, *Macromolecules* **18**, 2246–2252 (1985).
- [177] C. W. M. Bastiaansen, Influence of initial polymer concentration in solution and weight-average molecular weight on the drawing behavior of polyethylenes, *J. Polym. Sci., Part B: Polym. Phys.* **28**, 1475–1482 (1990).
- [178] M. Doi, *Introduction to polymer physics* (OUP Oxford, 1995).
- [179] P. G. de Gennes, Reptation of a polymer chain in the presence of fixed obstacles, *J. Chem. Phys.* **55**, 572–579 (1971).
- [180] S. F. E. Masao Doi, *The theory of polymer dynamics* (Oxford University Press, 1988).
- [181] P. Smith and P. J. Lemstra, Ultra-drawing of high molecular weight polyethylene cast from solution, *Colloid Polym. Sci.* **258**, 891–894 (1980).
- [182] P. Smith, P. J. Lemstra, and H. C. Booij, Ultradrawing of high-molecular-weight polyethylene cast from solution. II. influence of initial polymer concentration, *J. Polym. Sci., Polym. Phys. Ed.* **19**, 877–888 (1981).
- [183] H. Murase, Y. Ohta, and T. Hashimoto, A new scenario of shish-kebab formation from homogeneous solutions of entangled polymers: visualization of structure evolution along the fiber spinning line, *Macromolecules* **44**, 7335–7350 (2011).
- [184] H. Murase, T. Kume, T. Hashimoto, and Y. Ohta, Time evolution of structures under shear-induced phase separation and crystallization in semidilute solution of ultrahigh molecular weight polyethylene<sup>†</sup>, *Macromolecules* **38**, 8719–8728 (2005).
- [185] H. Murase, T. Kume, T. Hashimoto, and Y. Ohta, Shear-induced structures in semidilute solution of ultrahigh molecular weight polyethylene at temperature close to equilibrium dissolution temperature<sup>†</sup>, *Macromolecules* **38**, 6656–6665 (2005).
- [186] T. Hashimoto, H. Murase, and Y. Ohta, A new scenario of flow-induced shish-kebab formation in entangled polymer solutions, *Macromolecules* **43**, 6542–6548 (2010).
- [187] A. J. Pennings and A. M. Kiel, Fractionation of polymers by crystallization from solution, III. on the morphology of fibrillar polyethylene crystals grown in solution, *Kolloid-Z. u. Z. Polymere* **205**, 160–162 (1965).

- [188] S. Kimata, T. Sakurai, Y. Nozue, T. Kasahara, N. Yamaguchi, T. Karino, M. Shibayama, and J. A. Kornfield, Molecular basis of the shish-kebab morphology in polymer crystallization, *Science* **316**, 1014–1017 (2007).
- [189] M. Seki, D. W. Thurman, J. P. Oberhauser, and J. A. Kornfield, Shear-mediated crystallization of isotactic polypropylene: the role of long chain-long chain overlap, *Macromolecules* **35**, 2583–2594 (2002).
- [190] R. H. Somani, L. Yang, L. Zhu, and B. S. Hsiao, Flow-induced shish-kebab precursor structures in entangled polymer melts, *Polymer* **46**, 8587–8623 (2005).
- [191] L. Balzano, S. Rastogi, and G. W. M. Peters, Crystallization and precursors during fast short-term shear, *Macromolecules* **42**, 2088–2092 (2009).
- [192] B. Nazari, H. Tran, B. Beaugregard, M. Flynn-Hepford, D. Harrell, S. T. Milner, and R. H. Colby, Two distinct morphologies for semicrystalline isotactic polypropylene crystallized after shear flow, *Macromolecules* **51**, 4750–4761 (2018).
- [193] S. L. Wingstrand, B. Shen, J. A. Kornfield, K. Mortensen, D. Parisi, D. Vlassopoulos, and O. Hassager, Rheological link between polymer melts with a high molecular weight tail and enhanced formation of shish-kebabs, *ACS Macro Letters* **6**, 1268–1273 (2017).
- [194] N. A. J. M. V. Aerle and A. W. M. Braam, A structural study on solid state drawing of solution-crystallized ultra-high molecular weight polyethylene, *J. Mater. Sci.* **23**, 4429–4436 (1988).
- [195] J.-T. Yeh, S.-C. Lin, C.-W. Tu, K.-H. Hsie, and F.-C. Chang, Investigation of the drawing mechanism of UHMWPE fibers, *J. Mater. Sci.* **43**, 4892–4900 (2008).
- [196] H. Xu, M. An, Y. Lv, L. Zhang, and Z. Wang, Structural development of gel-spinning UHMWPE fibers through industrial hot-drawing process analyzed by small/wide-angle x-ray scattering, *Polym. Bull.* **74**, 721–736 (2016).
- [197] G. Stubbs, Developments in fiber diffraction, *Curr. Opin. Struct. Biol.* **9**, 615–619 (1999).
- [198] C. Burger, B. S. Hsiao, and B. Chu, Preferred orientation in polymer fiber scattering, *Polym. Rev.* **50**, 91–111 (2010).
- [199] N. Striebeck, *X-ray scattering of soft matter* (Springer Berlin Heidelberg, 2007).
- [200] R. Lovell and G. R. Mitchell, Molecular orientation distribution derived from an arbitrary reflection, *Acta Crystallogr. A* **37**, 135–137 (1981).
- [201] C. P. Lafrance, M. Pezolet, and R. E. Prud’homme, Study of the distribution of molecular orientation in highly oriented polyethylene by X-ray diffraction, *Macromolecules* **24**, 4948–4956 (1991).
- [202] W. Ruland and H. Tompa, The effect of preferred orientation on the intensity distribution of (hk) interferences, *Acta Crystallogr. A* **24**, 93–99 (1968).
- [203] W. Ruland, Elimination of the effect of orientation distributions in fiber diagrams, *Colloid Polym. Sci.* **255**, 833–836 (1977).
- [204] H. D. Deas, The diffraction of X-rays by a random assemblage of molecules having partial alignment, *Acta Crystallogr.* **5**, 542–546 (1952).

- [205] J. H. Park and G. C. Rutledge, Ultrafine high performance polyethylene fibers, *J. Mater. Sci.* **53**, 3049–3063 (2017).
- [206] K. Koziol, J. Vilatela, A. Moisala, M. Motta, P. Cunniff, M. Sennett, and A. Windle, High-performance carbon nanotube fiber, *Science* **318**, 1892–1895 (2007).
- [207] C.-P. Lafrance and R. E. Prud'homme, Characterization of the molecular orientation in highly oriented rolled polypropylene sheets by X-ray diffraction, *Polymer* **35**, 3927–3935 (1994).
- [208] N. Stribeck, U. Nöchel, and A. A. Camarillo, Scanning microbeam X-ray scattering of fibers analyzed by one-dimensional tomography, *Macromol. Chem. Phys.* **209**, 1976–1982 (2008).
- [209] N. H. Abel, Auflösung einer mechanischen aufgabe., *J. Reine Angew. Math.* **1826**, 153–157 (1826).
- [210] N. Stribeck, U. Nöchel, S. Fakirov, J. Feldkamp, C. Schroer, A. Timmann, and M. Kuhlmann, SAXS-fiber computer tomography. method enhancement and analysis of microfibrillar-reinforced composite precursors from PEBA and PET, *Macromolecules* **41**, 7637–7647 (2008).
- [211] C. J. Dasch, One-dimensional tomography: a comparison of abel, onion-peeling, and filtered backprojection methods, *Appl. Opt.* **31**, 1146 (1992).
- [212] V. Dribinski, A. Ossadtchi, V. A. Mandelshtam, and H. Reisler, Reconstruction of abel-transformable images: the gaussian basis-set expansion abel transform method, *Rev. Sci. Instrum.* **73**, 2634–2642 (2002).
- [213] P. Kraft, O. Bunk, F. A. Reifler, R. Hufenus, M. Heuberger, and F. Pfeiffer, One-dimensional small-angle X-ray scattering tomography of dip-coated polyamide 6 monofilaments, *J. Synchrotron Radiat.* **17**, 257–262 (2010).
- [214] S. Roth, M. Burghammer, A. Janotta, and C. Riekell, Rotational disorder in poly(p-phenylene terephthalamide) fibers by X-ray diffraction with a 100 nm beam, *Macromolecules* **36**, 1585–1593 (2003).
- [215] R. J. Davies, C. Koenig, M. Burghammer, and C. Riekell, On-axis microbeam wide- and small-angle scattering experiments of a sectioned poly(p-phenylene terephthalamide) fiber, *Appl. Phys. Lett.* **92**, 101903 (2008).
- [216] D. T. Grubb, Comments on “axial X-ray scattering on high performance polymeric fibers”, *J. Polym. Sci., Part B: Polym. Phys.* **34**, 1159–1161 (1996).
- [217] W. Ruland, The evaluation of the small-angle scattering of lamellar two-phase systems by means of interface distribution functions, *Colloid Polym. Sci.* **255**, 417–427 (1977).
- [218] G. R. Strobl and M. Schneider, Direct evaluation of the electron density correlation function of partially crystalline polymers, *J. Polym. Sci., Polym. Phys. Ed.* **18**, 1343–1359 (1980).
- [219] D. Blundell, Models for small-angle X-ray scattering from highly dispersed lamellae, *Polymer* **19**, 1258–1266 (1978).
- [220] W. Ruland and B. Smarsly, SAXS of self-assembled oriented lamellar nanocomposite films: an advanced method of evaluation, *J. Appl. Crystallogr.* **37**, 575–584 (2004).

- [221] N. Stribeck, A. A. Camarillo, U. Nöchel, C. Schroer, M. Kuhlmann, S. V. Roth, R. Gehrke, and R. K. Bayer, Volume-resolved nanostructure survey of a polymer part by means of SAXS microtomography, *Macromol. Chem. Phys.* **207**, 1139–1149 (2006).
- [222] J. M. Feldkamp, M. Kuhlmann, S. V. Roth, A. Timmann, R. Gehrke, I. Shakhverdova, P. Paufler, S. K. Filatov, R. S. Bubnova, and C. G. Schroer, Recent developments in tomographic small-angle X-ray scattering, *Phys. Status Solidi A* **206**, 1723–1726 (2009).
- [223] A. Kak and M. Slaney, *Principles of computerized tomographic imaging* (IEEE Press, New York, 1988).
- [224] M. Álvarez-Murga, P. Bleuet, and J.-L. Hodeau, Diffraction/scattering computed tomography for three-dimensional characterization of multi-phase crystalline and amorphous materials, *J. Appl. Crystallogr.* **45**, 1109–1124 (2012).
- [225] F. Schaff, M. Bech, P. Zaslansky, C. Jud, M. Liebi, M. Guizar-Sicairos, and F. Pfeiffer, Six-dimensional real and reciprocal space small-angle X-ray scattering tomography, *Nature* **527**, 353–356 (2015).
- [226] M. Liebi, M. Georgiadis, A. Menzel, P. Schneider, J. Kohlbrecher, O. Bunk, and M. Guizar-Sicairos, Nanostructure surveys of macroscopic specimens by small-angle scattering tensor tomography, *Nature* **527**, 349–352 (2015).
- [227] J. M. Feldkamp, Scanning small-angle X-ray scattering tomography: non-destructive access to local nanostructure, PhD thesis (Technischen Universität Dresden, 2009).
- [228] E. Y. Sidky, C.-M. Kao, and X. Pan, Accurate image reconstruction from few-views and limited-angle data in divergent-beam CT, *J. X-Ray Sci. Technol.* **14**, 119–139 (2009).
- [229] A. Biguri, Iterative reconstruction and motion compensation in computed tomography on gpus, PhD thesis (University of Bath, 2018).
- [230] A. Andersen, Simultaneous algebraic reconstruction technique (SART): a superior implementation of the ART algorithm, *Ultrason. Imaging* **6**, 81–94 (1984).
- [231] P. Clancy, Application of molecular simulation techniques to the study of factors affecting the thin-film morphology of small-molecule organic semiconductors<sup>†</sup>, *Chem. Mater.* **23**, 522–543 (2011).
- [232] M. K. Huss-Hansen, M. Hansteen, J. Linnet, A. R. Walther, J. Kjelstrup-Hansen, and M. Knaapila, Structural basis for a naphthyl end-capped oligothiophene with embedded metallic nanoparticles for organic field-effect transistors, *Appl. Phys. Lett.* **113**, 251903 (2018).
- [233] S. Pang, Y. Hernandez, X. Feng, and K. Müllen, Graphene as transparent electrode material for organic electronics, *Adv. Mater.* **23**, 2779–2795 (2011).
- [234] R. Li, J. W. Ward, D.-M. Smilgies, M. M. Payne, J. E. Anthony, O. D. Jurchescu, and A. Amassian, Direct structural mapping of organic field-effect transistors reveals bottlenecks to carrier transport, *Adv. Mater.* **24**, 5553–5558 (2012).

## **Part II**

### **Results and Publications**



## Paper I

---

Reproduced from Ref. [232], with the permission of AIP Publishing.

This letter was published in the first year of the PhD project and is based on experimental data from two beamtimes at ESRF and PETRA III. The aim of the study was to investigate the thin-film structure of NaT3 in an OFET device with and without embedded silver nanoparticles. The study builds upon previous work by Linnet et al. [57], in which they show that the photoresponsivity of NaT3 based organic photo-transistors can be significantly enhanced by utilizing the plasmonic properties of embedded silver nanoparticles. Here, we employ GIWAXS and GISAXS with a microfused X-ray beam, allowing us to precisely determine the thin-film microstructure in the area of the embedded nanoparticles. Moreover, by utilizing the microbeam approach, we are able to successfully describe the complex GISAXS scattering observed by isolating the contributions from each layer of the device.

# Structural basis for a naphthyl end-capped oligothiophene with embedded metallic nanoparticles for organic field-effect transistors

Cite as: Appl. Phys. Lett. **113**, 251903 (2018); <https://doi.org/10.1063/1.5080006>

Submitted: 05 November 2018 . Accepted: 05 December 2018 . Published Online: 20 December 2018

 Mathias K. Huss-Hansen, Marie Hansteen, Jes Linnet, Anders Runge Walther,  Jakob Kjelstrup-Hansen, and  Matti Knaapila



View Online



Export Citation



CrossMark

## ARTICLES YOU MAY BE INTERESTED IN

[X-ray study of anisotropically shaped metal halide perovskite nanoparticles in tubular pores](#)  
Applied Physics Letters **113**, 251901 (2018); <https://doi.org/10.1063/1.5054271>

[Capillary-assisted localized crystallization on discrete micropillar rings](#)  
Applied Physics Letters **113**, 251904 (2018); <https://doi.org/10.1063/1.5063608>

[Impurity-derived p-type conductivity in cubic boron arsenide](#)  
Applied Physics Letters **113**, 251902 (2018); <https://doi.org/10.1063/1.5058134>



## Your Qubits. Measured.

Meet the next generation of quantum analyzers

- Readout for up to 64 qubits
- Operation at up to 8.5 GHz, mixer-calibration-free
- Signal optimization with minimal latency

Find out more



## Structural basis for a naphthyl end-capped oligothiophene with embedded metallic nanoparticles for organic field-effect transistors

Mathias K. Huss-Hansen,<sup>1,a)</sup> Marie Hansteen,<sup>1</sup> Jes Linnet,<sup>2,3,b)</sup> Anders Runge Walther,<sup>2,4</sup> Jakob Kjelstrup-Hansen,<sup>2</sup> and Matti Knaapila<sup>1</sup>

<sup>1</sup>Department of Physics, Technical University of Denmark, 2800 Kgs. Lyngby, Denmark

<sup>2</sup>NanoSYD, Mads Clausen Institute, University of Southern Denmark, 6400 Sønderborg, Denmark

<sup>3</sup>The Mærsk Mc-Kinney Møller Institute, University of Southern Denmark, 5230 Odense, Denmark

<sup>4</sup>Department of Chemical Engineering, Biotechnology and Environmental Technology, University of Southern Denmark, 5230 Odense, Denmark

(Received 5 November 2018; accepted 5 December 2018; published online 20 December 2018)

We report on the apparent structure of 5,5''-bis(naphth-2-yl)-2,2':5',2''-terthiophene (NaT3) in organic field-effect transistors (OFETs) with and without embedded silver nanoparticles. Using regular- and microbeam grazing incidence wide- and small-angle X-ray scattering, the device structure is characterized locally in the area with the embedded particles. The NaT3 thin film order is reduced and the found unit cell ( $a = 25.7 \text{ \AA}$ ,  $b = 5.87 \text{ \AA}$ ,  $c = 8.03 \text{ \AA}$ , and  $\beta = 98.9^\circ$ ) differs significantly from the one reported in the bulk, but shows no significant change, when the particles corresponding to the crystal size are incorporated into the device structure. At the same time, the apparent thin film crystal sizes in OFETs are found to be similar with and without the embedded particles. In both cases, the carrier mobilities are of the order of  $10^{-4} \text{ cm}^2/(\text{Vs})$ .

Published by AIP Publishing. <https://doi.org/10.1063/1.5080006>

Organic field-effect transistors (OFETs) are subject to interest for use in modern electronics due to their inexpensive, low-temperature processing, low materials costs, and application potential in, e.g., flexible electronics,<sup>1</sup> gas sensors,<sup>2</sup> pressure sensors,<sup>3</sup> and optical sensors (organic phototransistors, OPTs).<sup>4</sup> Numerous studies have been carried out on conjugated oligomers and polymers, whose properties can be tuned through design and functionalization.<sup>5,6</sup> Of particular interest are thiophene-based oligomers because of their hole transport properties and stable device performance under atmospheric conditions.<sup>7–9</sup> By end-capping the thiophene rings with aryl groups, the polymerization potential is hindered and intermolecular packing is promoted.<sup>9</sup>

We have recently shown that the photoresponsivity in naphthyl end-capped oligothiophene based OPTs can be enhanced by utilizing the plasmonic properties of embedded metallic nanoparticles.<sup>10</sup> However, while it is well known that the carrier mobility is connected to the orientation and crystal size of the organic molecules,<sup>11–13</sup> the literature of structural evaluation of oligothiophenes in OFETs with embedded metallic particles remains less comprehensive.

The molecular structure of organic thin film devices is often evaluated by the use of grazing incidence X-ray scattering.<sup>14–16</sup> OFETs with embedded nanoparticle arrays are prepared using electron-beam lithography, which does not allow for a simple preparation of suitably large samples for grazing-incidence studies. Therefore, it remains difficult to probe the micrometer scaled areas of interest. Nevertheless, recent advances in synchrotron radiation have made it possible to probe structures locally in devices using micro- and nanobeams.<sup>17</sup>

In this letter, we use micro-focused X-rays to investigate 5,5''-bis(naphth-2-yl)-2,2':5',2''-terthiophene (NaT3) and establish its structural fundamentals in OFETs with and without embedded silver nanoparticles.

Figure 1(a) shows the chemical structure of NaT3. The synthesis of NaT3 follows the Suzuki cross-coupling protocols reported in Ref. 9.

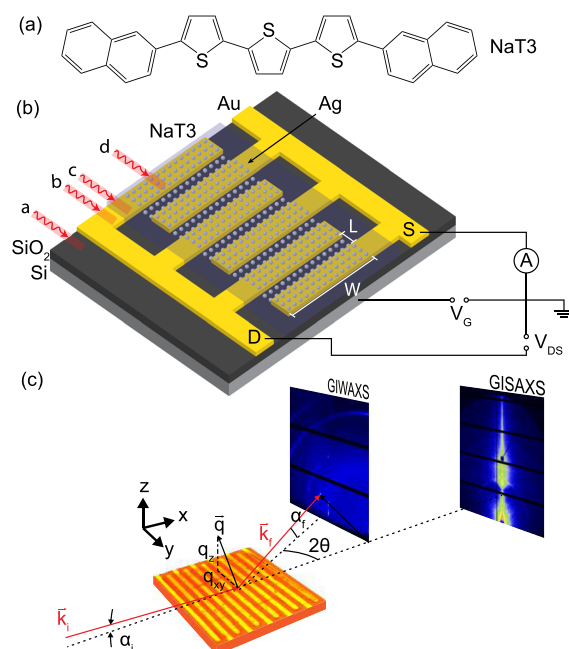


FIG. 1. (a) Chemical structure of NaT3. (b) Illustration of the OFET design with interdigitated gold drain (D) and source (S) electrodes. W and L are the width and length of the transistor channels, respectively. The positions of the  $\mu$ -beam corresponding to Figs. 3(a)–3(d) are indicated by wavy red lines. Not drawn to scale. (c) Illustration of the employed GIWAXS/GISAXS setup.

<sup>a)</sup>Electronic mail: mathias.huss-hansen@fysik.dtu.dk

<sup>b)</sup>Present address: Center for Nano Optics, University of Southern Denmark, 5230 Odense, Denmark.

Figure 1(b) shows the structure of the investigated OFETs fabricated by the following procedure, as described in Ref. 10. A highly n-doped Si substrate formed the back electrode with a 200 nm thick thermally grown SiO<sub>2</sub> layer as a gate dielectric. The interdigitated source and drain electrodes were fabricated by E-beam evaporation of 30 nm Au on top of 3 nm of Ti, structured by photolithography and lift-off in acetone. The transistor channel dimensions were 2 mm × 10 μm (width × length) corresponding to a width/length (W/L) ratio of 200:1. Ag nanoparticles with diameters of ~40 nm were subsequently patterned in a nominal square lattice (period = 200 nm, corresponding to a surface coverage of ~3%) on top of the gate dielectric and electrodes by E-beam lithography in poly(methyl methacrylate) (PMMA) followed by thermal evaporation of 40 nm of Ag on top of 3 nm Ti and lift-off in acetone. Finally, a 55 nm thick NaT3 layer was deposited atop the substrate by vacuum sublimation. The film thickness was determined by atomic force microscopy (AFM). Each substrate contained two transistors: one with and one without nanoparticles. This allowed direct comparison to investigate the influence of the nanoparticles on devices that had been processed in exactly the same manner.

Figure 1(c) illustrates the employed experimental setup. The devices were investigated by means of regular and micro-beam ( $\mu$ -beam) grazing incidence X-ray scattering in wide- and small-angle configurations (GIWAXS/GISAXS). The measurements with a regular beam were carried out at XMaS (BM28) at the European Synchrotron Radiation Facility (ESRF), Grenoble. The X-ray energy was 10 keV, and the beam size 100 μm × 260 μm (vert. × hor.). The angle of incidence was 0.17°, slightly above the critical angle of NaT3 (0.11°), and the data were recorded using a MAR 165 CCD detector. The sample-to-detector distance was 330 mm. The  $\mu$ -beam measurements were carried out at the MicroFocus end station at the P03 beamline (MiNaXS) at PETRA III, Hamburg. The X-ray energy was 13.19 keV, and the beam size was 16 μm × 22 μm (vert. × hor.) at the sample. The employed incidence angle was 0.42°. The GIWAXS and GISAXS images were recorded separately without moving the sample using Pilatus 300 K and Pilatus 1M detectors, respectively. The sample-to-detector distances were 220 mm for GIWAXS and 5 m for GISAXS, calibrated by lanthanum hexaboride and silver behenate.

The GIWAXS images were transformed to the reciprocal space by reciprocal space mapping (RSM) using the *Pygix* python library and the fiber transformation originally described by Stribeck.<sup>18</sup> This transformation is valid since the film exhibits fiber texture in the  $x$ - $y$  plane around the

surface normal ( $z$ -axis). The GISAXS images were converted to the  $\mathbf{q}$  space using *FitGISAXS*.<sup>19</sup> The crystal grain-sizes were analyzed using Scherrer grain-size analysis adapted for grazing-incidence scattering with an area detector.<sup>20</sup> In this procedure, the tangential full width half maximum (FWHM) of the RSM peak intensities was fitted with a Lorentzian distribution. By carrying out resolution analysis, the experimental contribution to the peak broadening (including smearing from the beam divergence, energy bandwidth, and the finite length of the beam footprint) was determined to be less than 10% of the total peak width and was therefore treated as negligible.

To obtain a qualitative understanding of the molecular packing inside the thin film unit cell, density functional theory (DFT) was employed using the GPAW package.<sup>21</sup> The A Form packing reported in Ref. 8 was used as a starting point together with the experimentally found unit cell, and the atoms were allowed to relax until the atomic forces were below  $1 \times 10^{-2}$  eV/Å. The Bayesian error estimation functional<sup>22</sup> (BEEF-vdW) and projector-augmented wave potentials were used, with a plane-wave cutoff of 700 eV and a converged  $1 \times 6 \times 4$  Monkhorst-Pack grid.

The electric characterization of the OFETs was performed with a custom-built characterization set-up based on a LabVIEW-controlled data acquisition card connected to voltage and current amplifiers, providing the input, and a probe station measuring the output signal from the OFET. The gate voltage ( $V_G$ ) was swept from 0 → -15 V with a constant drain-source voltage  $V_{DS} = -15$  V.

Figure 2(a) shows a 2D GIWAXS pattern of the NaT3 thin film from the OFET by a regular beam. The pattern exhibits a series of vertically smeared peaks (Bragg rods) originating from the mosaicity of the NaT3 crystallites, with the molecules standing nearly vertically on the substrate. The smearing of the Bragg peaks along  $\mathbf{q}_z$  suggests that NaT3 exhibits a higher degree of disorder along the stacking direction perpendicular to the surface normal compared with the closely related but symmetrical 5,5'-bis(naphth-2-yl)-2,2'-bithiophene (NaT2), which shows equally resolved Bragg peaks (rather than rods) in both directions.<sup>7</sup> Yet the pattern has a prominent similarity to what is reported for 5-decyl-5''-(naphthalen-2-yl)-2,2':5',2''-terthiophene (D3TN) in Ref. 23, which likewise contains three thiophene rings with one end-group replaced by an alkyl-group. The observed Bragg peaks can be consistently indexed assuming a monoclinic unit cell with parameters  $a = 25.7$  Å,  $b = 5.87$  Å,  $c = 8.03$  Å, and  $\beta = 98.9^\circ$  and volume  $V = 1.20 \times 10^4$  Å<sup>3</sup>.

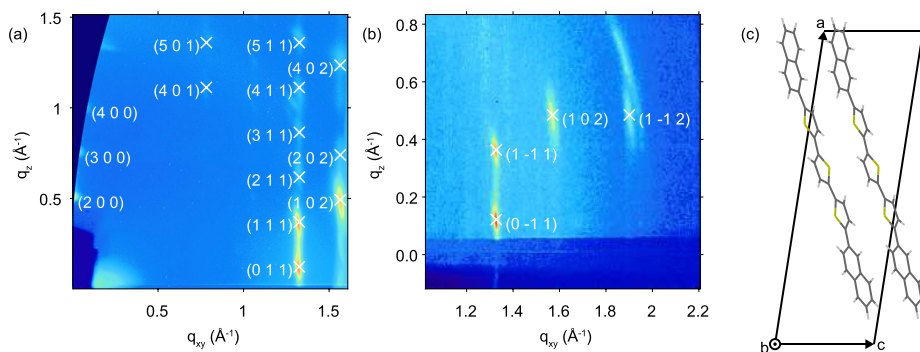


FIG. 2. GIWAXS pattern from (a) entire OFET device and (b) area of OFET with embedded nanoparticles, measured from the same sample. The Bragg peaks (and corresponding Miller indices) originate from the fiber-textured NaT3 film crystallites. (c) Proposed NaT3 unit cell and molecular packing in OFETs.

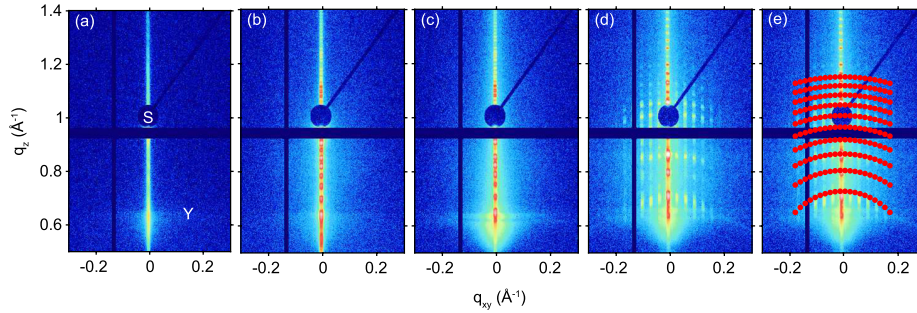


FIG. 3. GISAXS images from different areas of the OFET: (a) SiO<sub>2</sub> substrate, (b) Au electrodes on SiO<sub>2</sub>, (c) NaT3 atop the electrodes, and (d) and (e) Ag nanoparticles embedded in NaT3 atop the electrodes [the corresponding positions of the  $\mu$ -beam are indicated in Fig. 1(b)]. S indicates the position of the specular beamstop; Y indicates the Yoneda peaks of SiO<sub>2</sub> and NaT3. The red dots indicate the calculated positions of the reflections from the interdigitated electrodes with a 10  $\mu$ m period.

Our unit cell choice follows the notation described in Ref. 7 with (100)-texture and standing molecules (defined with **a** as the long axis nearly along the backbone of the molecule). The unit cell observed in our thin film devices differs significantly from the unit cell reported for bulk NaT3 in Ref. 8. The reported bulk unit cell has 6 molecules (and the volume  $3.44 \times 10^4 \text{ \AA}^3$ ), compared to  $Z=2$  for the thin film case. This suggests that the long range order along the long axis is reduced for films.

Figure 2(b) shows a typical GIWAXS pattern from the area of the OFET with embedded particles measured by a  $\mu$ -beam. The data are consistently indexed with the same unit cell parameters, indicating that there are no significant changes in the NaT3 unit cell with and without embedded particles. The proposed molecular packing is shown in Fig. 2(c).

Table I compiles the determined crystal sizes for NaT3 in devices with and without embedded particles. There are no significant changes in the crystal sizes between these two cases within the given error bounds (calculated as one standard deviation from the least squares fitting). Interestingly, the typical crystal sizes of NaT3 in films are on the same order of magnitude as the nominal size of the embedded particles. It is therefore likely that the particles are incorporated into the mosaic crystal structure causing only local hindrance to the molecular growth. The opposite could be the case if the average crystallite size was much larger.

Figure 3 shows the GISAXS images from different areas of the device when the incident X-ray was perpendicular to the interdigitated electrodes, with  $\mathbf{q}_z$  and  $\mathbf{q}_{xy}$  corresponding to the out-of-plane and in-plane wave vectors, respectively. The image from the bare SiO<sub>2</sub> substrate [Fig. 3(a)] features a bright specular rod along  $\mathbf{q}_z$  with the specular reflected beam covered by the beamstop (indicated with an S). The specular beam is located at an exit angle equal to the incidence angle of  $\alpha_i = 0.42^\circ$ . At  $q_z = 0.65$ , the observed horizontal scattering feature is the so-called Yoneda peak (indicated with a Y) from

SiO<sub>2</sub> that appears at the critical angle of the material ( $\alpha_c = 0.146^\circ$  for SiO<sub>2</sub>). On the image from the area with Au electrodes on top of SiO<sub>2</sub> [Fig. 3(b)], multiple bright scattering peaks are found along the specular rod at  $q_{xy} = 0$ . These peaks are consistent with the diffraction pattern from a 1D lateral grating formed by the Au electrodes, aligned perpendicular to the incoming beam. The same feature is present on the image from the area with NaT3 deposited on top of the electrodes [Fig. 3(c)] with small modulations due to reflection/refraction effects in the thin film overlayer. The Yoneda peak for NaT3 ( $\alpha_c = 0.11^\circ$ ) appears at  $q_z = 0.61$ , just below the Yoneda peak of SiO<sub>2</sub>. Furthermore, there is an increase in diffuse scattering from the disorder of the thin film structure.

Figure 3(d) shows the image from the area with Ag particles embedded in NaT3 on top of the interdigitated Au electrodes. The scattering intensity in the in-plane  $\mathbf{q}_{xy}$  direction is dominated by a series of sharp peaks that appear to be correlated with the peaks found along the specular rod and are located on arcs extending from  $q_{xy} = 0$ . The high scattering order and sharpness of peaks found along  $\mathbf{q}_{xy}$  point to a high correlation between particles, and due to the large footprint of the beam, it is inferred that the particles are well-aligned across the device. From the peak spacing, the average interparticle distance can be derived as  $d_{particle} = 2\pi/\Delta q_{xy}$ , leading to a distance of  $198 \pm 2 \text{ nm}$ . The peaks found along the specular rod are spaced further apart than in Figs. 3(b) and 3(c) due to the electrode spacing being halved in the area, where the electrodes are interdigitated. The diffraction from a one-dimensional grating perpendicular to the incoming beam can be written as

$$\cos(\alpha_f) - \cos(\alpha_i) \cos(2\theta) = \frac{m\lambda}{d}, \quad (1)$$

where  $\alpha_i$  and  $\alpha_f$  are the incidence and exit angles,  $2\theta$  is the in-plane scattering angle,  $m$  is the order of diffraction,  $\lambda$  is the X-ray wavelength, and  $d$  is the grating period. The observed scattering patterns correspond to the computed diffraction peaks for a grating with  $d = 10 \mu\text{m}$  [red dots in Fig. 3(e)]. Here, the diffraction patterns are shown for  $m = -5$  to 4 for 20 equally spaced values of  $2\theta$  in the range of  $\pm 0.2^\circ$ .

Figure 4 shows the transfer curves of the OFET with and without embedded particles. The saturation mobilities are extracted from the slopes of the  $I_{DS}^{-1/2}$  vs  $V_G$  curves (not shown) in the high bias regime between  $V_G = -10$  and  $-15$ .

TABLE I. Crystal sizes of various crystallographic planes with their corresponding Miller indices.

Sample	(0 $\bar{1}$ 1) (nm)	(1 $\bar{1}$ 1) (nm)	(102) (nm)	(1 $\bar{1}$ 2) (nm)
With nanoparticles	$28 \pm 2$	$28 \pm 2$	$19 \pm 1$	$17 \pm 2$
Without nanoparticles	$30 \pm 3$	$33 \pm 3$	$21 \pm 2$	$22 \pm 2$

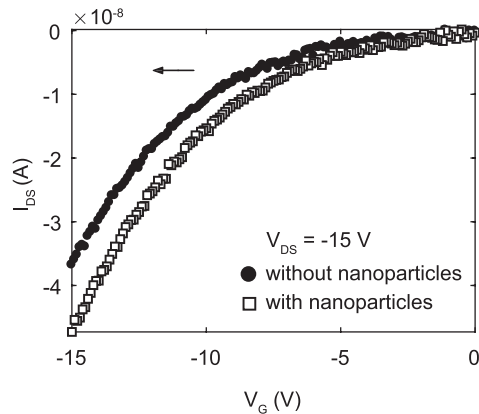


FIG. 4. Transfer curves of NaT3 OFETs with and without embedded particles. The arrow indicates the sweeping direction.

TABLE II. Saturated mobilities of OFETs with and without particles. Reported values are in  $\times 10^{-4} \text{ cm}^2/(\text{V s})$ .

Sample	1	2	3	4	Mean
With nanoparticles	0.38	1.09	2.02	1.40	$1.2 \pm 0.59$
Without nanoparticles	0.41	0.69	1.77	1.56	$1.1 \pm 0.57$

The saturation mobilities from 8 devices are compiled in Table II. The mean value for devices with embedded particles is  $1.2 \times 10^{-4} \text{ cm}^2/(\text{V s})$  compared to  $1.1 \times 10^{-4} \text{ cm}^2/(\text{V s})$  for devices without the embedded particles. The two results lie within the range of uncertainty, indicating that the particles do not notably affect the field-effect mobility of the device. Since the charge transport in OFETs occurs near the interface between the semiconductor and the gate dielectric, where the particles are also positioned, we expect that the particles would influence the FET performance. However, this is not observed. This could be due to the fact that the particles only occupy  $\sim 3\%$  of the channel area and that a noticeable change in performance would only be visible if a larger fraction of the channel area was covered.

In conclusion, we have found that the NaT3 thin film unit cell differs significantly from the one reported for the bulk, with a decreased long range order and only two molecules per unit cell. When E-beam deposited silver particles are embedded in the OFET device structure, there is no further change in the NaT3 unit cell or apparent crystal sizes. The measured field-effect mobility in the saturated regime averaged as  $1.2 \times 10^{-4} \text{ cm}^2/(\text{V s})$  for OFETs with the particles compared to  $1.1 \times 10^{-4} \text{ cm}^2/(\text{V s})$  for devices without

particles. These results form a structural base for designing field-effect transistors with aryl end-capped oligothiophenes.

The authors thank A. Osadnik and A. Lützen of Univ. Bonn for providing NaT3, O. Bikondoa of ESRF and M. Schwartzkopf of Petra III for experimental assistance, M. Torkkeli of Technical Univ. Denmark and M. J. Winokur of Univ. Wisconsin-Madison for discussions, and DANSCATT for financial support.

- <sup>1</sup>H. Sirringhaus, *Adv. Mater.* **26**, 1319 (2014).
- <sup>2</sup>C. Zhang, P. Chen, and W. Hu, *Chem. Soc. Rev.* **44**, 2087 (2015).
- <sup>3</sup>Y. Zang, F. Zhang, D. Huang, X. Gao, C. Di, and D. Zhu, *Nat. Commun.* **6**, 6269 (2015).
- <sup>4</sup>K.-J. Baeg, M. Binda, D. Natali, M. Caironi, and Y.-Y. Noh, *Adv. Mater.* **25**, 4267 (2013).
- <sup>5</sup>A. N. Aleshin, J. Y. Lee, S. W. Chu, J. S. Kim, and Y. W. Park, *Appl. Phys. Lett.* **84**, 5383 (2004).
- <sup>6</sup>H. Tian, Y. Chen, W. Li, D. Yan, Y. Geng, and F. Wang, *Org. Electron.* **15**, 1088 (2014).
- <sup>7</sup>M. K. Huss-Hansen, A. E. Lauritzen, O. Bikondoa, M. Torkkeli, L. Tavares, M. Knaapila, and J. Kjelstrup-Hansen, *Org. Electron.* **49**, 375 (2017).
- <sup>8</sup>H. Tian, J. Shi, B. He, N. Hu, S. Dong, D. Yan, J. Zhang, Y. Geng, and F. Wang, *Adv. Funct. Mater.* **17**, 1940 (2007).
- <sup>9</sup>F. Balzer, M. Schiek, A. Osadnik, I. Wallmann, J. Parisi, H.-G. Rubahn, and A. Lützen, *Phys. Chem. Chem. Phys.* **16**, 5747 (2014).
- <sup>10</sup>J. Linnet, A. R. Walther, O. Albrektsen, L. Tavares, R. L. Eriksen, P. B. W. Jensen, A. Osadnik, S. Hassing, A. Lützen, and J. Kjelstrup-Hansen, *Org. Electron.* **46**, 270 (2017).
- <sup>11</sup>A. D. Carlo, F. Piacenza, A. Bolognesi, B. Stadlober, and H. Maresch, *Appl. Phys. Lett.* **86**, 263501 (2005).
- <sup>12</sup>A. E. Lauritzen, M. Torkkeli, O. Bikondoa, J. Linnet, L. Tavares, J. Kjelstrup-Hansen, and M. Knaapila, *Langmuir* **34**, 6727 (2018).
- <sup>13</sup>X. Liu, L. Tavares, A. Osadnik, J. L. Lausen, J. Kongsted, A. Lützen, H.-G. Rubahn, and J. Kjelstrup-Hansen, *Org. Electron.* **15**, 1273 (2014).
- <sup>14</sup>D. M. DeLongchamp, R. J. Kline, D. A. Fischer, L. J. Richter, and M. F. Toney, *Adv. Mater.* **23**, 319 (2010).
- <sup>15</sup>H. Yoshida, K. Inaba, and N. Sato, *Appl. Phys. Lett.* **90**, 181930 (2007).
- <sup>16</sup>J.-H. Kim, Y.-N. Kwon, E. Lee, J. Y. Jung, J.-Y. Kim, J. Shin, J.-I. Park, and A. Choi, *Appl. Phys. Lett.* **111**, 233301 (2017).
- <sup>17</sup>M. Ruderer, V. Körstgens, E. Metwalli, M. Al-Hussein, U. Vainio, S. Roth, R. Döhrmann, R. Gehrke, R. Gebhardt, M. Burghammer, and P. Müller-Buschbaum, *Nucl. Instrum. Methods Phys. Res., Sect. B* **268**, 403 (2010).
- <sup>18</sup>N. Stribeck and U. Nöchel, *J. Appl. Crystallogr.* **42**, 295 (2009).
- <sup>19</sup>D. Babonneau, *J. Appl. Crystallogr.* **43**, 929 (2010).
- <sup>20</sup>D.-M. Smilgies, *J. Appl. Crystallogr.* **42**, 1030 (2009).
- <sup>21</sup>J. J. Mortensen, L. B. Hansen, and K. W. Jacobsen, *Phys. Rev. B* **71**, 035109 (2005).
- <sup>22</sup>J. Wellendorff, K. T. Lundgaard, A. Møgelhøj, V. Petzold, D. D. Landis, J. K. Nørskov, T. Bliigaard, and K. W. Jacobsen, *Phys. Rev. B* **85**, 235149 (2012).
- <sup>23</sup>T. K. An, S. H. Jang, S.-O. Kim, J. Jang, J. Hwang, H. Cha, Y. R. Noh, S. B. Yoon, Y. J. Yoon, L. H. Kim, D. S. Chung, S.-K. Kwon, Y.-H. Kim, S.-G. Lee, and C. E. Park, *Chem. Eur. J.* **19**, 14052 (2013).

## Paper II

---

Reprinted with permission from Ref. [99]. Copyright 2020 American Chemical Society.

In the second paper, we turn our attention towards NaT2 and investigate the growth of the molecule on monolayer graphene films. Graphene has shown promising potential as a transparent electrode material in OPVs [233], and can be used as a templating material for controlling the molecular orientation during growth (see e.g. Ref. [108]). This paper is the culmination of joint experimental work with the group of Peter Siffalovic at the Slovak Academy of Sciences.

# Surface-Controlled Crystal Alignment of Naphthyl End-Capped Oligothiophene on Graphene: Thin-Film Growth Studied by in Situ X-ray Diffraction

Mathias K. Huss-Hansen,\* Martin Hodas, Nada Mrkyvkova, Jakub Hagara, Bjarke B. E. Jensen, Andreas Osadnik, Arne Lützen, Eva Majková, Peter Siffalovic, Frank Schreiber, Luciana Tavares, Jakob Kjelstrup-Hansen, and Matti Knaapila



Cite This: *Langmuir* 2020, 36, 1898–1906



Read Online

ACCESS |



Metrics & More

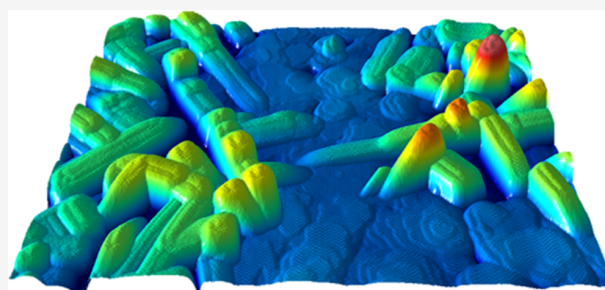


Article Recommendations



Supporting Information

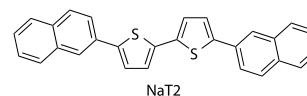
**ABSTRACT:** We report on the microstructure, morphology, and growth of 5,5'-bis(naphth-2-yl)-2,2'-bithiophene (NaT2) thin films deposited on graphene, characterized by grazing incidence X-ray diffraction (GIXRD) and complemented by atomic force microscopy (AFM) measurements. NaT2 is deposited on two types of graphene surfaces: custom-made samples where chemical vapor deposition (CVD)-grown graphene layers are transferred onto a Si/SiO<sub>2</sub> substrate by us and common commercially transferred CVD graphene on Si/SiO<sub>2</sub>. Pristine Si/SiO<sub>2</sub> substrates are used as a reference. The NaT2 crystal structure and orientation depend strongly on the underlying surface, with the molecules predominantly lying down on the graphene surface (face-on orientation) and standing nearly out-of-plane (edge-on orientation) on the Si/SiO<sub>2</sub> reference surface. Post growth GIXRD and AFM measurements reveal that the crystalline structure and grain morphology differ depending on whether there is polymer residue left on the graphene surface. In situ GIXRD measurements show that the thickness dependence of the intensity of the (111) reflection from the crystalline edge-on phase does not intersect zero at the beginning of the deposition process, suggesting that an initial wetting layer, corresponding to 1–2 molecular layers, is formed at the surface–film interface. By contrast, the (111) reflection intensity from the crystalline face-on phase grows at a constant rate as a function of film thickness during the entire deposition.



## INTRODUCTION

Organic semiconductors attract great interest for use in organic electronics, including organic field-effect transistors (OFETs),<sup>1,2</sup> organic photovoltaics (OPVs),<sup>3,4</sup> and various chemo- and biosensors<sup>5–8</sup> and mechanical sensors.<sup>9</sup> Much of this application potential, as well as fundamental interest, stems from the facile tuning of their electronic and spectral properties. These optoelectronic properties are directly related to the structure and morphology in a thin-film environment, including intermolecular packing, molecular orientation, and molecular–surface interactions.<sup>10–13</sup> Among organic semiconductors, oligothiophenes form one of the most important and extensively studied material families.<sup>11,14–18</sup> As a prime example, Geng et al. introduced a family of symmetric naphthyl end-capped oligothiophenes with high crystallinity and stability.<sup>19</sup> The end-capping of the thiophene rings with aryl groups hinders polymerization and promotes intermolecular packing. We have recently started to focus on the most symmetric variant of these materials, 5,5'-bis(naphth-2-yl)-2,2'-bithiophene (NaT2, Scheme 1), and investigated the relation between structure and OFET environment and

## Scheme 1. Chemical Structure of NaT2



confirmed the stability hypotheses of Geng and co-workers by X-ray investigations of NaT2 OFETs in operando.<sup>20</sup> At the same time, Balzer et al.<sup>21</sup> have found how NaT2 forms an extraordinary fiberlike surface morphology on muscovite mica, presumably originating from the anisotropy of the muscovite surface. These findings make NaT2 an intriguing new candidate when turning to the fundamentals of surface-controlled crystal growth.

Graphene and other two-dimensional (2D) materials have attracted immense attention owing to their unique mechanical

Received: November 6, 2019

Revised: February 6, 2020

Published: February 6, 2020

and electronic properties.<sup>22–24</sup> The use of graphene as a transparent electrode material in combination with organic semiconductors has significant potential in OFETs, OPVs, and elsewhere.<sup>25–27</sup> As most organic semiconductors are  $\pi$ -conjugated molecules by nature, they are able to interact with the surface of the graphene through  $\pi$ - $\pi$  and CH- $\pi$  interactions. Numerous studies using graphene or other 2D materials as templates for molecular growth of small organic molecules have been reported.<sup>14,15,27–34</sup> A common trend found in these studies is that the organic molecules, which can commonly be thought of as small rigid rods, tend to adopt a face-on (or “lying down”) orientation on graphene, with the molecular backbone oriented parallel to the surface. Being able to manipulate the orientation of the highly anisotropic semiconductor molecules allows for better control of the vertical charge transport and light absorption when designing new devices, especially for OPVs.

A number of studies have shown that the quality of the graphene film, which is typically grown by chemical vapor deposition (CVD) on a metallic foil and subsequently transferred onto the device substrate,<sup>16</sup> has a large influence on the growth behavior of the deposited molecules.<sup>27,29,35,36</sup> In particular, the presence of residual materials from the transfer process, e.g., poly(methyl methacrylate) (PMMA), can lead to growth of molecular phases with different, and often undesirable, orientation. This means a careful study cannot rely on one type of graphene surface but several alternatives should be investigated.

Real-time investigations of small molecule growth, where the measured data is collected in situ during the thin-film deposition, is an increasingly popular strategy when studying growth behavior. These include real-time studies using atomic force microscopy (AFM)/low energy electron microscopy (LEEM)<sup>37</sup> and optical spectroscopy.<sup>38</sup> In situ grazing incidence X-ray diffraction (GIXRD) combines real-time measurements during the thin-film deposition with a commonly employed structural characterization technique for organic molecules.<sup>39–42</sup> Several studies on conjugated oligomers using in situ GIXRD have been reported.<sup>43–50</sup> The real-time nature of these experiments allows for detection of transient structural phases and orientational transitions during the film formation, which would otherwise be impossible to detect by studying the film post growth.

In this paper, we investigate the structural evolution and crystal orientation of NaT2 deposited on monolayer (ML) graphene films employing in situ real-time GIXRD measurements complemented by steady-state GIXRD and AFM measurements. Two representative graphene-covered substrate types are used for the depositions: custom-made samples where CVD-grown graphene layers are transferred onto a Si/SiO<sub>2</sub> substrate by us and common commercially transferred CVD graphene on Si/SiO<sub>2</sub>. Pristine SiO<sub>2</sub> substrates are used as a reference. We find that the orientation of the NaT2 molecules is highly sensitive to the nature of the substrate (graphene vs SiO<sub>2</sub>) and to the quality of the graphene surface (polymer residue vs no polymer residue) and that the emerging crystalline phases exhibit different growth behavior during the early stages of deposition. These findings provide new insight into fundamental growth processes, which are at the same time crucial to control the supramolecular orientation of naphthyl end-capped oligothiophenes on 2D template materials for application.

## ■ EXPERIMENTAL SECTION

**Materials.** Scheme 1 shows the chemical structure of the NaT2 molecules used in this study. They were synthesized following the Suzuki cross-coupling protocols reported in the literature.<sup>21</sup>

**Substrate Fabrication.** Two types of graphene surfaces were employed in this study prepared in a similar manner.

Type I: SiO<sub>2</sub>/Si substrates with CVD graphene were prepared according to the standard procedure.<sup>51</sup> In short, CVD graphene on Cu, purchased from Graphenea S.A. (Monolayer Graphene on Cu), was spin-coated with a homemade solution of PMMA dissolved in anisole. After a short baking step, electrochemical delamination proceeded to separate the PMMA-supported graphene from Cu. The graphene/PMMA was then transferred to a silicon substrate with 90 nm SiO<sub>2</sub>, and a final baking step was performed to remove water remnants and to increase the adhesion between graphene and SiO<sub>2</sub>. Last, the PMMA was removed by placing the substrate in hot acetone for a couple of hours.

Type II: Common commercial CVD graphene on SiO<sub>2</sub>/Si substrates were purchased from Graphenea S.A. (Monolayer Graphene on SiO<sub>2</sub>/Si 90 nm) and used as is. According to the manufacturer,<sup>52</sup> CVD graphene is transferred from Cu to SiO<sub>2</sub>/Si by a wet transfer process. The graphene is protected with a sacrificial PMMA layer, and a ferric chloride solution is used for Cu etching. After the etching process, graphene is washed and transferred onto the SiO<sub>2</sub>/Si substrate. The PMMA layer is then thermally treated at 150 °C for 10 h in inert atmosphere and subsequently removed by submerging in acetone for 30 min and isopropyl alcohol for 30 min.

**Substrate Characterization.** The surface energies of the substrates were estimated from contact angle measurements of three test liquids: water, diiodomethane, and ethylene glycol (thioglycol in the case of pristine SiO<sub>2</sub>). Contact angles were measured using an automated liquid dispenser and a digital camera and averaged from at least three measurements per test liquid. The surface energies were then evaluated by linear regression (shown in Figure S1 in the Supporting Information) using the Owens–Wendt–Rabel–Kaelble (OWRK) model incorporated in Young’s equation, yielding

$$\frac{\sigma_l(1 + \cos \theta)}{2\sqrt{\sigma_l^d}} = \sqrt{\sigma_s^p} \sqrt{\frac{\sigma_l^p}{\sigma_l^d}} + \sqrt{\sigma_s^d} \quad (1)$$

where  $\theta$  is the contact angle,  $\sigma_l$  is the surface tension of the test liquid, and  $\sigma_s^p$ ,  $\sigma_s^d$ ,  $\sigma_l^p$ , and  $\sigma_l^d$  are the polar and dispersive components of the surface energies of solid and liquid.

The Helium-ion microscope (HIM) images were recorded with a Zeiss Nanofab instrument operated at an imaging voltage of 25 kV, a beam current of 0.1 pA, and no charge compensation. An Everhart–Thornley detector was used to acquire the secondary electron signal.

**NaT2 Thin-Film Deposition.** The NaT2 thin film was deposited atop the employed substrates by vacuum sublimation. The base vacuum pressure was below  $3 \times 10^{-8}$  mbar. The custom-made deposition chamber is equipped with a 360° cylindrical X-ray beryllium window,<sup>53</sup> allowing the incoming and outgoing X-rays to penetrate for simultaneous GIXRD measurements (vide infra). Prior to deposition, the graphene substrates were annealed at 300 °C. The substrate temperature was kept at 50 °C during deposition. The typical deposition rate was 0.03 Å s<sup>-1</sup>, and the deposition was controlled by a mechanical shutter.

**UV–vis Absorption Measurements.** NaT2 was deposited atop two BK7 glass substrates in a similar manner to what is described above with a nominal film thickness of 51 nm. One substrate had a monolayer of graphene transferred according to the same procedure as described above. The absorption spectra were measured using a Shimadzu UV-2700 spectrometer in the UV–vis spectrum. The spectrometer used an integrating sphere add-on to measure absorption. The absorption curve of graphene was measured separately and has been subtracted from the NaT2 on graphene absorption curve.

Table 1. Surface Energy of Substrates<sup>a</sup>

substrate	contact angle (deg)				$\sigma_s^p$ (mJ m <sup>-2</sup> )	$\sigma_s^d$ (mJ m <sup>-2</sup> )	$\sigma_s$ (mJ m <sup>-2</sup> )
	water	diiodomethane	ethylene glycol	thioglycol <sup>b</sup>			
type I graphene	82.3 ± 0.9	38.3 ± 1.0	50.4 ± 1.1		2.19	38.1	40.3
type II graphene	83.4 ± 1.5	36.5 ± 1.3	54.1 ± 1.1		1.60	39.0	40.6
SiO <sub>2</sub>	36.3 ± 0.2	46.4 ± 0.1		46.4 ± 0.9	39.9	17.3	57.2

<sup>a</sup> $\sigma_s$ ,  $\sigma_s^p$ , and  $\sigma_s^d$  are the total surface energy and its polar and dispersive components. <sup>b</sup>Due to almost perfect wetting of ethylene glycol on SiO<sub>2</sub>, thioglycol was used instead.

**Characterization of Final NaT2 Thin Films.** The final thin films were characterized by AFM (Dimension 3100, Veeco) operated in tapping mode. The AFM images were subsequently flattened and analyzed using the SPIP software package from Image Metrology.

Post growth 2D GIXRD measurements were performed using a custom-designed laboratory X-ray scattering setup (Nanostar, Bruker AXS) equipped with a liquid-metal jet anode X-ray source (MetalJet D2+, Excillum). The X-ray energy was 9.25 keV (Ga K $\alpha$  line), and the angle of incidence was 0.18°. In this configuration, the X-ray footprint spans across the entire sample. The scattering patterns were collected within hours of the deposition using an imaging plate detector with an exposure time of 30 min. The GIXRD patterns are invariant to azimuthal rotation of the sample due to the polycrystalline nature of the CVD transferred graphene; i.e., some amount of the NaT2 crystallites will always be in the Bragg condition due to the random in-plane orientation of the individual graphene domains.

**Real-Time Characterization of NaT2 Thin Films during Deposition.** In situ GIXRD measurements were performed during the deposition process using the same setup as in the post growth experiments but with a two-dimensional hybrid pixel detector (Pilatus 300, Dectris) used to collect the 2D images. The sample-to-detector distance was calibrated to 219.4 mm, and the exposure time was 3 min per image. A custom-made beamstop was placed directly after the exit window of the deposition chamber to minimize air scattering from the primary beam. The data was processed using a combination of GIXSGUI<sup>54</sup> and self-programmed MATLAB scripts. To obtain a sufficient peak-to-background ratio for the peak fitting procedure, the GIXRD images were grouped in time. The diffracted intensity profiles were fitted with a Gaussian function after texture- and solid-angle corrections and background subtraction. Consequently, the low-thickness range at the beginning of the deposition process is inaccessible due to the low diffraction intensity of the Bragg reflections and insufficient peak-to-background ratio. Nevertheless, the relatively high crystallinity of the NaT2 thin film allowed for tracking of all three phases in real time. The intensity of the diffraction spot is proportional to the number of crystallites in the Bragg condition if we assume that the typical separation of the diffracting crystallites is much larger than the transverse coherence length of the laboratory X-ray source.<sup>55</sup>

## RESULTS AND DISCUSSION

**Substrates.** Table 1 lists surface energies of the employed substrates. The data shows that the surface energy of the graphene-covered substrates is significantly lowered by the addition of graphene when compared with pristine SiO<sub>2</sub>. There are no significant differences in the surface energies between the type I and type II surfaces, as can be seen by the fact that both are several times less polar than pristine SiO<sub>2</sub> but show twice as much possibility to undergo dispersive (van der Waals type) interactions based on the measured dispersive component of the surface energies.

To further characterize the substrate surface, helium-ion microscopy (HIM) was employed. Figure 1 shows HIM images of the type I graphene-covered substrate (Figure 1a) and the type II graphene-covered substrate (Figure 1b). The HIM images indicate that both the type I and type II graphene films display a high degree of surface coverage with some

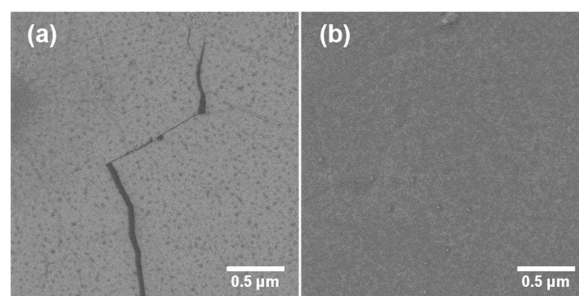
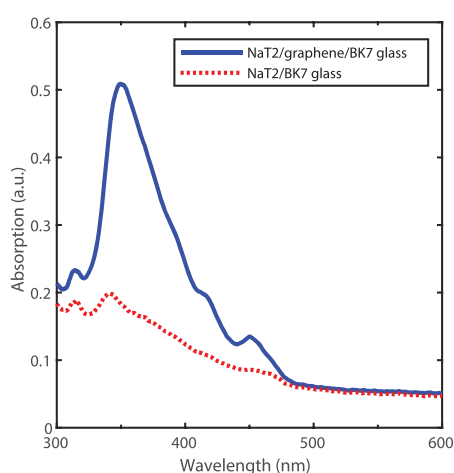


Figure 1. HIM images of the graphene surfaces. (a) Type I graphene. (b) Type II graphene.

cracks, which appear darker on the HIM image. On the type I graphene, there are several dark spots (Figure 1a) speckled throughout. Identical features can be seen on AFM topographies of the surface (see the Supporting Information, Figure S2a,b), and we attribute this to leftover PMMA residue from the graphene transfer process, since the features shown are similar to the ones observed in the literature.<sup>56</sup> By comparison, the type II graphene does not exhibit similar surface imperfections (Figure 1b). The typical surface roughness of the graphene, as measured by AFM, is tabulated in Table S1 (see Supporting Information). The typical surface roughness of the type I graphene surface is approximately 3 times higher than that of the type II graphene surface, suggesting that the residual PMMA is lying on top the otherwise flat graphene.

**Photophysical Properties.** Figure 2 shows the UV–vis absorption spectra of the as-prepared NaT2 films with and without a monolayer (ML) graphene film. It is immediately apparent that the absorption of the NaT2 film on graphene is much higher than its counterpart, with an approximate increase of 250% in absorption at the absorption peak. The absorption peak of the NaT2 film without graphene has a maximum at 340 nm, which is consistent with previous literature reports,<sup>19</sup> and corresponds to the  $\pi$ – $\pi^*$  transition. By contrast, the NaT2 film on graphene is slightly red-shifted, with an absorption maximum at 350 nm and two shoulders at 416 and 450 nm. The two shoulders are also present in the absorption spectrum of the NaT2 film without graphene, as shown by the normalized absorption curves in Figure S3 (Supporting Information). The increase in absorption from the NaT2 film on graphene hints at a preferential orientation of the molecules along the graphene substrate, since the absorption transition dipole of NaT2 lies in the direction parallel to the long molecular axis along the backbone, which is often the case for conjugated oligomers.<sup>57</sup> We propose that the minor spectral changes occur because the incoming light couple with different strengths to the different transitions depending on whether the molecules are oriented face-on or edge-on,



**Figure 2.** Absorption spectra of NaT2 (nominal thickness = 51 nm) on monolayer graphene (transferred to BK7 glass substrate) and on the BK7 glass substrate. The absorption spectrum from monolayer graphene transferred to BK7 glass was measured separately and subtracted from the NaT2/graphene/BK7 glass spectrum.

similar to the polarization-dependent absorption observed in other organic crystals.<sup>58</sup>

**Postgrowth Thin Film.** Figure 3a,b shows AFM topographies and corresponding characteristic cross-sectional

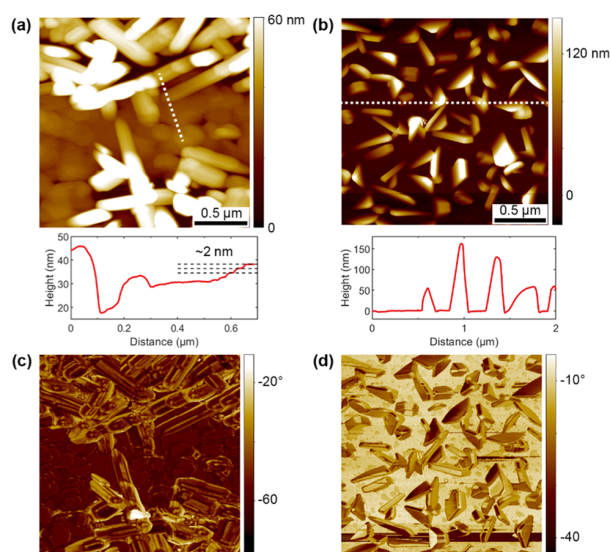


**Figure 3.** AFM images of the final NaT2 thin films grown on graphene films. (a, b) AFM topographies of the films deposited on type I and type II graphene, respectively, with corresponding characteristic cross-sectional height profiles. (c, d) AFM phase images corresponding to the topographies above.

height profiles of the final NaT2 thin films after deposition on the two types of graphene. NaT2 grown on type I graphene exhibits two distinct grain morphologies, as evidenced by the topographic map in Figure 3a: islandlike flat formations with distinct terraces (middle right and bottom left of Figure 3a) and needlelike structures (top and bottom of Figure 3a). Flat-island formations are also observed for NaT2 grown on SiO<sub>2</sub> (Figure S4) and self-assembled monolayers (SAMs) of octadecyltrichlorosilane (OTS),<sup>59</sup> and generally correspond

to standing molecules with near upright orientation (i.e., edge-on) for small rodlike molecules. The cross-sectional height profile furthermore reveals that the terrace step height corresponds almost exactly to the length of one molecule ( $\sim 2$  nm). The needlelike structures, also referred to as nanofibers, have widths in the hundred-nanometer range and are several tens of nanometers tall. The fibers appear to locally grow in well-defined directions with 6-fold symmetry as illustrated by the Fourier transformation of the phase image (Figure S5 in the Supporting Information), which might correspond to the 6-fold symmetry of the underlying graphene domain. Such nanofiber structures have previously been observed for NaT2 grown on muscovite mica sheets<sup>21</sup> and for other conjugated oligomers, including pentacene grown on thermally treated graphene,<sup>27,47</sup> and are also known for conjugated polymers like polyfluorenes.<sup>60</sup> The corresponding AFM phase image (Figure 3c) likewise shows a difference in phase contrast between the nanofibers and the flat-island formations. A phase contrast also exists between the center and edge of the terraced islands highlighting the individual steps.

In contrast, NaT2 film grown on type II graphene (Figure 3b) exhibits a morphology of faceted crystalline grains with extremely well-defined growth direction and sharp edges. The visually apparent grains range from 50 to 150 nm in height and display relatively incomplete surface coverage. The corresponding AFM phase image (Figure 3d) shows a phase contrast between the different edges of the faceted crystals as well as a phase contrast between the crystal phases and the underlying substrate. The phase contrast together with the sharp edges of the topography map suggests that NaT2 forms large “single crystal-like” crystal grains atop the type II graphene with well-defined crystal facets.

Figure 4 shows two-dimensional GIXRD patterns of the final NaT2 films. NaT2 film grown on type I graphene (Figure 4a) displays intense (100) reflections (originating from the molecular long axis) along the out-of-plane  $q_z$  direction, indicating that a large proportion of the molecules adopts an edge-on orientation with the ( $h00$ ) plane vectors directed parallel to the surface normal. The true ( $h00$ ) reflections are in principle forbidden in grazing incidence geometry but are nevertheless observed due to the orientation distribution of crystallites around the true ( $h00$ ) axis. In addition, several reflections from the edge-on phase are present at higher values of  $q_{xy}$ , indicating that the NaT2 molecules adopt a multilayer structure with a high degree of alignment in plane as well as out of plane. The unit cell choice with mosaic (100)-texture and  $a$  as the molecular long axis follows the notation described elsewhere.<sup>20</sup> The reflections from the observed edge-on phase correspond closely to the molecular packing previously reported for NaT2 thin film on SiO<sub>2</sub> ( $a = 20.31$  Å,  $b = 6.00$ ,  $c = 8.17$ , and  $\beta = 96.64^\circ$ ).<sup>20</sup>

Moreover, NaT2 film grown on type I graphene shows (100) reflections that are azimuthally inclined at  $27^\circ$  with respect to  $q_{xy}$  indicating that some of the molecules adopt face-on orientation, with the molecular long axis directed mostly along the substrate surface (Figure 4c). Two highly visible (111) reflections found equidistant from the primary beam are angled 18 and  $49^\circ$  from  $q_z$ , respectively, suggesting the existence of two different crystalline phases with face-on orientation. Using these reflections together with the (102) reflections, that are azimuthally rotated 45 and  $-13^\circ$  from the (111) reflections, we can determine the tilt of the  $b$ -axis with respect to the surface. The primary face-on phase (i.e., the

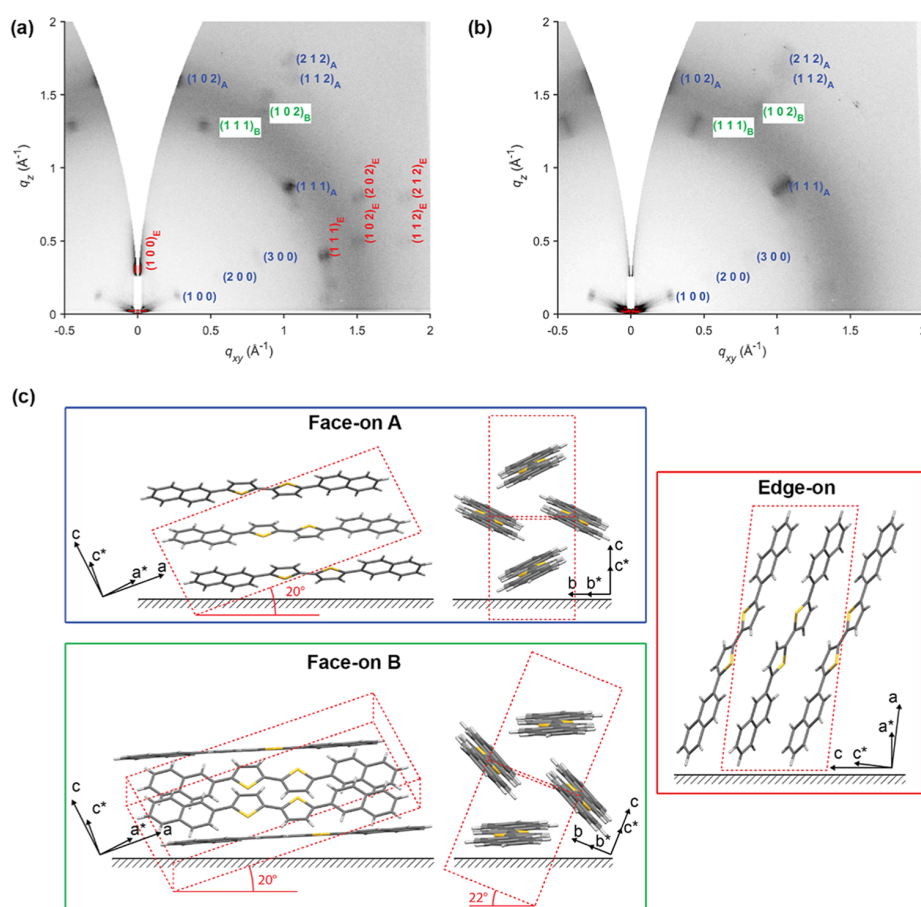


**Figure 4.** (a, b) GIXRD patterns of NaT2 thin films deposited on type I and type II graphene substrates, respectively. (c) Proposed arrangements of NaT2 molecules with face-on and edge-on orientation. For all schematics, the view is taken to be parallel to the substrate plane. The right view in the two face-on schematics is rotated by  $90^\circ$  to illustrate the difference in the tilt of the  $b$ -axis (corresponding to a view along the molecular backbone). The direct- and reciprocal lattice vectors are shown in the bottom corner, and the unit cell is marked by the dotted lines. The border colors correspond to the color of the reflection indices in (a) and (b).

phase with the brightest (111) reflection spot), denoted “A” from now on, corresponds to the case where the  $b$ -axis is parallel to the substrate surface. Conversely, the secondary face-on phase (“B”) has the  $b$ -axis tilted  $22^\circ$  from the surface. The reflections from both phases are successfully indexed (see Figure S6 in the Supporting Information) with the same lattice parameters as those in the edge-on phase, indicating that the three phases are identical except for their orientation with respect to the substrate surface.

Figure 4c summarizes the proposed packing schemes for all three phases. Here, we have assumed that the packing of the molecules inside the unit cell is identical to what is reported for single crystalline NaT2. Due to the herringbone packing of the NaT2 molecules, a face-on orientation of the unit cell implies that either both molecules are oriented with a small tilt between the molecular short-edge and the surface (which is the case for the face-on A phase) or that half the molecules adopt a near flat orientation while the other half are significantly inclined toward the surface normal (as indicated by the face-on B phase). The isotropic halo observed at  $q = 1.5 \text{ \AA}^{-1}$  can be attributed to scattering from the underlying amorphous  $\text{SiO}_2$ , since the choice of the incidence angle is slightly above the critical angle of  $\text{SiO}_2$  to maximize the film peak intensities.

The NaT2 thin film grown on type II graphene (Figure 4b) does not display clear ( $h00$ ) crystalline reflections along the  $q_z$  direction nor does it display any off-axis peaks attributed to the edge-on phase, indicating that a few or none of the molecules adopt edge-on orientation on type II graphene. Only reflections from the two phases with molecular face-on orientation are clearly present.

The differences in NaT2 thin-film structure on the two types of graphene surfaces are attributed to residual PMMA left over from the graphene transfer process present on the type I graphene. This is likely because the polymer acts as a template for growth of crystals with molecules adopting edge-on orientation, or because the nucleation of the edge-on oriented crystal phase is facilitated by the increased surface roughness on the type I graphene, or due to a combination of both. The latter scenario agrees with the literature where rough surfaces are known to accelerate heterogeneous nucleation by lowering the nucleation barrier height.<sup>61</sup> In areas with no PMMA residue on the type I graphene, the strong interactions between the  $\pi$ -electrons and graphene facilitate the growth of NaT2 crystals with the molecules oriented face-on and we observe nanofiber morphology. Likewise, on type II graphene with no PMMA residue, the graphene–NaT2 interactions dominate and only crystals phases with face-on orientation of the

molecules are observed. These results indicate that the supramolecular orientation of the NaT2 thin-films deposited on graphene can vary significantly depending on the amount of residual PMMA left on the graphene film.

### In Situ GIXRD Measurements during Deposition.

During the deposition of the samples, in situ GIXRD measurements were performed to monitor the growth of competing crystalline phases. Figure 5 evaluates (111)

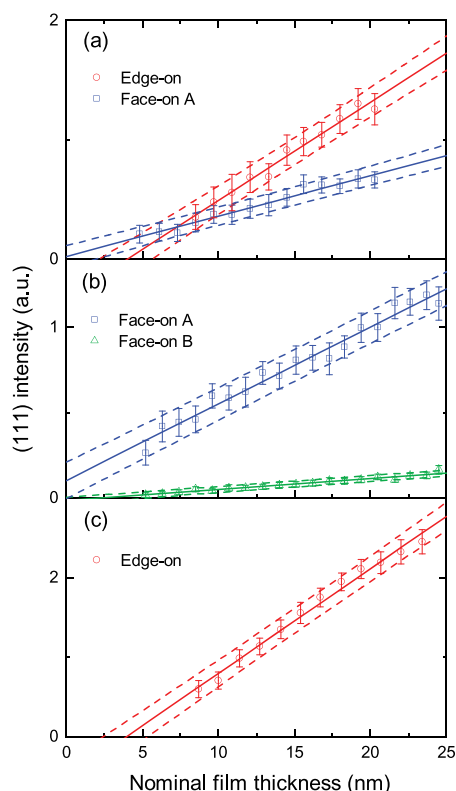


**Figure 5.** Integrated intensity of the (111) reflection as a function of nominal film thickness. (a) NaT2 deposited on type I graphene. (b) NaT2 deposited on type II graphene. (c) NaT2 deposited on 90 nm SiO<sub>2</sub>. The solid lines are linear fits to the data, and the dashed lines indicate the corresponding 95% confidence intervals.

reflection intensity for the three phases identified by postgrowth characterization. Figure 5a shows the evolution of the integrated (111) reflection intensity for the deposition of NaT2 on type I graphene substrate. The growth of the crystalline face-on A phase is evidently linear during the deposition. The fitted slope intersects zero at the start of the deposition, suggesting that the volume of the face-on A phase grows linearly immediately upon opening the deposition shutter. The same tendency is observed for the crystalline face-on A phase grown on type II graphene (Figure 5b), where the linear fit to the (111) reflection similarly passes through zero at the onset of the deposition (within the given confidence interval). Likewise, the NaT2 face-on B phase displays a linear growth of the (111) reflection on both types of graphene. The integrated (111) reflection intensity of the NaT2 face-on B phase on type I graphene is shown in Figure S7 in the Supporting Information. In contrast, although the (111) reflection intensity pertaining to the crystalline edge-on phase shows linear growth on type I graphene (Figure 5a); the

corresponding linear fit does not cross zero at the beginning of the deposition (within the given confidence interval). Instead, the extrapolated (111) reflection intensity starts at approximately 4 nm nominal film thickness (corresponding to two molecular layers). A similar behavior is found for the NaT2 edge-on phase on SiO<sub>2</sub> (Figure 5c), suggesting that the initial nonlinear growth behavior is in part decoupled from the surface interaction and could be inherent to the formation of the edge-on phase. The evolution of the NaT2 edge-on (111) reflection intensity hints at changes from early stage (sub-ML) to later stage (several MLs) growth. The trend is mirrored by the strong (100) reflection; see Figure S8 in the Supporting Information.

The trends identified in Figure 5 provide the following scenarios. Following the growth of the two phases on type I graphene (Figure 5a), one could be inclined to infer that the edge-on phase grows on top of the face-on phase. In this scenario, the edge-on structure only starts to nucleate after a certain number of face-on layers have formed. This behavior has previously been observed for pentacene grown on another two-dimensional material, hexagonal boron nitride (h-BN).<sup>28</sup> However, this scenario does not account for the growth behavior of the edge-on phase on SiO<sub>2</sub> (Figure 5c) and it does not agree with the postgrowth morphology, where the two phases appear to be forming in separate areas (Figure 3a).

Another scenario is the formation of a transient structure during the early stages of deposition with an accompanying change in lattice parameters. Such transient structures have been observed in other small molecules<sup>11,43</sup> and are commonly attributed to substrate-induced strain effects. In this scenario, the position of the (111) reflection would change according to the lattice parameters of the transient structure during the deposition. Unfortunately, the signal-to-noise ratio is not sufficiently high during the early deposition stages and thus does not allow for detection of transient structures within the first few MLs. Previous postgrowth studies of thin-film NaT2 on SiO<sub>2</sub> using synchrotron radiation revealed a singular crystalline phase,<sup>20</sup> suggesting that if the molecular structure is indeed different within the first ML/few MLs, it is strictly a transient phase. The thin film is likely to undergo reordering after stopping the deposition,<sup>43</sup> and therefore the lifetime of any transient structure cannot reliably be determined from postgrowth measurements.

Assuming that the total volume of crystals is accounted for, the intensity of the (111) reflection after the deposition of several MLs would be identical whether the molecules had directly formed the resolved edge-on phase or had undergone a transformation from a transient phase. Therefore, the formation of a transient phase within the first few MLs alone cannot explain the growth behavior observed for the edge-on phase (Figure 5).

Instead, we propose that the nonlinear growth of the edge-on phase during the early stages of deposition is due to the formation of an initial wetting layer. In this scenario, the wetting layer might be fully or partially disordered or crystalline with a different crystal structure compared with the subsequent layers. In the case that the wetting layer forms partially or fully ordered crystals with a similar crystal structure as the rest of the film, the growth rate of the wetting layer is apparently slower than that for the subsequent layers. We speculate that several kinetic factors, such as interlayer transport or slower nucleation rate, might contribute to a slower initial growth rate of the wetting layer. We also note

that no wetting layer appears to form during the growth of the face-on phase on graphene since the curve extrapolates through zero intensity. The formation of a wetting layer at the film-surface interface for only certain crystal phases has previously been observed for chemically similar molecules.<sup>62</sup>

## CONCLUSIONS

The structure and crystalline orientation of NaT2 depend heavily on the underlying surface and surface quality. We find that the NaT2 crystallites stand out-of-plane on SiO<sub>2</sub> and predominantly lie down on the graphene surface, which is reflected by a 2.5 times higher photoabsorption in the latter case when measured along the surface normal. GIXRD measurements reveal three distinct crystal phases of NaT2 (two face-on phases and one edge-on phase) on the investigated custom-transferred graphene, while NaT2 films deposited on commercially transferred graphene show only the two face-on phases. AFM measurements show that the edge-on phase and the face-on phases grow with two distinct grain morphologies on the custom-transferred graphene (fiberlike and islandlike grains, respectively), while on commercially transferred graphene, NaT2 grows as faceted crystal grains. We attribute the difference in observed thin-film structure and morphology on the two types of graphene to residual PMMA left over from the transfer process, which is only found on custom-transferred graphene. In situ GIXRD measurements show how the intensity of (111) reflection grows linearly with time (at a constant deposition rate) for all three phases of NaT2. However, extrapolation of the data to the early stages of deposition (i.e., within the first few molecular layers) shows that the edge-on phase does not grow linearly from the onset. Instead, the extrapolated growth intersects zero intensity at a nominal thickness of ~4 nm (corresponding to 2 molecular layers), suggesting that an initial wetting layer is formed. In comparison, the (111) reflection intensity of both crystal phases with face-on orientation intersect zero at 0 nm nominal film thickness, indicating uninterrupted linear growth from the beginning of the deposition.

The surface-controlled crystal alignment demonstrated here provides an insight into the complex dynamics of small molecule growth for graphene-based electronic devices. This can be further expanded to studies of other molecules and surfaces, including raising the length of the thiophene rod up to the oligomer-polymer limit as shown elsewhere for oligopolyfluorenes.<sup>63,64</sup>

## ASSOCIATED CONTENT

### Supporting Information

The Supporting Information is available free of charge at <https://pubs.acs.org/doi/10.1021/acs.langmuir.9b03467>.

Linear regression lines against contact angle data (eq 1), additional AFM topographies, surface roughness data, normalized absorption spectra, Fourier transformation of the AFM phase image in Figure 3c, GIXRD peak indexation, and additional thickness-dependent GIXRD reflection intensity data (PDF)

## AUTHOR INFORMATION

### Corresponding Author

Mathias K. Huss-Hansen – Department of Physics, Technical University of Denmark, Kgs. Lyngby 2800, Denmark;

orcid.org/0000-0003-4487-508X; Email: mathias.huss-hansen@fysik.dtu.dk

## Authors

**Martin Hodas** – Institut für Angewandte Physik, Universität Tübingen, Tübingen 72076, Germany; orcid.org/0000-0001-6328-1717

**Nada Mrkyvkova** – Institute of Physics, Slovak Academy of Sciences, Bratislava 84511, Slovakia; Centre of Excellence for Advanced Materials Application, Bratislava 84511, Slovakia; orcid.org/0000-0002-2619-0872

**Jakub Hagara** – Institute of Physics, Slovak Academy of Sciences, Bratislava 84511, Slovakia; Centre of Excellence for Advanced Materials Application, Bratislava 84511, Slovakia

**Bjarke B. E. Jensen** – Newtec Engineering A/S, Odense M 5230, Denmark

**Andreas Osadnik** – Kekulé-Institute for Organic Chemistry and Biochemistry, University of Bonn, Bonn 53121, Germany

**Arne Lützen** – Kekulé-Institute for Organic Chemistry and Biochemistry, University of Bonn, Bonn 53121, Germany; orcid.org/0000-0003-4429-0823

**Eva Majkova** – Institute of Physics, Slovak Academy of Sciences, Bratislava 84511, Slovakia; Centre of Excellence for Advanced Materials Application, Bratislava 84511, Slovakia

**Peter Siffalovic** – Institute of Physics, Slovak Academy of Sciences, Bratislava 84511, Slovakia; Centre of Excellence for Advanced Materials Application, Bratislava 84511, Slovakia; orcid.org/0000-0002-9807-0810

**Frank Schreiber** – Institut für Angewandte Physik, Universität Tübingen, Tübingen 72076, Germany

**Luciana Tavares** – NanoSYD, Mads Clausen Institute, University of Southern Denmark, Sønderborg 6400, Denmark; orcid.org/0000-0002-1432-524X

**Jakob Kjelstrup-Hansen** – NanoSYD, Mads Clausen Institute, University of Southern Denmark, Sønderborg 6400, Denmark

**Matti Knaapila** – Department of Physics, Technical University of Denmark, Kgs. Lyngby 2800, Denmark; orcid.org/0000-0002-4114-9798

Complete contact information is available at: <https://pubs.acs.org/10.1021/acs.langmuir.9b03467>

## Notes

The authors declare no competing financial interest.

## ACKNOWLEDGMENTS

M.K.H.-H. acknowledges the COST Action CA15107 (Multi-Comp). M.H. acknowledges the financial support of Alexander von Humboldt Foundation. The authors also acknowledge the support of the APVV-17-0352 project, the DAAD/SAV grant, and the DFG agency.

## REFERENCES

- (1) Murphy, A. R.; Fréchet, J. M. J. Organic Semiconducting Oligomers for Use in Thin Film Transistors. *Chem. Rev.* **2007**, *107*, 1066–1096.
- (2) Sirringhaus, H. 25th Anniversary Article: Organic Field-Effect Transistors: The Path Beyond Amorphous Silicon. *Adv. Mater.* **2014**, *26*, 1319–1335.
- (3) McDowell, C.; Abdelsamie, M.; Toney, M. F.; Bazan, G. C. Solvent Additives: Key Morphology-Directing Agents for Solution-Processed Organic Solar Cells. *Adv. Mater.* **2018**, *30*, 1–30.
- (4) Coughlin, J. E.; Henson, Z. B.; Welch, G. C.; Bazan, G. C. Design and Synthesis of Molecular Donors for Solution-Processed

- High-Efficiency Organic Solar Cells. *Acc. Chem. Res.* **2014**, *47*, 257–270.
- (5) Evans, R. C.; Douglas, P. Design and Color Response of Colorimetric Multilumophore Oxygen Sensors. *ACS Appl. Mater. Interfaces* **2009**, *1*, 1023–1030.
- (6) Thomas, S. W.; Joly, G. D.; Swager, T. M. Chemical Sensors Based on Amplifying Fluorescent Conjugated Polymers. *Chem. Rev.* **2007**, *107*, 1339–1386.
- (7) Wu, J.; Liu, W.; Ge, J.; Zhang, H.; Wang, P. New Sensing Mechanisms for Design of Fluorescent Chemosensors Emerging in Recent Years. *Chem. Soc. Rev.* **2011**, *40*, 3483–3495.
- (8) Wang, B.; Queenan, B. N.; Wang, S.; Nilsson, K. P. R.; Bazan, G. C. Precisely Defined Conjugated Oligoelectrolytes for Biosensing and Therapeutics. *Adv. Mater.* **2019**, *31*, 1–21.
- (9) Cingil, H. E.; Boz, E. B.; Wang, J.; Stuart, M. A. C.; Sprakel, J. Probing Nanoscale Coassembly with Dual Mechanochromic Sensors. *Adv. Funct. Mater.* **2016**, *26*, 1420–1427.
- (10) Fichou, D. Structural Order in Conjugated Oligothiophenes and Its Implications on Opto-Electronic Devices. *J. Mater. Chem.* **2000**, *10*, 571–588.
- (11) Mannebach, E. M.; Cai, Z.; Himpsel, F. J.; Evans, P. G.; Spalanka, J. W.; Johnson, P. S. High Hole Mobility and Thickness-Dependent Crystal Structure in  $\alpha,\omega$ -Diethylhexylthiophene Single-Monolayer Field-Effect Transistors. *Adv. Funct. Mater.* **2012**, *23*, 554–564.
- (12) Jones, A. O. F.; Chattopadhyay, B.; Geerts, Y. H.; Resel, R. Substrate-Induced and Thin-Film Phases: Polymorphism of Organic Materials on Surfaces. *Adv. Funct. Mater.* **2016**, *26*, 2233–2255.
- (13) Knaapila, M. *Conjugated Polymers and Oligomers: Structural and Soft Matter Aspects*; World Scientific: Singapore, 2018.
- (14) Surin, M.; Leclère, P.; De Feyter, S.; Abdel-Mottaleb, M. M. S.; De Schryver, F. C.; Henze, O.; Feast, W. J.; Lazzaroni, R. Molecule - Molecule versus Molecule - Substrate Interactions in the Assembly of Oligothiophenes at Surfaces. *J. Phys. Chem. B* **2006**, *110*, 7898–7908.
- (15) Gus'kova, O. A.; Mena-Osteritz, E.; Schillinger, E.; Khalatur, P. G.; Bäuerle, P.; Khokhlov, A. R. Self-Assembled Monolayers of  $\beta$ -Alkylated Oligothiophenes on Graphite Substrate: Molecular Dynamics Simulation. *J. Phys. Chem. C* **2007**, *111*, 7165–7174.
- (16) Kim, K. S.; Zhao, Y.; Jang, H.; Lee, S. Y.; Kim, J. M.; Kim, K. S.; Ahn, J.-H.; Kim, P.; Choi, J.-Y.; Hong, B. H. Large-Scale Pattern Growth of Graphene Films for Stretchable Transparent Electrodes. *Nature* **2009**, *457*, 706–710.
- (17) Wang, J.; De Jeu, W. H.; Ziener, U.; Polinskaya, M. S.; Ponomarenko, S. A.; Ruecker, U.; Ruderer, M. A.; Herzig, E. M.; Müller-Buschbaum, P.; Moeller, M.; et al. Monolayer Properties of Asymmetrically Substituted Sexithiophene. *Langmuir* **2014**, *30*, 2752–2760.
- (18) De Jeu, W. H.; Rahimi, K.; Ziener, U.; Vill, R.; Herzig, E. M.; Müller-Buschbaum, P.; Möller, M.; Mourran, A. Substituted Septithiophenes with End Groups of Different Size: Packing and Frustration in Bulk and Thin Films. *Langmuir* **2016**, *32*, 1533–1541.
- (19) Tian, H.; Shi, J.; He, B.; Hu, N.; Dong, S.; Yan, D.; Zhang, J.; Geng, Y.; Wang, F. Naphthyl and Thionaphthyl End-Capped Oligothiophenes as Organic Semiconductors: Effect of Chain Length and End-Capping Groups. *Adv. Funct. Mater.* **2007**, *17*, 1940–1951.
- (20) Huss-Hansen, M. K.; Lauritzen, A. E.; Bikondoa, O.; Torkkeli, M.; Tavares, L.; Knaapila, M.; Kjelstrup-Hansen, J. Structural Stability of Naphthyl End-Capped Oligothiophenes in Organic Field-Effect Transistors Measured by Grazing-Incidence X-Ray Diffraction in Operando. *Org. Electron.* **2017**, *49*, 375–381.
- (21) Balzer, F.; Schiek, M.; Osadnik, A.; Wallmann, I.; Parisi, J.; Rubahn, H. G.; Lützen, A. Substrate Steered Crystallization of Naphthyl End-Capped Oligothiophenes into Nanofibers: The Influence of Methoxy-Functionalization. *Phys. Chem. Chem. Phys.* **2014**, *16*, 5747–5754.
- (22) Geim, A. K.; Novoselov, K. S. The Rise of Graphene. *Nat. Mater.* **2007**, *6*, 183–191.
- (23) Zhu, Y.; Murali, S.; Cai, W.; Li, X.; Suk, J. W.; Potts, J. R.; Ruoff, R. S. Graphene and Graphene Oxide: Synthesis, Properties, and Applications. *Adv. Mater.* **2010**, *22*, 3906–3924.
- (24) Lin, L.; Deng, B.; Sun, J.; Peng, H.; Liu, Z. Bridging the Gap between Reality and Ideal in Chemical Vapor Deposition Growth of Graphene. *Chem. Rev.* **2018**, *118*, 9281–9343.
- (25) Pang, S.; Hernandez, Y.; Feng, X.; Müllen, K. Graphene as Transparent Electrode Material for Organic Electronics. *Adv. Mater.* **2011**, *23*, 2779–2795.
- (26) Park, J.; Lee, W. H.; Huh, S.; Sim, S. H.; Kim, S.; Bin, Cho, K.; Hong, B. H.; Kim, K. S. Work-Function Engineering of Graphene Electrodes by Self-Assembled Monolayers for High-Performance Organic Field-Effect Transistors. *J. Phys. Chem. Lett.* **2011**, *2*, 841–845.
- (27) Lee, W. H.; Park, J.; Sim, S. H.; Lim, S.; Kim, K. S.; Hong, B. H.; Cho, K. Surface-Directed Molecular Assembly of Pentacene on Monolayer Graphene for High-Performance Organic Transistors. *J. Am. Chem. Soc.* **2011**, *133*, 4447–4454.
- (28) Park, B.; Kim, K.; Park, J.; Lim, H.; Lanh, P. T.; Jang, A.-R.; Hyun, C.; Myung, C. W.; Park, S.; Kim, J. W.; et al. Anomalous Ambipolar Transport of Organic Semiconducting Crystals via Control of Molecular Packing Structures. *ACS Appl. Mater. Interfaces* **2017**, *9*, 27839–27846.
- (29) Nguyen, N. N.; Jo, S. B.; Lee, S. K.; Sin, D. H.; Kang, B.; Kim, H. H.; Lee, H.; Cho, K. Atomically Thin Epitaxial Template for Organic Crystal Growth Using Graphene with Controlled Surface Wettability. *Nano Lett.* **2015**, *15*, 2474–2484.
- (30) Nguyen, N. N.; Lee, H. C.; Kang, B.; Jo, M.; Cho, K. Electric-Field-Tunable Growth of Organic Semiconductor Crystals on Graphene. *Nano Lett.* **2019**, *19*, 1758–1766.
- (31) Hlawacek, G.; Khokhar, F. S.; Van Gestel, R.; Poelsema, B.; Teichert, C. Smooth Growth of Organic Semiconductor Films on Graphene for High-Efficiency Electronics. *Nano Lett.* **2011**, *11*, 333–337.
- (32) Chen, W.; Huang, H.; Thye, A.; Wee, S. Molecular Orientation Transition of Organic Thin Films on Graphite: The Effect of Intermolecular Electrostatic and Interfacial Dispersion Forces. *Chem. Commun.* **2008**, *36*, 4276–4278.
- (33) Balzer, F.; Henrichsen, H. H.; Klarskov, M. B.; Booth, T. J.; Sun, R.; Parisi, J.; Schiek, M.; Bøggild, P. Directed Self-Assembled Crystalline Oligomer Domains on Graphene and Graphite. *Nanotechnology* **2014**, *25*, No. 035602.
- (34) Ha, T. J.; Akinwande, D.; Dodabalapur, A. Hybrid Graphene/Organic Semiconductor Field-Effect Transistors. *Appl. Phys. Lett.* **2012**, *101*, 99–102.
- (35) Chhikara, M.; Pavlica, E.; Matković, A.; Beltaos, A.; Gajić, R.; Bratina, G. Pentacene on Graphene: Differences between Single Layer and Bilayer. *Carbon* **2014**, *69*, 162–168.
- (36) Zhou, L.; Fox, L.; Wlodek, M.; Islas, L.; Slastanova, A.; Robles, E.; Bikondoa, O.; Harniman, R.; Fox, N.; Cattelan, M.; et al. Surface Structure of Few Layer Graphene. *Carbon* **2018**, *136*, 255–261.
- (37) Yoshikawa, G.; Sadowski, J. T.; Al-Mahboob, A.; Fujikawa, Y.; Sakurai, T.; Tsuruma, Y.; Ikeda, S.; Saiki, K. Spontaneous Aggregation of Pentacene Molecules and Its Influence on Field Effect Mobility. *Appl. Phys. Lett.* **2007**, *90*, No. 251906.
- (38) Heinemeyer, U.; Broch, K.; Hinderhofer, A.; Kytka, M.; Scholz, R.; Gerlach, A.; Schreiber, F. Real-Time Changes in the Optical Spectrum of Organic Semiconducting Films and Their Thickness Regimes during Growth. *Phys. Rev. Lett.* **2010**, *104*, No. 257401.
- (39) Mannsfeld, S. C. B.; Tang, M. L.; Bao, Z. Thin Film Structure of Triisopropylsilylthiophene-Functionalized Pentacene and Tetraceno-[2,3-b]Thiophene from Grazing Incidence x-Ray Diffraction. *Adv. Mater.* **2011**, *23*, 127–131.
- (40) Thomas, E. M.; Brady, M. A.; Nakayama, H.; Popere, B. C.; Segalman, R. A.; Chabinyk, M. L. X-Ray Scattering Reveals Ion-Induced Microstructural Changes During Electrochemical Gating of Poly(3-Hexylthiophene). *Adv. Funct. Mater.* **2018**, *28*, No. 1803687.
- (41) Saito, M.; Koganezawa, T.; Osaka, I. Understanding Comparable Charge Transport Between Edge-on and Face-on

Polymers in a Thiazolothiazole Polymer System. *ACS Appl. Polym. Mater.* **2019**, *1*, 1257–1262.

(42) Huang, Y.-F.; Wang, C.-K.; Lai, B.-H.; Chung, C.-L.; Chen, C.-Y.; Ciou, G.-T.; Wong, K.-T.; Wang, C.-L. Influences of Structural Modification of S, N -Hexacenes on the Morphology and OFET Characteristics. *ACS Appl. Mater. Interfaces* **2019**, *11*, 21756–21765.

(43) Kowarik, S.; Gerlach, A.; Sellner, S.; Schreiber, F.; Cavalcanti, L.; Konovalov, O. Real-Time Observation of Structural and Orientational Transitions during Growth of Organic Thin Films. *Phys. Rev. Lett.* **2006**, *96*, No. 125504.

(44) Kowarik, S.; Gerlach, A.; Schreiber, F. Organic Molecular Beam Deposition: Fundamentals, Growth Dynamics, and in Situ Studies. *J. Phys.: Condens. Matter* **2008**, *20*, No. 184005.

(45) Kowarik, S.; Gerlach, A.; Skoda, M. W. A.; Sellner, S.; Schreiber, F. Real-Time Studies of Thin Film Growth: Measurement and Analysis of X-Ray Growth Oscillations beyond the Anti-Bragg Point. *Eur. Phys. J.: Spec. Top.* **2009**, *167*, 11–18.

(46) Richter, L. J.; Delongchamp, D. M.; Amassian, A. Morphology Development in Solution-Processed Functional Organic Blend Films: An in Situ Viewpoint. *Chem. Rev.* **2017**, *117*, 6332–6366.

(47) Hodas, M.; Siffalovic, P.; Nádáždy, P.; Mrkyvková, N.; Bodík, M.; Halahovets, Y.; Duva, G.; Reisz, B.; Konovalov, O.; Ohm, W.; et al. Real-Time Monitoring of Growth and Orientational Alignment of Pentacene on Epitaxial Graphene for Organic Electronics. *ACS Appl. Nano Mater.* **2018**, *1*, 2819–2826.

(48) Liscio, F.; Albonetti, C.; Broch, K.; Shehu, A.; Quiroga, S. D.; Ferlauto, L.; Frank, C.; Kowarik, S.; Nervo, R.; Gerlach, A.; et al. Molecular Reorganization in Organic Field-Effect Transistors and Its Effect on Two-Dimensional Charge Transport Pathways. *ACS Nano* **2013**, *7*, 1257–1264.

(49) Bommel, S.; Kleppmann, N.; Weber, C.; Spranger, H.; Schäfer, P.; Novak, J.; Roth, S. V.; Schreiber, F.; Klapp, S. H. L.; Kowarik, S. Unravelling the Multilayer Growth of the Fullerene C60 in Real Time. *Nat. Commun.* **2014**, *5*, No. 5388.

(50) Hong, S.; Amassian, A.; Woll, A. R.; Bhargava, S.; Ferguson, J. D.; Malliaras, G. G.; Brock, J. D.; Engstrom, J. R. Real Time Monitoring of Pentacene Growth on SiO<sub>2</sub> from a Supersonic Source. *Appl. Phys. Lett.* **2008**, *92*, No. 253304.

(51) Wang, Y.; Zheng, Y.; Xu, X.; Dubuisson, E.; Bao, Q.; Lu, J.; Loh, K. P. Electrochemical Delamination of CVD-Grown Graphene Film: Toward the Recyclable Use of Copper Catalyst. *ACS Nano* **2011**, *5*, 9927–9933.

(52) Graphenea, S. A. GFET for Sensing Applications. <https://www.graphenea.com/> (accessed Dec 18, 2019).

(53) Ritley, K. A.; Krause, B.; Schreiber, F.; Dosch, H. A Portable Ultrahigh Vacuum Organic Molecular Beam Deposition System for in Situ X-Ray Diffraction Measurements. *Rev. Sci. Instrum.* **2001**, *72*, 1453–1457.

(54) Jiang, Z. GIXSGUI: A MATLAB Toolbox for Grazing-Incidence X-Ray Scattering Data Visualization and Reduction, and Indexing of Buried Three-Dimensional Periodic Nanostructured Films. *J. Appl. Crystallogr.* **2015**, *48*, 917–926.

(55) Als-Nielsen, J.; McMorrow, D. *Elements of Modern X-Ray Physics*, 2nd ed.; John Wiley & Sons, Inc.: Hoboken, NJ, 2011; pp 25–27.

(56) Choi, W.; Shehzad, M. A.; Park, S.; Seo, Y. Influence of Removing PMMA Residues on Surface of CVD Graphene Using a Contact-Mode Atomic Force Microscope. *RSC Adv.* **2017**, *7*, 6943–6949.

(57) Ribierre, J.; Tanaka, T.; Zhao, L.; Yokota, Y.; Matsumoto, S.; Hashizume, D.; Takaishi, K.; Muto, T.; Heinrich, B.; Méry, S.; et al. Simultaneous Edge-on to Face-on Reorientation and 1D Alignment of Small  $\pi$ -Conjugated Molecules Using Room-Temperature Mechanical Rubbing. *Adv. Funct. Mater.* **2018**, *28*, No. 1707038.

(58) Lee, H.; Kim, J. H.; Dhakal, K. P.; Lee, J. W.; Jung, J. S.; Joo, J.; Kim, J. Anisotropic Optical Absorption of Organic Rubrene Single Nanoplates and Thin Films Studied by  $\mu$ -Mapping Absorption Spectroscopy. *Appl. Phys. Lett.* **2012**, *101*, No. 113103.

(59) Lauritzen, A. E.; Torkkeli, M.; Bikondoa, O.; Linnet, J.; Tavares, L.; Kjelstrup-Hansen, J.; Knaapila, M. Structural Evaluation of 5,5'-Bis(Naphth-2-Yl)-2,2'-Bithiophene in Organic Field-Effect Transistors with n -Octadecyltrichlorosilane Coated SiO<sub>2</sub> Gate Dielectric. *Langmuir* **2018**, *34*, 6727–6736.

(60) Surin, M.; Hennebicq, E.; Ego, C.; Marsitzky, D.; Grimsdale, A. C.; Müllen, K.; Brédas, J. L.; Lazzaroni, R.; Leclère, P. Correlation between the Microscopic Morphology and the Solid-State Photoluminescence Properties in Fluorene-Based Polymers and Copolymers. *Chem. Mater.* **2004**, *16*, 994–1001.

(61) Mannsfeld, S. C. B.; Briseno, A. L.; Liu, S.; Reese, C.; Roberts, M. E.; Bao, Z. Selective Nucleation of Organic Single Crystals from Vapor Phase on Nanoscopically Rough Surfaces. *Adv. Funct. Mater.* **2007**, *17*, 3545–3553.

(62) Wrana, D.; Kratzer, M.; Szajna, K.; Nikiel, M.; Jany, B. R.; Korzekwa, M.; Teichert, C.; Krok, F. Growth of Para-Hexaphenyl Thin Films on Flat, Atomically Clean versus Air-Passivated TiO<sub>2</sub>(110) Surfaces. *J. Phys. Chem. C* **2015**, *119*, 17004–17015.

(63) Knaapila, M.; Lyons, B. P.; Hase, T. P. A.; Pearson, C.; Petty, M. C.; Bouchenoire, L.; Thompson, P.; Serimaa, R.; Torkkeli, M.; Monkman, A. P. Influence of Molecular Weight on the Surface Morphology of Aligned, Branched Side-Chain Polyfluorene. *Adv. Funct. Mater.* **2005**, *15*, 1517–1522.

(64) Chi, C.; Lieser, G.; Enkelmann, V.; Wegner, G. Packing and Uniaxial Alignment of Liquid Crystalline Oligofluorenes. *Macromol. Chem. Phys.* **2005**, *206*, 1597–1609.

## Supporting Information

# Surface-Controlled Crystal Alignment of Naphthyl End-Capped Oligothiophene on Graphene: Thin-Film Growth Studied by In Situ X-ray Diffraction

*Mathias K. Huss-Hansen*<sup>\*.1</sup>, *Martin Hodas*<sup>2</sup>, *Nada Mrkyvkova*<sup>3,4</sup>, *Jakub Hagara*<sup>3,4</sup>, *Bjarke B. E. Jensen*<sup>5</sup>, *Andreas Osadnik*<sup>6</sup>, *Arne Lützen*<sup>6</sup>, *Eva Majková*<sup>3,4</sup>, *Peter Siffalovic*<sup>3,4</sup>, *Frank Schreiber*<sup>2</sup>,  
*Luciana Tavares*<sup>7</sup>, *Jakob Kjelstrup-Hansen*<sup>7</sup>, and *Matti Knaapila*<sup>1</sup>

<sup>1</sup>Department of Physics, Technical University of Denmark, Kgs. Lyngby, 2800, Denmark

<sup>2</sup>Institut für Angewandte Physik, Universität Tübingen, Tübingen, 72076, Germany

<sup>3</sup>Institute of Physics, Slovak Academy of Sciences, Bratislava, 84511, Slovakia

<sup>4</sup>Centre of Excellence for Advanced Materials Application, Bratislava, 84511, Slovakia

<sup>5</sup>Newtec Engineering A/S, Odense M, 5230, Denmark

<sup>6</sup>Kekulé-Institute for Organic Chemistry and Biochemistry, University of Bonn, Bonn, 53121,  
Germany

<sup>7</sup>NanoSYD, Mads Clausen Institute, University of Southern Denmark, Sønderborg, 6400,  
Denmark

\*E-mail: [mathias.huss-hansen@fysik.dtu.dk](mailto:mathias.huss-hansen@fysik.dtu.dk)

Number of pages: 7

Number of figures: 8

Number of tables: 1

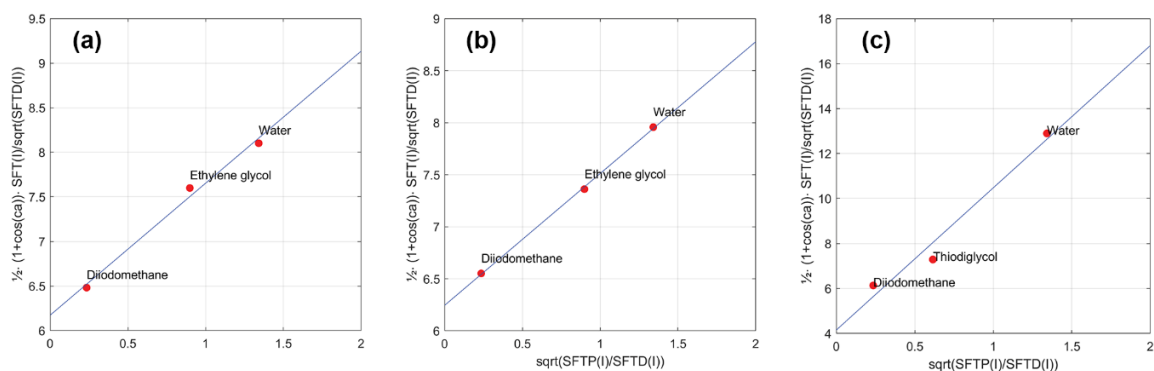


**Figure S1.** Linear regression lines against contact angle data according to Eq. 1 for (a) custom-made graphene, (b) commercial graphene and (c) pristine SiO<sub>2</sub>.

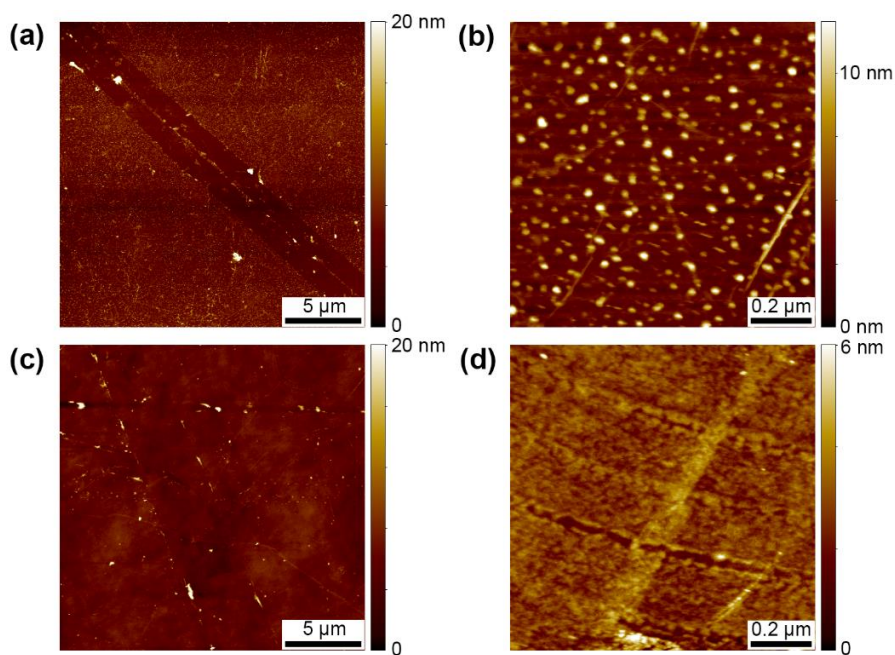


**Figure S2.** AFM topographies of the CVD graphene surfaces. (a,b) Custom-made graphene. (c,d) Commercial graphene.

**Table S1.** Surface Roughness<sup>a)</sup>

Surface	Roughness Average (nm)	Root Mean Square (nm)	Peak-Peak (nm)	Max Peak Height (nm)
Custom-made graphene film	1.24	1.83	15.3	12.0
Commercial graphene film	0.476	0.624	7.52	4.72

a) Based on AFM data from a 2 $\mu$ m by 2 $\mu$ m area shown in Figure S1b,d

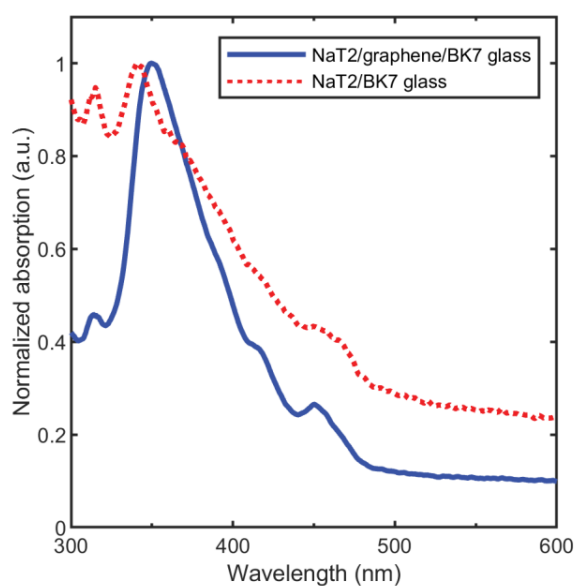


**Figure S3.** Absorption spectra of NaT2 on monolayer graphene (transferred to BK7 glass substrate) and BK7 glass substrate. The absorption curves are normalized to the maximum of the absorption peak.

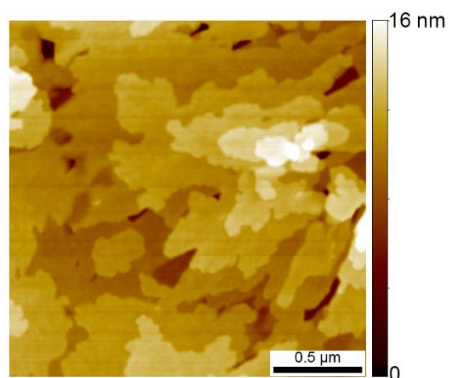


**Figure S4.** AFM topography of NaT2 (16 nm nominal thickness) on SiO<sub>2</sub>

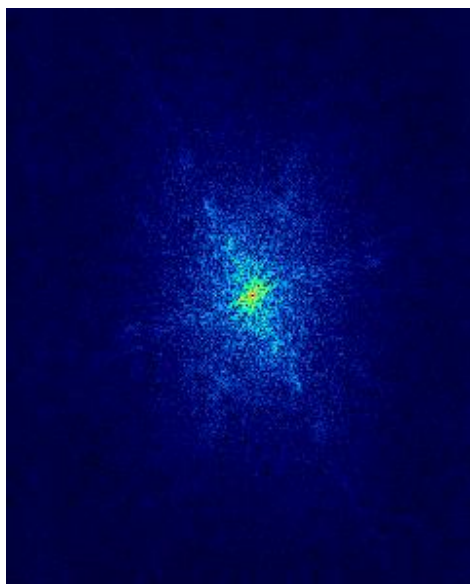


**Figure S5.** Fourier transform of the AFM phase-image in Figure 3c showing the six-fold symmetry of the NaT2 nanofibers.

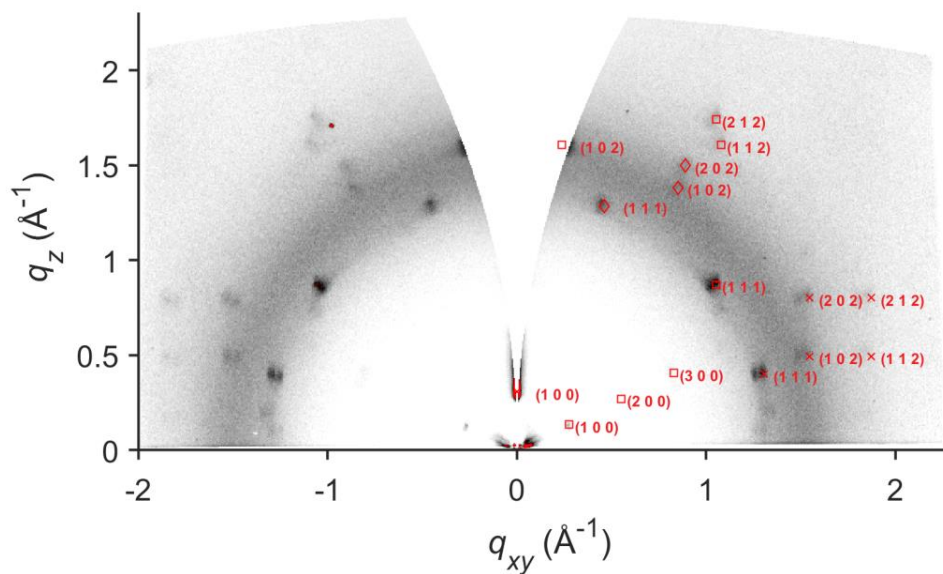


**Figure S6.** GIXRD pattern of NaT2 thin film deposited on Type I graphene. The diffraction peak positions are calculated using the lattice parameters previously reported<sup>1</sup> for NaT2 on SiO<sub>2</sub>/Si ( $a = 20.31 \text{ \AA}$ ,  $b = 6.00$ ,  $c = 8.17$  and  $\beta = 96.64^\circ$ ) with edge-on orientation (crosses), face-on A orientation (squares) and face-on B orientation (diamonds).

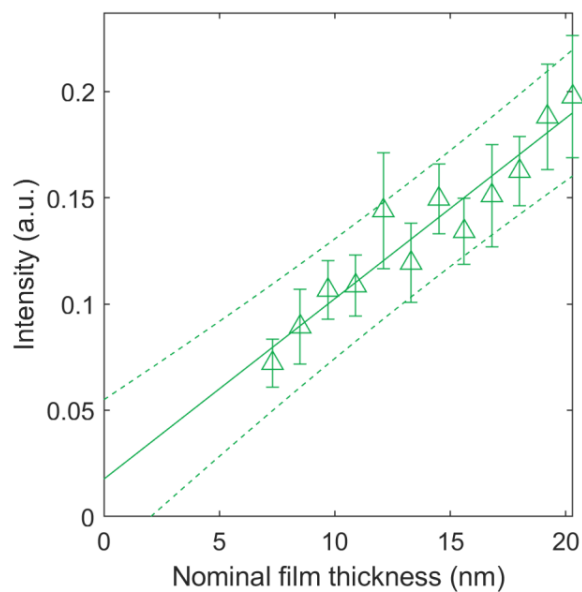


**Figure S7.** Integrated intensity of the crystalline face-on B (111) reflection of NaT2 deposited on custom-made graphene substrate.

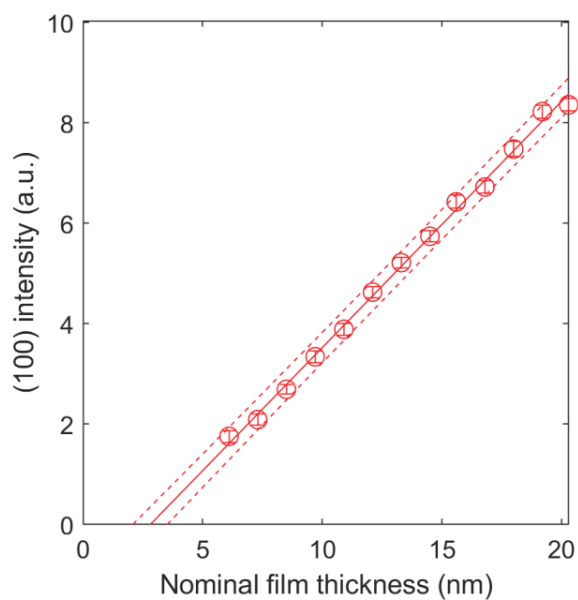


**Figure S8.** Integrated intensity of the strong crystalline edge-on (100) reflection of NaT2 deposited on custom-made graphene substrate.

## References

- (1) Huss-Hansen, M. K.; Lauritzen, A. E.; Bikondoa, O.; Torkkeli, M.; Tavares, L.; Knaapila, M.; Kjelstrup-Hansen, J. Structural Stability of Naphthyl End-Capped Oligothiophenes in Organic Field-Effect Transistors Measured by Grazing-Incidence X-Ray Diffraction in Operando. *Org. Electron.* **2017**, *49*, 375–381.



## Paper III

---

Submitted to *Phys. Rev. Mater.* in revised form on January 7, 2021.

It is well known that the first few layers are essential from optical and, if the device electrodes are located in the plane, charge-transport point of view. The aim of this paper is to investigate and compare the early-stage growth of the two chemically similar, yet symmetrically different rigid-rod organic semiconductors. This is facilitated by the use of *in situ* real-time GIWAXS measurements of the growth during vacuum deposition. The high brilliance available at synchrotron allows us to probe the growth of the critical first few molecular layers, thus building upon the results presented in Paper II. Moreover, since the molecule-substrate interactions at the substrate interface are critically important to the formation of the final film structure, we present results from multiple substrate types. This paper is the culmination of two joint beamtimes with the groups of Peter Siffalovic (Slovak Academy of Sciences) and Frank Schreiber (University of Tübingen).

# Early-stage growth observations of orientation-controlled vacuum-deposited naphthyl end-capped oligothiophenes

Mathias K. Huss-Hansen,<sup>1,\*</sup> Martin Hodas,<sup>2</sup> Nada Mrkyvkova,<sup>3,4</sup>  
Jakub Hagara,<sup>3</sup> Peter Nadazdy,<sup>3</sup> Michaela Sojkova,<sup>5</sup> Simon O. Høegh,<sup>6</sup>  
Alina Vlad,<sup>7</sup> Pallavi Pandit,<sup>8</sup> Eva Majkova,<sup>3,4</sup> Peter Siffalovic,<sup>3,4</sup>  
Frank Schreiber,<sup>2</sup> Jakob Kjelstrup-Hansen,<sup>6</sup> and Matti Knaapila<sup>1</sup>

<sup>1</sup>*Department of Physics, Technical University of Denmark, 2800 Kgs. Lyngby, Denmark*

<sup>2</sup>*Institut für Angewandte Physik, Universität Tübingen, 72076 Tübingen, Germany*

<sup>3</sup>*Institute of Physics, Slovak Academy of Sciences, 84511 Bratislava, Slovakia*

<sup>4</sup>*Center for Advanced Materials Application,  
Slovak Academy of Sciences, 84511 Bratislava, Slovakia*

<sup>5</sup>*Institute of Electrical Engineering,  
Slovak Academy of Sciences, 84104 Bratislava, Slovakia*

<sup>6</sup>*NanoSYD, Mads Clausen Institute,  
University of Southern Denmark, 6400 Sønderborg, Denmark*

<sup>7</sup>*Synchrotron SOLEIL, L'Orme des Merisiers, 91190 Saint-Aubin, France*

<sup>8</sup>*Photon Science, Deutsches Elektronen-Synchrotron (DESY), 22607 Hamburg, Germany*

(Dated: January 7, 2021)

## Abstract

We report on the real-time structure formation and growth of two thiophene-based organic semiconductors, 5,5'-bis(naphth-2-yl)-2,2'-bi- and 5,5''-bis(naphth-2-yl)-2,2':5',2''-terthiophene (NaT2 and NaT3), studied in situ during vacuum deposition by grazing-incidence X-ray diffraction and supported by atomic force microscopy and photoabsorption spectroscopy measurements on corresponding ex situ samples. On device-relevant silicon dioxide substrates, Stranski-Krastanov growth is observed for both molecules, where the growth transitions from two-dimensional (2D) layer-by-layer growth to 3-dimensional (3D) growth after the formation of a few-molecule-thick wetting layer. The crystal structure of the NaT2 film is considerably more ordered than the NaT3 counterpart, and there is a significant collective change in the unit cell during the initial stage of growth, indicating strain relief from substrate induced strain as the growth transitions from 2D to 3D. In addition, the orientation of the film molecules are controlled by employing substrates of horizontally and vertically oriented few-layer molybdenum disulfide. Both molecules form needle-like crystals on horizontally oriented MoS<sub>2</sub> layers, while the NaT3 molecules form tall, isolated islands on vertically oriented MoS<sub>2</sub> layers. The molecules are standing on silicon dioxide and on vertically oriented MoS<sub>2</sub> but lying flat on horizontally oriented MoS<sub>2</sub>. These results demonstrate the importance of film-substrate interactions on the thin-film growth and microstructure formation in naphthyl-terminated oligothiophenes.

## I. INTRODUCTION

Organic semiconductors (OSCs) offer many possibilities as materials in organic electronics, owing to their low-cost, large area processing techniques and, in particular, the ability to tailor electronic- and charge transport properties using synthetic procedures. Applications include organic field effect transistors (OFETs) [1, 2], organic photovoltaics (OPVs) [3], organic light-emitting diodes (OLEDs) [4, 5], and OFET-based sensors [6, 7]. The electronic and optical properties of the OSCs are directly influenced by the microstructure within the organic thin films [8–10], and solving the full complexity of the structure-function relationships remains an important goal in understanding OSC behavior, their processing and

---

\* Author to whom correspondence should be addressed: mathias.huss-hansen@fysik.dtu.dk

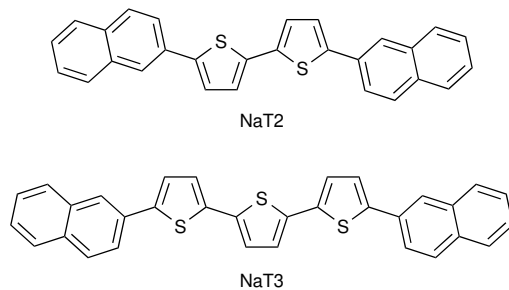


FIG. 1. Chemical structures of 5,5'-bis(naphth-2-yl)-2,2'-bithiophene (NaT2) and 5,5''-bis(naphth-2-yl)-2,2':5',2''-terthiophene (NaT3)

device physics. The device-relevant thin-film morphology and microstructure differ from bulk, and factors such as molecular and macroscopic orientation [11, 12], polymorphism including surface-induced phases (SIPs) [13–15], non-equilibrium growth conditions and interfacial interactions all play important roles. Several methods can be used to investigate the structural properties of OSC films, including X-ray scattering and near edge X-ray absorption fine structure techniques [16–18], in situ variations of thereof [19–22], fluorescence spectroscopy and microscopy [23], Raman spectroscopy [24], optical spectroscopy [25], and electron microscopy [26–28], to name a few.

Dinaphthyl terminated oligothiophenes are OSCs belonging to the extensively studied group of oligothiophenes [16, 18, 29], and have been shown to display good oxidative and thermal stability, surpassing their alkyl-terminated counterparts. Figure 1 shows the chemical structure of NaT $n$  [30] with  $n = 2, 3$  representing the number of thiophene rings. The two molecules represent two distinct anisotropic cases, with the shorter thiophene dimer having inversion symmetry with respect to its geometric center, while the thiophene trimer has mirror symmetry about the centerline through the middle thiophene ring. Both compounds were found to form monoclinic crystals in bulk with the molecules packed in the well-known herringbone pattern [30], with NaT3 adopting a three-layer repeat along the long axis, where the molecule in the middle layer is tilted slightly different than the other two layers. We have recently expanded pioneering single crystal studies of Tian *et al.* [30] to the film structure and structure formation on various substrates. Molecular mechanics modeling on the two systems in thin-film configuration has revealed that the NaT3 form films with significantly greater structural disorder than NaT2 [31], making the two molecules prime candidates for further growth studies. In an earlier article, we reported on the early stage growth of NaT2

on SiO<sub>2</sub> and on chemical vapor deposition (CVD)-grown graphene transferred onto a Si/SiO<sub>2</sub> substrate [32]. We found that the molecular orientation and growth behavior were different in the two cases, but the employed experimental approach did not allow for probing of the critical first few monolayers (MLs). These first few layers are essential from optical and, if the device electrodes are located in the plane, charge-transport point of view. The goal of the present study is to shed light on the fundamental questions of the growth within these first few layers.

In this paper we investigate the early stages of growth in NaT2 and NaT3 films and demonstrate how this growth can be controlled by the surface interactions. Films of NaT2 and NaT3 were prepared by vacuum deposition onto silicon dioxide and onto oriented few-layer molybdenum disulfide (MoS<sub>2</sub>) substrates. The films were studied by real-time in situ grazing incidence X-ray diffraction (GIXRD) experiments during the deposition and complemented by ex situ AFM and UV/Vis absorption experiments. Performing the experiments in real-time and in vacuum conditions ensures no degradation of the films due to ambient exposure, and allows us to capture transient structures. Moreover, results from many different film thicknesses can be directly compared, since they are obtained under absolutely identical conditions and on the same substrate for a given deposition, which is obviously much more difficult for a series of individual films, considering that the exact conditions will inevitably vary. By exploiting the interactions between  $\pi$ -conjugated OSCs and distinct substrates, we are able to preferentially align the molecular backbone of our molecules with respect to the surface, and identify distinct growth modes. This work builds upon previous characterization studies of NaTn films [31–35], and provides insight into the growth of small-molecule OSC thin films.

## II. EXPERIMENTAL

### A. Materials and substrates

NaT2 and NaT3 molecules (see the chemical structures in Fig. 1) used in this study were synthesized following the Suzuki cross-coupling approach reported in Ref. [36]. The MoS<sub>2</sub> layers were prepared by rapid sulfurization of Mo films on Al<sub>2</sub>O<sub>3</sub> substrates, as described in Ref. [37]. This technique produces crystalline MoS<sub>2</sub> layers of high quality. Depending on the

thickness of the initial Mo film [38], the resulting MoS<sub>2</sub> layers are aligned either parallel to the substrate plane (hereafter referred to as ||-MoS<sub>2</sub>), or perpendicular to the substrate plane (hereafter referred to as ⊥-MoS<sub>2</sub>). The resulting film thicknesses of the ||-MoS<sub>2</sub> and ⊥-MoS<sub>2</sub> are 3 and 9 nm, respectively. Commercial Si substrates, with a native oxide layer of 1.5 nm thickness, were purchased from Silicon Materials (Germany) and BK7 glass substrates were purchased from UniversityWafer (USA).

### B. Grazing incidence X-ray scattering (GIXRD)

In situ GIXRD measurements were performed at the PETRA III micro- and nanofocus X-ray scattering (P03) beamline [39], and at the SOLEIL Surface(s) and Interface(s) X-ray Scattering (SIXS) beamline. NaTn films were deposited by vacuum sublimation in a custom-built vacuum chamber (base pressure of  $4 \times 10^{-8}$  mbar) equipped with a cylindrical beryllium window, allowing the incoming and outgoing X-rays to penetrate similar to Ref. [40]. The molecules were evaporated onto the substrate from a Knudsen evaporation cell, and the film thickness was monitored by a quartz crystal microbalance (QCM) inside the deposition chamber. Prior to deposition, the substrates were annealed at 573 K in order to desorb any impurities and residual contamination. NaTn was deposited onto the substrate (temperature 323 K) at typical evaporation temperatures of 468 K (NaT2) and 508 K (NaT3), corresponding to rates of 0.03 Å/s as monitored by the QCM. 2D GIXRD images were recorded every 20 s with an attenuated beam to prevent X-ray induced damage of the films. The lack of beam damage was verified by comparing images of films exposed to prolonged illumination with unexposed films. The X-ray beam energy was 11.6 keV at PETRA III and 12 keV at SOLEIL. The incidence angle was kept between the critical angle of the films and the critical angle of the substrate, typically 0.17°. Scattering images were collected using a Pilatus 300K detector (PETRA III) and a Si-XPAD3 detector (SOLEIL), with a sample-to-detector distance (SDD) of 149 mm and 218 mm, respectively.

Ex situ GIXRD measurements were performed at the PETRA III P03 beamline with an X-ray energy of 12.98 keV and an incidence angle of 0.17°. Images were collected using a LAMBDA detector at a SDD of 159 mm. Data reduction was performed in DAWN [41], with additional analysis performed using self-programmed MATLAB scripts. The X-ray data was normalized to the incoming beam intensity and corrected for standard geometrical contri-

butions. The peak positions were determined by fitting linecuts of the reciprocal space map (RSM) by Gaussian or Lorentzian functions depending on the peak shape. The integrated peak intensity was determined as the area under the peak minus the local background. The in-plane and out-of-plane unit cell parameters were determined separately by weighted least squares minimization of the difference between experimental and calculated  $q_{xy}$  and  $q_z$  positions of selected Bragg peaks. For the full set of equations, please see the work of Merlo *et al.* [42]. The reported single crystal structure was used as a starting point for the minimization [30]. In the employed experimental geometry, we are essentially resolution-limited due to the width of the beam footprint on the sample [43]. We will therefore refrain from doing Scherrer-type grain-size analysis on the data.

### C. Atomic force microscopy (AFM) and UV/Vis absorption spectroscopy

Thin films for ex situ characterization were prepared in the same manner as the in situ samples described above with constant evaporation rates of 0.03 Å/s. The evaporation source shutter was closed once the desired thickness was reached, as determined by QCM readings. Samples on different substrate types were prepared simultaneously, resulting in identical nominal film thicknesses. AFM images were collected in ambient conditions immediately upon removing the samples from vacuum using a Veeco Dimension 3100 operated in tapping mode. Image software Gwyddion was used to flatten and analyze the images [44]. UV/Vis absorption spectra were measured using a Shimadzu UV-2700 spectrometer with an integrating sphere ad-on. The absorption curves of the clean substrates were measured separately prior to the thin film deposition and later subtracted from the thin film absorption spectra.

## III. RESULTS AND DISCUSSION

### A. Grazing incidence diffraction

GIXRD studies of the final films were performed to characterize the crystalline structure. The films were deposited onto Si substrates with a native oxide layer, and onto few-layer MoS<sub>2</sub> surfaces, with the layers oriented either horizontally ( $\parallel$ ) or vertically ( $\perp$ ) on the underlying Al<sub>2</sub>O<sub>3</sub> substrates. We expect the orientation of the MoS<sub>2</sub> layers to influence the

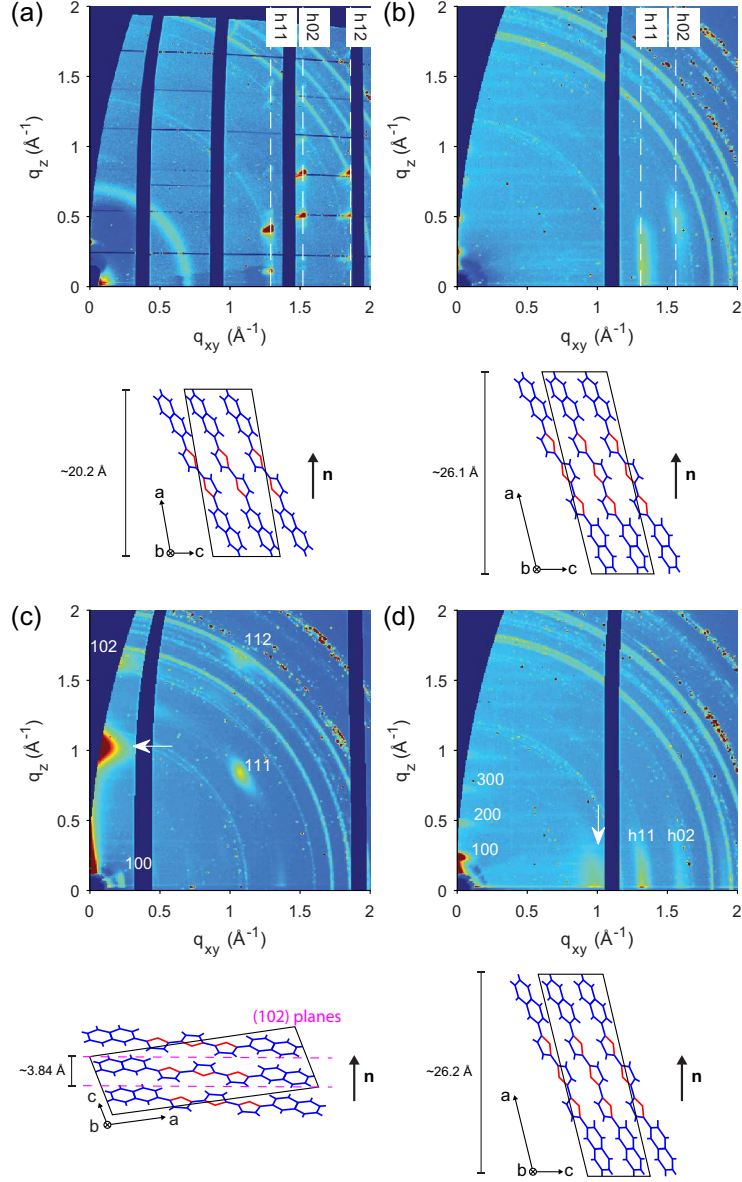


FIG. 2. Two-dimensional RSMs, with proposed packing motifs and approximate layer height, of (a) NaT2 film on  $\text{SiO}_2$ , (b) NaT3 on  $\text{SiO}_2$ , (c) NaT3 on  $\parallel\text{-MoS}_2$  and (d) NaT3 on  $\perp\text{-MoS}_2$ . Dashed lines in (a) and (b) indicate diffraction from planes with matching  $k$  and  $l$  indices, highlighting the 2D in-plane ordering. Arrows in (c) and (d) indicate the scattering peak from the  $\text{MoS}_2$  (002) plane. Rings arising from the deposition chamber are visible at  $q \simeq 0.7 \text{ \AA}^{-1}$ ,  $q \simeq 1.3 \text{ \AA}^{-1}$  and  $q > 1.7 \text{ \AA}^{-1}$ . The surface normal direction is indicated by  $\mathbf{n}$ .

molecular orientation of the NaTn films, as has been previously shown for diindenoperylene (DIP) molecules [37]. On  $\parallel$ -MoS<sub>2</sub>, we expect strong interaction between the molecules and the surface through  $\pi - \pi$  and CH- $\pi$  interactions. On the other hand,  $\perp$ -MoS<sub>2</sub> layers exhibit a large amount of dangling bonds that are readily oxidized [45]. As a result, the oxidized surface of the  $\perp$ -MoS<sub>2</sub> is expected to interact weakly with the film molecules.

Figure 2 shows the reciprocal space maps (RSMs) of the final films (thickness varying from 15 to 30 nm). The data in Fig. 2a shows that the shorter NaT2 molecule form highly ordered crystals on silicon dioxide, as indicated by the apparent sharpness of the Bragg reflections. Identical scattering patterns were observed irrespective of the sample rotation around the surface normal, indicating isotropic orientation of the mosaic crystallites in the surface plane, also known as fiber-texture. All the Bragg reflections were successfully indexed with a monoclinic unit cell, and by minimizing the difference between experimental and calculated peak positions of the 14 most intense Bragg peaks, the lattice parameters were determined to be  $a = 20.2 \pm 0.2 \text{ \AA}$ ,  $b = 6.0 \pm 0.2 \text{ \AA}$ ,  $c = 8.3 \pm 0.1 \text{ \AA}$  and  $\beta = 97.2 \pm 0.2^\circ$ . The NaT2 molecules are oriented edge-on, which is confirmed by the 100 diffraction peak located perpendicular to the substrate at  $q_z = 0.3 \text{ \AA}^{-1}$ . Reflections along  $q_{xy} = 0 \text{ \AA}^{-1}$  are in principle inaccessible in GIXRD due to the curvature of the Ewald sphere. Nevertheless, their tails are still observed due to broadening of the orientation distribution of the crystallites.

By contrast, the RSM of the NaT3 film (Fig. 2b) is distinctly different with broad reflections at  $q_{xy} = 1.33 \text{ \AA}^{-1}$  and  $q_{xy} = 1.55 \text{ \AA}^{-1}$ . A full refinement of the lattice parameters is not possible from these data. However, we have previously shown that the NaT3 films likewise form monoclinic crystals on silicon dioxide [46], with similar in-plane lattice parameters to NaT2 and a longer  $a$ -axis to accommodate the longer NaT3 molecule. The broadening of the reflections along  $q_z$  indicates a significant disorder in the out-of-plane structure, which we have previously speculated is due to a SIP with a large number of flipped molecules [31]. Several orders of the  $h00$  reflections along  $q_{xy} = 0 \text{ \AA}^{-1}$  confirm the edge-on orientation of the molecules.

The RSM of the NaT3 film deposited on few-layer  $\parallel$ -MoS<sub>2</sub> (Fig. 2c) shows that the molecules are oriented face-on, which is expected considering the strong substrate-molecule interactions at the interface. This is exemplified by the 100 reflection pointing close to parallel to the  $q_{xy}$  direction. Considering the 102 reflection pointing along  $q_z$ , we are able to successfully identify all four visible reflections with a monoclinic unit cell. In this configura-

tion, the (102) planes lie parallel to the substrate surface, as indicated on the packing motif in Fig. 2c. The film crystals exhibit a considerable degree of order, as indicated by the relative sharpness of the 111 reflection. At  $q_z = 1 \text{ \AA}^{-1}$ , an intense reflection originating from the (002) planes of MoS<sub>2</sub> is visible, verifying the horizontal orientation of the MoS<sub>2</sub> layers relative to the Al<sub>2</sub>O<sub>3</sub> substrate. NaT2 molecules deposited on few-layer  $\parallel$ -MoS<sub>2</sub> likewise adopt face-on orientation (see Fig. S1 in [47]).

The RSM of the NaT3 film prepared on few-layer  $\perp$ -MoS<sub>2</sub> (Fig. 2d) also show  $h00$  reflections consistent with edge-on oriented molecules, but unlike the NaT3 film on silicon dioxide, the reflections along the in-plane direction appear as rods emanating from  $q_z = 0$ . Together, these observations suggest a crystal structure where the NaT3 molecules have strong ordering along the stacking ( $a$ -axis) direction, but have little to no ordering between the crystallites in the plane. The broadening of the  $h00$  reflections indicates a large distribution in the tilts of long molecular axes with respect to the surface normal.

## B. Real-time grazing-incidence diffraction

We performed in situ GIXRD measurements of the NaT2 and NaT3 films during the deposition process in order to follow and characterize the crystallographic structure of the thin film during growth. Figure 3a shows the unit cell parameters of the NaT2 film on silicon dioxide with increasing nominal film thickness, which determined by time  $\times$  deposition rate. The unit cell parameters are determined from the peak positions of the 100, 111, 102 and 202 reflections. The unit cell changes significantly within the first 4-6 nm, corresponding approximately to 2-3 MLs, both in the plane ( $b$ - and  $c$ -axis) and out-of-plane ( $a$ -axis). We attribute the changes in the in-plane lattice dimensions to strain relief from surface induced strain. After approximately 6 nm, the in-plane lattice parameters remain almost unchanged for larger thicknesses of the film, indicating that the surface induced strain is fully relieved after  $\sim$ 3 MLs. On the other hand, the  $a$ -axis continues to compress throughout the entire deposition. The  $a$ -axis compression is most pronounced within the first 2 MLs, and is accompanied by a  $2^\circ$  shift in the unit cell tilt. After 2 MLs, the  $a$ -axis compression and change in  $\beta$  slow down but continue until the final thickness of 22 nm is reached. We attribute the  $a$ -axis compression and change in  $\beta$  to reorganization of the molecules inside the unit cell. The change in unit cell volume is shown in Fig. 3b, revealing an 8% decrease

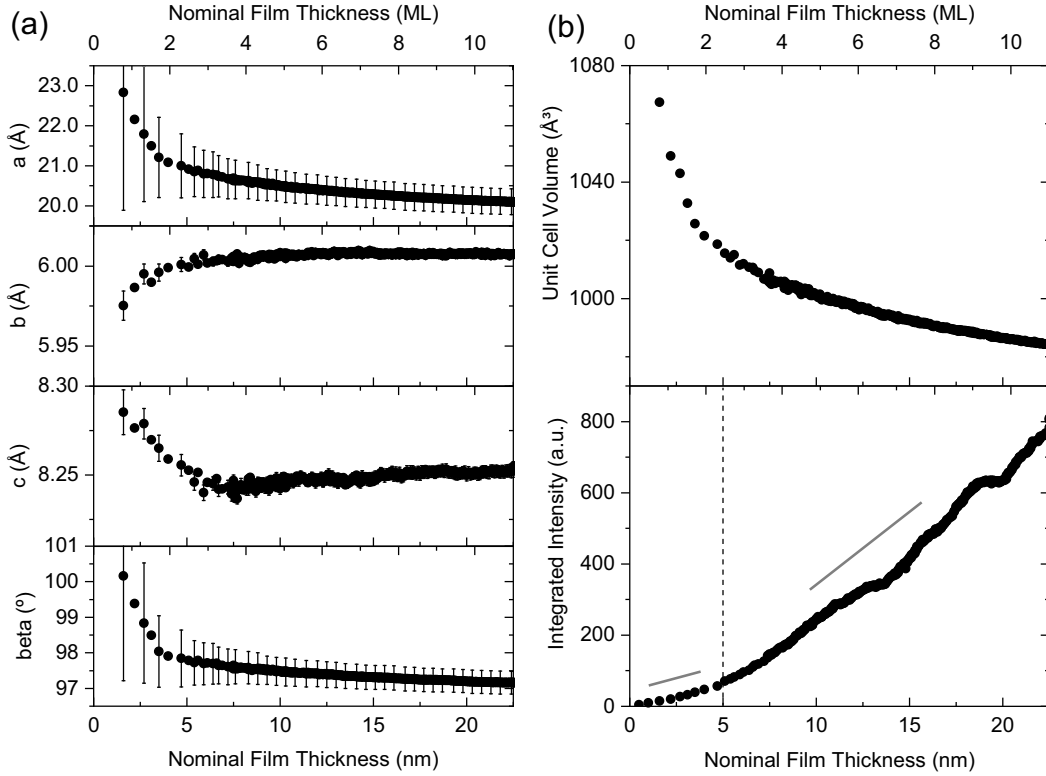


FIG. 3. Real-time GIXRD data of NaT2 deposited on silicon dioxide as a function of nominal film thickness (time  $\times$  deposition rate). (a) Unit cell parameters calculated from peak positions of the 100, 111, 102 and 202 reflections on the RSM. The secondary abscissa on top denotes the approximate number of molecular layers, given by the average layer thickness during the deposition. (b) Unit cell volume and integrated scattering intensity from the 111 reflection. The dashed line indicates the approximate separation between regions of linear growth with different scaling factors. Solid lines are guides for the eye only.

in between the initial ML and the final film.

The integrated scattering intensity of the 111 reflection is plotted in Figure 3b. For perfect epitaxial layer-by-layer growth [48], the integrated scattering intensity of a Bragg reflection is expected to scale linearly with film thickness. In the case of NaT2 on silicon dioxide, we can distinguish two region based on the slope of curve: (1) early-stage growth, from 0 to 5 nm, and (2) late-stage growth, which comprises everything above 5 nm. In both regions, the integrated scattering intensity is found to scale approximately linearly with the film thickness, albeit with different scaling factors. We speculate that this is caused by the film molecules undergoing a restructuring and/or reordering in the transition from

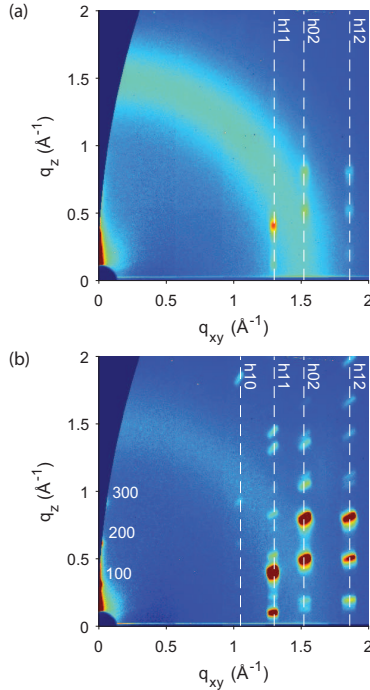


FIG. 4. Ex situ RSMs of (a) 4 nm and (b) 11 nm thick NaT2 films prepared on silicon dioxide. The diffuse scattering ring at  $q \simeq 1.5 \text{ \AA}^{-1}$  originates from the substrate. Dashed lines indicate scattering from planes with identical  $k$  and  $l$  indices.

early-stage to late-stage growth. This change in molecular conformation and/or orientation changes the films structure factor, which results in different electron densities, and therefore scattering intensities, of different layers. There is no evidence of peak splitting in the Bragg reflections, indicating that the structure changes as a whole and not just with the formation of a new layer. This picture is consistent with the observed change in the unit cell within the first few MLs. A similar change in the electron density within the first MLs was observed for DIP grown on silicon dioxide by Kowarik *et al.* [49].

Figure 4 shows RSMs of NaT2 on silicon dioxide measured by ex situ GIXRD, corresponding to 4 nm and 11 nm nominal film thickness, and thus the situation from the separate growth domains identified in Fig. 3b. Ex situ GIXRD measurements allows for longer exposure times and fine tuning of the incidence angle, resulting in higher signal to noise ratio of the RSMs. The 4 nm thick sample, corresponding nominally to 2 MLs, shows Bragg peaks elongated along  $q_z$  and virtually no  $h00$  reflections, indicative of limited out-of-plane order (often seen in liquid-crystal like films). In comparison, the 11 nm thick sample, corre-

sponding to 5 nominal layers, shows many more reflections (including several order of  $h00$  reflections) pointing to a full 3-dimensional (3D) crystal. The results imply a transition from predominantly two-dimensional (2D) crystals with little out-of-plane order, to fully 3D crystals with high in-plane and out-of-plane order. This transition coincides with the transition from early-stage growth to late-stage growth on Fig. 3b. Yet, we emphasize that the experiment is not identical to the above-described in situ GIXRD measurements, and that the films have been exposed to ambient conditions prior to measurements.

For the NaT3 film deposited on silicon dioxide, it is not possible to refine the full unit cell from the RSM, but we can still identify the essential structural characteristics with increasing film thickness. Figure 5a shows the time evolution of the (100) and ( $h11$ )  $d$ -spacings, measured along the substrate normal and substrate plane, respectively. The values are calculated from  $2\pi/q$ , where  $q$  is the peak position of the 200 and  $h11$  reflections on the RSM. The shaded area indicates the cut-off before which peak fitting is impossible due to overlap between the (200) reflection and the off-specular diffuse scattering from the surface. Once again we observe a significant compression of the out-of-plane component of the unit cell, with the value seemingly starting to plateau after 5 MLs. The ( $h11$ ) dimension of the unit cell expands by almost 0.1 Å within the first 2 nm, after which it continues to expand at a relatively constant albeit slower rate until the final film thickness is reached. These findings point towards a greater surface induced strain in the NaT3 films, as compared with the shorter molecule NaT2 films.

Figure 5b shows the integrated scattering intensity of the  $h11$  reflection together with the off-specular diffuse scattering from the area just above the beamstop on the RSM. From the figure, it is evident that the integrated scattering intensity increases linearly with the film thickness, in contrast to the NaT2 film, where two different regions could be identified. The off-specular diffuse scattering, which is known to be caused by surface roughness [50], can be used to gain information about the film growth. For perfect layer-by-layer growth, the off-specular diffuse scattering is expected to oscillate with a period of 1 ML. As the first layer starts to form on the surface, the surface roughness and therefore the intensity of the diffuse scattering will rise due to the formation of islands. The surface roughness (and therefore the diffuse scattering) will reach its maximum at around 0.5 ML, corresponding to half surface coverage. As the islands starts to coalesce, the surface roughness and diffuse scattering will start to decrease, reaching a minimum at exactly 1 ML (perfectly smooth film with complete

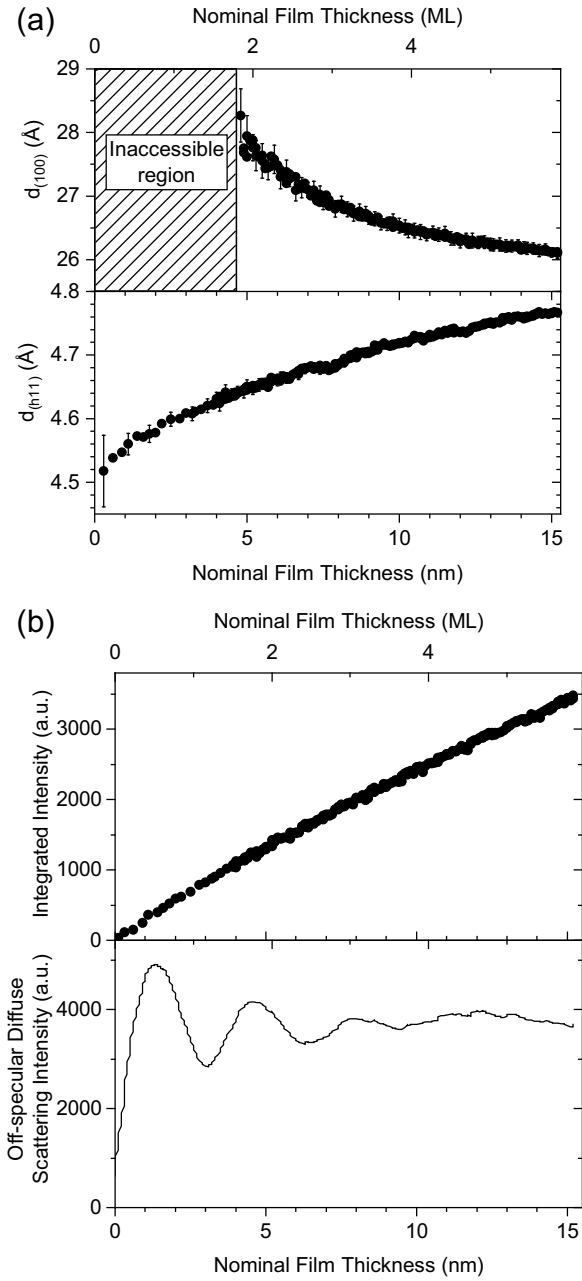


FIG. 5. Real-time GIXRD data of NaT3 deposited on SiO<sub>2</sub> as a function of nominal film thickness. (a) Evolution of out-of-plane and in-plane lattice parameters. The inaccessible region is due to overlap between the 200 reflection and off-specular diffuse scattering. (b) Integrated scattering intensity of the  $h11$  reflection and off-specular diffuse scattering with increasing film thickness.

surface coverage). The same pattern would be expected for the formation of the second layer and third layer etc., manifesting as oscillations in the diffusely scattered intensity with matching amplitude and a periodicity of 1 ML. An example of these oscillations in the diffusely scattered intensity in layer-by-layer growth of the isotropic fullerene C60 can be found in the work of Bommel *et al.* [51]. The diffuse scattering intensity on Fig. 5b does not follow the pattern expected for perfect layer-by-layer growth. Instead, the period is slightly larger than 1 ML (1.2 ML) for the first oscillation, and the amplitude is seemingly damped with each subsequent oscillation. The attenuation of the diffuse scattering and the oscillation period not exactly matching 1 ML points towards imperfect layer-by-layer growth of the NaT3 film. Similar findings for the off-specular diffuse scattering intensity was reported for imperfect layer-by-layer growth of  $\alpha, \omega$ -hexyl-distyryl thieno thiophene (DH-DSTT) [52], which by nature is closer to our system than the fullerene C60 model system. The lack of oscillations after 3 ML in the diffuse scattering intensity suggest that the growth has fully transitioned from imperfect layer-by-layer growth to 3D island growth (*vide infra*).

Finally, we consider the case of NaT3 films deposited on oriented MoS<sub>2</sub> surfaces. Figure 6 shows the lattice spacings as a function of nominal film thickness (i.e. measured by the QCM) for NaT3 deposited on both  $\parallel$ -MoS<sub>2</sub> and  $\perp$ -MoS<sub>2</sub>. For the NaT3 film deposited on  $\perp$ -MoS<sub>2</sub>, the compression of the (100) d-spacing is similar to the observed pattern for NaT3 on silicon dioxide, while the (*h*11) d-spacing is approximately 3% larger at a film thickness of 0.9 nm (4.69 Å compared to 4.55 Å on silicon dioxide). This could be an indications of a slightly better lattice match between the NaT3 thin film and the MoS<sub>2</sub>. An increase in the (*h*11) direction of the lattice is also observed on the  $\perp$ -MoS<sub>2</sub> with increasing film thickness, reaching a final value of 4.81 Å at 15.3 nm. As previously shown, the NaT3 molecules deposited on  $\parallel$ -MoS<sub>2</sub> adopt face-on configuration. The crystalline face-on phase is significantly larger than the crystalline edge-on phase found growing on  $\perp$ -MoS<sub>2</sub>, clearly evident by the larger (100) and (*h*11) d-spacings shown in Fig. 6. For NaT3 deposited on  $\parallel$ -MoS<sub>2</sub>, the (100) d-spacing first expands slightly and, after certain film thickness is reached, starts to compress at a slower albeit constant rate. A similar evolution of the (100) lattice plane spacing was observed for the thiophene-based molecule 1-[5-(2-naphthyl)-2,2-bithiophen-5-yl]hexan-1-one (NCOH) [53]. The (*h*11) d-spacing exhibits the opposite behavior, first undergoing a small compression followed by a slow expansion. The *h*11 integrated scattering intensity increases linearly with the nominal film thickness for NaT3 deposited on  $\perp$ -MoS<sub>2</sub>, For the

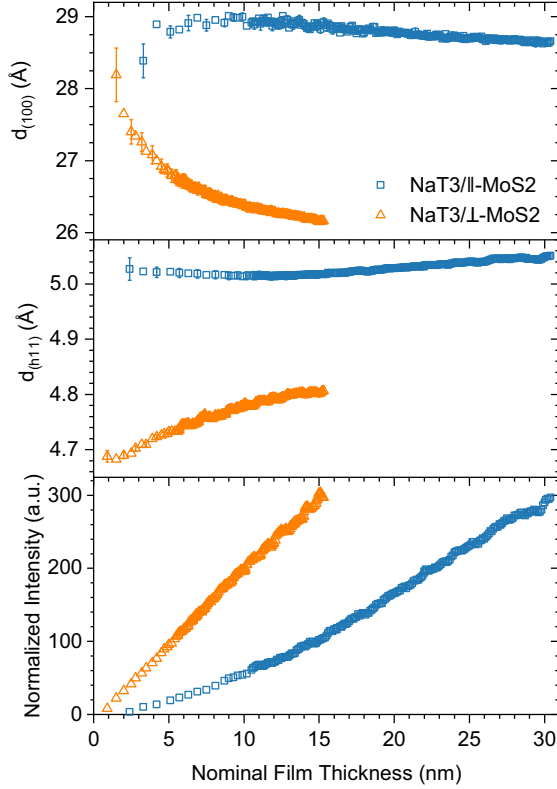


FIG. 6. Lattice parameters and integrated scattering intensity of the  $h11$  reflection for NaT3 molecules with face-on orientation on  $\parallel$ -MoS<sub>2</sub> (blue squares) and edge-on orientation on  $\perp$ -MoS<sub>2</sub> (orange triangles) with increasing nominal film thickness. The intensity values are normalized to the final intensity value.

NaT3 film deposited on  $\parallel$ -MoS<sub>2</sub>, the integrated scattering intensity of the  $h11$  reflection scales non-linearly with effective film thickness.

### C. Atomic force microscopy

To characterize the surface morphologies of the thin films, we used ex situ AFM on samples at various stages of film growth. We prepared vacuum deposited films with nominal thicknesses of 2.0 nm, 4.8 nm, and 14.9 nm, respectively, by closing the deposition shutter at corresponding readings of the QCM. Figure 7 shows the AFM results for NaT3 films deposited on all three types of substrates. On silicon dioxide (Fig. 7a), the sample with a nominal film thickness of 2.0 nm, corresponding to 0.8 MLs, displays a morphology of

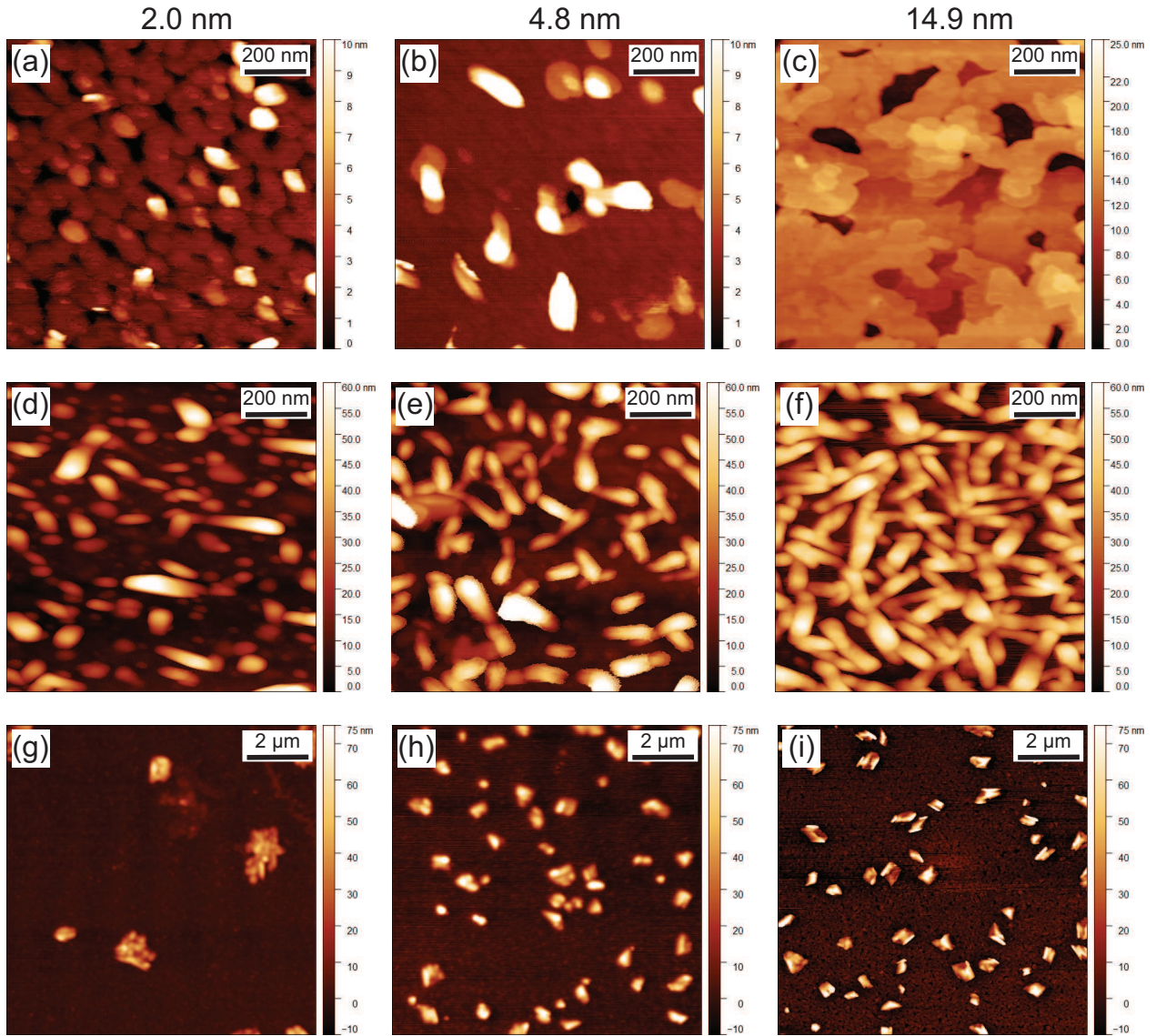


FIG. 7. AFM images of vacuum deposited NaT3 films with different nominal thicknesses, as determined by corresponding QCM readings, on silicon dioxide (a-c),  $\parallel$ -MoS<sub>2</sub> (d-f) and  $\perp$ -MoS<sub>2</sub> (g-i).

connected islands that form a near complete ML. A few islands are observed on top of the first ML, indicating the nucleation of the second and third layer. The second image (Fig. 7b), corresponding to the sample with a nominal film thickness of 4.8 nm, shows a completed first layer with taller islands on top that range in height from 2.5 nm (1 ML) to 15 nm (6 ML). The final sample (Fig. 7c) displays a film morphology comprised of repeated 3D island formations, with individual islands exceeding 25 nm in height. Figure S2 in [47] shows the

corresponding height distributions of the AFM data, where clearly distinguishable peaks can be identified and attributed to the silicon dioxide substrate, and the first and second ML of the NaT3 film, respectively. The NaT2 film on silicon dioxide follows a similar morphological progression (see Fig. S3 in [47]).

The AFM images of samples with NaT3 deposited on  $\parallel$ -MoS<sub>2</sub> (Figs. 7d-f) show that the NaT3 molecules form thin needle-like crystals with height up to  $\sim 60$  nm. The surface coverage of the needle-like crystals increases with increasing nominal film thickness, progressing from isolated needles at 2.0 nm to a network of interconnect crystals at 14.9 nm. However, the maximum height of the needles does not appear to change with increased film coverage. The film morphology of NaT2 on  $\parallel$ -MoS<sub>2</sub> is shown on Fig. S4 in [47].

Lastly, the AFM image sequence of NaT3 deposited on  $\perp$ -MoS<sub>2</sub> (Figs. 7g-i) reveals that the NaT3 molecules form tall, isolated islands on the  $\perp$ -MoS<sub>2</sub> surface. From the image of the first sample (Fig. 7g), with a nominal film thickness of 2 nm, it is evident that the islands are comprised of tall pillar formations, some of which exceeds 60 nm in height. From Figs 7h and 7i, it appears that the number of islands is increasing with the amount of material deposited on the substrate, while the individual island morphology remains unchanged. The surface coverage is mostly incomplete for all three samples.

#### D. UV-Vis absorption spectroscopy

Figure 8 shows the UV-Vis absorption spectra measured for NaT3 films of different thicknesses deposited on  $\parallel$ -MoS<sub>2</sub>. Corresponding data for NaT3 on BK7 optical glass are presented for comparison. These cases represent the face-on on and edge-on configurations of the NaT3 molecules, respectively. The absorption of the pure NaT3 film was obtained by separately measuring and subtracting the substrate absorption curve. The spectra prior to the background subtraction are shown on Fig. S5 in [47]. The UV-Vis data shows an apparent increase of the absorbance with increasing film thickness for both face-on and edge-on oriented NaT3 molecules, with the absorbance being significantly higher for the face-on oriented molecules at the same nominal film thickness. This is expected, since the transition dipole moment  $\mu$  of NaT3 is aligned parallel to its molecular long axis. In the experimental configuration, the incident light is perpendicular to the surface, while the electric field  $E$  is within the surface plane. Thus the absorption is maximized when  $\mu$  and  $E$  are aligned

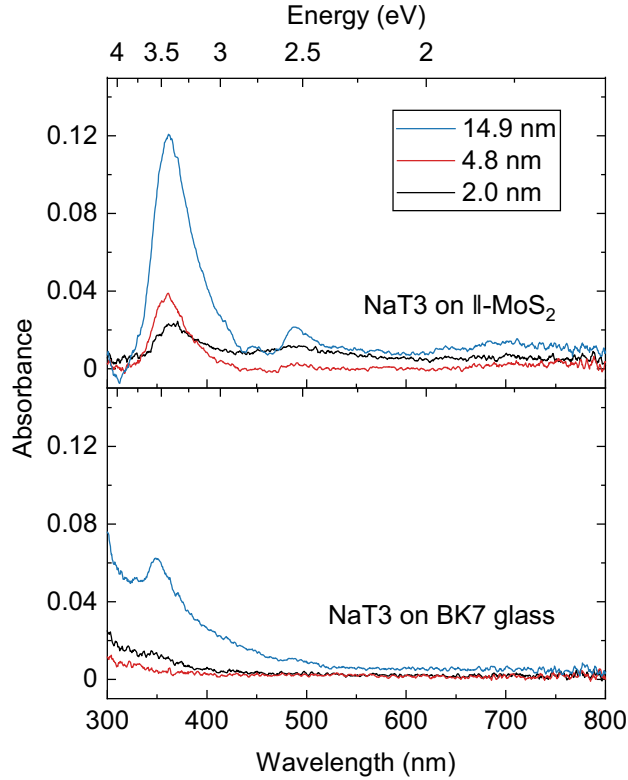


FIG. 8. UV-Vis absorption spectra of NaT3 films with different nominal film thicknesses deposited on  $\parallel$ -MoS<sub>2</sub> and BK7 optical glass, corresponding the face-on and edge-on molecular configuration, respectively.

[54], which is the case for the face-on oriented molecules. Similar results were obtained for diindenoperylene (DIP) molecules on  $\parallel$ -MoS<sub>2</sub> [37], and for other small molecules in face-on configurations [55, 56].

The absorption spectra of the face-on oriented molecules exhibits clear maxima at 364-358 nm, corresponding to the  $\pi - \pi^*$  transition, in order of increasing film thickness. A blueshift of the absorption maximum is observed, which is most prominent from 2 nm to 4.8 nm nominal film thickness. We suspect that the blueshift of the absorption maximum is caused by a change in the molecular conformation, especially considering the change in the lattice  $a$ -parameter within the first few deposited layers (Fig. 6). This result is interesting, since one would expect the absorption peak to be redshifted with increased film thickness due to dielectric screening effects with increasing number of molecular neighbors [57, 58]. In comparison, the absorption maximum of the edge-on oriented molecules is at 350 nm. Again, we attribute the shift in transition energy between the two configurations

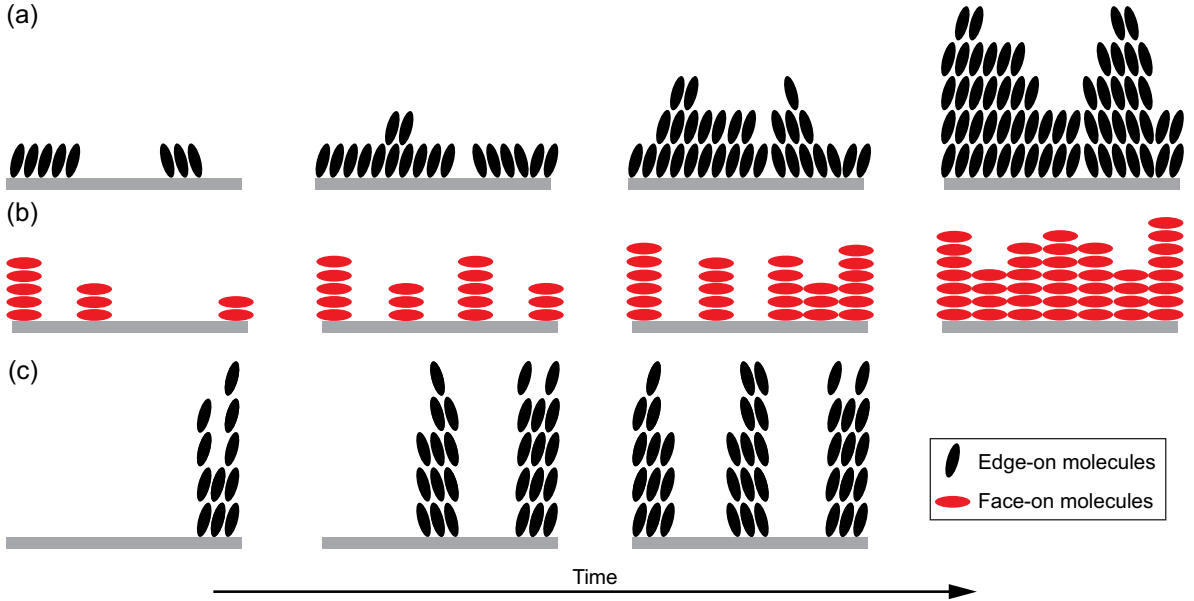


FIG. 9. Schematic of the different growth scenarios reported. (a) NaT2 and NaT3 deposited on SiO<sub>2</sub> with edge-on oriented molecules and SK type growth. (b) NaT3 deposited on ||-MoS<sub>2</sub> with face-on oriented molecules and Volmer-Weber type growth. (c) NaT3 deposited on ⊥-MoS<sub>2</sub> with edge-on oriented molecules and Volmer-Weber type growth.

to changes in the molecular conformation. We point out that the absorption spectrum in the edge-on configuration is mostly in agreement with previous reports, with a slight shift of the absorption maximum [30]. We speculate that this is due to slight changes in molecular conformation in the very thin films measured here.

### E. Growth discussion

From the real-time GIXRD data and the ex situ AFM images, we can infer certain characteristics of the thin film growth. Figure 9a illustrates the suggested growth of NaT2 and NaT3 on silicon dioxide. The two molecules grow in a similar way with a few notable differences. Both films form crystals with edge-on oriented molecules, but the NaT2 film is more ordered than the NaT3 counterpart. The surface morphology indicates that the NaT2 molecules initially form a ML that wets the substrate, and that this wetting layer is not fully completed before nucleation of the second ML begins. The second and third MLs are then formed by epitaxial growth, and once again the third layer nucleates before the completion

of the second layer. The imperfect layer-by-layer growth observed in the first 2-3 MLs is then followed by a transition to 3D island growth. This behavior is typical for Stranski-Krastanov (SK) growth, where 2D layer-by-layer growth of a wetting layer is followed by 3D-growth at a system-dependent threshold thickness. Moreover, the GIXRD measurements indicate that the unit cell structure of the first few layers undergoes a collective change, with further indications that the molecules inside the unit cell undergoes a restructuring and/or reordering.

The picture is very similar for NaT3 grown on silicon dioxide. The off-specular diffuse scattering and the surface morphology both indicate that the first ML is formed by imperfect layer-by-layer growth, i.e. the onset of the second layer nucleation occurs before the completions of the first layer. Furthermore, the observed morphology indicates that the molecules start to form 3D islands already on top of the first ML, suggesting that the substrate-wetting layer has a thickness of 1 ML, while the oscillations of the diffuse scattering intensity indicate that at least 2 MLs are formed by imperfect layer-by-layer growth before the growth has fully transitioned to 3D islands growth. We speculate that the discrepancy between these two results might be due to the real-time GIXRD measurements better capturing the kinetics of the growth, and effects such as post-growth dewetting [23, 25, 59] are evidently not seen.

SK-growth is often observed in other systems of rod-like small-molecules, including other molecules from the family of oligothiophenes such as  $\alpha$ Sexithiophene ( $\alpha$ -6T) [22], which has been shown to form a 2 ML thick substrate-wetting layer on glass substrates before 3D-growth sets in. In comparison, DIP on silicon dioxide exhibits layer-by-layer growth for seven monolayers before 3D-growth sets in [19]. The transition from 2D to 3D growth in DIP (also referred to as rapid roughening) has been attributed to spatial inhomogeneities, that arise at the boundaries between coalesced islands in the first ML due to different in-plane orientation of the molecular tilt vector [60]. Furthermore, the transition from 2D to 3D-growth is temperature dependent, as demonstrated for the model system 3,4,9,10-perylene-tetracarboxylic dianhydride (PTCDA) in the work of Krause *et al.* [61].

Figure 9b illustrates the growth of NaT3 deposited on  $\parallel$ -MoS<sub>2</sub>. The growth is dominated by substrate-molecules interactions, and this leads to nucleation of needle-like crystal structures, that grow as isolated islands (Volmer-Weber type growth) with the molecules oriented face-on on the substrate. The surface morphology indicate that the fibers nucleate

immediately upon the substrate without forming an initial wetting layer, and that the needle density is proportional to the amount of material deposited on the substrate. Considering that the needle height does not appear to exceed 60 nm as the density increases, we suspect that the growth is thermodynamically limited, and that the observed needle shape is the energetically favored under these conditions. The change in lattice parameters indicate a slow expansion of the molecular molecular long axis (situated along the (100)-direction of the crystal) followed by a slow compression, combined with compression of the (h11)-direction of the crystal followed by an expansion. Interestingly, the turnover point in the GIXRD data might correspond to the nominal film thickness at which the needles start to coalesce. Needle growth is commonly observed for organic semiconductors on strongly interacting templated substrates [23, 62, 63], and has previously been demonstrated for NaT3 on muscovite mica [36]. Furthermore, DIP molecules deposited onto similar  $\parallel$ -MoS<sub>2</sub> substrates have been shown to form needle-like crystals, where the average needle height appear to increase with increasing nominal film thickness [37].

Figure 9c illustrates the growth of NaT3 on  $\perp$ -MoS<sub>2</sub>, where the molecules are standing edge-on on the surface. Edge-on orientation of the molecules points towards weaker substrate-molecules interactions than for  $\parallel$ -MoS<sub>2</sub>, presumably because the  $\perp$ -MoS<sub>2</sub> exhibit chemically active dangling bonds that are readily oxidized [45], leading to an oxidized surface, which is expected to interact weaker with the deposited molecules. The surface morphology reveal Volmer-Weber type growth, with tall isolated islands. A low nucleation density of the islands suggests a high nucleation barrier on the  $\perp$ -MoS<sub>2</sub> substrate, and the lack of in-plane correlation agrees well with the GIXRD data. Furthermore, the surface morphology indicates that the average island size remains relatively constant with increasing nominal thickness, and we therefore assume a linear increase in islands density with increasing nominal thickness based on the integrated scattering intensity. The results are surprising, since the aforementioned DIP molecules grow in accordance to the SK-growth mode on a similar substrate [37].

#### IV. CONCLUSIONS

We have investigated the molecular structure and growth of vacuum deposited NaT2 and NaT3 on silicon dioxide and vertically and horizontally aligned few-layer MoS<sub>2</sub>, using

real-time in situ GIXRD complemented by AFM and UV/Vis absorption spectroscopy. On device-relevant silicon dioxide, we found that the NaT2 unit cell undergoes collective in-plane changes within the first 3 molecular layers, indicating that surface-induced strain is relieved beyond this point. This was accompanied by a significant compression of the out-of-plane  $a$ -axis (molecular long axis), which continued, albeit at a slower rate, until the final film thickness (22 nm) was reached. On the other hand, the NaT3 film on silicon dioxide was found to undergo changes in the in-plane and out-of-plane lattice parameters throughout all of the deposition (0-15 nm). The changes in the in-plane unit cell dimensions are greater compared to NaT2, and indicating a greater surface-induced strain compared to NaT2, which is not fully relieved after 6 ML. Both films were found to follow Stranski-Krastanov type growth, where 2D layer-by-layer growth is followed by 3D islands growth. Neither molecule exhibited perfect layer growth of the first, substrate-wetting ML. In the case of NaT3, the growth was fully transitioned to 3D islands growth after no more than 3 MLs.

By employing vertically and horizontally aligned few-layer MoS<sub>2</sub> substrates, the orientation of the molecules could be controlled during the growth. On  $\parallel$ -MoS<sub>2</sub>, both NaT2 and NaT3 molecules adopted face-on orientation, while NaT3 adopted edge-on orientation on  $\perp$ -MoS<sub>2</sub>. In both cases, the NaT3 unit cell underwent changes in its (100) and (h11) d-spacings during the deposition, with the largest changes observed during the initial stages of the film formation. Direct images of the surface morphology revealed that the NaT2 and NaT3 molecules both formed needle-like crystals on  $\parallel$ -MoS<sub>2</sub>, while the NaT3 molecules formed isolated islands consisting of tall pillars on  $\perp$ -MoS<sub>2</sub>. Furthermore, the UV-Vis absorption (monitored along the surface normal) was significantly increased in the NaT3 film on  $\parallel$ -MoS<sub>2</sub> as a result of the molecules adopting face-on orientation.

These results, in addition to highlighting the capabilities of in situ GIXRD, manifest the importance of film-substrate interactions on the growth and structure formation in vacuum deposited organic thin films. This is important in both organic transistors, where the charge transport typically takes place in plane within the first few MLs, and where the transport may be limited by grain boundaries, as well as in OLED/OPV applications with out-of-plane charge transport. It would be desirable to investigate the charge transport in situ to enable direct comparison with the here reported variations in unit cell packing and intergrain connectivity.

## ACKNOWLEDGMENTS

The authors acknowledge DESY (Hamburg, Germany) and SOLEIL (Saint-Aubin, France) for the provision of experimental facilities, Arne Ltzen and Andreas Osadnik of the University of Bonn for providing NaTn powders, and Michael Winokur of the University of Wisconsin-Madison for discussions. This work was financially supported by the instrument center DanScatt, the projects APVV-17-0352 and ITMS 313021T081, the German Academic Exchange Service (DAAD)/Slovak Academy of Sciences (SAV) grant, and the German Research Foundation (DFG).

---

- [1] Y. Wang, L. Sun, C. Wang, F. Yang, X. Ren, X. Zhang, H. Dong, and W. Hu, Organic crystalline materials in flexible electronics, *Chem. Soc. Rev.* **48**, 1492 (2019).
- [2] P. R. Warren, J. F. M. Hardigree, A. E. Lauritzen, J. Nelson, and M. Riede, Tuning the ambipolar behaviour of organic field effect transistors via band engineering, *AIP Advances* **9**, 035202 (2019).
- [3] J. Yuan, Y. Zhang, L. Zhou, G. Zhang, H.-L. Yip, T.-K. Lau, X. Lu, C. Zhu, H. Peng, P. A. Johnson, M. Leclerc, Y. Cao, J. Ulanski, Y. Li, and Y. Zou, Single-junction organic solar cell with over 15% efficiency using fused-ring acceptor with electron-deficient core, *Joule* **3**, 1140 (2019).
- [4] V. Jankus, P. Data, D. Graves, C. McGuinness, J. Santos, M. R. Bryce, F. B. Dias, and A. P. Monkman, Highly efficient TADF OLEDs: How the emitter-host interaction controls both the excited state species and electrical properties of the devices to achieve near 100% triplet harvesting and high efficiency, *Adv. Funct. Mater.* **24**, 6178 (2014).
- [5] Y. Liu, C. Li, Z. Ren, S. Yan, and M. R. Bryce, All-organic thermally activated delayed fluorescence materials for organic light-emitting diodes, *Nat. Rev. Mater.* **3**, 18020 (2018).
- [6] J. Lu, D. Liu, J. Zhou, Y. Chu, Y. Chen, X. Wu, and J. Huang, Porous organic field-effect transistors for enhanced chemical sensing performances, *Adv. Funct. Mater.* **27**, 1700018 (2017).
- [7] H. Li, W. Shi, J. Song, H.-J. Jang, J. Dailey, J. Yu, and H. E. Katz, Chemical and biomolecule sensing with organic field-effect transistors, *Chem. Rev.* **119**, 3 (2018).
- [8] S. Fratini, M. Nikolka, A. Salleo, G. Schweicher, and H. Sirringhaus, Charge transport in high-

- mobility conjugated polymers and molecular semiconductors, *Nat. Mater.* **19**, 491 (2020).
- [9] M. Brinkmann, L. Hartmann, N. Kayunkid, and D. Djurado, Understanding the structure and crystallization of regioregular poly (3-hexylthiophene) from the perspective of epitaxy, in *P3HT Revisited – From Molecular Scale to Solar Cell Devices* (Springer Berlin Heidelberg, 2014) pp. 83–106.
- [10] R. Hildner, A. Köhler, P. Müller-Buschbaum, F. Panzer, and M. Thelakkat,  $\pi$ -conjugated donor polymers: Structure formation and morphology in solution, bulk and photovoltaic blends, *Adv. Energy Mater.* **7**, 1700314 (2017).
- [11] H. Sirringhaus, R. J. Wilson, R. H. Friend, M. Inbasekaran, W. Wu, E. P. Woo, M. Grell, and D. D. C. Bradley, Mobility enhancement in conjugated polymer field-effect transistors through chain alignment in a liquid-crystalline phase, *Appl. Phys. Lett.* **77**, 406 (2000).
- [12] J.-C. Ribierre, T. Tanaka, L. Zhao, Y. Yokota, S. Matsumoto, D. Hashizume, K. Takaishi, T. Muto, B. Heinrich, S. Méry, F. Mathevet, T. Matsushima, M. Uchiyama, C. Adachi, and T. Aoyama, Simultaneous edge-on to face-on reorientation and 1d alignment of small  $\pi$ -conjugated molecules using room-temperature mechanical rubbing, *Adv. Funct. Mater.* **28**, 1707038 (2018).
- [13] E. M. Mannebach, J. W. Spalenka, P. S. Johnson, Z. Cai, F. J. Himpsel, and P. G. Evans, High hole mobility and thickness-dependent crystal structure in  $\alpha,\omega$ -dihexylsexithiophene single-monolayer field-effect transistors, *Adv. Funct. Mater.* **23**, 554 (2012).
- [14] A. O. F. Jones, B. Chattopadhyay, Y. H. Geerts, and R. Resel, Substrate-induced and thin-film phases: Polymorphism of organic materials on surfaces, *Adv. Funct. Mater.* **26**, 2233 (2016).
- [15] L. Pithan, D. Nabok, C. Cocchi, P. Beyer, G. Duva, J. Simbrunner, J. Rawle, C. Nicklin, P. Schäfer, C. Draxl, F. Schreiber, and S. Kowarik, Molecular structure of the substrate-induced thin-film phase of tetracene, *J. Chem. Phys.* **149**, 144701 (2018).
- [16] C. E. Mauldin, K. Puntambekar, A. R. Murphy, F. Liao, V. Subramanian, J. M. J. Frchet, D. M. DeLongchamp, D. A. Fischer, and M. F. Toney, Solution-processable  $\alpha,\omega$ -distyryl oligothiophene semiconductors with enhanced environmental stability, *Chem. Mater.* **21**, 1927 (2009).
- [17] A. Hexemer and P. Müller-Buschbaum, Advanced grazing-incidence techniques for modern soft-matter materials analysis, *IUCrJ* **2**, 106 (2015).

- [18] D. M. DeLongchamp, Y. Jung, D. A. Fischer, E. K. Lin, P. Chang, V. Subramanian, A. R. Murphy, and J. M. J. Fréchet, Correlating molecular design to microstructure in thermally convertible oligothiophenes: the effect of branched versus linear end groups, *J. Phys. Chem. B* **110**, 10645 (2006).
- [19] S. Kowarik, A. Gerlach, and F. Schreiber, Organic molecular beam deposition: fundamentals, growth dynamics, and in situ studies, *J. Phys.: Condens. Matter* **20**, 184005 (2008).
- [20] C. Lorch, K. Broch, V. Belova, G. Duva, A. Hinderhofer, A. Gerlach, M. Jankowski, and F. Schreiber, Growth and annealing kinetics of  $\alpha$ -sexithiophene and fullerene c60mixed films, *J. Appl. Crystallogr.* **49**, 1266 (2016).
- [21] L. J. Richter, D. M. DeLongchamp, and A. Amassian, Morphology development in solution-processed functional organic blend films: An in situ viewpoint, *Chem. Rev.* **117**, 6332 (2017).
- [22] T. L. Derrien, A. E. Lauritzen, P. Kaienburg, J. F. M. Hardigree, C. Nicklin, and M. Riede, In situ observations of the growth mode of vacuum-deposited  $\alpha$ -sexithiophene, *J. Phys. Chem. C* **124**, 11863 (2020).
- [23] R. Zimmerleiter, M. Hohage, and L. Sun, Real-time in situ fluorescence study of  $\alpha$ -6t thin film growth on muscovite mica, *Phys. Rev. Mater.* **3**, 083402 (2019).
- [24] M. Ando, M. Yoneya, T. B. Kehoe, H. Ishii, T. Minakata, M. Kawasaki, C. M. Duffy, R. Phillips, and H. Sirringhaus, Disorder and localization dynamics in polymorphs of the molecular semiconductor pentacene probed by in situ micro-raman spectroscopy and molecular dynamics simulations, *Phys. Rev. Mater.* **3** (2019).
- [25] L. Zhang, X. Fu, M. Hohage, P. Zeppenfeld, and L. D. Sun, Growth of pentacene on  $\alpha$ -al<sub>2</sub>O<sub>3</sub> (0001) studied by in situ optical spectroscopy, *Phys. Rev. Mater.* **1** (2017).
- [26] A. J. Fleming, F. P. Netzer, and M. G. Ramsey, Nucleation and 3d growth of para-sexiphenyl nanostructures from an oriented 2d liquid layer investigated by photoemission electron microscopy, *J. Phys.: Condens. Matter* **21**, 445003 (2009).
- [27] O. Panova, C. Ophus, C. J. Takacs, K. C. Bustillo, L. Balhorn, A. Salleo, N. Balsara, and A. M. Minor, Diffraction imaging of nanocrystalline structures in organic semiconductor molecular thin films, *Nat. Mater.* **18**, 860 (2019).
- [28] A. Sarbu, P. Hermet, D. Maurin, D. Djurado, L. Biniek, M. Diebold, J.-L. Bantignies, P. Mésini, and M. Brinkmann, Supramolecular organization of a h-bonded perylene bisimide organogelator determined by transmission electron microscopy, grazing incidence x-ray diffrac-

- tion and polarized infra-red spectroscopy, *Phys. Chem. Chem. Phys.* **19**, 32514 (2017).
- [29] M. Surin, P. Sonar, A. C. Grimsdale, K. Müllen, S. D. Feyter, S. Habuchi, S. Sarzi, E. Braeken, A. V. Heyen, M. V. der Auweraer, F. C. D. Schryver, M. Cavallini, J.-F. Moulin, F. Biscarini, C. Femoni, R. Lazzaroni, and P. Leclère, Solid-state assemblies and optical properties of conjugated oligomers combining fluorene and thiophene units, *J. Mater. Chem.* **17**, 728 (2007).
- [30] H. Tian, J. Shi, B. He, N. Hu, S. Dong, D. Yan, J. Zhang, Y. Geng, and F. Wang, Naphthyl and thionaphthyl end-capped oligothiophenes as organic semiconductors: Effect of chain length and end-capping groups, *Adv. Funct. Mater.* **17**, 1940 (2007).
- [31] M. J. Winokur, M. K. Huss-Hansen, A. E. Lauritzen, M. Torkkeli, J. Kjelstrup-Hansen, and M. Knaapila, Modeling of grazing-incidence x-ray diffraction from naphthyl end-capped oligothiophenes in organic field-effect transistors, *Cryst. Growth Des.* **20**, 3968 (2020).
- [32] M. K. Huss-Hansen, M. Hodas, N. Mrkyvkova, J. Hagara, B. B. E. Jensen, A. Osadnik, A. Lützen, E. Majková, P. Siffalovic, F. Schreiber, L. Tavares, J. Kjelstrup-Hansen, and M. Knaapila, Surface-controlled crystal alignment of naphthyl end-capped oligothiophene on graphene: Thin-film growth studied by in situ x-ray diffraction, *Langmuir* **36**, 1898 (2020).
- [33] M. K. Huss-Hansen, A. E. Lauritzen, O. Bikondoa, M. Torkkeli, L. Tavares, M. Knaapila, and J. Kjelstrup-Hansen, Structural stability of naphthyl end-capped oligothiophenes in organic field-effect transistors measured by grazing-incidence x-ray diffraction in operando, *Org. Electron.* **49**, 375 (2017).
- [34] J. Linnet, A. R. Walther, O. Albrektsen, L. Tavares, R. L. Eriksen, P. B. W. Jensen, A. Osadnik, S. Hassing, A. Ltzen, and J. Kjelstrup-Hansen, Enhanced photoresponsivity in organic field effect transistors by silver nanoparticles, *Org. Electron.* **46**, 270 (2017).
- [35] A. E. Lauritzen, M. Torkkeli, O. Bikondoa, J. Linnet, L. Tavares, J. Kjelstrup-Hansen, and M. Knaapila, Structural evaluation of 5,5'-bis(naphth-2-yl)-2,2'-bithiophene in organic field-effect transistors with n-octadecyltrichlorosilane coated SiO<sub>2</sub> gate dielectric, *Langmuir* **34**, 6727 (2018).
- [36] F. Balzer, M. Schiek, A. Osadnik, I. Wallmann, J. Parisi, H.-G. Rubahn, and A. Lützen, Substrate steered crystallization of naphthyl end-capped oligothiophenes into nanofibers: the influence of methoxy-functionalization, *Phys. Chem. Chem. Phys.* **16**, 5747 (2014).
- [37] J. Hagara, N. Mrkyvkova, P. Nádaždy, M. Hodas, M. Bodík, M. Jergel, E. Majková, K. Tokár, P. Hutár, M. Sojková, A. Chumakov, O. Konovalov, P. Pandit, S. Roth, A. Hinderhofer,

- M. Hulman, P. Siffalovic, and F. Schreiber, Reorientation of  $\pi$ -conjugated molecules on few-layer MoS<sub>2</sub> films, *Phys. Chem. Chem. Phys.* **22**, 3097 (2020).
- [38] M. Sojková, P. Siffalovic, O. Babchenko, G. Vanko, E. Dobročka, J. Hagara, N. Mrkyvkova, E. Majková, T. Ižák, A. Kromka, and M. Hulman, Carbide-free one-zone sulfurization method grows thin MoS<sub>2</sub> layers on polycrystalline CVD diamond, *Sci. Rep.* **9**, 2001 (2019).
- [39] A. Buffet, A. Rothkirch, R. Döhrmann, V. Körstgens, M. M. A. Kashem, J. Perlich, G. Herzog, M. Schwartzkopf, R. Gehrke, P. Müller-Buschbaum, and S. V. Roth, P03, the microfocus and nanofocus x-ray scattering (MiNaXS) beamline of the PETRA III storage ring: the microfocus endstation, *J. Synchrotron Radiat.* **19**, 647 (2012).
- [40] K. A. Ritley, B. Krause, F. Schreiber, and H. Dosch, A portable ultrahigh vacuum organic molecular beam deposition system for in situ x-ray diffraction measurements, *Rev. Sci. Instrum.* **72**, 1453 (2001).
- [41] M. Basham, J. Filik, M. T. Wharmby, P. C. Y. Chang, B. E. Kassaby, M. Gerring, J. Aishima, K. Levik, B. C. A. Pulford, I. Sikharulidze, D. Sneddon, M. Webber, S. S. Dhesi, F. Maccherozzi, O. Svensson, S. Brockhauser, G. Náray, and A. W. Ashton, Data analysis Work-beNch(DAWN), *J. Synchrotron Radiat.* **22**, 853 (2015).
- [42] J. A. Merlo, C. R. Newman, C. P. Gerlach, T. W. Kelley, D. V. Muyres, S. E. Fritz, M. F. Toney, and C. D. Frisbie, p-channel organic semiconductors based on hybrid acene-thiophene molecules for thin-film transistor applications, *J. Am. Chem. Soc.* **127**, 3997 (2005).
- [43] D.-M. Smilgies, Scherrer grain-size analysis adapted to grazing-incidence scattering with area detectors, *J. Appl. Crystallogr.* **42**, 1030 (2009).
- [44] D. Nečas and P. Klapetek, Gwyddion: an open-source software for SPM data analysis, *Cent. Eur. J. Phys.* **10**, 181 (2012).
- [45] D. Kong, H. Wang, J. J. Cha, M. Pasta, K. J. Koski, J. Yao, and Y. Cui, Synthesis of MoS<sub>2</sub> and MoSe<sub>2</sub> films with vertically aligned layers, *Nano Lett.* **13**, 1341 (2013).
- [46] M. K. Huss-Hansen, M. Hansteen, J. Linnet, A. R. Walther, J. Kjelstrup-Hansen, and M. Knaapila, Structural basis for a naphthyl end-capped oligothiophene with embedded metallic nanoparticles for organic field-effect transistors, *Appl. Phys. Lett.* **113**, 251903 (2018).
- [47] See Supplemental Material at [URL will be inserted by publisher] for additional data figures.
- [48] D. Bowen and B. Tanner, *High Resolution X-Ray Diffractometry And Topography* (CRC Press, Lon, 1998).

- [49] S. Kowarik, A. Gerlach, S. Sellner, F. Schreiber, L. Cavalcanti, and O. Konovalov, Real-time observation of structural and orientational transitions during growth of organic thin films, *Phys. Rev. Lett.* **96**, 125504 (2006).
- [50] S. K. Sinha, E. B. Sirota, S. Garoff, and H. B. Stanley, X-ray and neutron scattering from rough surfaces, *Phys. Rev. B* **38**, 2297 (1988).
- [51] S. Bommel, N. Kleppmann, C. Weber, H. Spranger, P. Schäfer, J. Novak, S. Roth, F. Schreiber, S. Klapp, and S. Kowarik, Unravelling the multilayer growth of the fullerene c60 in real time, *Nat. Commun.* **5**, 1 (2014).
- [52] T. Watanabe, T. Koganezawa, M. Kikuchi, H. Muraoka, S. Ogawa, N. Yoshimoto, and I. Hirose, In situ characterization of the film coverage and the charge transport in the alkylated-organic thin film transistor, *Jpn. J. Appl. Phys.* **57**, 03EG14 (2018).
- [53] J. Hagara, N. M. Tesarova, L. Feriancova, M. Putala, P. Nadazdy, M. Hodas, A. Shaji, V. Nádaždy, M. Huss-Hansen, M. Knaapila, J. Hagenlocher, N. Rußegger, M. Zwadlo, L. Merten, M. Sojkova, M. Hulman, alina vlad, P. Pandit, S. V. Roth, M. Jergel, E. Majkova, A. Hinderhofer, P. Siffalovic, and F. Schreiber, Novel highly substituted thiophene-based n-type organic semiconductor: Structural study, optical anisotropy and molecular control, *CryStEngComm* (2020).
- [54] C. Schünemann, D. Wynands, K.-J. Eichhorn, M. Stamm, K. Leo, and M. Riede, Evaluation and control of the orientation of small molecules for strongly absorbing organic thin films, *J. Phys. Chem. C* **117**, 11600 (2013).
- [55] N. Shioya, R. Murdey, K. Nakao, H. Yoshida, T. Koganezawa, K. Eda, T. Shimoaka, and T. Hasegawa, Alternative face-on thin film structure of pentacene, *Sci. Rep.* **9** (2019).
- [56] K. Yamada, M. Suzuki, T. Suenobu, and K. Nakayama, High vertical carrier mobilities of organic semiconductors due to a deposited laid-down herringbone structure induced by a reduced graphene oxide template, *ACS Appl. Mater. Interfaces* **12**, 9489 (2020).
- [57] H. Proehl, T. Dienel, R. Nitsche, and T. Fritz, Formation of solid-state excitons in ultrathin crystalline films of PTCDA: From single molecules to molecular stacks, *Phys. Rev. Lett.* **93**, 097403 (2004).
- [58] U. Heinemeyer, K. Broch, A. Hinderhofer, M. Kytka, R. Scholz, A. Gerlach, and F. Schreiber, Real-time changes in the optical spectrum of organic semiconducting films and their thickness regimes during growth, *Phys. Rev. Lett.* **104**, 257401 (2010).

- [59] S. Kowarik, A. Gerlach, S. Sellner, L. Cavalcanti, and F. Schreiber, Dewetting of an organic semiconductor thin film observed in real-time, *Adv. Eng. Mater.* **11**, 291 (2009).
- [60] A. C. Dürr, F. Schreiber, K. A. Ritley, V. Kruppa, J. Krug, H. Dosch, and B. Struth, Rapid roughening in thin film growth of an organic semiconductor (diindenoperylene), *Phys. Rev. Lett.* **90**, 016104 (2003).
- [61] B. Krause, F. Schreiber, H. Dosch, A. Pimpinelli, and O. H. Seeck, Temperature dependence of the 2d-3d transition in the growth of PTCDA on ag(111): A real-time x-ray and kinetic monte carlo study, *Europhys. Lett.* **65**, 372 (2004).
- [62] L. Kankate, F. Balzer, H. Niehus, and H.-G. Rubahn, Organic nanofibers from thiophene oligomers, *Thin Solid Films* **518**, 130 (2009).
- [63] G. Koller, S. Berkebile, J. R. Krenn, G. Tzvetkov, G. Hlawacek, O. Lengyel, F. P. Netzer, C. Teichert, R. Resel, and M. G. Ramsey, Oriented sexiphenyl single crystal nanoneedles on TiO<sub>2</sub> (110), *Adv. Mater.* **16**, 2159 (2004).

## SUPPORTING INFORMATION

### Early-stage growth observations of orientation-controlled vacuum-deposited naphthyl end-capped oligothiophenes

Mathias K. Huss-Hansen,<sup>1,\*</sup> Martin Hodas,<sup>2</sup> Nada Mrkyvkova,<sup>3,4</sup>

Jakub Hagara,<sup>3</sup> Peter Nadazdy,<sup>3</sup> Michaela Sojkova,<sup>5</sup> Simon O. Høegh,<sup>6</sup>

Alina Vlad,<sup>7</sup> Pallavi Pandit,<sup>8</sup> Eva Majkova,<sup>3,4</sup> Peter Siffalovic,<sup>3,4</sup>

Frank Schreiber,<sup>2</sup> Jakob Kjelstrup-Hansen,<sup>6</sup> and Matti Knaapila<sup>1</sup>

<sup>1</sup>*Department of Physics, Technical University of Denmark, 2800 Kgs. Lyngby, Denmark*

<sup>2</sup>*Institut für Angewandte Physik, Universität Tübingen, 72076 Tübingen, Germany*

<sup>3</sup>*Institute of Physics, Slovak Academy of Sciences, 84511 Bratislava, Slovakia*

<sup>4</sup>*Center for Advanced Materials Application,*

*Slovak Academy of Sciences, 84511 Bratislava, Slovakia*

<sup>5</sup>*Institute of Electrical Engineering,*

*Slovak Academy of Sciences, 84104 Bratislava, Slovakia*

<sup>6</sup>*NanoSYD, Mads Clausen Institute,*

*University of Southern Denmark, 6400 Sønderborg, Denmark*

<sup>7</sup>*Synchrotron SOLEIL, L'Orme des Merisiers, 91190 Saint-Aubin, France*

<sup>8</sup>*Photon Science, Deutsches Elektronen-Synchrotron (DESY), 22607 Hamburg, Germany*

(Dated: October 16, 2020)

---

\* Author to whom correspondence should be addressed: mathias.huss-hansen@fysik.dtu.dk

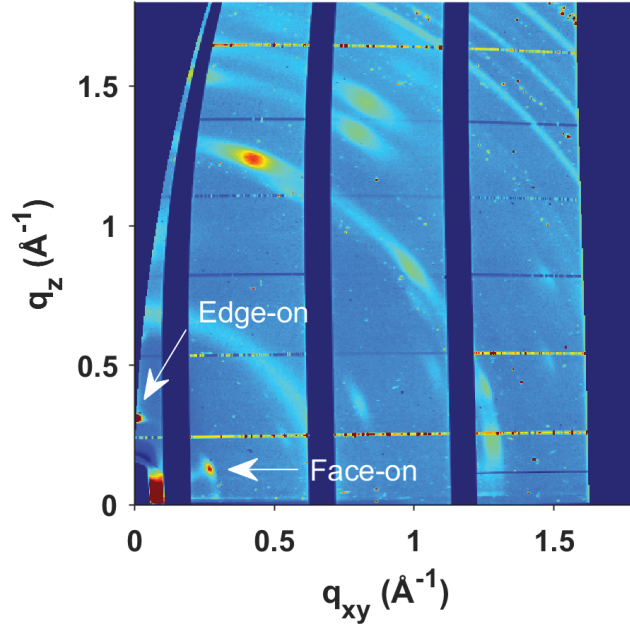


FIG. S1. Reciprocal space map of NaT2 film deposited on  $\parallel$ -MoS<sub>2</sub>. The two (100) Bragg reflections (indicated by white arrows) are indicative of two crystalline phases: one where the NaT2 molecules are oriented edge-on and one where they are oriented face-on. We speculate that the MoS<sub>2</sub> surface coverage is incomplete on the employed substrate, resulting in the growth of the edge-on structure in areas where the underlying Al<sub>2</sub>O<sub>3</sub> is exposed.

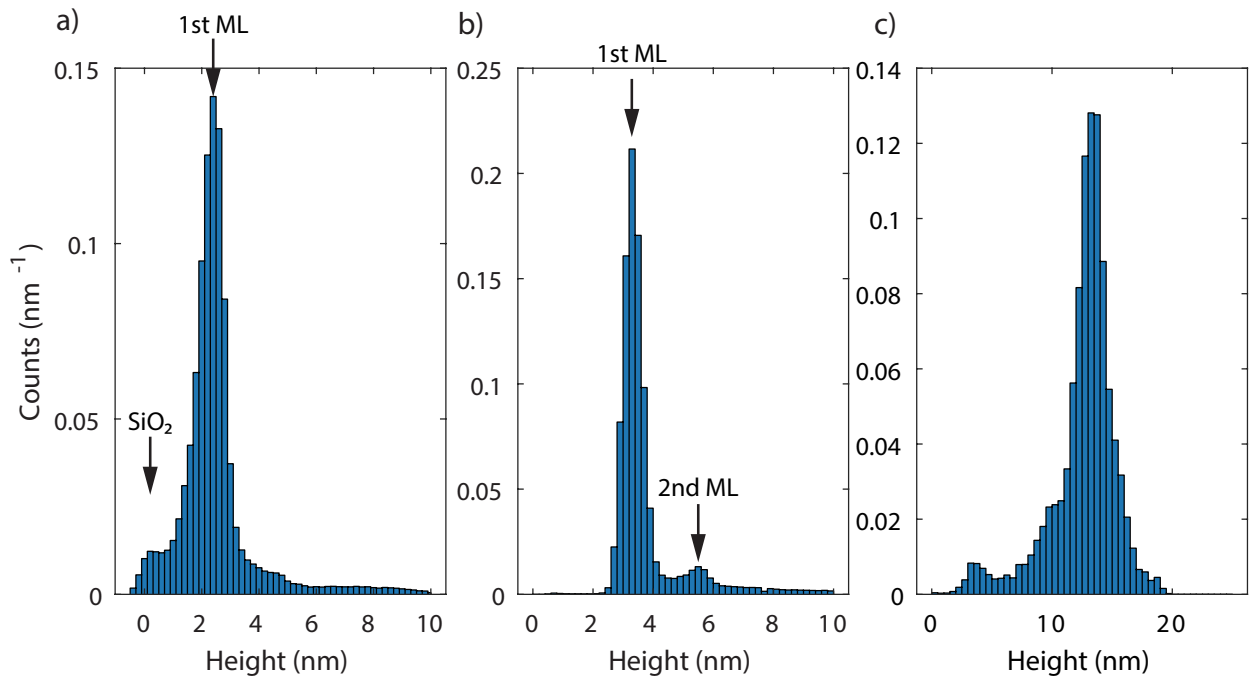


FIG. S2. Height distributions of AFM data from NaT3 films on silicon dioxide with nominal thicknesses of (a) 2.0 nm, (b) 4.8 nm, and (c) 14.9 nm. The arrows indicate the distribution peaks of the SiO<sub>2</sub> substrate, 1st, and 2nd ML, respectively

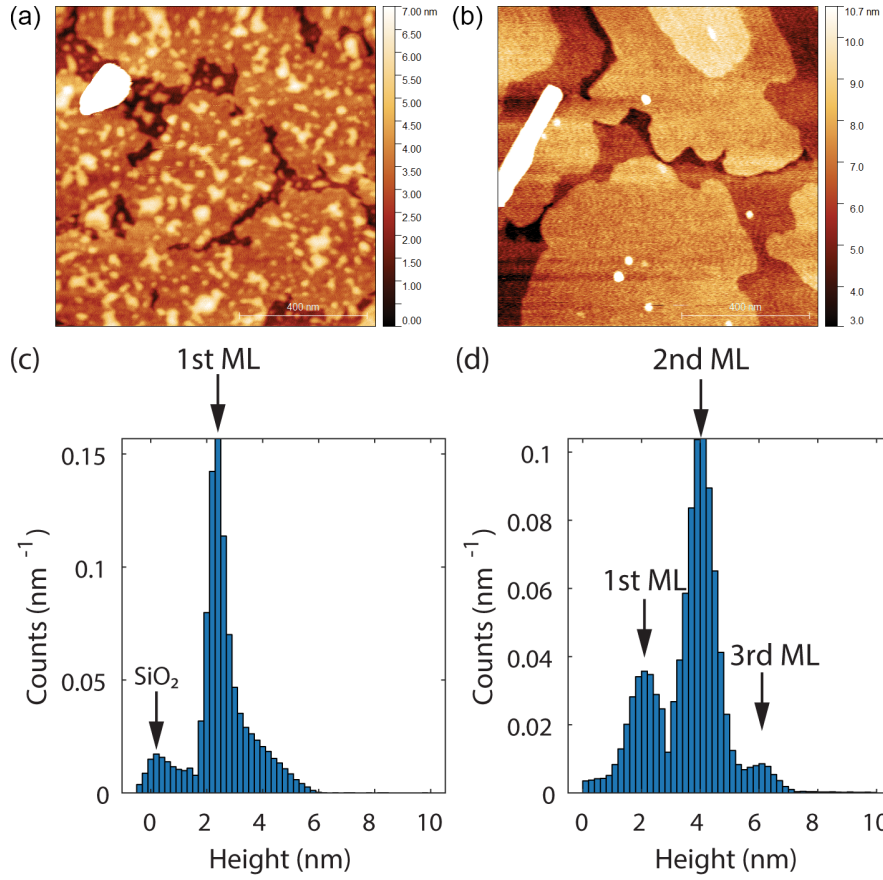


FIG. S3. AFM images of NaT2 film on silicon dioxide at (a) 2.0 nm ( $\sim 1.0$  ML) and (b) 5.0 nm ( $\sim 2.4$  MLs) nominal film thickness. (c-d) Corresponding height distributions of AFM data. The image at 1.0 ML shows a nearly completed first monolayer with the second layer starting to nucleate. At 2.4 MLs, the first monolayer is completed, the second monolayer is nearly completed and the third layer has begun to nucleate. The distribution peaks of the  $\text{SiO}_2$  substrate, 1st, 2nd, and 3rd ML are all clearly identified and marked with arrows.

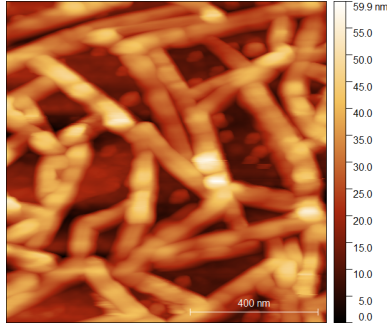


FIG. S4. AFM image of NaT2 film on  $\parallel$ -MoS<sub>2</sub> with nominal film thickness of 20 nm. The molecules adopt fiber-like morphology on the  $\parallel$ -MoS<sub>2</sub> substrate.

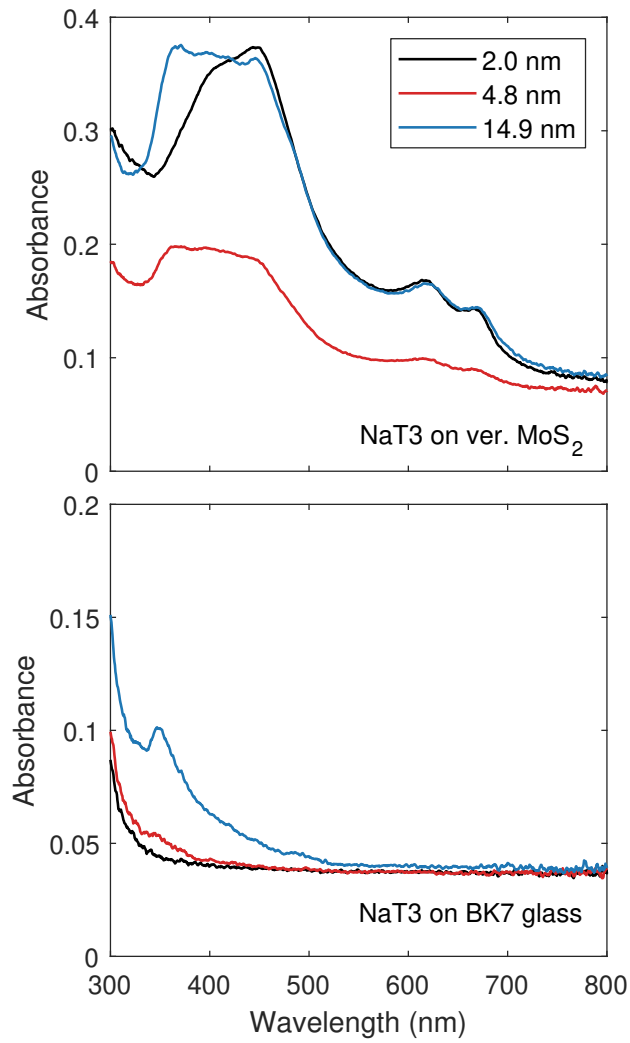


FIG. S5. UV-Vis absorption spectra of NaT3 films as measured.



## Paper IV

---

Submitted to *Adv. Eng. Mater.* on January 22, 2021.

Paper IV is a feature article written for a special issue of *Advanced Engineering Materials* on the use of synchrotron applications in the field of materials science. It concerns the use of microfocused GIWAXS ( $\mu$ GIWAXS) to probe the lateral variations in the microstructure of OFETs. The first reported use of this technique was in 2012 by Amassian and co-workers [234], in which they map lateral variations in the microstructure across a OFET channel in diF-TES-ADT film (c.f. Fig. 2.1). In the paper, we review two pioneering uses of  $\mu$ GIWAXS (including Ref. [234]), and present our own results from using  $\mu$ GIWAXS to map the microstructure of NaT3 in an OFET across an array of interdigitated electrodes. The results are then discussed in view of mobility contact limiting proximity effects, including grain boundaries and paracrystalline disorder. Finally, we give our perspective on how the  $\mu$ GIWAXS technique can benefit the field of organic electronics, in a world where contemporary X-ray optics allows for well collimated beams at virtually every synchrotron source.

# Structural effects of electrode proximity in vacuum deposited organic semiconductors studied by microfocussed X-ray scattering

Mathias K. Huss-Hansen\* and Matti Knaapila

*Department of Physics, Technical University of Denmark, 2800 Kgs. Lyngby, Denmark*

Jakob Kjelstrup-Hansen

*NanoSYD, Mads Clausen Institute, University of Southern Denmark, 6400 Sønderborg, Denmark*

(Dated: February 9, 2021)

Organic semiconductors have seen widespread application in thin-film devices, such as organic field-effect transistors (OFETs), whose performance is closely linked to the molecular level microstructure and crystalline orientation. In actual OFETs, the microstructure can vary significantly based on the local environment, for example in the proximity of contact electrodes. Here we highlight recent examples where microfocussed grazing incidence wide-angle X-ray scattering ( $\mu$ GIWAXS) maps structural information in between the OFET electrodes. Moreover, we employ  $\mu$ GIWAXS to study the microstructure of naphthyl end-capped oligothiophenes across interdigitated electrode arrays in a bottom-contact OFET and identify lateral proximity effects of the contact electrodes in terms of crystalline misorientation, crystallite size and disorder. Our results, as well as those highlighted, classify essential structural parameters on and in between the electrodes; and demonstrate capabilities of microfocussed X-rays to map microstructure in actual devices. The ideas presented in this article bring us towards guidelines for understanding electrode proximity and device performance in molecular semiconductors. We also believe that they are readily expanded from OFETs to other devices and from small molecules to polymers and other materials.

## I. INTRODUCTION

A great deal of interest has been placed on studies of (opto-)electronic devices made from organic semiconductors (OSCs), including organic field-effect transistors (OFETs), organic LEDs (OLEDs), organic photovoltaics and diverse photosensors among other [1–4]. The prospects of these materials are many: low manufacturing costs and large scale processing, mechanical flexibility for use in flexible devices, and facile chemical modifications to tailor their optical and electronic properties.

Device performance is closely linked to the morphology and microstructure of the OSCs, and much attention has been devoted to study this correlation. Important structural features include crystallinity, molecular orientation [5], crystal grain size [6], grain boundaries [7], and polymorphism and surface-induced phases [8]. The primary focus in the open literature lies on reporting microstructure of devices as a whole. Yet, single measurements over entire devices may not be sufficient to account for local structural inhomogeneities.

The thin-film structure in OSCs is controlled by two competing forces: surface-molecule interactions and intermolecular interactions, including weak van der Waals forces. The former is affected by the local surface chemistry, and variations in e.g. the surface energy can lead to disparities in microstructure [5, 9]. Such microstructural variations are commonly studied across the substrate-OSC interface, and across interfaces within multilayer devices (i.e. along the surface normal), but less attention

is placed on lateral proximity effects, for example those arising from patterned electrodes in bottom-contact devices. In OFETs, these contact proximity effects become increasingly important when the channel dimensions are minimized, since the channel resistance generally decreases with channel length, while the contact resistance remains unaffected [10].

Grazing incidence wide-angle scattering (GIWAXS), or sometimes grazing-incidence X-ray diffraction (GIXRD), is an increasingly popular surface sensitive technique for probing the microstructure of thin films. For a full discussion of GIWAXS applications in organic thin-films, we direct the reader to the large body of literature in the subject [11–13]. In the typical grazing-incidence geometry, the incoming X-ray beam is directed towards the sample surface at a shallow angle, that is carefully controlled by the sample tilt. The small incidence angle (typically below  $1^\circ$ ) causes most of the X-rays to be reflected of the sample surface or of the substrate surface, depending on the critical angle of the given material. Assuming that the substrate is heavier than the OSC film, its critical angle for X-rays is also larger. If the incidence angle is kept below the critical angle of the substrate and slightly above the critical angle of the material, the microstructure of the entire film can be characterized in one measurement, or alternatively, the structure can be profiled as a function of sample depth by varying the incidence angle [14]. Because most OSC thin-films are macroscopically isotropic within the plane (sometimes called as fiber-textured), a single scattering pattern can give information on the in-plane structure (along the  $Q_{xy}$  momentum transfer axis) and the out-of-plane structure ( $Q_z$ ) simultaneously.

By combining GIWAXS with recent advances in mi-

---

\* mathias.huss-hansen@fysik.dtu.dk

crofocussed X-ray beams [15–17], it is possible to map or profile local inhomogeneities OSC films on device relevant length scales [18]. With this article, we present the reader with an overview of how microfocused GIWAXS ( $\mu$ GIWAXS) is employed to study local microstructure within metal electrodes in actual OFET devices. First, we review two cases highlighting the ability of the  $\mu$ GIWAXS technique to map single OSC channels between two parallel electrodes, and to map the OSC on top of the contact electrodes themselves. We subsequently move on to another application, where we use  $\mu$ GIWAXS to map local microstructure in an OFET across an array of interdigitated electrodes. The employed bottom-contact OFET is fabricated by vacuum-depositing a prototypical rigid OSC, 5,5''-bis(naphth-2-yl)-2,2' : 5',5''-terthiophene (NaT3) atop a Si/SiO<sub>2</sub> substrate with patterned Au electrodes. Our findings show that the crystalline misorientation, crystal size and lattice disorder depend on the film location in the channel or atop the contact electrodes, and can be discussed in view of mobility limiting proximity effects, including grain boundaries and disorder. Finally, we give our perspective on how the technique can benefit the field of organic electronics, polymer science and beyond.

## II. HIGHLIGHTED APPLICATIONS OF $\mu$ GIWAXS

We first highlight two pioneering articles where  $\mu$ GIWAXS has been used to probe the difference in microstructure between electrode and channel in OFETs. In the first study, Li et al. [18] used  $\mu$ GIWAXS to map the local microstructure of organic OSC films in bottom-contact OFETs. Specifically, they fabricated films of fluorinated 5,11-bis(triethylsilylethynyl) anthradithiophene (diF-TES-ADT) by spin casting a 2% wt. molecule-chlorobenzene solution on top of Si/SiO<sub>2</sub> substrates with patterned Au electrodes. Prior to spin casting, the bottom Au contacts were treated with pentafluorobenzene thiol (PFBT). The authors chose two different sets of spin casting parameters in order to obtain films with either larger (type 1) or smaller (type 2) grain extensions from the Au contacts. Devices with varying channel length were then investigated by  $\mu$ GIWAXS, with the employed X-ray beam focused to 10  $\mu$ m in the transverse direction, enabling device mapping with similar spatial resolution.

Figure 1 shows the mapped microstructure across devices of sample type 2 (a and b) and sample type 1 (c and d) with channel lengths of 80  $\mu$ m (a and c) and 20  $\mu$ m (b and d), respectively. For each device, the structural parameters are shown along with a schematic map and a polarized optical micrograph of the device. The  $\mu$ GIWAXS patterns (Fig. 1 in Ref.[18]) revealed two distinct diF-TES-ADT film textures:  $\langle 001 \rangle$  texture with the molecules oriented edge-on on the substrate and  $\langle 111 \rangle$  texture with the molecules oriented face-on with respect to the substrate. The integrated scattering intensities

of these phases are plotted together with the integrated intensities of the Au contacts, allowing for easy identification of channel and contact areas. The mapping reveals that the  $\langle 111 \rangle$  texture only appears in the channel of the type 2 device with a channel length of 80  $\mu$ m. In both type 1 devices, and in the type 2 device with shorter channel length, the edge-on  $\langle 001 \rangle$  phase is able to bridge the channel gap. In addition to mapping the phase composition, the authors also use the  $\mu$ GIWAXS results to obtain information about local misorientation and grain size. Figure 1 shows, moreover, that while the out-of-plane grain size and misorientation of the  $\langle 001 \rangle$  textured crystallites remains unchanged across the smaller channels, there is a significant change towards the center of the 80  $\mu$ m channel in both type 1 and 2 devices.

From the  $\mu$ GIWAXS results presented in Fig. 1, the authors are able to elucidate the drop-off in mobility obtained in type 2 devices when the channel length exceeds 50  $\mu$ m (mobility data shown in Fig. 3 of Ref.[18]), which can be attributed to the onset of formation of  $\langle 111 \rangle$  textured crystallites. These findings are not necessarily possible with direct imaging methods, which are not specific probes for crystals. For example, the polarized optical micrograph in Fig. 1b would suggest that the crystallites formed at the Au contact might not bridge the channel. However, the  $\mu$ GIWAXS results find the structure to be uniform throughout the length of the channel.

In another study, Lampert et al.[19] likewise employed  $\mu$ GIWAXS to study the local microstructure of diF-TES-ADT on Au contacts treated with PFBT. They prepared devices by varying the deposition rate for the bottom Au contacts between 0.5  $\text{\AA}/\text{s}$  and 3  $\text{\AA}/\text{s}$ . The  $\mu$ GIWAXS results revealed no discernible differences in the microstructure of the film deposited on top of the electrodes in the two cases. These findings demonstrate that the reported increase in mobility obtained from using a slower contact deposition rate does not stem from a change in the thin-film microstructure. Rather, it is an effect intrinsic to the structure of the electrode.

## III. RESULTS

Here we present the results of  $\mu$ GIWAXS employed to map an NaT3 OFET across multiple electrodes. Figure 2 shows the experimental setup together with examples of individual  $\mu$ GIWAXS measurements. Figure 2a and b show the chemical structure of NaT3 and its preferential orientation atop OFET surfaces. The molecules adopt edge-on orientation, where the  $b,c$ -plane is aligned parallel to the substrate and the molecular long-axis is pointed out-of-plane at a small angle. Individual crystallites are randomly oriented in-plane, resulting in a mosaic structure of the film (fiber-texture). This texture is easily identified by the lack of change in the scattering pattern when rotating the sample about its surface normal. In addition to the random in-plane orientation, the crystallites also exhibit a degree of misorientation with respect

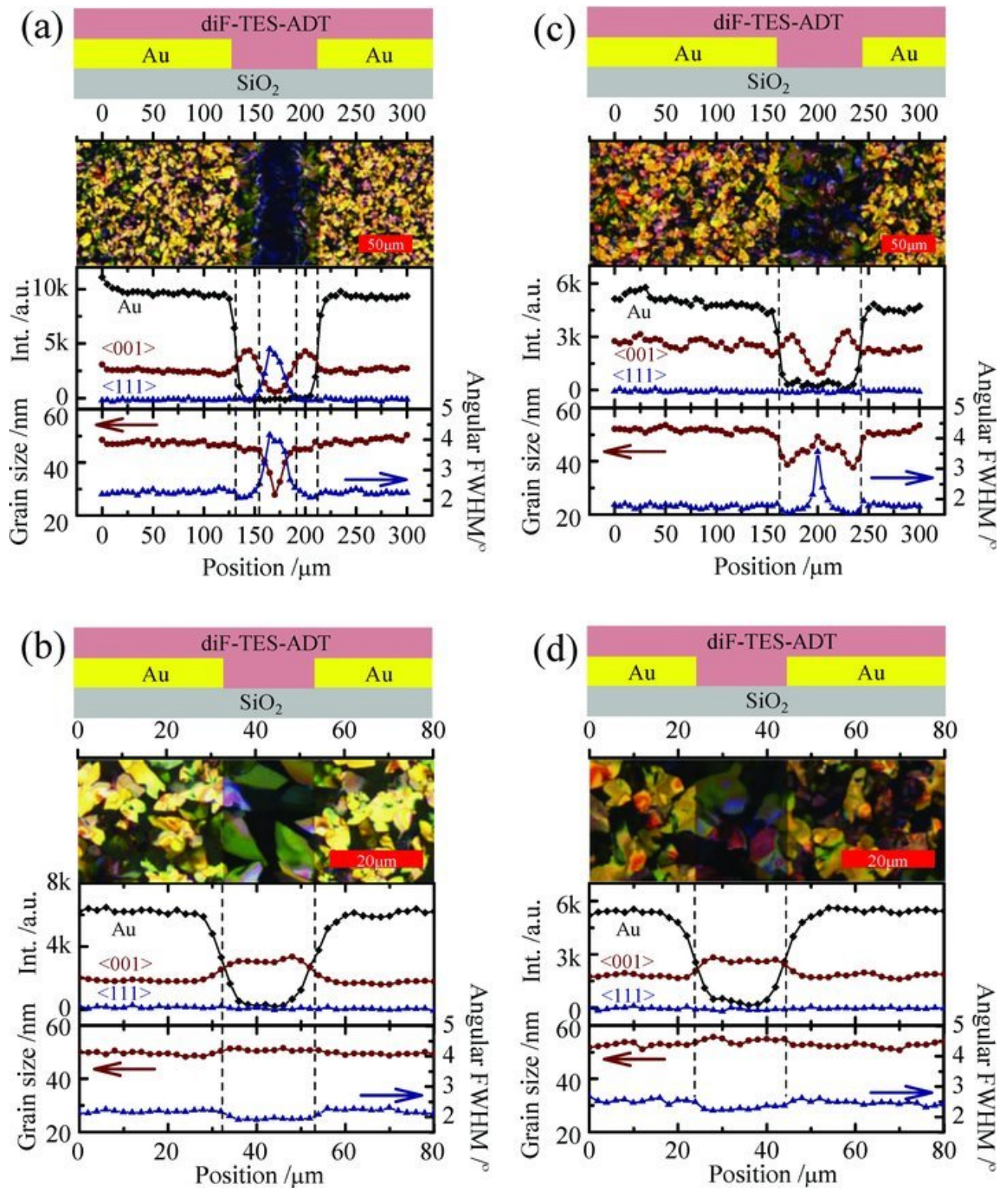


FIG. 1. Microstructural mapping of solution-casted diF-TES-ADT devices of (a,b) type 2 and (c,d) type 1 with channel lengths of (a,c) 80  $\mu\text{m}$  and (b,d) 20  $\mu\text{m}$ , respectively. Each panel shows a schematic map of the device, a polarized optical micrograph of the film, the integrated intensity map of the diffraction peaks associated to Au,  $\langle 001 \rangle$  and  $\langle 111 \rangle$  diF-TES-ADT textures, and the out-of-plane lamellar crystal size and angular FWHM obtained from the 001 Bragg reflection of  $\langle 001 \rangle$ -textured crystals. Reproduced with permission.<sup>[Ref.[18]]</sup> Copyright 2012, Wiley-VCH Verlag GmbH & Co.

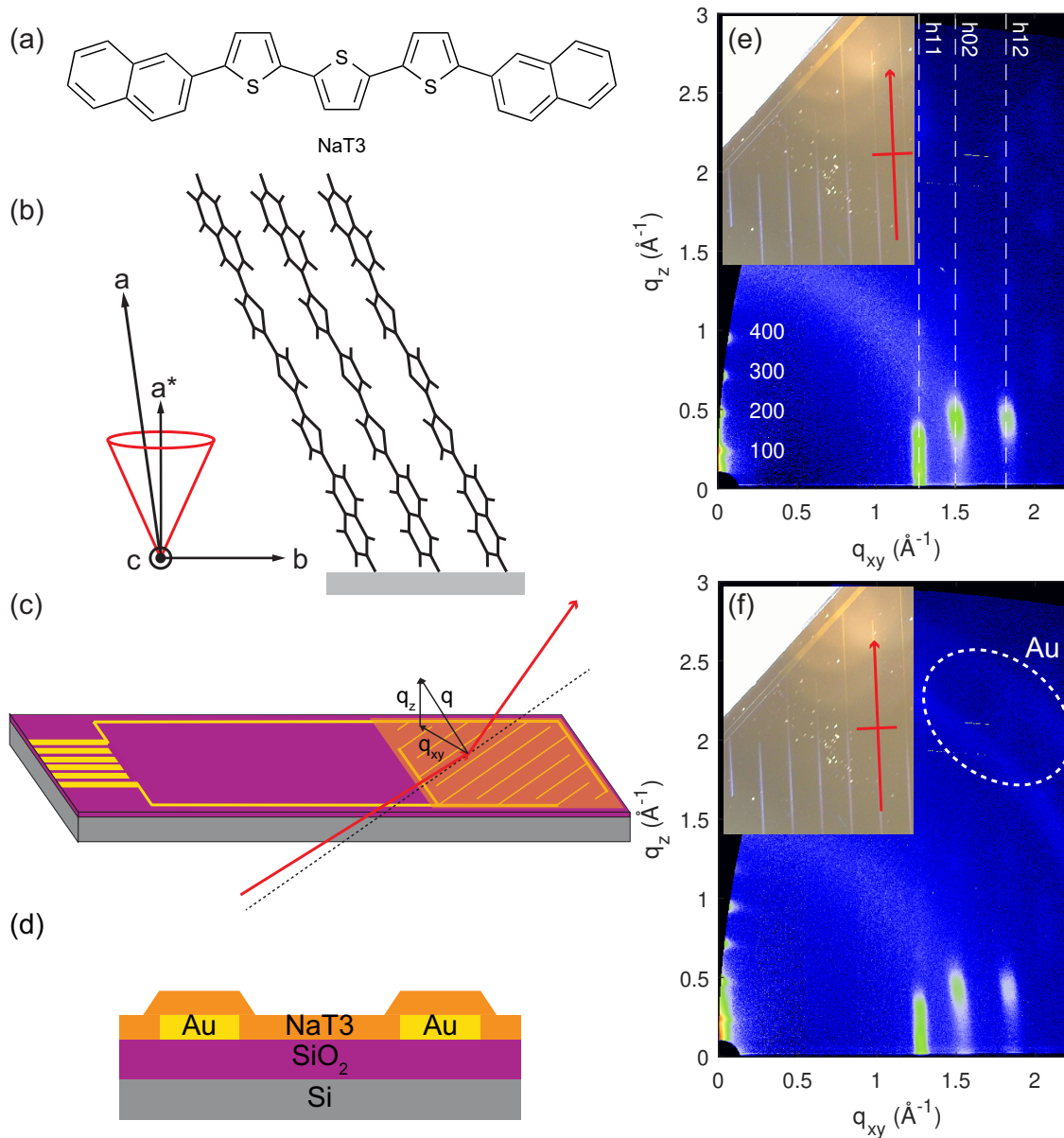


FIG. 2. (a) Chemical structure of NaT3. (b) Illustration of the packing structure in the NaT3 thin-film. The cone represents the orientation distribution of the fiber-textured crystallites. (c) Schematic of the  $\mu$ GIWAXS geometry and the bottom-contact OFET. (d) Schematic side-view of the same device. (e)-(f)  $\mu$ GIWAXS patterns at two key locations (channel and electrode) of the device. The inserts show optical micrographs of the corresponding beam positions. Dashed line in (e) indicates scattering from planes with same  $k$  and  $l$  Miller indices. The circled area in (f) indicates the scattering from the Au electrode.

the surface normal. This orientation distribution can be visualized by the distribution cone of the  $a^*$ -axis shown in Fig. 2b. Figures 2c and d illustrate the  $\mu$ GIWAXS setup and the OFET configuration. The small transverse footprint of the beam allows us to probe areas of

the OFET with a resolution of  $30\ \mu\text{m}$ , while the extended longitudinal footprint due to the (very shallow) grazing angle ensures that the thin film volume is statistically significant. By carefully aligning the X-ray beam parallel to the interdigitated electrodes, we are able to obtain spa-

tial information from the OFET device where the channel and electrode areas can be identified and treated separately. Our bottom-contact OFET design has 30  $\mu\text{m}$  wide interdigitated electrodes with 470  $\mu\text{m}$  channel length (distance between source and drain electrode), allowing us to resolve individual electrodes with the employed microbeam. Figures 2e and f show typical  $\mu\text{GIWAXS}$  patterns corresponding to channel and electrode areas of the OFET device, respectively. The inserts show optical micrographs of the OFET device with a crosshair to indicate the approximate position of the X-ray microbeam. From the  $\mu\text{GIWAXS}$  images, it is apparent that the overall thin film texture is the same in both areas, with the molecules adopting the previously described edge-on orientation. On the electrode, two faint diffraction rings are visible arising from the Au 111 and 200 diffraction rings. These diffraction signals can be used as markers to indicate the position of the microbeam in the data. The scattering pattern can be indexed with a monoclinic unit cell as shown by lines corresponding to crystal planes with same  $k$  and  $l$  Miller indices in Fig. 2e.

Figure 3 shows the microstructure of an OFET with a 30 nm NaT3 thin-film. For this device, the integrated intensity of the Au 111 reflections and the NaT3 100 reflection is plotted together with the angular full-width half-maximum (FWHM) of the NaT3 100 reflection and the in-plane crystal grain-size. The intensity of the Au 111 reflection allows us to distinguish the data from the electrode area from that of the channel area. We point out that the measurement step size being smaller than the actual footprint of the X-ray beam (10  $\mu\text{m}$  vs 31  $\mu\text{m}$ ) leads to the edges of the electrodes appearing blurred in the Au (111) intensity map.

Placing our attention on the NaT3 100 reflection intensity, we find that it decreases in an approximately linear fashion as the beam is scanned across the device. This is a consequence of the employed electrode layout, where the electrodes are oriented at a  $45^\circ$  angle with respect to the substrate edge (see Fig. 2c). Therefore, as the beam moves towards the corner of the interdigitated electrodes, the effective width of the illuminated film decreases, decreasing the scattering volume. At the same time, we observe an even further decrease in the NaT3 100 reflection intensity on top of the electrodes. This trend is mirrored in the intensity of the  $h11$  Bragg reflection (not shown). Similarly, the NaT3 crystallites exhibit a significant broadening of the angular 100 FWHM on top of the electrodes, indicating an increase out-of-plane misorientation of the crystallites. The increased misorientation of the crystallites atop the electrodes as compared to in the channel is also evident by the increased broadening of the tail in higher order  $h00$  reflection (Figs. 2e and f).

Finally, we map the in-plane crystalline grain size by applying the Scherrer equation to the  $q_{xy}$  peak profile of the  $h02$  reflection. To account for the change in effective sample width, the geometric smearing of the Bragg peak was modeled and subtracted before the grain size analysis. Nevertheless, the grain size obtained in this manner

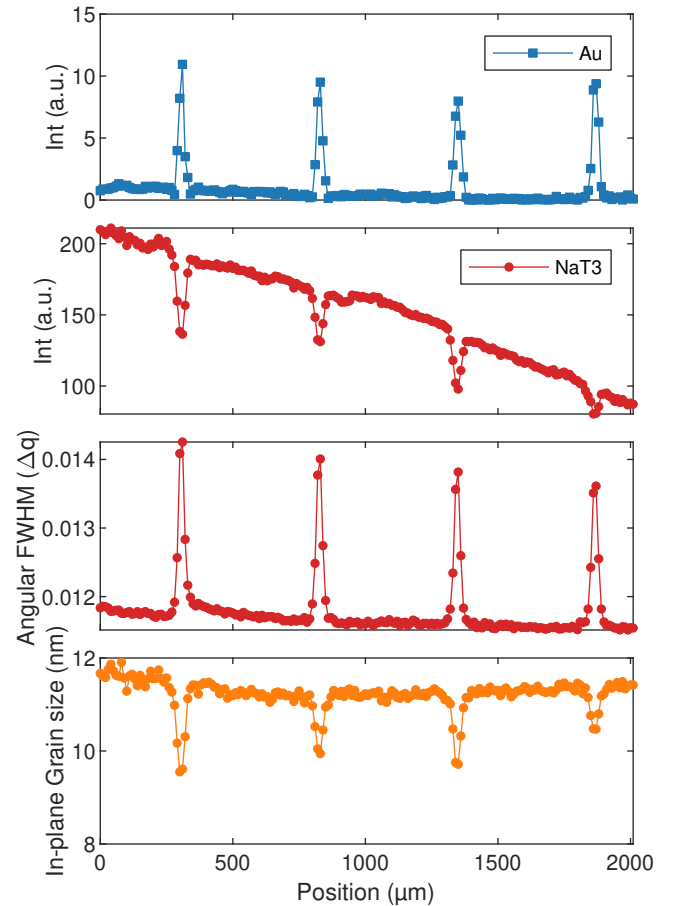


FIG. 3. Selected structural parameters plotted against the horizontal position in the studied OFET. From top to bottom: integrated Au 111 reflection intensity, integrated NaT3 100 reflection intensity, angular FWHM of the NaT3 100 reflection and in-plane grain size obtained by applying the Scherrer formula to the  $q_{xy}$  FWHM of the NaT2  $h02$  reflection. The data set spans over 5 channels and 4 electrodes.

can be thought of only as a lower limit of the true grain size. We find that the in-plane grain size is slightly lower on top of the electrodes compared to in the channel. All these findings together point toward an overall improved microstructure in the channel, possibly due to lower surface roughness in the channel or a better lattice match between the NaT3 and the channel oxide.

Further analysis of the NaT3 crystallites in the out-of-plane direction is possible owing to the multiple orders of reflections visible in the scattering pattern. Figure 4 shows the out-of-plane FWHM of the  $h00$  reflections with  $h = 2-4$  after desmearing of the geometric broadening due to the effective sample width. Irrespective of the measurement point, it is apparent that the FWHM increases with diffraction order. The sample-related peak broadening includes broadening from the finite crystallite size and strain broadening related to crystal imperfection. These two broadening contributions are deconvoluted by applying Williamson-Hall (W-H) analysis to

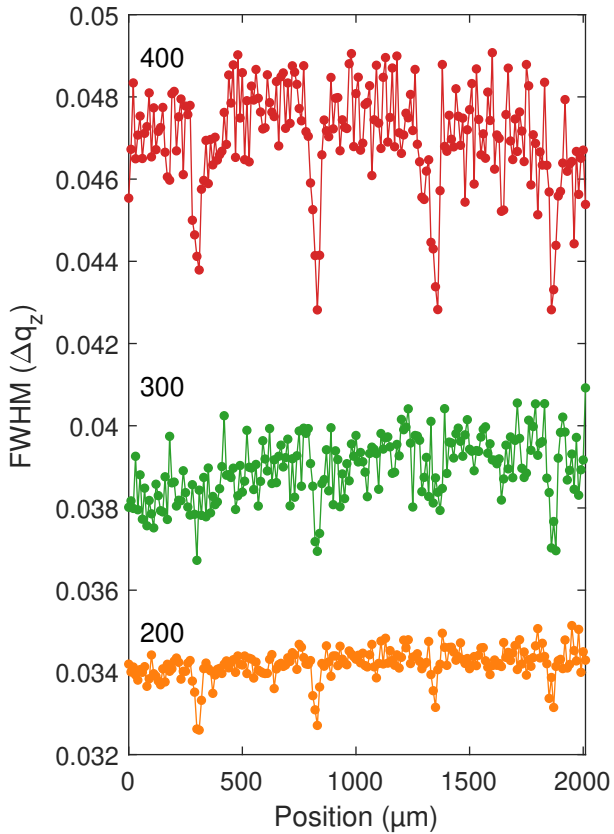


FIG. 4. Profiles of the out-of-plane FWHM of NaT3  $h00$  reflections for  $h = 2-4$  (bottom to top) in the studied OFET.

the data. The W-H analysis plots the diffraction peak width ( $\beta^* = \beta \cos \theta / \lambda$ ) as a function of the diffraction vector ( $d^* = 2 \sin \theta / \lambda$ ). The intercept of the slope then relates to finite size broadening while the magnitude of the slope relates to the strain broadening [20, 21].

Figure 5 shows the W-H plots for the out of plane  $h00$  reflections ( $h = 2-4$ ) measured in the channel and on top of the electrode. Each value is given as an average of all points in the respective areas. The  $h = 1$  diffraction is omitted from the W-H analysis, as it proved difficult to isolate the out-of-plane peak profile from the diffuse surface scattering. The W-H plots show a non-zero slope, indicating that the observed peak broadening is not only due to the crystallites size, but also due to lattice imperfections and preferential microstrain in the film. The crystallite size broadening is similar in the two cases, corresponding to average out-of-plane crystallite sizes of 28.5 nm on top of the electrodes, and 30.5 nm in the channel. Both values are in good agreement with the nominal film thickness of 30 nm. Furthermore, the film in the channel exhibits a steeper slope of the W-H plot, indicating an increased film strain in the channel as compared to the film on top of the electrode.

Figure 6a and b show atomic force microscopy (AFM) micrographs of the the surface morphology of the NaT3 thin-film at the edge of an electrode and elsewhere in

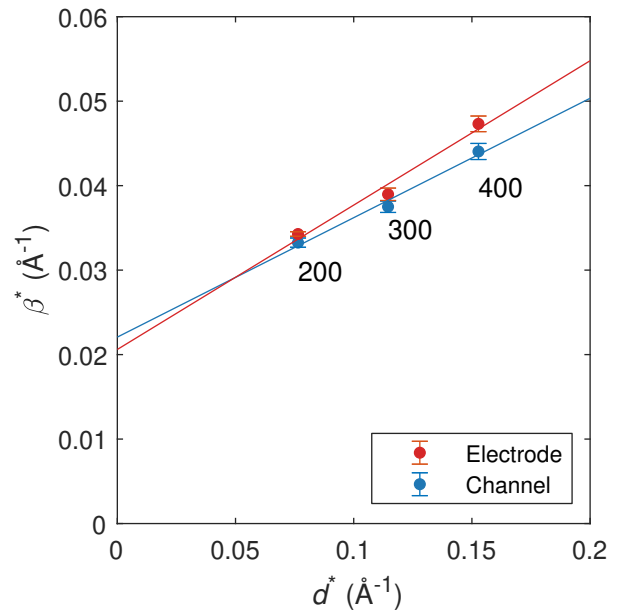


FIG. 5. William-Hall plots for NaT3  $h00$  reflections from the channel and electrode areas. Each value is given as an average over individual measurements. Solid lines are linear fits to the data.

the channel itself. The film in the channel (left-side of Fig. 6a) lies lower than the film on top of the electrode by approximately 30 nm, corresponding to the patterned thickness of Au. The morphology appears qualitatively similar in both areas of the film, with the molecules forming three-dimensional (3D) islands with staggered terraces. This type of surface morphology is typical for thin-films growing according to 3D-type growth (Volmer-Weber or Stranski-Krastanov) [22]. The root mean square (RMS) of the surfaces (indicated in Fig. 6a) indicates that the film roughness in top of the electrode is slightly higher than in the channel. However, in a different area of the channel (Fig. 6b), the RMS is even higher. The average RMS in the channel and on the electrode are almost identical (3.0 nm vs 3.1 nm), indicating that the differences in microstructure observed by 1D  $\mu$ GIWAXS profiles are not readily observed by considering the surface morphology alone.

Figure 6c shows the transfer curve of the working OFET device. The slope of the  $I_{DS}^{1/2}$  vs  $V_G$  curve (not shown) in the saturated regime yielded the field-effect mobility of  $\mu = 2.4 \times 10^{-5} \text{ cm}^2/\text{Vs}$ .

#### IV. DISCUSSION

Our results, and the results presented by Li, Lamport [18, 19], and other authors, clearly demonstrate local structural variations across OFET devices. While NaT3 does not form different textures in the channels like diF-TES-ADT, the microstructural heterogeneity on the

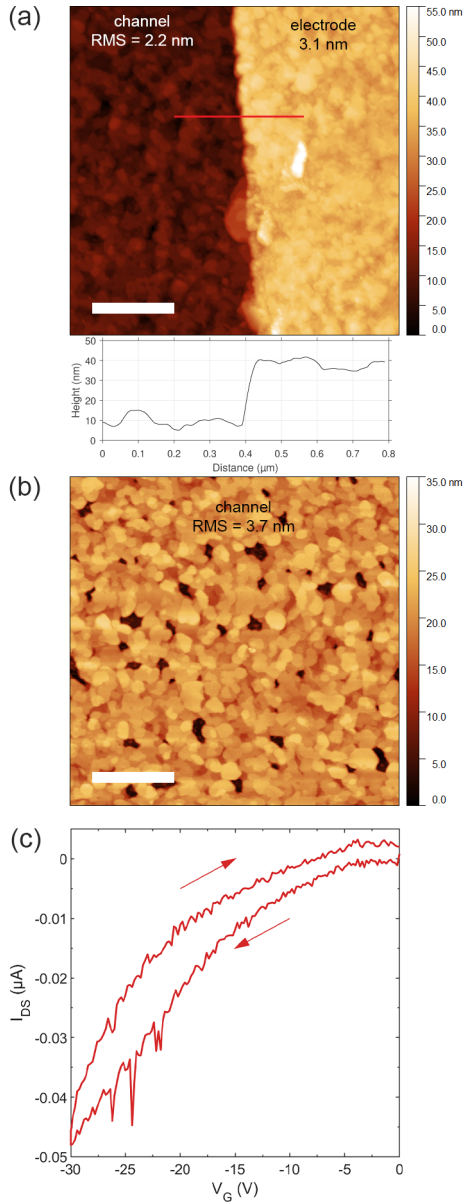


FIG. 6. AFM micrographs of (a) the electrode edge (b) channel. The height RMS is indicated for the respective areas in the micrographs. Insert plots cross-sectional profile is marked by the red line in panel (a). (c) Transfer curve of studied OFET acquired with  $V_D = -30$  V. Scale bars are  $0.5 \mu\text{m}$ .

electrodes could still be a limiting factor in charge transport. The pathways for charge transport in OSCs are determined by the overlap of neighboring molecular orbitals, and their charge transport properties are typically highly anisotropic [23]. At the same time, the charge transport is often limited by grain-boundaries, that introduces localized trap states in the material [24, 25]. This suggests that misorientation between neighboring grains can detrimentally effect charge transport, since two crystalline domains meeting at a sufficiently large angle necessarily creates a series of edge dislocations at

the boundary. Indeed, it has been shown that increased out-of-plane misorientation in solution-processed 6,13-bis(triisopropylsilyl)ethynyl)pentacene (TIPS-PEN) leads to lower field-effect mobilities in OFETs [26]. Moreover, it has been suggested that the effect on transport properties of misorientation at the grain boundaries is less significant in materials with herringbone-packing (such as NaT3) than in slip-stacked materials [7], due to the lower charge transport anisotropy of the herringbone motif (two-dimensional versus one-dimensional). Although this might be the case, the higher degree of misorientation with respect to the surface normal found in the film on the electrodes in the NaT3 OFET (Fig. 3), as well as in the channels in diF-TES-ADT OFETs (Fig. 2), could still be a potentially limiting factor in the OFET charge transport at the contact interface, due to increased grain-boundary densities. The grain-boundary limiting effect on charge transport is indeed suggested by the mobility results reported by Li et al [18], where the diF-TES-ADT devices with large grains show the highest mobilities.

On the other hand, grain boundaries are not the only limiting factor for charge transport [27]. All crystal exhibit some degree of paracrystalline disorder, which induces variations in the crystalline lattice and intermolecular distances. As a result, the transfer integral between neighboring molecules are perturbed, and the charge carriers are subjected to fluctuations in the electronic landscape [28]. While the paracrystalline disorder is typically low for small molecule OSCs [28], our results indicate that the local disorder is different in areas of the channel and electrodes. For polymers, the paracrystalline disorder is typically much higher [29], and therefore constitutes a much more transport-limiting effect in devices made from these materials.

While grain-boundaries attributed to high-angle misorientations are mostly visible in optical characterization techniques or scanning probes (see the individual grains in the AFM image in Fig. 6 or in optical micrographs in Fig. 1), it is much more difficult to discern low-angle grain boundaries with these techniques. Features in the optical micrographs/scanning probe maps that appear as single grains are often polycrystalline and contain many low-angle grain boundaries [28]. This is readily apparent when comparing the grain boundaries observed for NaT3 by AFM with the crystallite size obtained from the  $\mu\text{GIWAXS}$  mapping, or by comparing the grain sizes in the optical micrograph in Fig. 1 with the corresponding  $\mu\text{GIWAXS}$  grain size. This emphasizes the fact that one cannot always rely on optical microscopy or scanning probes when characterizing the morphology of OSC devices. If the material under consideration contains well-ordered crystals, whether within amorphous domains or not,  $\mu\text{GIWAXS}$  combined with methods such as Williamson-Hall analysis, or more detailed analyses such as the Warren-Averbach analysis [30, 31], provide good insight into the crystalline "true" grain size of the film.

## V. OUTLOOK

As contemporary X-ray optics now allows for well collimated beams at virtually every synchrotron source, we expect surface maps or profiling, allowing for electrode proximity data and other data, to become a standard for structural studies of organic electronics. Investigating the microstructure near the device contacts is especially important in devices where the performance is in some way limited by contact resistance, which is the case for many high performing OFETs [10]. The ideas presented here are not limited to the case of small molecule OSCs, and they can readily be expanded to polymers and organic-inorganic hybrid materials. Because of the relative novelty of the  $\mu$ GIWAXS technique, these fields will benefit greatly from its widespread utilization, and it should be used vis-à-vis probe microscopies including AFM and Kelvin probe microscopy. For polymer-based OSC devices the paracrystalline disorder is much higher than in small molecule OSC devices, and we propose to expand the quantitative analysis of local strain and paracrystalline disorder to these materials. The same is true for probing amorphous domains within crystals, dominant for polymer materials. As demonstrated here,  $\mu$ GIWAXS would be an obvious choice for resolving these aspects. Another key use for  $\mu$ GIWAXS is the study of working devices in operando, as very recently demonstrated by Grodd et al. [32]. We also see obvious benefits from microfocused grazing-incidence small-angle X-ray scattering ( $\mu$ GISAXS) for probing nanoparticles and other larger structures incorporated within the electrodes [33].

All in all,  $\mu$ GIWAXS makes it possible to map diverse structural details, otherwise inaccessible by scanning probes or optical microscopy, with high spatial resolution. The technique holds great promise for linking structure and device performance, which is crucial in the development of new organic electronics and beyond.

## VI. EXPERIMENTAL SECTION

*OFET fabrication and characterization:* NaT3 molecules used in this study was synthesized following the Suzuki cross-coupling protocols reported in Ref. [34]. The field-effect transistors used in this study were fabricated using a highly n-doped Si substrate as the back gate electrode with a 200 nm thick thermally grown SiO<sub>2</sub> gate dielectric. A 1 cm<sup>2</sup> array of interdigitated source and drain electrodes were structured by photolithography and deposited by E-beam evaporation of Au (30 nm) atop Ti (3 nm). All substrate were ultrasonically cleaned in acetone and isopropanol followed by rinse with de-ionized water. A 30 nm thick NaT3 film was deposited on top of the substrate by vacuum sublimation (base pressure  $2 \times 10^{-8}$  mbar and deposition rate  $< 0.1$  Å/min). The device was electrically characterized using a custom-built characterization set-up based on a

LabVIEW-controlled data acquisition card connected to voltage and current amplifiers, providing the input, and a probe station measuring the output signal from the OFET. The gate voltage ( $V_G$ ) was swept with constant drain-source voltage  $V_{DS} = -30$  V. The field-effect mobility was extracted from the slope of the  $I_{DS}^{1/2}$  vs  $V_G$  curve via

$$\mu = \frac{2L}{WC_i} \left( \frac{\partial I_{DS}^{1/2}}{\partial V_G} \right)^2 \quad (1)$$

where  $C_i = 17.3$  nF cm<sup>-2</sup> is the geometrical capacitance of the dielectric, and  $W$  and  $L$  the width and length (distance between source and drain electrodes) of the channel, respectively. For the employed test device, the  $W/L$  ratio was  $134.39\mu\text{m}/0.47\mu\text{m} = 285.94$

*$\mu$ GIWAXS:*  $\mu$ GIWAXS experiment were conducted at the P03 Micro- and Nanofocus X-ray Scattering (MiNaXS) beamline of PETRA III, DESY. The X-ray beam with an energy of 12.9 keV was focused to a spot size of  $31\mu\text{m} \times 26\mu\text{m}$  (horizontal FWHM  $\times$  vertical FWHM) at the sample. The grazing incidence angle was optimized against the scattering data, with the typical angle ranging between  $0.16^\circ$  and  $0.18^\circ$ . The resulting footprint of the beam spanned the full width of the device in the longitudinal direction and  $31\mu\text{m}$  in the transverse direction.  $\mu$ GIWAXS images were recorded with a LAMBDA 10M detector (Spectrum) with a pixel size of  $55\mu\text{m}$  placed 159 mm downstream from the sample. The X-ray beam was carefully aligned to be parallel with the OFET electrodes by an alternating two-step process. First, the sample was scanned along the transverse direction of the beam to find the position with the maximal signal from the electrode. Then the sample was rotated about its surface normal, again maximizing the electrode signal. This process was then repeated until a satisfactory alignment was achieved. To avoid radiation induced damage in the thin-film by the X-ray beam, the sample alignment was performed on a separate electrode from the ones measured. The  $\mu$ GIWAXS data were collected by scanning the beam across multiple electrodes in steps of  $10\mu\text{m}$  and with 3 s exposure time per measurement.

The  $\mu$ GIWAXS data were analyzed using DPDAK [35]. The integrated film and electrode intensities were extracted from linecuts of the Au 111 and NaT3 100 reflections, respectively. To obtain information on the orientation distribution of the thin-film crystallites, the angular FWHM was extracted by fitting a pseudo-Voigt function to the angular 100 intensity profile. Detailed analysis of the grain-size was carried out using the  $h02$  reflection for the in-plane dimension, and the 200, 300 and 400 reflection for out-of-plane dimension. The peaks were first fitted by Gaussian functions along  $q_{xy}$  and  $q_z$ , respectively, and the extracted peak width was subsequently corrected followed ideas presented in Ref. [36]. To account for the geometric broadening of the peak shapes due the longitudinal beam footprint on the sample, the effective sample width was modeled as a linear function

of the transverse position of the beam on the sample. The geometric smearing was then calculated from the effective sample width using the equation

$$\Delta q_{geo} = \frac{4\pi}{\lambda} \cos\left(\frac{2\theta}{2}\right) \frac{w \tan(2\theta)}{2L} \quad (2)$$

where  $\lambda$  is the X-ray wavelength,  $2\theta$  is the scattering angle,  $w$  is the effective sample width, and  $L$  is the distance from sample to detector. The 'true' broadening of the Bragg peak (i.e. corrected for the instrumental contribution) was then obtained using the relation

$$\Delta q_{hkl} = (\Delta q_{exp}^2 - \Delta q_{res}^2)^{1/2} \quad (3)$$

where  $\Delta q_{exp}$  denotes the experimentally determined broadening and  $\Delta q_{res}$  the broadening due to the instrumental resolution. Contributions to the instrumental broadening from the divergence of the X-ray beam and from the energy bandwidth are small and have thus been neglected, i.e.  $\Delta q_{res} = \Delta q_{geo}$ . The in-plane grain size was then calculated according to the Scherrer equation,  $D_{hkl} = 2\pi K / \Delta q_{hkl}$ , where  $D_{hkl}$  is average grain size, and  $K$  is the Scherrer constant, taken to be 0.9 in our case. The out-of-plane broadening of the  $h00$  reflections were analyzed using the Williamson-Hall (W-H) method [20]. The sample-related broadening of the Bragg peaks includes broadening due to finite crystal size and broadening due to strain. The W-H method assumes

that the crystal size broadening and the strain broadening have difference dependence on the Bragg angle  $\theta$ , namely  $\beta_{size} = K\lambda/D \cos\theta$  (from the Scherrer formula) and  $\beta_{strain} = 4\epsilon \tan\theta$ . By rearranging, we obtain the expression

$$\beta^* = K/D + 2\epsilon d^* \quad (4)$$

where  $\beta^* = \beta \cos\theta/\lambda$  is the peak broadening in reciprocal space units and  $d^* = 2 \sin\theta/\lambda$  is the diffraction vector. The W-H analysis plots  $\beta^*$  against  $d^*$ , and thus the size broadening and the strain broadening can be obtained from the intersect and the slope of the plot, respectively.

*AFM:* AFM was performed using a Dimension 3100 instrument (Veeco) operated in tapping mode and the images were analyzed using Gwyddion [37].

## ACKNOWLEDGMENTS

This research was carried out at the light source PETRA III at DESY, a member of the Helmholtz Association (HGF). We thank Pallavi Pandit and Stephan Roth of DESY, and Jes Linnet of the University of Southern Denmark for experimental assistance. The research leading to this result has been supported by the project CALIPSOplus under the Grant Agreement 730872 from the EU Framework Programme for Research and Innovation HORIZON 2020. We thank the instrument center DanScatt for travel support.

- 
- [1] H. Sirringhaus, 25th anniversary article: Organic field-effect transistors: The path beyond amorphous silicon, *Adv. Mater.* **26**, 1319 (2014).
- [2] S. R. Marder and J.-L. Bredas, *The WSPC Reference on Organic Electronics: Organic Semiconductors* (WORLD SCIENTIFIC, 2016).
- [3] H. Klauk, ed., *Organic Electronics II* (Wiley-VCH Verlag GmbH & Co. KGaA, 2012).
- [4] Y. Wang, L. Sun, C. Wang, F. Yang, X. Ren, X. Zhang, H. Dong, and W. Hu, Organic crystalline materials in flexible electronics, *Chem. Soc. Rev.* **48**, 1492 (2019).
- [5] L. H. Jimison, A. Salleo, M. L. Chabiny, D. P. Bernstein, and M. F. Toney, Correlating the microstructure of thin films of poly[5,5-bis(3-dodecyl-2-thienyl)-2,2-bithiophene] with charge transport: Effect of dielectric surface energy and thermal annealing, *Phys. Rev. B* **78**, 125319 (2008).
- [6] G. Horowitz and M. E. Hajlaoui, Mobility in polycrystalline oligothiophene field-effect transistors dependent on grain size, *Adv. Mater.* **12**, 1046 (2000).
- [7] J. Rivnay, L. H. Jimison, J. E. Northrup, M. F. Toney, R. Noriega, S. Lu, T. J. Marks, A. Facchetti, and A. Salleo, Large modulation of carrier transport by grain-boundary molecular packing and microstructure in organic thin films, *Nat. Mater.* **8**, 952 (2009).
- [8] A. O. F. Jones, B. Chattopadhyay, Y. H. Geerts, and R. Resel, Substrate-induced and thin-film phases: Polymorphism of organic materials on surfaces, *Adv. Funct. Mater.* **26**, 2233 (2016).
- [9] M. Fahlman, S. Fabiano, V. Gueskine, D. Simon, M. Berggren, and X. Crispin, Interfaces in organic electronics, *Nat. Rev. Mater.* **4**, 627 (2019).
- [10] M. Waldrip, O. D. Jurchescu, D. J. Gundlach, and E. G. Bittle, Contact resistance in organic field-effect transistors: Conquering the barrier, *Adv. Funct. Mater.* **30**, 1904576 (2019).
- [11] A. Hexemer and P. Müller-Buschbaum, Advanced grazing-incidence techniques for modern soft-matter materials analysis, *IUCrJ* **2**, 106 (2015).
- [12] L. J. Richter, D. M. DeLongchamp, and A. Amassian, Morphology development in solution-processed functional organic blend films: An in situ viewpoint, *Chem. Rev.* **117**, 6332 (2017).
- [13] P. Müller-Buschbaum, The active layer morphology of organic solar cells probed with grazing incidence scattering techniques, *Adv. Mater.* **26**, 7692 (2014).
- [14] E. Gann, M. Caironi, Y.-Y. Noh, Y.-H. Kim, and C. R. McNeill, Diffractive x-ray waveguiding reveals orthogonal crystalline stratification in conjugated polymer thin films, *Macromolecules* **51**, 2979 (2018).
- [15] C. Riekel, M. Burghammer, and R. Davies, Progress in micro- and nano-diffraction at the ESRF ID13 beamline, *IOP Conf. Ser.: Mater. Sci. Eng.* **14**, 012013 (2010).

- [16] A. Buffet, A. Rothkirch, R. Döhrmann, V. Körstgens, M. M. A. Kashem, J. Perlich, G. Herzog, M. Schwartzkopf, R. Gehrke, P. Müller-Buschbaum, and S. V. Roth, P03, the microfocus and nanofocus x-ray scattering (MiNaXS) beamline of the PETRA III storage ring: the microfocus endstation, *J. Synchrotron Radiat.* **19**, 647 (2012).
- [17] G. Santoro, A. Buffet, R. Döhrmann, S. Yu, V. Körstgens, P. Müller-Buschbaum, U. Gedde, M. Hedenqvist, and S. V. Roth, Use of intermediate focus for grazing incidence small and wide angle x-ray scattering experiments at the beamline p03 of PETRA III, DESY, *Rev. Sci. Instrum.* **85**, 043901 (2014).
- [18] R. Li, J. W. Ward, D.-M. Smilgies, M. M. Payne, J. E. Anthony, O. D. Jurchescu, and A. Amassian, Direct structural mapping of organic field-effect transistors reveals bottlenecks to carrier transport, *Adv. Mater.* **24**, 5553 (2012).
- [19] Z. A. Lamport, K. J. Barth, H. Lee, E. Gann, S. Engmann, H. Chen, M. Guthold, I. McCulloch, J. E. Anthony, L. J. Richter, D. M. DeLongchamp, and O. D. Jurchescu, A simple and robust approach to reducing contact resistance in organic transistors, *Nat. Commun.* **9**, 5130 (2018).
- [20] G. Williamson and W. Hall, X-ray line broadening from filed aluminium and wolfram, *Acta Metall.* **1**, 22 (1953).
- [21] X. Jiao, M. Statz, L. Lai, S. Schott, C. Jellett, I. McCulloch, H. Sirringhaus, and C. R. McNeill, Resolving different physical origins toward crystallite imperfection in semiconducting polymers: Crystallite size vs paracrystallinity, *J. Phys. Chem. B* **124**, 10529 (2020).
- [22] S. Kowarik, A. Gerlach, and F. Schreiber, Organic molecular beam deposition: fundamentals, growth dynamics, and in situ studies, *J. Phys.: Condens. Matter* **20**, 184005 (2008).
- [23] S. Fratini, M. Nikolka, A. Salleo, G. Schweicher, and H. Sirringhaus, Charge transport in high-mobility conjugated polymers and molecular semiconductors, *Nat. Mater.* **19**, 491 (2020).
- [24] A. B. Chwang and C. D. Frisbie, Temperature and gate voltage dependent transport across a single organic semiconductor grain boundary, *J. Appl. Phys.* **90**, 1342 (2001).
- [25] W. L. Kalb, S. Haas, C. Krellner, T. Mathis, and B. Batlogg, Trap density of states in small-molecule organic semiconductors: A quantitative comparison of thin-film transistors with single crystals, *Phys. Rev. B* **81**, 155315 (2010).
- [26] K.-Y. Wu, C.-T. Hsieh, L.-H. Wang, C.-H. Hsu, S.-T. Chang, S.-T. Lan, Y.-F. Huang, Y.-M. Chen, and C.-L. Wang, Influences of out-of-plane lattice alignment on the OFET performance of TIPS-PEN crystal arrays, *Cryst. Growth Des.* **16**, 6160 (2016).
- [27] N. Ohashi, H. Tomii, R. Matsubara, M. Sakai, K. Kudo, and M. Nakamura, Conductivity fluctuation within a crystalline domain and its origin in pentacene thin-film transistors, *Appl. Phys. Lett.* **91**, 162105 (2007).
- [28] A. Salleo, Impact of organic semiconductor microstructure on transport: Basic concepts, in *The WSPC Reference on Organic Electronics: Organic Semiconductors*, edited by J.-L. Bredas and S. R. Marder (WORLD SCIENTIFIC, 2016) Chap. 9, pp. 293–323.
- [29] R. Noriega, J. Rivnay, K. Vandewal, F. P. V. Koch, N. Stingelin, P. Smith, M. F. Toney, and A. Salleo, A general relationship between disorder, aggregation and charge transport in conjugated polymers, *Nat. Mater.* **12**, 1038 (2013).
- [30] T. J. Prosa, J. Moulton, A. J. Heeger, and M. J. Winokur, Diffraction line-shape analysis of poly(3-dodecylthiophene): a study of layer disorder through the liquid crystalline polymer transition, *Macromolecules* **32**, 4000 (1999).
- [31] J. Rivnay, R. Noriega, R. J. Kline, A. Salleo, and M. F. Toney, Quantitative analysis of lattice disorder and crystallite size in organic semiconductor thin films, *Phys. Rev. B* **84**, 045203 (2011).
- [32] L. S. Grodd, E. Mikayelyan, T. Dane, U. Pietsch, and S. Grigorian, Local scale structural changes of working OFET devices, *Nanoscale* **12**, 2434 (2020).
- [33] M. K. Huss-Hansen, M. Hansteen, J. Linnet, A. R. Walther, J. Kjelstrup-Hansen, and M. Knaapila, Structural basis for a naphthyl end-capped oligothiophene with embedded metallic nanoparticles for organic field-effect transistors, *Appl. Phys. Lett.* **113**, 251903 (2018).
- [34] F. Balzer, M. Schiek, A. Osadnik, I. Wallmann, J. Parisi, H.-G. Rubahn, and A. Lützen, Substrate steered crystallization of naphthyl end-capped oligothiophenes into nanofibers: the influence of methoxy-functionalization, *Phys. Chem. Chem. Phys.* **16**, 5747 (2014).
- [35] G. Benecke, W. Wägermaier, C. Li, M. Schwartzkopf, G. Flucke, R. Hoerth, I. Zizak, M. Burghammer, E. Metwalli, P. Müller-Buschbaum, M. Trebbin, S. Förster, O. Paris, S. V. Roth, and P. Fratzl, A customizable software for fast reduction and analysis of large x-ray scattering data sets: applications of the newDPDAK package to small-angle x-ray scattering and grazing-incidence small-angle x-ray scattering, *J. Appl. Crystallogr.* **47**, 1797 (2014).
- [36] D.-M. Smilgies, Scherrer grain-size analysis adapted to grazing-incidence scattering with area detectors, *J. Appl. Crystallogr.* **42**, 1030 (2009).
- [37] D. Nečas and P. Klapetek, Gwyddion: an open-source software for SPM data analysis, *Open Phys.* **10**, 181 (2012).



## Paper V

---

To be submitted to *Macromolecules*.

The fifth and final paper of this thesis concerns the local structure of UHWMPE fibers. An outstanding challenge for improving the mechanical performance in UHWMPE fibers is the need for a comprehensive understanding of the microstructure and morphology on a local scale, which is known to be inhomogeneous in the radial direction of the fiber [2, 3]. At the same time, the lack of quantitative results on the local (inhomogeneous) structure means that the interplay between processing conditions and final structure, and thus mechanical properties, is not yet fully understood. To this end, we employ a combination of X-ray based techniques and Polarized Raman Spectroscopy to investigate the structural and morphological uniformity of aligned high-performance gel-spun UHMWPE fibers with a spatial resolution of  $1\ \mu\text{m}$ . The work is a collaborative effort between DTU, KU Leuven and the dutch company Royal DSM. The Polarized Raman Spectroscopy measurements and analysis was largely carried out by Erik Hedlund of KU Leuven.

# Local Structure Mapping of Gel-Spun Ultrahigh-Molecular-Weight Polyethylene Fibers

*Mathias K. Huss-Hansen,<sup>\*,†,1</sup> Erik G. Hedlund,<sup>\*,†,2</sup> Anton Davydok,<sup>3</sup> Marie Hansteen,<sup>1,4</sup> Jildert Overdijk,<sup>4</sup> Gert de Cremer,<sup>4</sup> Maarten Roeffaers,<sup>2</sup> Matti Knaapila<sup>1</sup> and Luigi Balzano<sup>4</sup>*

<sup>1</sup>Department of Physics, Technical University of Denmark, Kgs. Lyngby, 2800, Denmark

<sup>2</sup>cMACS, KU Leuven, Leuven, 3001, Belgium

<sup>3</sup>Institute of Materials Physics, Helmholtz-Zentrum Geesthacht, Notkestrasse 85, 22607

Hamburg, Germany

<sup>4</sup>DSM, Applied Science Center, Urmonderbaan 22, 6167RD Geleen, The Netherlands

**KEYWORDS:** Gel-spun polymer fibers, skin-core structure, alignment, fiber diffraction

**ABSTRACT:** We report on 1  $\mu\text{m}$  spatial resolution investigations of structural and morphological uniformity of aligned high-performance gel-spun ultrahigh-molecular-weight polyethylene (UHMWPE) fibers (thicknesses spanning from 50  $\mu\text{m}$  to 300  $\mu\text{m}$ ) whose processing includes draw and quench. The degree of orientation of PE crystallites were found to increase near the surface of the fiber filaments (skin-core structure) in all samples when considering the  $\langle P_2 \rangle$  orientation parameter calculated from wide-angle X-ray scattering (WAXS). The degree of orientation increases with drawn down ratio (keeping the quench temperature constant) and decreases with an increase in quench temperature (keeping the draw down ratio constant). Orientation parameters calculated from polarized Raman spectroscopy measurements of the symmetric C-C stretching ( $1130\text{ cm}^{-1}$ ) bond of PE showed clear skin-core structure in the samples with the highest overall orientation. We also employ small-angle X-ray scattering (SAXS) computed tomography to show that morphology (on the length scale of tens of nm) exhibit clear skin-core structure in two of the samples. The thickness of the skin region was estimated from the real-space SAXS morphology and found to be similar in undrawn and drawn filaments.

## Introduction

Man-made fibers are found in products ranging from textiles, thermal insulation, and composite reinforcements to specialized applications in high-demand areas, including heavy-lifting, off-shore anchoring, ballistic protection, and bio-medical engineering.

Out of the fiber families, fibers made from ultra-high molecular weight polyethylene (UHMWPE) have the highest specific modulus and strength. The ultra-high strength of UHMWPE fibers was achieved with the invention of the gel-spinning process by Smith and Lemstra in the late 1970s.<sup>1-4</sup> In this process, UHMWPE ( $M_w > 1 \times 10^6$  g/mol) is dissolved in a solvent, then spun and subsequently hot drawn at temperatures close to the melting point of the pure polymer.

The favorable mechanical properties of high strength fibers are directly related to the orientation and alignment of the molecules in the semi-crystalline structure.<sup>5</sup> In the ideal case, all the polymeric chains are oriented along the same direction, i.e. along the fiber axis, and the axial strength of the fiber is limited by the polymers molecular weight.<sup>6</sup> In order to achieve the highest mechanical properties, the process of spinning followed by drawing has been established to preferentially orient the UHMWPE molecules along the fiber axis.

As discussed in the literature, the local molecular orientation and morphology can vary significantly inside the fiber. For example, aramid fibers including poly(p-phenylene terephthalamide) (PPTA) fibers are known to exhibit skin-core morphologies,<sup>7-9</sup> where the core region tends to possess a higher degree of crystallinity than the outer layer, also known as the skin.<sup>8</sup> Most importantly, heterogeneous morphology along the radial direction of the PPTA fibers has disadvantageous effect on their mechanical properties,<sup>7,8,10</sup> as the fibers tend to break at the interfaces between different morphologies as shown for the skin-core border of PPTA.<sup>8</sup>

Skin-core morphology has also been observed and elegantly studied for gel-spun UHMWPE fibers by Ohta et al.<sup>11</sup> The authors isolated individual filaments from the spinning line and

showed detailed real-space images of the transverse filament cross-section by use of transmission electron microscopy (TEM). These TEM images revealed a heterogeneous morphology with a core region composed of typical shish-kebab structures<sup>12,13</sup> in a solvent rich matrix and a polymer rich skin region composed so-called interlocked shish-kebab structures, where the lamellae of neighboring shish-kebab intercalate, oriented along the fiber axis. Furthermore, they showed that the heterogeneous morphology is even more pronounced in filaments obtained at lower spinning speeds.<sup>14</sup>

In this work, we investigate the occurrence of a skin-core morphology in gel spun UHMWPE fibers by means of conventional and novel morphology sensitive analytical techniques.

On hand, we make use of X-ray scattering that has the advantage of reaching quite high spatial resolution (nm range) in transmission mode. However, when operating in transmission mode, morphological information in the depth direction (parallel to the beam) is not directly accessible. On the other hand, to resolve morphology in the depth direction, we make use of Raman microscopy in confocal mode. Eventually, we validate the morphological picture that emerges by means of a novel X-ray tomography technique based on Small Angle X-ray Scattering Computed Tomography (SAXS-CT).

Spatially resolved X-ray scattering studies on polymer fibers are common, yet the literature is less comprehensive concerning fibers made from UHMWPE. In the typical geometry, the fiber specimen is scanned by a narrowly focused X-ray beam (typical diameter on the order of a few  $\mu\text{m}$ ) in the direction perpendicular to the fiber axis. Individual scattering patterns are then recorded at each position across the fiber. Riekel et al.<sup>15</sup> studied single PPTA fibers in this geometry to obtain maps of the crystalline degree of orientation parallel and perpendicular the fiber axis. However, the scattering information obtained in this geometry is inherently smeared and contains information from the entire irradiated volume along the path of the X-ray beam. Roth et al.<sup>16</sup> used Monte Carlo simulations to model the projected scattering patterns, while

Stribeck et al.<sup>17,18</sup> proposed using mathematical models to desmear the scattering information by exploiting the local fiber symmetry of the samples. Davies et al.<sup>9</sup> avoided the problem of radially smeared scattering patterns altogether by employing a different scattering geometry in which fiber sections of 15  $\mu\text{m}$  length were prepared by laser dissection and irradiated with the X-ray beam parallel to the fiber axis. However, this so-called “on-axis” experiment limits the amount of information available in each individual scattering pattern,<sup>19</sup> and requires sophisticated preparation of the sample.

An emerging method to study spatially resolved structures is tomographic small-angle X-ray scattering (SAXS) [or SAXS computed tomography (SAXS-CT)],<sup>20</sup> where scattering projections are collected while rotating the sample and used to reconstruct the scattering from individual voxels. State of the art SAXS-CT studies are commonly performed on materials that are resistant to radiation-induced damage, such as teeth<sup>21</sup> and bone<sup>22,23</sup>. Polymers are much more susceptible to radiation-induced damage, and thus the use of SAXS-CT is non-trivial on these systems due to the prolonged irradiation with the high energy X-ray beam. Schroer et al.<sup>24</sup> successfully used SAXS-CT to gain information about the local nanoscale structure inside an injection molded PE rod with a spatial resolution of 80  $\mu\text{m}$ . In this work, we aim to increase the spatial resolution for the first time to less than 2  $\mu\text{m}$ . This breakthrough will allow for a detailed investigation of thin specimens, e.g. UHMWPE filaments.

In this paper, we prepare UHMWPE filaments under specific processing conditions chosen to yield samples with distinct skin-core structure. First, we employ polarized Raman microscopy, a widely available characterization method, to determine the local orientation distribution of the polymer chains inside UHMWPE filaments at a 3D resolution of less than 2  $\mu\text{m}$ . Then, we study the same filaments in more detail with microfocused synchrotron X-ray diffraction to further investigate the local orientation distribution of the crystalline phase. Finally, we use tomographic SAXS with a microfocused beam to fully map the local polymer

morphology in two of the filament samples. These complementary methods provide detailed understanding of the microscopic skin-core morphology in UHMWPE filaments. This pushes the applicability limit of SAXS tomography towards fine details of engineering polymer filaments where experimental challenges including low scattering contrast and radiation damage have to be addressed.

## Materials and Methods

### Samples preparation

The filaments for this study were prepared by means of a mono-filament spinning device (DSM R&D facilities, Geleen). In this process an extruder is used to dissolve UHMWPE in decalin and then pump the thus formed gel through a spin hole to form a filament (see Figure 1). The filament is then quenched in a water bath and, after reaching room temperature is wound on a bobbin. The bobbin is then placed inside a fume-hood until decalin is almost completely evaporated. In order to study the effect of processing conditions on features of the skin-core morphology, the temperature of the water bath and the filament draw down (DD) were systematically changed (see Table 1). The filament draw down is defined as the ratio between the speed of the first roller and the speed of the extruded filament ( $DD=v_1/v_0$ ).

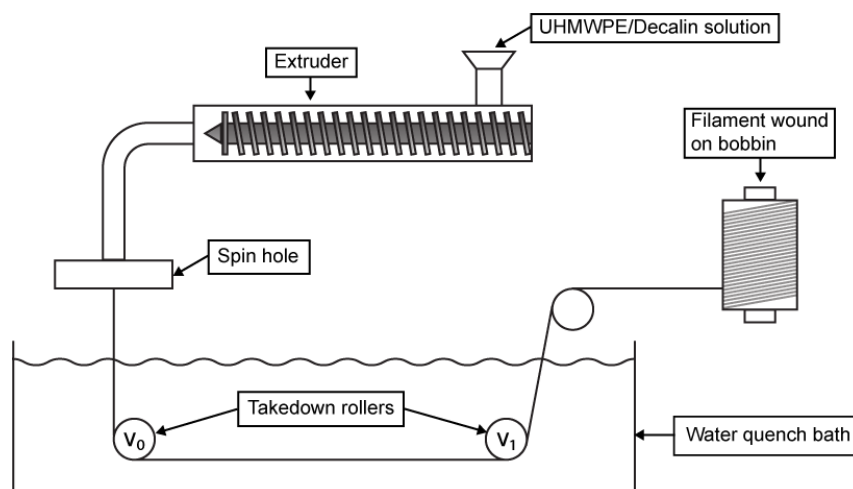


**Figure 1.** Schematic illustration of the gel-spinning process of the UHMWPE filaments

**Table 1.** Samples considered in the present study

filament code	draw dawn ratio	water temperature (°C)	nominal thickness (μm)
DD1-low	1	7.5	~300
DD10-low	10	7.5	~300
DD1-high	1	50	~80
DD10-high	10	50	~80

## Methods

### Polarized Raman Spectroscopy

Polarized Raman spectra of the filaments were acquired using a custom-made microscope setup following the sample positioning and experimental configuration found in the corresponding section of the supporting information. The approach targets a randomly selected position along the filament. At these positions, Raman spectra were acquired at varying depths along the radial direction of the filament, from the edge to the center, in order to determine how the orientation of the crystalline domains varies depending on the depth into the filament. The employed analysis focuses on two key fingerprint regions of the PE spectrum listed in Table 2, namely the symmetric and asymmetric stretching of carbon-carbon bonds.

**Table 2.** Raman fingerprint regions

frequency (cm <sup>-1</sup> )	mode	phase
1130	symmetric stretching C-C	crystalline
1063	asymmetric stretching C-C	crystalline
1295	twisting CH <sub>2</sub>	crystalline
1448	bending CH <sub>2</sub> , Fermi resonance	amorphous
1484	bending CH <sub>2</sub> , Fermi resonance	amorphous

By using the analysis described in the supporting information, the true orientation parameters,  $\langle P_2 \rangle$  and  $\langle P_4 \rangle$ , can be estimated directly from the polarized Raman spectra. The orientation parameters are defined as<sup>25–28</sup>

$$\langle P_2 \rangle = \frac{3\langle \cos^2 \theta \rangle - 1}{2} \quad (1)$$

$$\langle P_4 \rangle = \frac{35\langle \cos^4 \theta \rangle - 30\langle \cos^2 \theta \rangle + 3}{8} \quad (2)$$

where  $\theta$  is the relative angle between the crystallographic  $c$ -axis and the fiber axis. For the full experimental details, and for a description of how of the orientation parameters are calculated, please see the supporting information.

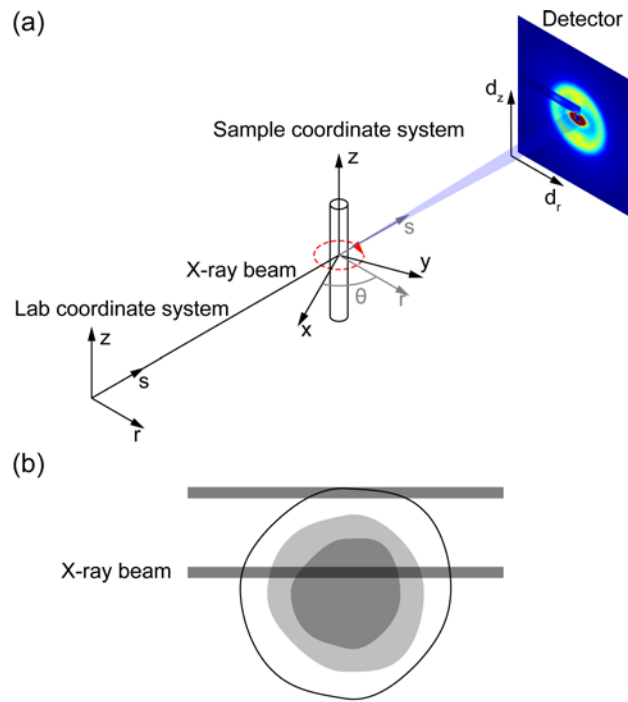


**Figure 2.** (a) Experimental geometry of X-ray scattering experiments. For WAXS  $\theta = 0$  and the sample coordinate axes are equivalent to the laboratory coordinate axes with  $\mathbf{x} = \mathbf{r}$  and  $\mathbf{y} = \mathbf{s}$ . During the tomography experiment, the filament is rotated around  $\mathbf{z}$  and for each angle the samples is scanned along  $\mathbf{r}$  with scattering patterns collected at each point. The detector coordinates are  $d_r$  and  $d_z$ . (b) Illustration of the X-rays path through the fiber in the employed

geometry. The X-ray beam is probing a superposition of all the structures along its path and the recorded scattering projection is a projection of this superposition. The effect of the superposition is less significant close to the fiber surface.

### **Microfocused X-ray Scattering**

Figure 2a illustrates the experimental geometry employed for WAXS and SAXS experiments. WAXS measurements were performed at the MaxIV NanoMax beamline.<sup>29</sup> A 13 keV X-ray beam was focused to 300 nm by 200 nm (horizontally  $\times$  vertically) at the sample position. The diffraction patterns were recorded on a PILATUS 1M detector (pixel size: 172  $\mu\text{m} \times 172 \mu\text{m}$ ) positioned 471 mm downstream from the sample. The filaments were positioned as shown in Figure 2a and the WAXS patterns were collected by continuously scanning the beam across the filament along  $\mathbf{r}$ . Images were collected every 500 ms corresponding to the beam having moved 1  $\mu\text{m}$ . After a completed line scan, the beam was stepped 1  $\mu\text{m}$  along  $\mathbf{z}$  and a new line scan was performed. In this way a 2D map ( $x, z$ ) of diffraction patterns were collected with a spatial resolution of 1  $\mu\text{m} \times 1 \mu\text{m}$ . The orientation of the PE crystallites was calculated according to the methods described in the Supporting Information.

SAXS computed tomography (SAXS CT) measurements were performed at the PETRA III Synchrotron (Hamburg, Germany) at Micro- and Nanofocus X-ray Scattering beamline (P03).<sup>30</sup> A 12.6 keV X-ray beam was focused to 1.4  $\mu\text{m} \times 1.4 \mu\text{m}$  at the sample position. The scattering images were recorded using a PILATUS 300K detector (pixel size: 172  $\mu\text{m} \times 172 \mu\text{m}$ ) placed 469 mm downstream from the sample. A custom-made beamstop allowed for a minimum  $q$ -value of 0.02  $\text{\AA}^{-1}$  (maximum feature size of 32 nm). The filaments were positioned as shown in Figure 2a and the X-ray beam was raster scanned along  $\mathbf{r}$  to collect the tomographic projections with 1.4  $\mu\text{m}$  step size and 500 ms exposure time per image. After completing the projection, the filament was rotated by  $\theta = 4^\circ$  and the X-ray beam moved 1  $\mu\text{m}$  along  $\mathbf{z}$  before

acquiring the next projection. A total of 45 projections were collected spanning one half 180° rotation of the filament. The sample transmission was measured separately by replacing the detector with a diode and used to normalize the scattering data. A detailed description of the tomographic problem and reconstruction is given in the Supporting Information along with discussion on radiation damage issues.

## **Results**

### **Local Crystallite Orientation**

During the filament making process, the UHMWPE molecules undergo flow (in the extrusion die + eventual draw down) that is likely to transform into morphological orientation upon crystallization. To investigate the local orientation distribution of the crystalline phase, we make use of nanofocused WAXS. The geometry of the experiment is shown in Figure 2a. The filaments are mapped perpendicular to the fiber axis and detailed analysis is performed by looking at the azimuthal profile of the 110 Bragg peak. Figure 3 shows the calculated orientation parameter as a function of position from the filament edge for all samples. The Herman's orientation parameter represents the degree of crystalline orientation about the filament fiber axis, with values ranging from -0.5 for complete perpendicular orientation to 1 for complete parallel orientation with zero value representing the isotropic case.

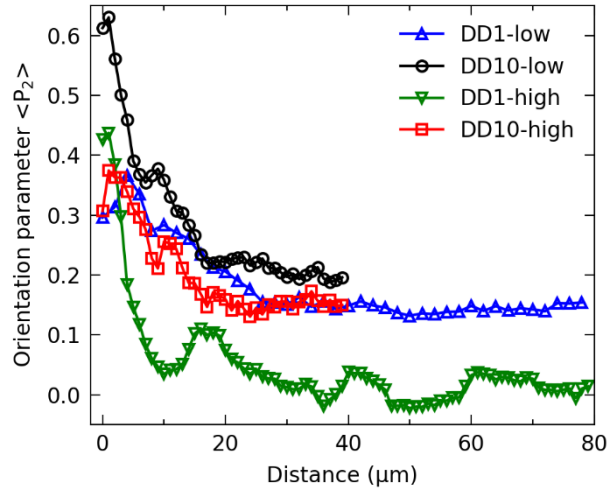


**Figure 3.** Orientation parameter ( $\langle P_2 \rangle$ ) profiles for all filaments calculated from the crystalline (110) reflection as measured by WAXS.

All four filaments show similar profile features with a lower degree of crystalline orientation in the center region of the filament compared to the surface (skin) region of the filament. The size of the skin region is comparable for filaments DD10-low and DD10-high (high draw down ratio) at approximately  $17 \mu\text{m}$ , while it is slightly larger for filament DD1-low ( $26 \mu\text{m}$ ). The irregular  $\langle P_2 \rangle_{\text{WAXS}}$  profile of the DD1-high filament leads to a surface region size of either  $10 \mu\text{m}$  or  $30 \mu\text{m}$ , depending on whether the first or second minimum of the orientation profile is considered the start of the skin region.

DD10-low (high draw down ratio and low quench temperature) has the highest degree of orientation out of the four samples, ranging from  $\sim 0.2$  in the core to  $\sim 0.6$  in the skin. Contrary, the sample with low draw down ratio and high quench temperature (DD1-high) has the lowest  $\langle P_2 \rangle_{\text{WAXS}}$  value in the filament core but the second highest value in the skin. DD10-high (high draw down ratio and high quench temperature) and DD1-low (low draw down ratio and low quench temperature) have very similar values of  $\langle P_2 \rangle_{\text{WAXS}}$  in the core and skin regions, with the main difference being the relative size of the skin region.

From these results, we can infer two trends of the crystalline orientation: the degree of alignment increases with drawn down ratio (keeping the quench temperature constant) and decreases with increased quench temperature (keeping the draw down ration constant).

We would like to stress that the values shown in Figure 3 are not representative of the actual intrinsic orientation distribution of the crystalline phase as a function of the filament radius, but rather represent the values calculated from a one-dimensional projection of a two-dimensional fiber slice. This distinction is inherent to the collection of the data. At every point, the beam passes through the entire longitudinal volume of the fiber slice and thus the resulting scattering pattern is a projection of this volume. The X-ray beam path and the projection effect are illustrated on Figure 2b. Since the filament cross-section is not cylindrically symmetric (this will become apparent later), it is not possible to apply mathematical models, such as the Abel transformation,<sup>17</sup> to transform the projections data to data along the filament radius. Nevertheless, the measured profiles give qualitative information about the local crystalline orientation distributions in the filaments.

One way to solve the issue of projected data is to do a full tomographic reconstruction of the filament. These results are presented below.

### **Crystal Alignment from a Molecular Perspective**

Figure 4 plots the characteristic Raman spectra collected by polarized Raman spectroscopy for all filaments with four different experimental settings. These spectra were measured for distinct filament positions and the peaks marked in red (1130  $\text{cm}^{-1}$  region; C-C symmetric and asymmetric stretching) were subsequently evaluated for calculating the orientation parameters.

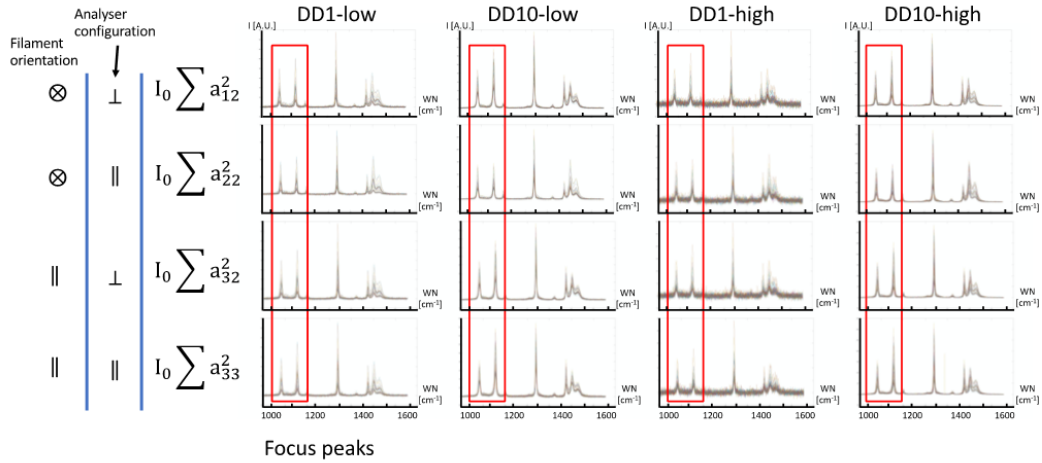


**Figure 4.** Fingerprint regions in the raw Raman spectra used for determining orientation encircled in red. Corresponding filament orientations and polarization orientations are shown on the left.

Figure 5 plots the overall orientation parameters calculated for all depths measured in the four fibers. An increasing extent of orientation is seen with an increase in drawing draw down. As expected, the samples with higher draw ratio (DD10; samples 2 and 4) have a higher orientation on average, while the effects of quench bath temperatures are less clear. The large error bars already indicate that the level of orientation can vary a lot depending on the exact position in the filaments.

We know from the work of Pigeon et al.<sup>28</sup> that the ratio between the symmetric and asymmetric C-C peaks ( $h_{1130}/h_{1063}$ ) should be dependent on the orientation parameters (Figure 6 in Ref.<sup>28</sup>), and also directly proportional to the orientation parameters. This can indeed be seen if we compare this to the previously shown mean area metric of the  $h_{1130}/h_{1063}$  ratio. Simply taking this peak ratio thus provides a practical and very easy method to estimate the extent of orientation from Raman experiments.

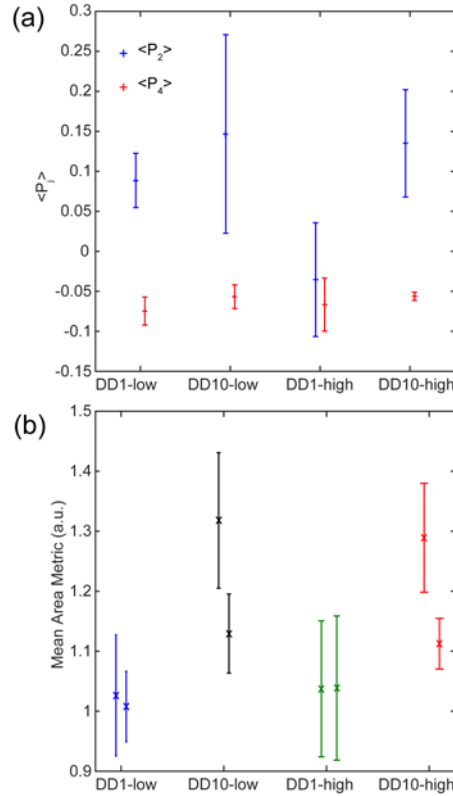


**Figure 5.** (a) Mean  $\langle P_2 \rangle_{\text{Raman}}$  and  $\langle P_4 \rangle_{\text{Raman}}$  values by sample, averaging all depths. Here it can be seen that the  $\langle P_4 \rangle_{\text{Raman}}$  parameter is a minor contribution in this regime. (b) Ratios of  $h_{1130}/h_{1063}$  calculated using the mean area metric, averaging all depths. Orientation 33 being the left bars and orientation 32 the rightmost ones. The ratio is a good estimate of the orientation parameters as shown by Pigeon.

Figure 6 shows profiles of the  $h_{1130}/h_{1063}$  ratio together with the orientation parameters  $\langle P_2 \rangle_{\text{Raman}}$  and  $\langle P_4 \rangle_{\text{Raman}}$  as a function of sample depth for all four samples (from skin to core). For the samples with higher draw down, a clear non-uniform orientation profile is obtained: from core to center, the extent of orientation increases steadily when getting closer to the edge. On the outside, there are indications that the orientation extent drops again (outer few  $\mu\text{m}$ ). This is particularly visible in sample 2, which had a low quench temperature. For the samples without draw down (DD1), an almost uniform orientation profile is obtained. It is at this stage unclear whether the orientation is truly uniform, or whether the overall lower orientation in

these samples doesn't allow eventual orientation differences to be identified with this Raman-based technique.

For all samples, the orientation profiles extracted from extensive  $\langle P_2 \rangle$ ,  $\langle P_4 \rangle$  determination qualitatively match those obtained from the method by Pigeon et al ( $h_{1130}/h_{1063}$  ratio), further confirming that this method can be used as a good and simple way to extract local orientation information in PE-based filaments.

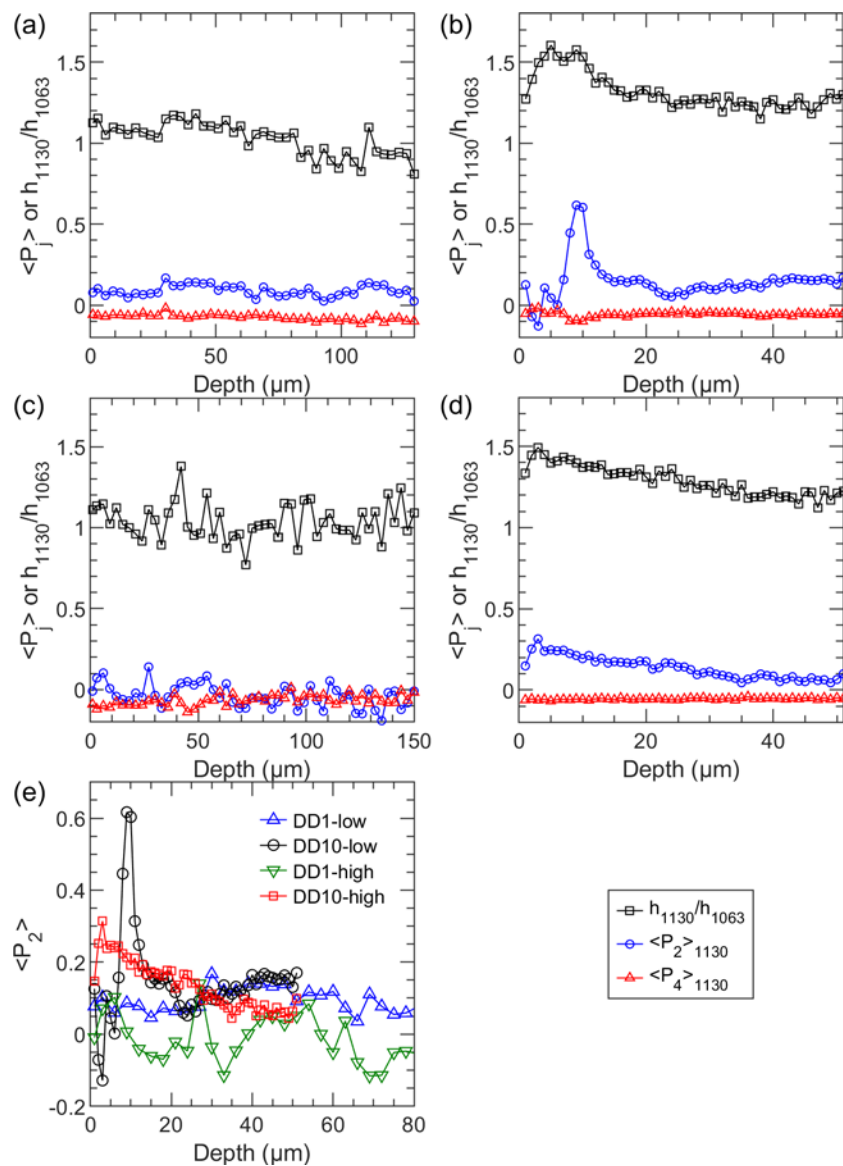


**Figure 6.** Ratio of  $h_{1130}/h_{1063}$  and orientation parameters profiles as calculated by polarized Raman spectroscopy for samples (a) DD1-low, (b) DD10-low, (c) DD1-high, and (d) DD10-

high. (e)  $\langle P_2 \rangle_{\text{Raman}}$  profiles for all four samples as a function of sample depth. Zero refers to the filament edge, while the curve ends at the (estimated) center of the filament.

### **Reconstructed Morphology**

Two of the four filaments were studied using SAXS CT in an attempt to obtain information about the local polymer morphology. Using the reconstruction technique described above, we have reconstructed the entire 2D scattering patterns for every voxel inside the filament specimen. Figure 7 shows the reconstructed scattering patterns at different locations inside the DD1-high filament (as indicated in Figure 8a) and suggests a change in the local filament morphology when moving from the core region towards the periphery. The first (leftmost) scattering pattern taken from the core region of the filament shows a mostly isotropic scattering ring at  $q \approx 0.5 \text{ \AA}^{-1}$  suggesting morphology of randomly oriented alternating crystalline and amorphous lamellae. The second pattern, taken from a position approximately 2/3 of the way towards the surface of the filament, shows a similar isotropy. Towards the filament periphery, we begin to observe a change in the patterns from isotropic to anisotropic. At the third position, the scattering feature takes an oval shape with increased intensity along the meridional, indicating a gradual alignment of the lamellae so that the stacking direction is perpendicular to the fiber axis. At the fourth position near the filament surface, we begin to observe two distinct lobes along the meridional, which become clearly separated at the outermost position (rightmost in Figure 7). The emerging streak at the equatorial near the filament periphery indicates the presence of fibrillar scatterers oriented along the fiber axis. These scattering entities could be either chain-extended structures (shish) oriented along the fiber axis or oriented microvoids in the polymer.

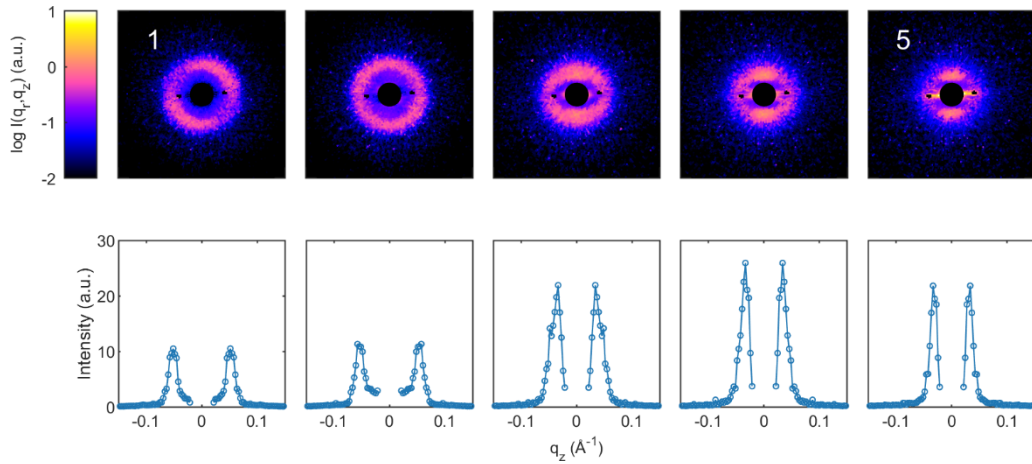


**Figure 7.** Reconstructed SAXS patterns (top) and intensity profiles along  $q_z$  (bottom) at different positions in the DD1-high filament indicated by dots in Figure 8a.

From the reconstructed data, standard 1D correlation function analysis was used to extract information about the lamellae long period ( $Lp$ ). Figure 8 shows the results of SAXS analysis for the DD1-high filament. The reconstructed attenuation coefficient (Figure 8a) reveals that the filament cross-section is not perfectly circular (we discuss this point further in an upcoming section). The attenuation coefficient is mostly uniform throughout the sample corresponding to polyethylene with a mostly homogenous density. The faint ring seen at the edge of the reconstructed volume is an artifact of the limited projection reconstruction.

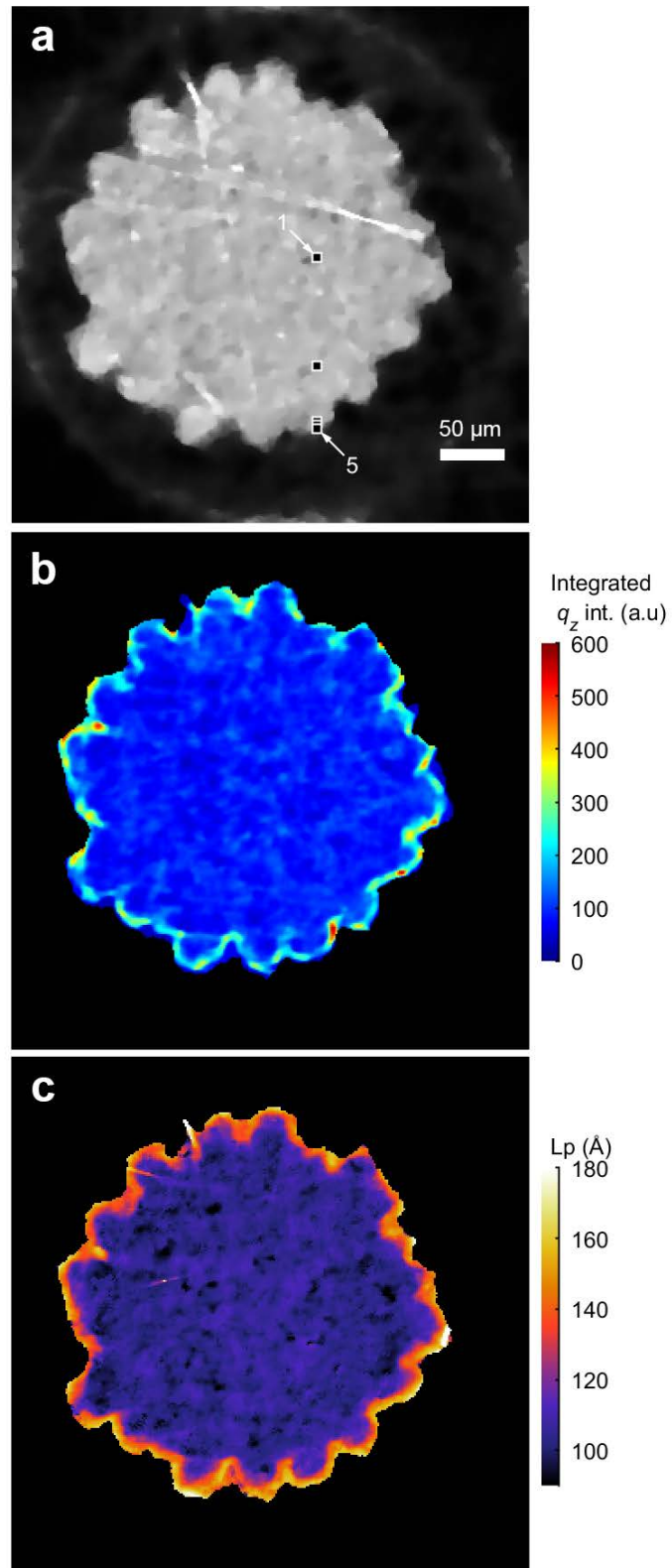


**Figure 8.** Reconstructed morphology of DD1-high filament. (a) Reconstructed attenuation coefficient. (b) Integrated scattering intensity along  $q_z$  axis. (c) Lamella long-period from 1D correlation function analysis. Each pixel corresponds to a voxel of size  $1.4 \mu\text{m} \times 1.4 \mu\text{m}$ .

The integrated scattering intensity along the  $q_z$ -axis (Figure 8b) further indicates a difference in structure between the skin and the core of the filament. The increase in integrated  $q_z$  intensity towards the periphery of the filament indicates either that the crystallinity of the polymer is higher in the skin, or that the crystalline lamellae are preferentially more aligned with the fiber axis in the skin region (i.e. the scattering is anisotropic with higher intensities along the meridional), or a combination of both. Considering that the scattering pattern goes from isotropic in the core to anisotropic in the skin (Figure 7), we can conclude that the increase in integrated  $q_z$  intensity is at least partially caused by realignment of the lamellae along the fiber axis.

Using the reconstructed SAXS data, the lamellae long period were obtained by 1D correlation function analysis of the intensity profiles along  $q_z$  (Figure 8c). The reconstructed  $Lp$  map shows a skin-core structure, with a mostly homogenous core (average interlamellar distance =  $104.6 \pm 3.6$  Å). There is a gradual increase in  $Lp$  towards the periphery of the filament with values reaching up to 180 Å at the outer edge.

Figure 9 shows the reconstructed scattering patterns from five different positions inside the DD10-high filament. Owing to the lack of rotational invariance in the sample, a correct reconstruction along the equatorial is not guaranteed. However, it does appear that there is a difference in the scattering features from position inside the core region to positions inside the skin region. In the skin region of the filament (first and fifth pattern), two clear diffraction peaks are found along the meridional along with an intense scattering streak along the equatorial, indicating chain-folded lamellae stacked perpendicular to the fiber direction and fibrillar scatterers oriented along the fiber direction. In the core region, the scattering appears to be less anisotropic with a scattering ring superimposed on top of the two meridional lobes. These features are also present in the raw projected scattering patterns (not shown), indicating

that the reconstructed patterns are at least quantitatively representative of the actual counterpart.

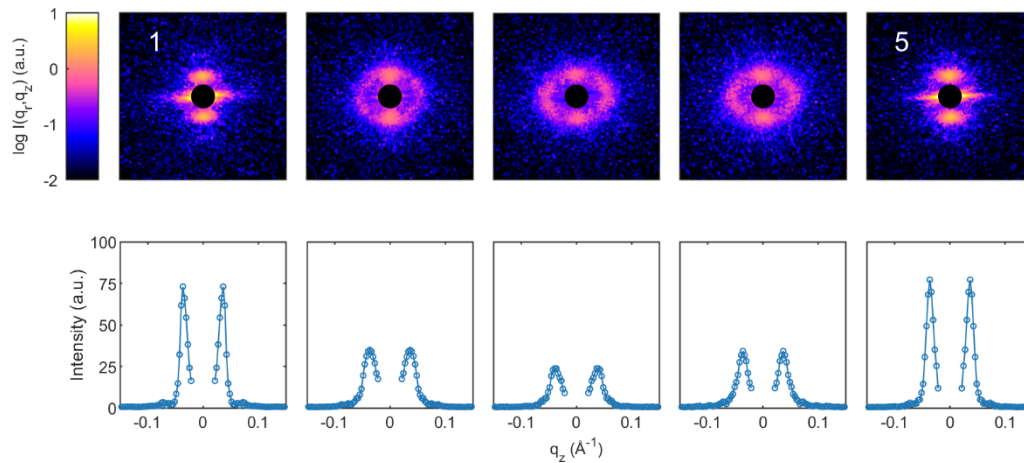


**Figure 9.** Reconstructed SAXS patterns (top) and intensity profiles along  $q_z$  (bottom) at different positions in the DD10-high filament indicated by dots in Figure 10a.

Figure 10 shows the SAXS CT results for the DD10-high filament. The reconstructed attenuation coefficient (Figure 10a) reveal a mostly homogenous filament with a flattened cross-section rather than a circular cross section. The nonzero background inside the reconstructed volume is an artifact of the low counting rate during the absorption measurement and limited number of angular projections. The integrated scattering intensity along  $q_z$  shows a clear skin-core structure of the filament (Figure 10b), similar to what was observed for the DD1-high filament. Furthermore, the  $L_p$  map obtained by 1D correlation function analysis (Figure 10c) likewise shows skin-core structure. The  $L_p$  goes from approximately 10 nm in the filament core to more than 15 nm at the periphery. The spot marked with an arrow is a low  $q$  reconstruction artifact that give rise to an erroneous 1D-correlation function.

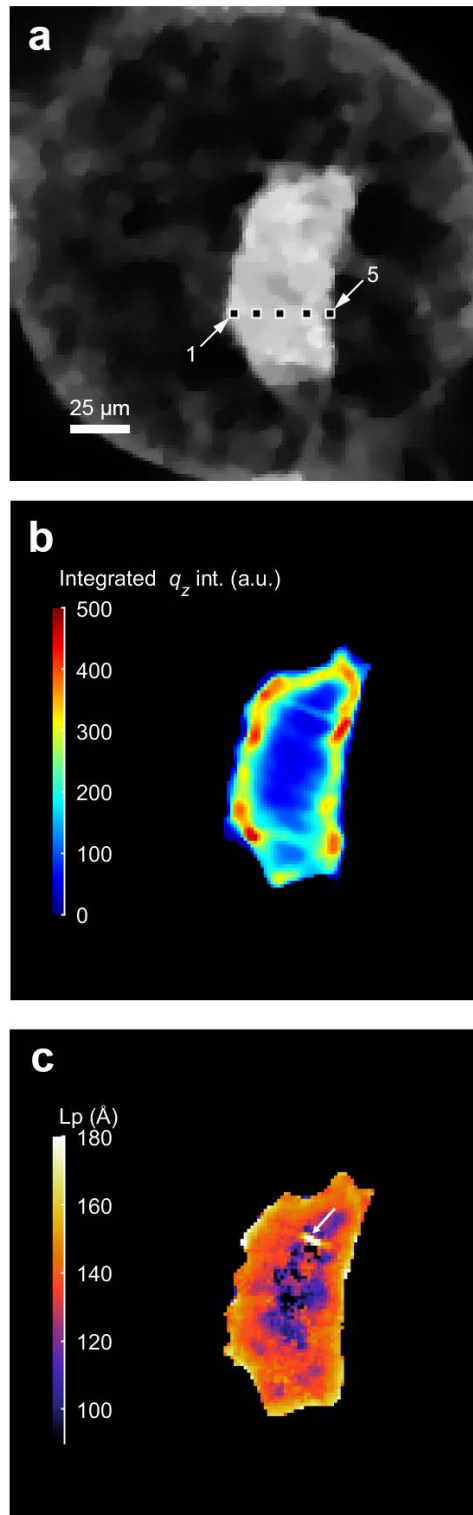


**Figure 10.** Reconstructed morphology of DD10-high filament. (a) Reconstructed attenuation coefficient. (b) Integrated scattering intensity along  $q_z$  axis. (c) Lamella long-period from 1D correlation function analysis. The arrow in (c) indicates a reconstruction artifact. Each pixel corresponds to a voxel of size  $1.4 \mu\text{m} \times 1.4 \mu\text{m}$ .

## **Discussion**

### **Structural observations of filaments**

Under the employed spinning conditions, all filaments display highly heterogeneous skin-core properties in the degree of crystalline orientation obtained from WAXS. In all cases, the crystalline orientation is higher towards the surface of the filaments. In the gel-spinning process, the orientation of the polymer chains is induced by the flow of the gel through the spinneret holes. In a first order approximation, the flow profile is uneven across the diameter of the spinneret hole due to the no-slip condition at the wall boundary. The shear stresses on the gel are maximized at the spinneret wall, and in turn, the chains extension during the flow is greater near the surface of the filament. Upon leaving the spinneret, the shear stresses are relaxed, and the polymer chains are subjected to relaxation. If the subsequent crystallization occurs on a timescale faster than the critical relaxation time, the flow-induced chain orientation is preserved in the final structure. The influence of the spinning parameters is discussed in the next section.

We would like to add a comment on the cross-sectional shapes of the filaments. As shown in Figure 8, the cross-sectional shape of the DD1-high filament is not cylindrically symmetric. Rather it is actinomorphic with multiple indents along its outer contour. We speculate that this shape could be a result of rapid evaporation of solvent in the air gap between the spinneret and the quenching bath, and subsequent reduction in volume. The shape could also be a result of minimizing the interfacial free energy of the filament in the quench bath itself. The flattened cross-section of the DD10-high (as seen in Figure 10) is most likely caused by the filament being deformed as it passes over the takedown rollers. This effect is more prominent in samples with high draw down ratio as the filaments arrive at the rollers with a higher temperature (due to the increase in takedown speed).

## Effects of spinning conditions on skin-core structure

The skin-core structure observed in the filaments is caused by two mechanisms in the filament spinning process: it is an effect of the aforementioned fluid mechanical considerations and thermodynamic phenomena inside the polymer gel.

In addition to the flow-induced alignment of the polymer chains in the spinneret, the filaments subjected to a high draw down ratio are essentially undergoing a uniaxial extension upon leaving the spinneret. This extensional flow will cause a further extension of the chains, counteracting the chain relaxation. The effect of the increased draw down is seen in the  $\langle P_2 \rangle_{\text{WAXS}}$  profiles, where the two samples prepared at draw down 10 (DD10-low and DD10-high) have overall higher orientation than their respective counterpart prepared at draw down 1. These findings are in agreement with the overall orientation as measured by polarized Raman spectroscopy.

The temperature of the quenching water likewise influences the overall crystalline orientation inside the filaments. A lower quenching temperature facilitates a faster crystallization of the polymer, leaving the polymer chains with less time to relax and lose their flow-induced orientation. For filaments with similar draw down, the overall degree of crystalline orientation is higher in the filaments with the lowest water quenching temperature, as seen by the  $\langle P_2 \rangle_{\text{WAXS}}$  profiles. In the case of high draw down, the degree of orientation in both skin and core is highest in the filaments with lowest quenching temperature. However, in the case of low draw down, the degree of orientation in the skin of the DD1-high filaments is higher than in the skin of the DD1-low filament. This suggests that the thermodynamic considerations are more nuanced than discussed here. We also point out that the high degree of orientation in the skin of the DD1-high filament might be a localized phenomenon.

Furthermore, lower draw down ratio will lead to a thicker diameter of the filament in the quench bath. Ohta et al.<sup>14</sup> speculate that a thicker filament diameter of dry-spun UHMWPE

filaments will lead to increased heterogeneity of the internal filament structure due to poor heat transfer from the filament surface. The poor surface heat transfer induces a temperature gradient and polymer concentration gradient perpendicular to the fiber axis, which in turn creates heterogeneity in the structure between skin and core. The  $\langle P_2 \rangle_{\text{WAXS}}$  profiles indicate that for the filaments quenched at high temperature (DD1-high and DD10-high), the filament with draw down 1 is less homogeneous perpendicular to the fiber axis than the filament with draw down 10. However, for the samples quenched at low temperature (DD1-low and DD10-low), we observe the opposite behavior. Our findings suggest that the speculated poor heat transfer at the surface of the dry-spun filaments of Ohta et al.<sup>14</sup> is not the dominant mechanism for the skin-core structure found in our wet-spun filaments, possibly due to better heat transfer at the surface during the quench.

We discuss the thickness of the skin region in the following section.

### **Skin-core structure across multiple length scales**

In the present study, we have employed different methods to investigate the local structure of UHMWPE filaments. All of these methods operate on different length scales within the material and provide information on different aspects of the semi-crystalline structure. Raman spectroscopy explores the vibration of the molecular bonds and thus represent the smallest length scale probed in this study. In principle, Raman spectroscopy can discriminate between amorphous and crystalline phases in the polymer structure, however, the results presented within this study are limited to vibrational modes located in the crystalline domains.

In the X-ray scattering techniques, the contrast is provided by the differences in electron density across a periodic structure. For WAXS, the length scale is at the level of the crystal lattice (in the order of an Å), and the information obtained from the WAXS data concerns only the crystalline phases of the polymer. For SAXS, the contrast is provided by variation across

crystalline and amorphous phases and thus the length scale probed is significantly larger than for WAXS (on the order of tens of nm) and the structural information provided by SAXS concerns the semi-crystalline superstructure. The application of all three method provides detailed information about the local structure across multiple length scales, which has not previously been reported for UHMWPE filaments.

While first indications of skin-core morphology could be readily derived from the polarized Raman results, obtaining a very detailed picture on the local orientation differences is not straightforward or even possible with Raman micro-spectroscopy for a few reasons. Firstly, the spatial resolution in Raman microscopy is limited by the laws of diffraction (about 1  $\mu\text{m}$  in  $xy$  and a few micrometers in  $z$ ). It is also not routine to measure the same location on a filament in two orientations as necessary as the filament will need to be embedded in resin for the edge-on measurements. Hence, there will be some averaging imposed by the technique itself. Moreover, the very irregular shape and heterogeneous density of the filaments, causes additional loss in spatial resolution, affecting the effective spatial resolution on the edge for observing very local orientation effects in such small samples. Secondly, in the current analysis, only molecular vibrations in the crystalline domain are targeted, and thus signal strength is highly dependent on crystallinity. This could explain less orientation differences could be identified in the draw down 1 samples.

**Table 3.** Skin region thickness as determined by WAXS, SAXS, and Raman.

sample	skin region thickness ( $\mu\text{m}$ )			
	WAXS	SAXS ( $L_p$ )	SAXS ( $q_z$ int.)	Raman
DD1-low	~ 26	n/a	n/a	n/a
DD10-low	~ 17	n/a	n/a	~ 10
DD1-high	~ 10	13.3 (4.0)	12.6 (5.8)	n/a
DD10-high	~ 17	16.5 (6.6)	12.9 (4.5)	~ 20

Of the two samples (DD1-high and DD10-high) studied by SAXS tomography, both exhibit skin-core properties in the semi-crystalline superstructure. In the DD1-high filament (low draw down and high quenching temperature), the core consists of lamellar structures with an inter-lamellar distance (long period) of  $104.6 \pm 3.6 \text{ \AA}$  and with an isotropic orientation distribution, while the lamellae in the skin region are preferentially aligned along the fiber axis with longer inter-lamellar distances (up to approximately  $180 \text{ \AA}$ ). One advantage of the real-space mapping provided by the SAXS reconstruction is that we can estimate the thickness of the superstructure skin region in a straightforward manner. For a detailed description of how this is done, please see the Supporting Information. The results are listed in Table 3. For the DD1-high filament, we obtain the same thickness of the skin region from the  $Lp$  map as from the integrated  $q_z$  intensity map. This suggests that increase in inter-lamellar distance towards the filament periphery follow the increase lamellar alignment somewhat closely. Moreover, the error on the calculated values are significant (almost 50% in the case of the  $q_z$  intensity), indicating that the skin thickness is not homogeneous along the periphery of the filament.

It is interesting to compare the skin thickness of the superstructure with the skin thickness obtained from the  $\langle P_2 \rangle_{\text{WAXS}}$  profile. For the DD1-high filament, the  $\langle P_2 \rangle_{\text{WAXS}}$  profile is irregular along the diameter and thus determining the skin thickness is not straightforward. We attribute the irregularities in the  $\langle P_2 \rangle_{\text{WAXS}}$  profile to the cross-sectional shape of the filament as follows: the orientation parameter profile obtained from the WAXS measurements is not a function of the filament radius, but rather a function of the entire filament volume illuminated by the X-ray beam when scanning perpendicular to the fiber direction. The reconstructed attenuation map emphasizes the lack of cylindrical symmetry in the DD1-high filament; rather, it is actinomorphic. The path of the X-rays through the filament is thus very dependent on the local edge contour, and the resulting profile could be highly irregular. If we consider the first minimum of the  $\langle P_2 \rangle_{\text{WAXS}}$  profile as the “true” skin thickness (and assume that the X-ray beam

only passes through one petal of the cross-sectional flower), the skin thickness obtained from the  $\langle P_2 \rangle_{\text{WAXS}}$  profile is close to the skin thickness measured by SAXS. This would indicate that the alignment of the crystallites follows the overall change in the lamellar structure rather closely.

The tomographic reconstruction of the DD10-high filament (high draw down and low quenching temperature) reveals a morphology of stacked chain-folded lamellae in both the core and the skin of the filament, with their alignment along the fiber axis and the inter-lamellae distance increasing in the skin region near the surface. Unlike the DD1-high filament, the estimated skin region of the  $Lp$  map is approximately 3-4  $\mu\text{m}$  thicker than the skin region of the  $q_z$  intensity map. Again, we obtain a significant uncertainty in the thickness value. The skin thickness estimated by the  $\langle P_2 \rangle_{\text{WAXS}}$  profile is 17  $\mu\text{m}$  for the DD10-high filament, thus falling within the experimental error of the estimated skin thickness by SAXS.

## Conclusions

In this study, the local structure of gel-spun UHMWPE filaments was investigated as a function of draw down ratio and water quenching temperature by means of polarized Raman spectroscopy, WAXS and SAXS tomography.

The local orientation of PE crystallites was investigated by nanofocused WAXS and profiles of the  $\langle P_2 \rangle$  orientation parameter were calculated from the 110 Bragg reflection. These results show skin-core structure in all filaments under the employed spinning conditions, with an increase in the degree of orientation towards the surface of the filaments. The skin-core structure is thought to originate from the flow of the polymer gel through the capillaries in the spinneret, causing increased shear and thus higher chain alignment at the filament surface. The overall crystalline orientation is highest in filaments obtained with high draw down ratio or in filaments with low water quenching temperature. However, the results are not conclusive on

the relationship between processing parameters and the degree of heterogeneity between skin and core regions.

Polarized Raman spectroscopy was able to discern skin-core structures in the filaments with highest overall degree of orientation of the molecular bonds in the crystalline phase, as calculated from the symmetric C-C stretching ( $1130\text{ cm}^{-1}$ ), obtained using a draw down ratio of 10 during the spinning process. A simplified analysis method based on peak ratios as proposed earlier by Pigeon was found to give qualitatively similar results as the extensive  $\langle P_2 \rangle$ ,  $\langle P_4 \rangle$  orientation parameter calculations. Clear skin-core effects were visualized in the samples with the highest overall orientation.

The real-space morphology of two filaments is investigated in detail using SAXS-CT with a microfocused beam and micrometer spatial resolution. Both samples (low and high draw down and high water quenching temperature) show skin-core structure. The core of the low draw down filament is composed of isotopically orientated lamellar structures with an inter-lamellar distance of  $104.6 \pm 3.6\text{ \AA}$ , while the skin is composed of lamellar structures preferentially aligned along to fiber axis with a higher inter-lamellar distance (up to  $180\text{ \AA}$ ). On the other hand, the high draw down sample are composed of stacked chain-folded lamellae in both the core and the skin of the filament, increased alignment and inter-lamellae distance in the skin region. In both samples prepared with high quenching temperature, the thickness of the skin regions is not well defined along the periphery of the filament. Moreover, the skin thickness estimated from the changes in superstructure was found to be on the same order as the skin thickness estimated from the change in the degree of crystalline orientation.

## ASSOCIATED CONTENT

### Supporting Information.

The following files are available free of charge.

Additional details on the experimental Raman work and analysis, orientation parameter calculations from WAXS data, additional discussion on SAXS-CT including reconstruction, rotational invariance and analysis, discussion on X-ray beam damage, and details on the method for estimating skin region thickness.

## AUTHOR INFORMATION

### Corresponding Authors

\*M.K.H-H: E-mail: [mathias.huss-hansen@fysik.dtu.dk](mailto:mathias.huss-hansen@fysik.dtu.dk)

\*E.G.H: E-mail [erik@physics.org](mailto:erik@physics.org)

### Author Contributions

†M.K.H-H. and E.G.H. contributed equally to this work. The manuscript was written through contributions of all authors. All authors have given approval to the final version of the manuscript.

### Notes

The authors declare no competing financial interest.

## ACKNOWLEDGMENTS

We would like to thank Collin Tan Yong Xiang who performed the initial Raman microscopy at KU Leuven, Florian Wieland of Helmholtz-Zentrum Geesthacht and Sven Kreisig from the DSM Applied Science Center (Geleen, NL) for discussions and Ulf Johansson, Alexander Björling and Sebastian Kalbfleisch of MAX IV for experimental assistance with the WAXS

experiment. We thank the Danish Agency for Science, Technology, and Innovation for funding the instrument center DanScatt. Authors acknowledge DESY for allocation of the beamtime at P03 beamline.

## REFERENCES

- (1) Smith, P.; Lemstra, P. J.; Kalb, B.; Pennings, A. J. Ultrahigh-Strength Polyethylene Filaments by Solution Spinning and Hot Drawing. *Polym. Bull.* **1979**, *1*, 733–736.
- (2) Smith, P.; Lemstra, P. J. Ultra-High-Strength Polyethylene Filaments by Solution Spinning/Drawing. *J. Mater. Sci.* **1980**, *15*, 505–514.
- (3) Smith, P.; Lemstra, P. J. Ultrahigh-Strength Polyethylene Filaments by Solution Spinning/Drawing. II. Influence of Solvent on the Drawability. *Die Makromol. Chemie* **1979**, *2986*, 2983–2986.
- (4) Smith, P.; Lemstra, P. J. Ultra-High Strength Polyethylene Filaments by Solution Spinning/Drawing. 3. Influence of Drawing Temperature. *Polymer (Guildf)*. **1980**, *21*, 1341–1343.
- (5) Balzano, L.; Coussens, B.; Engels, T.; Oosterlinck, F.; Vlasblom, M.; van der Werff, H.; Lellinger, D. Multiscale Structure and Microscopic Deformation Mechanisms of Gel-Spun Ultrahigh-Molecular-Weight Polyethylene Fibers. *Macromolecules* **2019**, *52*, 5207–5216.
- (6) Sawai, D.; Nagai, K.; Kubota, M.; Ohama, T.; Kanamoto, T. Maximum Tensile Properties of Oriented Polyethylene, Achieved by Uniaxial Drawing of Solution-Grown Crystal Mats: Effects of Molecular Weight and Molecular Weight Distribution. *J. Polym. Sci. Part B Polym. Phys.* **2006**, *44*, 153–161.
- (7) Morgan, R. J.; Pruneda, C. O.; Steele, W. J. The Relationship between the Physical Structure and the Microscopic Deformation and Failure Processes of Poly(p-Phenylene Terephthalamide) Fibers. *J. Polym. Sci. Polym. Phys. Ed.* **1983**, *21*, 1757–1783.
- (8) Graham, J. F.; McCague, C.; Warren, O. L.; Norton, P. R. Spatially Resolved

- Nanomechanical Properties of Kevlar® Fibers. *Polymer (Guildf)*. **2000**, *41*, 4761–4764.
- (9) Davies, R. J.; Koenig, C.; Burghammer, M.; Riekel, C. On-Axis Microbeam Wide- and Small-Angle Scattering Experiments of a Sectioned Poly(p -Phenylene Terephthalamide) Fiber. *Appl. Phys. Lett.* **2008**, *92*.
- (10) Şahin, K.; Clawson, J. K.; Singletary, J.; Horner, S.; Zheng, J.; Pelegri, A.; Chasiotis, I. Limiting Role of Crystalline Domain Orientation on the Modulus and Strength of Aramid Fibers. *Polymer (Guildf)*. **2018**, *140*, 96–106.
- (11) Ohta, Y.; Murase, H.; Hashimoto, T. Structural Development of Ultra-High Strength Polyethylene Fibers: Transformation from Kebabs to Shishs through Hot-Drawing Process of Gel-Spun Fibers. *J. Polym. Sci. Part B Polym. Phys.* **2010**, *48*, 1861–1872.
- (12) Pennings, A. J.; Kiel, A. M. Fractionation of Polymers by Crystallization from Solution, III. On the Morphology of Fibrillar Polyethylene Crystals Grown in Solution. *Kolloid-Zeitschrift Zeitschrift für Polym.* **1965**, *205*, 160–162.
- (13) Smook, J.; Pennings, A. J. Elastic Flow Instabilities and Shish-Kebab Formation during Gel-Spinning of Ultra-High Molecular Weight Polyethylene. *J. Mater. Sci.* **1984**, *19*, 31–43.
- (14) Ohta, Y.; Murase, H.; Hashimoto, T. Effects of Spinning Conditions on the Mechanical Properties of Ultrahigh-Molecular-Weight Polyethylene Fibers. *J. Polym. Sci. Part B Polym. Phys.* **2005**, *43*, 2639–2652.
- (15) Riekel, C.; Dieing, T.; Engström, P.; Vincze, L.; Martin, C.; Mahendrasingam, A. X-Ray Microdiffraction Study of Chain Orientation in Poly(p-Phenylene Terephthalamide). *Macromolecules* **1999**, *32*, 7859–7865.

- (16) Roth, S.; Burghammer, M.; Janotta, A.; Riekkel, C. Rotational Disorder in Poly(p-Phenylene Terephthalamide) Fibers by X-Ray Diffraction with a 100 Nm Beam. *Macromolecules* **2003**, *36*, 1585–1593.
- (17) Stribeck, N.; Nöchel, U.; Camarillo, A. A. Scanning Microbeam X-Ray Scattering of Fibers Analyzed by One-Dimensional Tomography. *Macromol. Chem. Phys.* **2008**, *209*, 1976–1982.
- (18) Stribeck, N.; Nöchel, U.; Fakirov, S.; Feldkamp, J.; Schroer, C.; Timmann, A.; Kuhlmann, M. SAXS-Fiber Computer Tomography. Method Enhancement and Analysis of Microfibrillar-Reinforced Composite Precursors from PEBA and PET. *Macromolecules* **2008**, *41*, 7637–7647.
- (19) Grubb, D. T. Comments on “Axial X-Ray Scattering on High Performance Polymeric Fibers.” *J. Polym. Sci. Part B Polym. Phys.* **1996**, *34*, 1159–1161.
- (20) Feldkamp, J. M.; Kuhlmann, M.; Roth, S. V.; Timmann, A.; Gehrke, R.; Shakhverdova, I.; Paufler, P.; Filatov, S. K.; Bubnova, R. S.; Schroer, C. G. Recent Developments in Tomographic Small-Angle X-Ray Scattering. *Phys. Status Solidi* **2009**, *206*, 1723–1726.
- (21) Schaff, F.; Bech, M.; Zaslansky, P.; Jud, C.; Liebi, M.; Guizar-Sicairos, M.; Pfeiffer, F. Six-Dimensional Real and Reciprocal Space Small-Angle X-Ray Scattering Tomography. *Nature* **2015**, *527*, 353–356.
- (22) Liebi, M.; Georgiadis, M.; Menzel, A.; Schneider, P.; Kohlbrecher, J.; Bunk, O.; Guizar-Sicairos, M. Nanostructure Surveys of Macroscopic Specimens by Small-Angle Scattering Tensor Tomography. *Nature* **2015**, *527*, 349–352.
- (23) Georgiadis, M.; Guizar-Sicairos, M.; Zwahlen, A.; Trüssel, A. J.; Bunk, O.; Müller, R.; Schneider, P. 3D Scanning SAXS: A Novel Method for the Assessment of Bone

- Ultrastructure Orientation. *Bone* **2015**, *71*, 42–52.
- (24) Schroer, C. G.; Kuhlmann, M.; Roth, S. V.; Gehrke, R.; Stribeck, N.; Almendarez-Camarillo, A.; Lengeler, B. Mapping the Local Nanostructure inside a Specimen by Tomographic Small-Angle x-Ray Scattering. *Appl. Phys. Lett.* **2006**, *88*, 1–4.
- (25) Kida, T.; Oku, T.; Hiejima, Y.; Nitta, K. H. Deformation Mechanism of High-Density Polyethylene Probed by in Situ Raman Spectroscopy. *Polymer (Guildf)*. **2015**, *58*, 88–95.
- (26) Hiejima, Y.; Kida, T.; Nitta, K. H. In Situ Monitoring of Orientation Parameters and Orientation Distribution Functions of Polyethylenes during Tensile Tests. *Macromol. Symp.* **2018**, *377*, 1–5.
- (27) Hiejima, Y.; Okuda, T.; Kono, K.; Nitta, K. hei. Orientation Behavior and Deformation Mechanism of Polyethylene Gels during Cold Drawing Determined by in Situ Raman Spectroscopy. *Polymer (Guildf)*. **2019**, *176*, 30–37.
- (28) Pigeon, M.; Prud'homme, R. E.; Pezolet, M. Characterization of Molecular Orientation in Polyethylene by Raman Spectroscopy. *Macromolecules* **1991**, *24*, 5687–5694.
- (29) Johansson, U.; Vogt, U.; Mikkelsen, A. NanoMAX: A Hard x-Ray Nanoprobe Beamline at MAX IV. *X-Ray Nanoimaging: Instruments and Methods* **2013**, *8851*, 88510L.
- (30) Krywka, C.; Keckes, J.; Storm, S.; Buffet, A.; Roth, S. V.; Döhrmann, R.; Müller, M. Nanodiffraction at MINAXS (P03) Beamline of PETRA III. *J. Phys. Conf. Ser.* **2013**, *425*, 4–8.

## SUPPORTING INFORMATION

# Local Structure Mapping of Gel-Spun Ultrahigh-Molecular-Weight Polyethylene (UHMWPE) Fibers

*Mathias K. Huss-Hansen,<sup>\*,†,1</sup> Erik G. Hedlund,<sup>\*,†,2</sup> Anton Davydok,<sup>3</sup> Marie Hansteen,<sup>1,4</sup> Jildert Overdijk,<sup>4</sup> Gert de Cremer,<sup>4</sup> Maarten Roeffaers,<sup>2</sup> Matti Knaapila<sup>1</sup> and Luigi Balzano<sup>4</sup>*

<sup>1</sup>Department of Physics, Technical University of Denmark, Kgs. Lyngby, 2800, Denmark

<sup>2</sup>cMACS, KU Leuven, Leuven, 3001, Belgium

<sup>3</sup>Institute of Materials Research, Helmholtz-Zentrum Geesthacht, Notkestrasse 85, 22607

Hamburg, Germany

<sup>4</sup>DSM, Applied Science Center, Urmonderbaan 22, 6167RD Geleen, The Netherlands

[\\*mathias.huss-hansen@fysik.dtu.dk](mailto:mathias.huss-hansen@fysik.dtu.dk)

[\\*erik@physics.org](mailto:*erik@physics.org)

## Polarized Raman Spectroscopy: Experiment and Analysis

The orientation of the fiber filaments were probed using a microscopy-based Raman analysis technique described here. The methodology for calculating the orientation parameters is based on the work by Pigeon<sup>1</sup> et al. and uses the Raman intensities measured perpendicular and parallel to the pump laser, which is aimed either along the longitudinal direction of the filament and edge-on into the filament cross-section. The geometry of the measurement system is shown in Figure S1 together with schematic views of idealized filament profiles for the two sample orientations used.

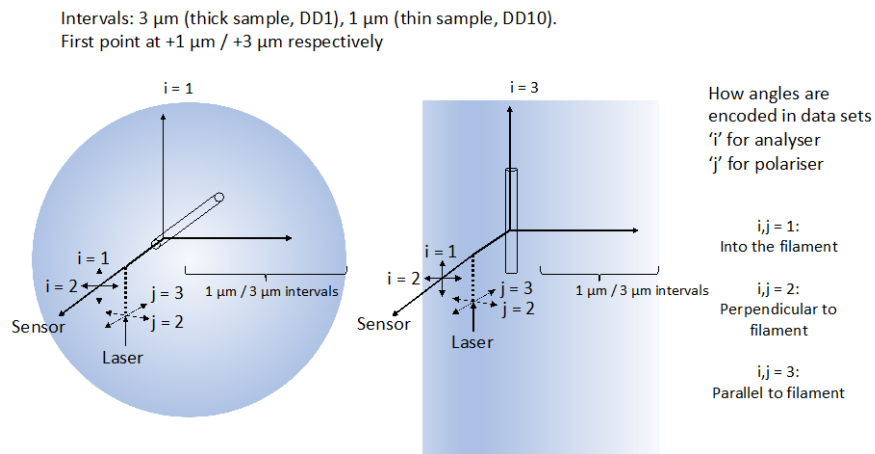


**Figure S1.** Raman microscopy measurement geometry – Polarizer, analyzer, and filament orientations. Also shown is a schematic representation of the measurement point locations in the filament as oriented. Measurement points are equal in number and equidistant, resulting in longer intervals for the thicker, DD1, fibers.

The necessary polarized Raman spectra were acquired using a custom-made microscope setup schematically shown in Figure S2a. Figure S2b shows a schematic of how the filament was embedded in resin for edge-on measurements. The microscope-based system allows the sample to be mounted directly on a coverslip with direct viewing using a camera for alignment. A 532

nm pump laser with selectable polarization is coupled into the beam path and the Raman back scattered spectrum is directly measured through a spectrometer after passing through an analyzer. The laser is focused to a diffraction limited spot at the sample and this spot is then scanned across the sample to acquire the Raman spectra.

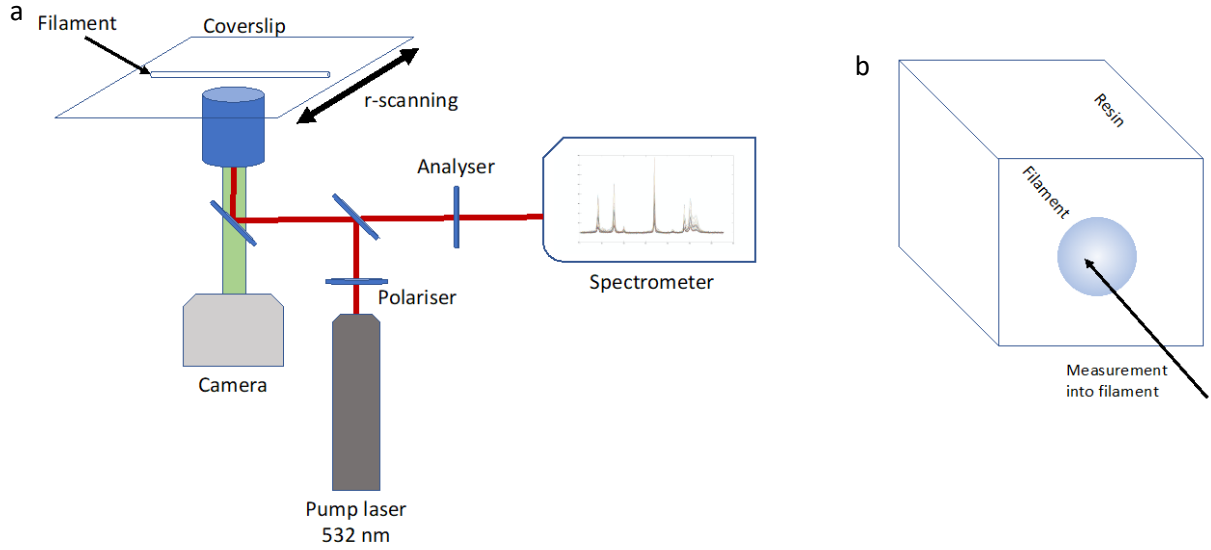


**Figure S2.** (a) Schematic of the Raman microscopy setup. (b) Filament mounted in resin for edge-on measurements.

From Pigeon<sup>1</sup>, we have that the orientation parameter can be obtained from the following five equations:

$$\begin{aligned}
 I_0 \sum \alpha_{22}^2 = b & \left[ \frac{3a_1^2 + 3a_2^2 + 3 + 2a_1a_2 + 2a_1 + 2a_2}{15} \right. \\
 & + \langle P_2 \rangle \frac{3a_1^2 + 3a_2^2 - 6 + 2a_1a_2 - a_1 - a_2}{21} \\
 & \left. + 3\langle P_4 \rangle \frac{3a_1^2 + 3a_2^2 + 8 + 2a_1a_2 - 8a_1 - 8a_2}{280} \right]
 \end{aligned} \tag{S1}$$

$$\begin{aligned}
I_0 \sum \alpha_{33}^2 = b & \left[ \frac{3a_1^2 + 3a_2^2 + 3 + 2a_1a_2 + 2a_1 + 2a_2}{15} \right. \\
& - 2\langle P_2 \rangle \frac{3a_1^2 + 3a_2^2 - 6 + 2a_1a_2 - a_1 - a_2}{21} \\
& \left. + \langle P_4 \rangle \frac{3a_1^2 + 3a_2^2 + 8 + 2a_1a_2 - 8a_1 - 8a_2}{35} \right]
\end{aligned} \tag{S2}$$

$$\begin{aligned}
I_0 \sum \alpha_{21}^2 = b & \left[ \frac{a_1^2 + a_2^2 + 1 - a_1a_2 - a_1 - a_2}{15} \right. \\
& + \langle P_2 \rangle \frac{a_1^2 + a_2^2 - 2 - 4a_1a_2 + 2a_1 + 2a_2}{21} \\
& \left. + \langle P_4 \rangle \frac{3a_1^2 + 3a_2^2 + 8 + 2a_1a_2 - 8a_1 - 8a_2}{280} \right]
\end{aligned} \tag{S3}$$

$$\begin{aligned}
I_0 \sum \alpha_{32}^2 = b & \left[ \frac{a_1^2 + a_2^2 + 1 - a_1a_2 - a_1 - a_2}{15} \right. \\
& - \langle P_2 \rangle \frac{a_1^2 + a_2^2 - 2 - 4a_1a_2 + 2a_1 + 2a_2}{42} \\
& \left. - \langle P_4 \rangle \frac{3a_1^2 + 3a_2^2 + 8 + 2a_1a_2 - 8a_1 - 8a_2}{70} \right]
\end{aligned} \tag{S4}$$

$$\begin{aligned}
I_0 \sum \alpha_{22} 2\alpha_{33} = b & \left[ \frac{a_1^2 + a_2^2 + 1 + 4a_1a_2 + 4a_1 + 4a_2}{15} \right. \\
& - \langle P_2 \rangle \frac{a_1^2 + a_2^2 - 2 + 10a_1a_2 - 5a_1 - 5a_2}{42} \\
& \left. - \langle P_4 \rangle \frac{3a_1^2 + 3a_2^2 + 8 + 2a_1a_2 - 8a_1 - 8a_2}{70} \right]
\end{aligned} \tag{S5}$$

of which the first four are directly given by the scattering intensities gathered as shown in Figure S1. However, with only four measurements, the system is underdetermined, and a fifth value would be necessary to solve for  $\langle P_2 \rangle$  and  $\langle P_4 \rangle$ . Using the original Pigeon method this would be acquired in the form of e.g. a  $45^\circ$  offset of the symmetry angle. Such a measurement

was not conducted for our samples and would still require solving for the solution. Instead, this work uses an alternative method based on a reduced set of four equations as described by Richard-Lacroix<sup>2</sup> and subsequently used by Kida<sup>3</sup>, Hiejima<sup>4,5</sup>. This alternative method requires only a subset of the measurements required for the full analysis as described by Pigeon.

If it can be assumed that the sample studied is rotationally symmetric, the system can be somewhat simplified, arriving at the reduced four equations

$$I_0 \sum \alpha_{22}^2 = b \left[ \frac{8a^2 + 4a + 3}{15} + \langle P_2 \rangle \frac{8a^2 - 2a - 6}{21} + 3\langle P_4 \rangle \frac{a^2 - 2a + 1}{35} \right] = I_{yy} \quad (S6)$$

$$I_0 \sum \alpha_{33}^2 = b \left[ \frac{8a^2 + 4a + 3}{15} - 2\langle P_2 \rangle \frac{8a^2 - 2a - 6}{21} + 8\langle P_4 \rangle \frac{a^2 - 2a + 1}{35} \right] = I_{zz} \quad (S7)$$

$$I_0 \sum \alpha_{32}^2 = b \left[ \frac{a^2 - 2a + 1}{15} - \langle P_2 \rangle \frac{-a^2 + 2a - 1}{21} - 4\langle P_4 \rangle \frac{a^2 - 2a + 1}{35} \right] = I_{yz} \quad (S8)$$

$$\frac{I_{yz}}{I_{zz}} = \frac{a^2 - 2a + 1}{8a^2 + 4a + 3} \quad (S9)$$

Here, Eq. S9 is used to determine the ‘ $a$ ’ parameter, which can thereafter be assumed constant. The parameters  $a$  and  $b$  are related to the principal elements of the polarizability tensor. Ideally, they should be determined from a perfectly randomized sample, i.e. the two orientation parameters defaulting to zero. Lacking such a measurement from a perfectly randomized sample, a measurement from the sample with the most random orientation was used instead. In our case, this was the DD1-low sample measured in the middle (core) of the filament.

The fingerprint regions for symmetric and asymmetric stretching (i.e. 1130 and 1063 cm<sup>-1</sup>, respectively) in the Raman spectra were used to determine the orientation parameters. The raw data was corrected for background noise using the MATLAB *msbackadj* tool and the fingerprint spectrum peaks were located. Then the Raman intensity was determined as the integrated value under the full width at half maximum for the two peaks and these values were used to solve for the orientation parameters. Using this mean area metric, the calculated

orientation values were robust. However, it must be noted that the data from the sample DD1-high was significantly noisier than the remaining DD1 and DD10 samples, so the calculated values for this sample are more uncertain.

Performing the calculations on the 1130 cm<sup>-1</sup> Raman peak (symmetric stretching), we obtain a value for the  $a$  parameter of -0.54, which corresponds well to comparable equivalent numbers measured by Kida et al. on HDPE samples. By assuming rotational symmetry and approximating the  $a$  parameter, the system is now fully determined and the orientation parameters  $\langle P_2 \rangle$  and  $\langle P_4 \rangle$  was solved for using MATLAB's *fsolve* function.

### Orientation Parameter Calculation from WAXS data

WAXS images from the 2D map were summed along the  $z$  direction to give a statistical average and improve the signal-to-noise ratio. The background scattering was subtracted from the normalized images and polarization and solid angle corrections were applied. The intensity profiles of the (110)-plane peak were extracted by azimuthal integration using pyFAI<sup>6</sup> in the interval  $q = 1.49\text{-}1.55 \text{ \AA}^{-1}$ . The resulting profiles were fitted with the sum of a linear and a Lorentzian distribution or with the sum of two Lorentzian distributions. Under the assumption of 'simple fiber symmetry' in the filament specimen (i.e. both the scattering structure and the orientation distribution of scattering structures have cylindrical symmetry), the Herman's orientation parameter can be calculated by

$$\langle P_2 \rangle = \frac{\int_0^{\pi} d\varphi I(\mathbf{q}, \varphi) P_2(\cos \varphi) \sin \varphi}{\int_0^{\pi} d\varphi I(\mathbf{q}, \varphi) \sin \varphi} \quad (\text{S10})$$

where  $\mathbf{q}$  is the momentum transfer in reciprocal space and  $\varphi$  is azimuthal scattering angle.  $\langle P_2 \rangle$  values calculated from the (110) plane can then be transformed to  $\langle P_2 \rangle_c$  coefficients relative to the  $c$ -axis (i.e. fiber axis) orientation, by the relation  $\langle P_2 \rangle_c = -2\langle P_2 \rangle_{110}$ .<sup>7,8</sup>

## SAXS Computed Tomography

Following the notation by Schroer et al.<sup>9</sup>, the full projected SAXS pattern measured at a given position  $r$  is

$$I_{\mathbf{q}}(r, \theta) = I_0 \int ds f(\theta, s, r) p_{\mathbf{q}, \theta}(x, y) g(\theta, s, r) \quad (\text{S11})$$

where  $I_{\mathbf{q}}(r, \theta)$  is a function of  $\mathbf{q} = (q_r, q_z)$ ,  $p_{\mathbf{q}, \theta}(x, y)$  is the SAXS cross section at sample position  $(x, y)$  with sample rotation  $\theta$ ,  $f(\theta, s, r) = \exp\{-\int_{-\infty}^s ds' \mu[x(s', r), y(s', r)]\}$  describe the attenuation of the incident X-ray beam and  $g(\theta, s, r) = \exp\{-\int_s^{\infty} ds' \mu[x(s', r), y(s', r)]\}$  describe the attenuation of the forward scattered beam. By combining  $f$  and  $g$  and pulling them out of the integral in Eq. (S11), one obtains the following expression

$$\frac{I_{\mathbf{q}}(r, \theta)}{I_1} = \int ds p_{\mathbf{q}, \theta}[x(s, r), y(s, r)] \quad (\text{S12})$$

where  $I_{\mathbf{q}}(r, \theta)/I_1$  is the transmission corrected intensity of the sample. The full SAXS pattern in Eq. (S11) can only be solved for cases where the signal is rotationally invariant, i.e., the sum of all line integrals forming a projection is constant under rotation of the sample. In general, rotational invariance does not exist for  $q_r \neq 0$ , where the momentum transfer vector is not parallel to the rotation axis, except in special cases where additional symmetry is present, such as isotropy or fiber symmetry along the  $q_z$  axis. If the scattering signal from the sample is rotationally invariant, the full SAXS pattern can be reconstructed at each location  $(x, y)$ . A full discussion on the rotational invariance in our samples follows below.

## Rotational Invariance

In order to verify that the full scattering patterns can be reconstructed, a rotational invariance check is performed following Ref.<sup>10</sup>. Each individual pixel on the detector represent a fixed point in q-space  $\mathbf{q} = (q_r, q_z)$  that remains constant during the measurement. For each pixel, a

value  $w_q$  is assigned to the sum of all intensities measured at this pixel during a single line scan:  $w_q(d_r, d_z) = \sum_{r=0}^N I_q(d_r, d_z, r)$ . For rotational invariance to be present in the sample this value must be constant under rotation, i.e. the information can change its translational position but is not lost. The pixel-wise rotational invariance is calculated by the ratio of the standard deviation to the mean of  $w_q(d_r, d_z)$  over all rotations.

$$\frac{\sigma(w_q(d_r, d_z))}{w_q(d_r, d_z)} \quad (\text{S13})$$

Figure S3 shows the pixel-wise rotational invariance calculated for samples DD1-high and DD10-high. Whereas the DD1-high sample displays rotational invariance for most of the scattering pattern, owing to the fiber symmetry of the sample, the DD10-high sample shows that rotational invariance is not present along the equatorial. We speculate that this lack of rotational invariance is due additional scattering from fibrillar scatterers inside the fiber or an artifact of the employed spiral scanning technique. Areas near  $\mathbf{q} = (0,0)$  are not rotationally invariant due to stray light from the partially transparent beamstop.

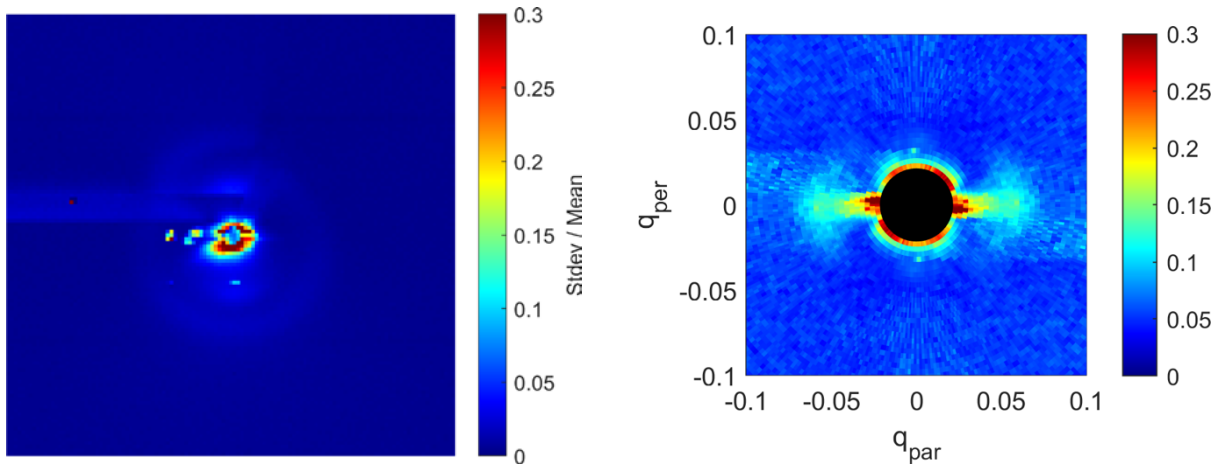


**Figure S3.** Pixel-wise rotational invariance for sample DD1-high (left) and DD10-high (right).

## Reconstruction

Before reconstruction, a rotational invariance check was performed on the data following Ref.<sup>10</sup>. All SAXS patterns were azimuthally integrated using pyFAI and regrouped into 360 azimuthal and 60 radial segments of  $1^\circ \times 0.03 \text{ \AA}^{-1}$  each. Since the scattering intensity is symmetric with respect to the fiber axis, the number of segments was further reduced to an azimuthal range of  $180^\circ$  by averaging. The intensity of each individual segment was then reconstructed; in total 10800 independent reconstructions were performed. Each reconstruction was performed using the TIGRE toolbox for MATLAB and the SART (simultaneous algebraic reconstruction technique) algorithm with applied total variation regularization.<sup>11</sup> The SART-TV reconstruction technique has shown to perform well in cases where the number of projections is undersampled,<sup>12,13</sup> as in this case. A single reconstruction took roughly 20 s to compute on an Nvidia Quadro P2200. After completing the reconstructions, the individual segments were regrouped to form the full SAXS patterns for further analysis. A step by step visualization of the reconstruction is found on Figure S4.

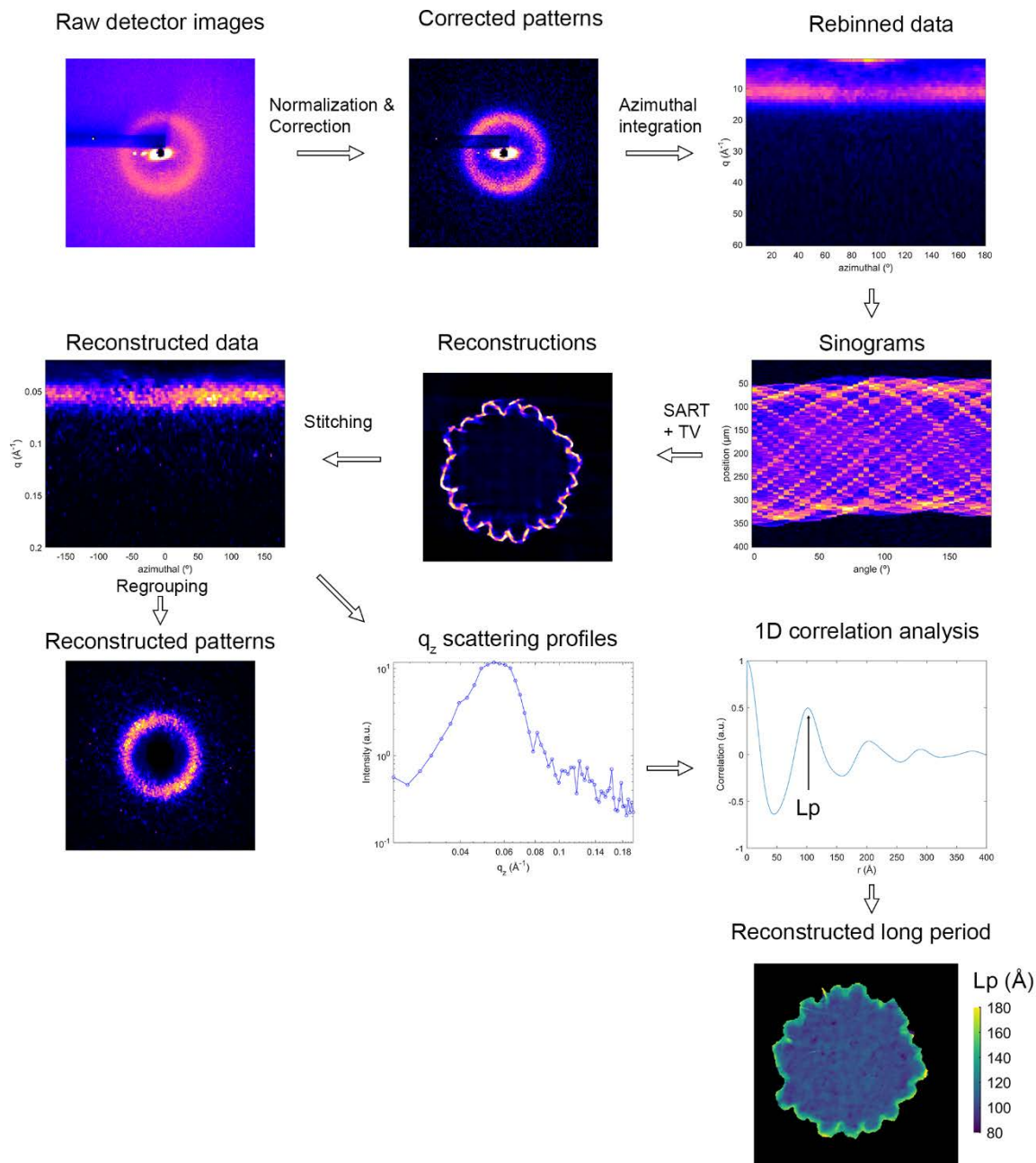


**Figure S4.** Successive SAXS-CT reconstruction steps. The raw detector images are normalized and transmission corrected followed by a background subtraction. The pixel-wise intensities are then azimuthally integrated and regrouped. Each individual segment is reconstructed and stitched together to obtain the reconstructed scattering pattern. Afterwards, additional analysis is performed on the reconstructed data to obtain morphological features, e.g. the lamellar long period is obtained from 1D correlation analysis.

## SAXS Analysis

The reconstructed SAXS patterns were radially integrated along  $q_z$  to obtain one-dimensional (1D) scattering intensities. From these intensity profiles, the 1D correlation function of the electron density distribution is calculated using the equation

$$\Gamma(x) = \frac{1}{Q^*} \int_0^\infty I(q) q^2 \cos q \, dq \quad (\text{S14})$$

where  $Q^*$  is the Scattering Invariant. Before performing the calculation, the 1D intensity needs to be extrapolated to  $q = 0$  and  $q = \infty$ . The intensity at low- $q$  is extrapolated by fitting the Guinier function

$$I(q) = A e^{Bq^2} \quad (\text{S15})$$

and the high- $q$  intensity is extrapolated using the Porod function

$$I(q) = K q^{-4} e^{-\sigma^2 q^2} + \text{Bg} \quad (\text{S16})$$

where Bg is the  $q$ -independent background. The long period ( $Lp$ ) of the stacked lamellae structure was estimated from the first maximum of the 1D correlation function.

## Beam Damage Issues

Radiation damage of the samples was a strong concern during the SAXS tomography experiments since polymers are particularly sensitive to radiation damage caused by X-ray irradiation.<sup>14,15</sup> These radiation damage issues become even more relevant as the spatial resolution of the experiment is increased. In our experiments, we use a narrowly focused X-ray beam (diameter on the order of 1  $\mu\text{m}$ ) leading to a highly localized X-ray dose in the sample. Moreover, conventional SAXS tomography requires multiple projection scans of the same sample volume. During our initial testing, we found that the radiation damage from performing multiple scans on the same slice of the fiber lead to a significant degradation of the scattering signal. In order to obtain projections from multiple angle while maintaining a sufficient signal-

to-noise, we implemented a scanning protocol where the fiber was raised by half the beam diameter after each projection. Control-scans before and after the experiment confirmed no significant change in scattering signal when using this scanning protocol. Furthermore, the samples were examined by optical microscope after the experiment. Figure S5 shows the optical micrograph of the DD1-high filament after exposure. The lower arrows indicates an area of the fiber where multiple scans were performed on the same slice. The upper area indicates an area of the fiber where the alternate scanning protocol was implemented. The darker color is caused by a chemistry changes in the fiber, likely a build-up of C due to breaking of C-H bonds subsequent release of H. From the optical micrograph, it is apparent that the part of the fiber exposed to multiple scans on the same slice is significantly darker than the area of the fiber exposed to our alternate scanning protocol. We emphasize that even though the optical micrograph suggests a change in the fiber chemistry in area exposed to the alternate scanning protocol, we did not observe any significant changes in the scattering pattern in our control-scans. We speculate that the mechanisms leading to changes in chemistry are different from the mechanisms leading to structural changes in the morphology, and that the total exposure using our alternate scanning protocol does not significantly change the morphology.

The experimental setup did not allow for placing the sample in vacuum. Instead, to minimize the ambient oxygen around the sample, it was continuously flushed with Ar during the measurements. Furthermore, it was not possible to cryo-cool the sample during measurements, as the vibrations from the cryo-chamber would cause excessive movement of the sample, effectively lowering the experimental resolution.

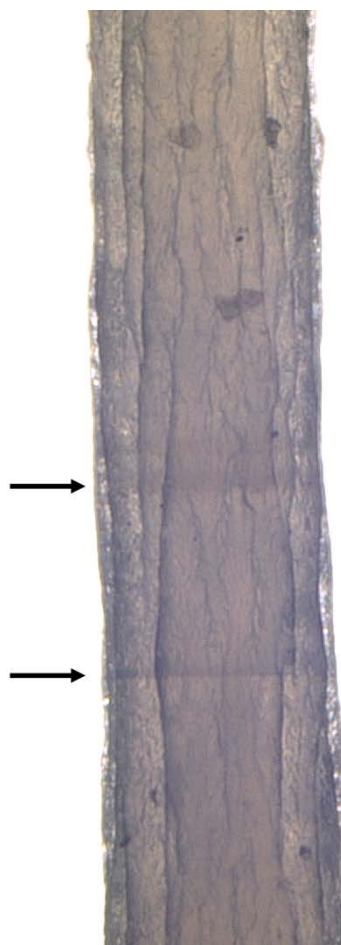


**Figure S5.** Optical micrograph of sample DD1-high after SAXS tomography measurements. The lower arrows indicates an area of the fiber where multiple scans were performed on the same slice. The upper area indicates an area of the fiber where the alternate scanning protocol was implemented (projection scan followed by raising of the fiber).

## Estimation of Skin Region Thickness

We have devised the following method to determine the thickness of the skin region from the reconstructed SAXS data:

The average value of  $Lp$  (or integrated  $q_z$  intensity) in the core region is determined along with its standard deviation. We consider the skin region to start when the value of  $Lp$  (or integrated  $q_z$  intensity) exceeds the average value in the core + 2 standard deviations. A threshold filter is then applied to the  $Lp$  (or integrated  $q_z$  intensity) map and pixels values below the average value of the core + 2 standard deviations is set to 0 and any pixels above this value is set to 1. Afterwards, any pixels not connected to the skin region (i.e. pixels in the core with values above the 95% confidence interval assuming a Gaussian distribution) are set to zero. The result of the threshold filter is a black and white image with white pixels representing the fiber skin. We then use the *ABSsnake* plugin<sup>16</sup> for ImageJ on the black and white threshold image to determine the inner and outer contour of the fiber skin. The plugin uses an iterative snake model to deform a curve along the edge of a grayscale image. To determine the inner (outer) contour of the fiber skin, we draw a crude starting contour for the initial step of the plugin's algorithm by hand on the inside (outside) of the skin region. The contours are then determined by the algorithm in 500 iterations with its default parameters. The results of the segmentation using the *ABSsnake* plugin is seen for sample DD1-high in Figure S6 and DD10-high in Figure S7. Finally, the average thickness of the skin region is quantified by calculating the average distance from every point on the outer contour to the closest point on the inner contour.

We point out that the devised method for determining the skin thickness is prone to errors in areas where two neighboring skin regions are bridged. This bridging is likely an artifact of the tomographic reconstruction. A prominent example of such bridge is found at the bottom of the reconstructed  $q_z$  intensity map of the DD1-high sample.

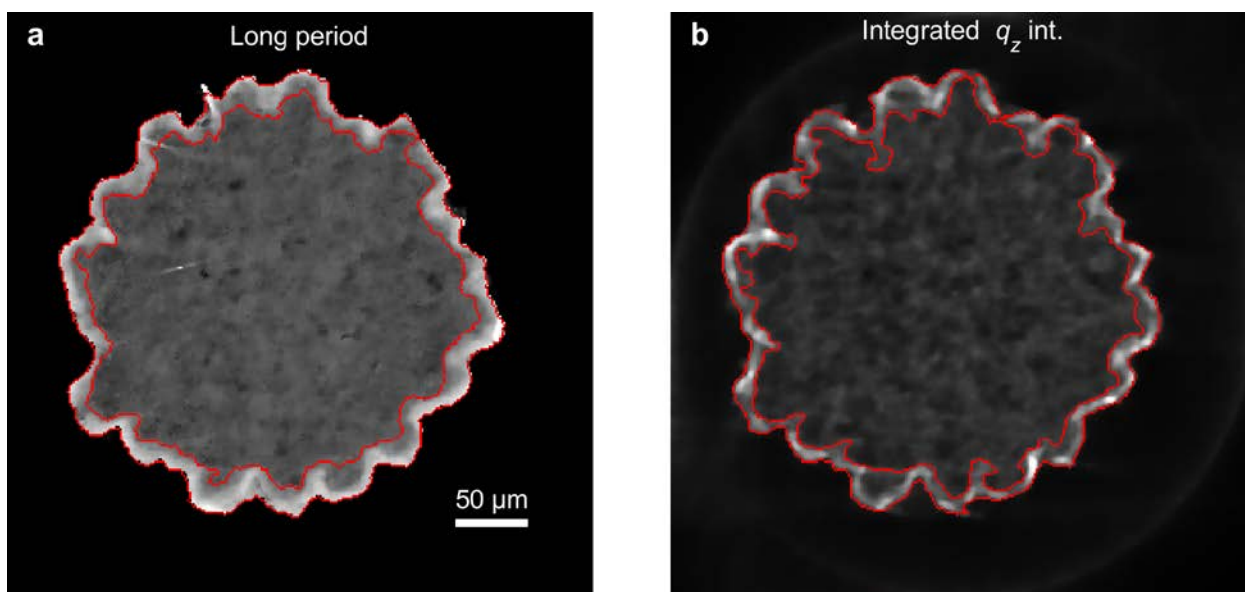


**Figure S6.** Inner and outer contour of the skin region in sample DD1-high based on the reconstructed (a) long period ( $Lp$ ) and (b) integrated  $q_z$  intensity as determined by the *ABSsnake* plugin.

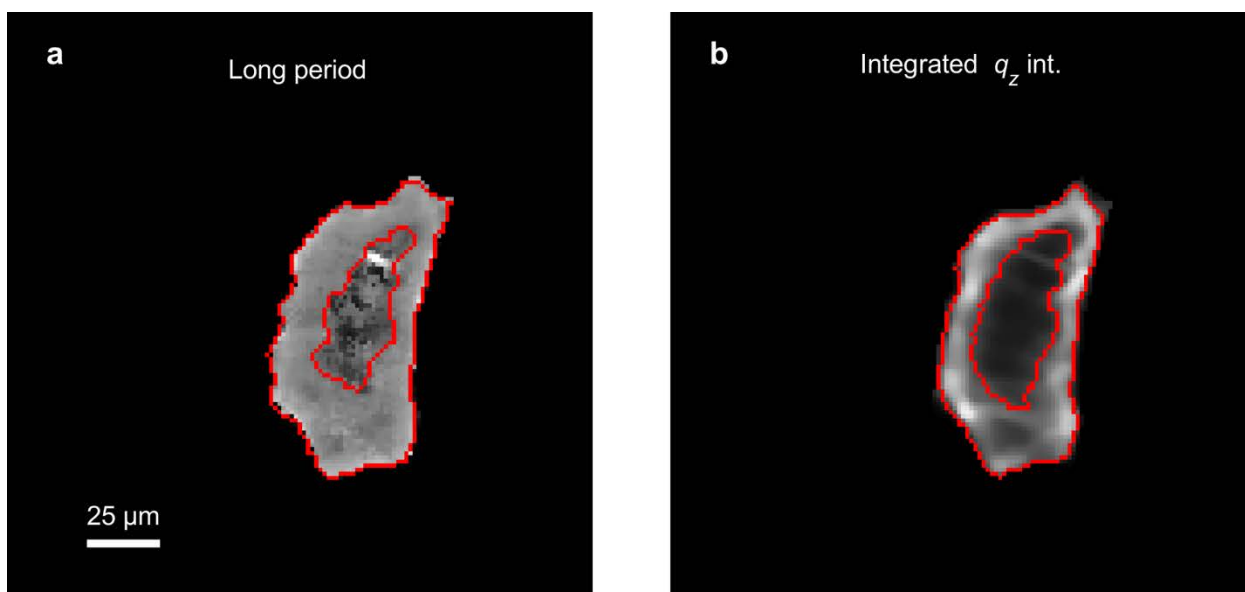


**Figure S7.** Inner and outer contour of the skin region in sample DD10-high based on the reconstructed (a) long period ( $Lp$ ) and (b) integrated  $q_z$  intensity as determined by the *ABSsnake* plugin.

## References

- (1) Pigeon, M.; Prud'homme, R. E.; Pezolet, M. Characterization of Molecular Orientation in Polyethylene by Raman Spectroscopy. *Macromolecules* **1991**, *24*, 5687–5694.
- (2) Richard-Lacroix, M.; Pellerin, C. Accurate New Method for Molecular Orientation Quantification Using Polarized Raman Spectroscopy. *Macromolecules* **2013**, *46*, 5561–5569.
- (3) Kida, T.; Oku, T.; Hiejima, Y.; Nitta, K. H. Deformation Mechanism of High-Density Polyethylene Probed by in Situ Raman Spectroscopy. *Polymer (Guildf)*. **2015**, *58*, 88–95.
- (4) Hiejima, Y.; Kida, T.; Nitta, K. H. In Situ Monitoring of Orientation Parameters and Orientation Distribution Functions of Polyethylenes during Tensile Tests. *Macromol. Symp.* **2018**, *377*, 1–5.
- (5) Hiejima, Y.; Okuda, T.; Kono, K.; Nitta, K. H. Orientation Behavior and Deformation Mechanism of Polyethylene Gels during Cold Drawing Determined by in Situ Raman Spectroscopy. *Polymer (Guildf)*. **2019**, *176*, 30–37.
- (6) Kieffer, J.; Wright, J. P. PyFAI: A Python Library for High Performance Azimuthal Integration on GPU. *Powder Diffr.* **2013**, *28*, S339–S350.
- (7) Lovell, R.; Mitchell, G. R. Molecular Orientation Distribution Derived from an Arbitrary Reflection. *Acta Crystallogr. Sect. A* **1981**, *37*, 135–137.
- (8) Lafrance, C. P.; Pézolet, M.; Prud'homme, R. E. Study of the Distribution of Molecular Orientation in Highly Oriented Polyethylene by X-Ray Diffraction. *Macromolecules* **1991**, *24*, 4948–4956.
- (9) Schroer, C. G.; Kuhlmann, M.; Roth, S. V.; Gehrke, R.; Stribeck, N.; Almendarez-

- Camarillo, A.; Lengeler, B. Mapping the Local Nanostructure inside a Specimen by Tomographic Small-Angle x-Ray Scattering. *Appl. Phys. Lett.* **2006**, *88*, 1–4.
- (10) Feldkamp, J. M. Scanning Small-Angle X-Ray Scattering Tomography: Non-Destructive Access to Local Nanostructure, Technischen Universität Dresden, 2009.
- (11) Biguri, A.; Dosanjh, M.; Hancock, S.; Soleimani, M. TIGRE: A MATLAB-GPU Toolbox for CBCT Image Reconstruction. *Biomed. Phys. Eng. Express* **2016**, *2*, 055010.
- (12) Sidky, E. Y.; Kao, C. M.; Pan, X. Accurate Image Reconstruction from Few-Views and Limited-Angle Data in Divergent-Beam CT. *J. Xray. Sci. Technol.* **2006**, *14*, 119–139.
- (13) Schaff, F.; Bech, M.; Zaslansky, P.; Jud, C.; Liebi, M.; Guizar-Sicairos, M.; Pfeiffer, F. Six-Dimensional Real and Reciprocal Space Small-Angle X-Ray Scattering Tomography. *Nature* **2015**, *527*, 353–356.
- (14) Coffey, T.; Urquhart, S. G.; Ade, H. Characterization of the Effects of Soft X-Ray Irradiation on Polymers. *J. Electron Spectros. Relat. Phenomena* **2002**, *122*, 65–78.
- (15) Murray, J. W.; Garman, E. F.; Ravelli, R. B. G. X-Ray Absorption by Macromolecular Crystals: The Effects of Wavelength and Crystal Composition on Absorbed Dose. *J. Appl. Crystallogr.* **2004**, *37*, 513–522.
- (16) Andrey, P.; Boudier, T. Adaptive Active Contours (Snakes) for the Segmentation of Complex Structures in Biological Images. *ImageJ Conf.* **2006**, 18–29.



Technical  
University of  
Denmark

Fysikvej, Building 311  
2800 Kgs. Lyngby  
Tlf. 4525 3344

[www.fysik.dtu.dk](http://www.fysik.dtu.dk)